Semiconductors, Vol. 34, No. 11, 2000, pp. 1229–1247. Translated from Fizika i Tekhnika Poluprovodnikov, Vol. 34, No. 11, 2000, pp. 1281–1299.

REVIEWS

Silicon–Germanium Nanostructures with Quantum Dots: Formation Mechanisms and Electrical Properties

O. P. Pchelyakov*, Yu. B. Bolkhovityanov*, A. V. Dvurechenskiĭ*, L. V. Sokolov*, A. I. Nikiforov*, A. I. Yakimov*, and B. Voigtländer**

** Institute of Semiconductor Physics, Siberian Division, Russian Academy of Sciences, pr. Akademika Lavrent'eva 13, Novosibirsk, 630090 Russia*

*** Research Center, Yuelich, Germany*

Submitted April 17, 2000; accepted for publication May 10, 2000

Abstract—The generally accepted notions about the formation mechanisms for germanium islands with nanometer-scale sizes in a Ge-on-Si system are reviewed on the basis of analysis of recent publications. The presence of elastic strains in the epilayers and in the three-dimensional Ge islands on Si is a key factor that not only initiates a morphological transition from a planar film to an island-containing film (the Stranski–Krastanov mechanism) but also influences the subsequent stages of the islands' evolution, including their shape, size, and spatial distribution. In many cases, this factor modifies appreciably the classical mechanisms of phase-formation and their sequence up to the quasi-equilibrium coexistence of three-dimensional Ge nanoislands at the surface of the Si substrate. The methods for improving the degree of the ordering of nanoislands to attain the smallest possible sizes and large density of areal distribution of these islands are discussed. The published data on optical absorption in the multilayered Ge–Si systems with quantum dots are considered; these data are indicative of an anomalously large cross section of intraband absorption, which makes this class of nanostructures promising for the development of photodetectors of the infrared region of the spectrum. The results of original studies of electrical and optical properties of heterostructures that involve Ge quantum dots and are synthesized by molecular-beam epitaxy on the Si substrates are reported. © *2000 MAIK "Nauka/Interperiodica".*

1. INTRODUCTION

Nanostructures based on the germanium-on-silicon heterosystem attract the attention of technologists owing to significant progress in the development of new quantum-effect devices in spite of a 4% difference between the lattice parameters of Ge and Si. We witness the appearance of silicon–germanium light-emitting and photodetecting devices that make silicon technology quite competitive with those of conventional optoelectronic materials, such as the III–V compounds [1–5]. In recent years, the potential applications of the Ge–Si-based semiconductor materials containing the nanometer-sized Ge clusters (quantum dots) embedded in the Si matrix have become apparent. Interest in the Ge and Si nanoclusters is related to the following circumstances: (i) progress in the development of technology for producing a Ge-nanocluster array that is fairly uniform in size; (ii) the sizes of nanoclusters have been reduced to the values that ensure the manifestation of the size-quantization effects and the electron–electron interaction up to room temperature; and (iii) compatibility of the developed methods with existing silicon technology for the production of discrete devices and circuits. Such designs that have been considered exotic until recently may bring about an actual revolution in silicon integration technology.

A steady increase in the number of publications worldwide devoted to low-dimensional heterostructures is indicative of the growing interest in these structures. Figure 1 shows the histograms for the number of annual publications that include the keywords "quantum wells" and "quantum dots." In the latter case, a steady increase in the annual number of relevant publications is observed. Starting in 1992, changes became evident in the technology producing the structures with quantum dots. Before that time, the main method for forming such structures was photolithography, with the constraint on the minimum sizes inherent in this method. Manifestation of the effect of ordering in the array of nanometer-sized islands in the Ge–Si and InAs–GaAs heterosystems made it possible to obtain quantum dots that had no defects, had the smallest possible size (10–100 nm), and had the density of 10^{10}–10^{11} cm^{-2}, which made the atomlike characteristics of these systems more pronounced in the relevant electronic and optical spectra. The development of studies in this field is illustrated in Fig. 2 by histograms of the annual number of publications devoted to a Ge–Si system. It is in this system that the arrays of islands were first used to observe the one-electron effects [6]. Later, most studies of electronic properties of quantum dots (QDs) were based on III–V compounds. This was caused by the following factors: (a) progress in the technology of heteroepitaxy for III–V compounds; (b) the possibility of producing the heterostructures of type I (the offsets of the conduction

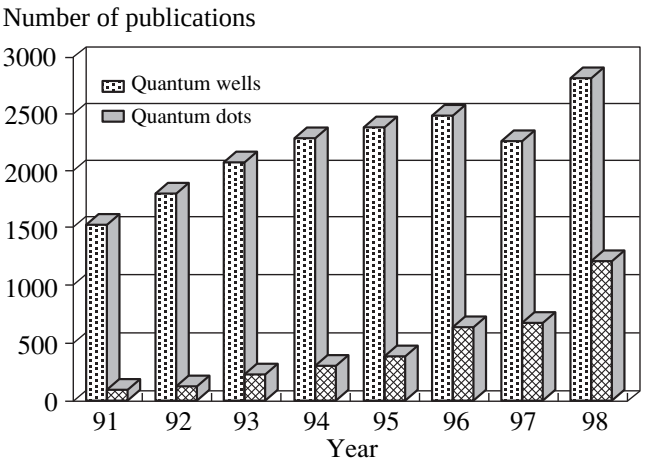

Fig. 1. The number of annual publications according to the data of the Materials Science Citation Index (MSCI) for 1990–1998. Search was based on the keywords "quantum wells" and "quantum dots."

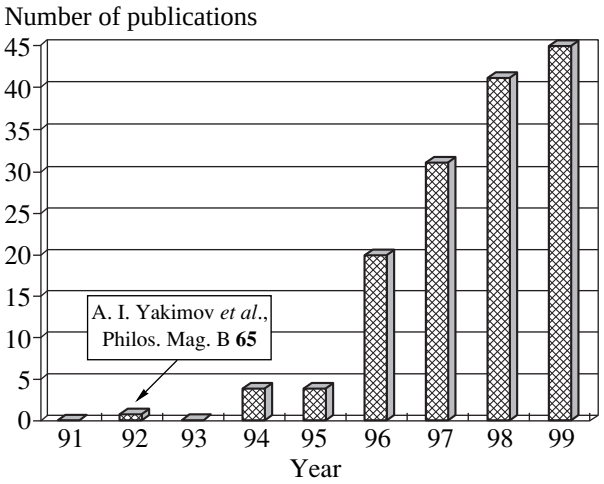

Fig. 2. Selection (from the complex "quantum dots," see Fig. 1) of publications devoted to the island growth of Ge (GeSi) on Si and also to the properties of these entities (for the year 1999, the data are given for 10 months; the data refer to the most important journals).

and valence bands are of opposite signs), which is important for the optical properties of these systems; and (c) the small value of the charge-carrier effective mass, which ensured the manifestation of size-quantization effects for islands of a relatively large size. The first studies of QDs in III–V compounds were performed on the basis of InAs–GaAs structures [7, 8].

A transition from the layer-by-layer [i.e., two-dimensional (2D)] growth of the film to the formation of three-dimensional (3D) islands (the Stranski–Krastanov mechanism) has been studied for a long time in the germanium-on-silicon heterosystem. The first publication devoted to this heterosystem, in which the observation of pseudomorphous Ge stripes (referred to now as quantum wires) that follow the outlines of steps and of the nanometer-sized islands (currently, quantum dots) was reported, was apparently that of the study [9] performed at the Institute of Semiconductor Physics (Siberian Division, Academy of Sciences of USSR) as far back as 1974. At relatively low temperatures of synthesis, such islands do not contain the misfit dislocations even if the thickness of the islands exceeds appreciably the critical value, which was demonstrated most clearly in studies of the Ge–Si [10] and InGaAs–GaAs [11] systems. Following these publications, a sharp increase in the study of the mechanisms of formation of strained islands and the special features of their ordering set in, because an opportunity arose to form 3D objects that have no defects (no misfit dislocations), have nanometer-scale sizes, and may find practical applications in nanoelectronics.

The objective of this review was to analyze the development and current ideas about the mechanisms of ordering of the QD ensembles in the course of heteroepitaxy. This has been the subject of a number of reviews [12–14]. However, without laying claim to completeness, as concerns a review of all heterosystems, we have attempted to outline the generally accepted concepts of the Ge-on-Si system and to supplement these with an analysis of the newest data, including the results of our experiments with synthesis of a Ge–Si heterosystem with QDs, and the study of the electronic and optical properties of this heterosystem.

In Section 2, we consider the driving forces and main mechanisms of evolution and ordering of nanoobjects in heterosystems with a large lattice mismatch in the course of molecular-beam epitaxy (MBE) and heat treatment. In Section 3, we analyze the experimental observations of cluster formation and self-organization for Ge–Si nanostructures at the silicon surface and discuss the feasible methods for enhancing the ordering, reducing the sizes, and increasing the density of the germanium QDs. In Section 4, we summarize the original results of our studies of the electronic and optical properties of heterostructures and multilayered compositions with Ge QDs.

2. BASIC PREMISES

It is possible to distinguish between the stages of nucleation and further development in the formation of 3D islands. The main pattern in the nucleation of islands in an epitaxial heterosystem is governed by the balance between the surface energies of the film and substrate and also between the energy of the film–substrate interface and internal energy of the island bulk. The free energy of a newly formed island nucleus at the substrate surface may be expressed as the sum of three terms [15]; i.e.,

$$\Delta G = -V\Delta\mu + \gamma s + E_i(V, h/l).$$

Here, the first term accounts for the formation energy of a new nucleus with the volume V, with $\Delta\mu$ standing for the thermodynamic force for crystallization in the event of supersaturation. The second term corresponds to the work required for the formation of additional surface area s, with γ standing for the nucleus surface energy. The third term describes additional energy that is brought about owing to elastic strain in the nucleus. The first and second terms in the above expression correspond to the classical version of the nucleation theory (see, for example, [16]), whereas the third term appears only in the case where strained films are grown. For large values of the lattice mismatch, such as those that occur in a Ge–Si system, this additional energy depends not only on the nucleus volume, but also on its shape (i.e., on the ratio h/l, where h is the height and l is the cross-sectional dimension of the nucleus), and is important in the transition from the 2D to 3D growth mechanisms. According to calculations [15], the contribution of this term is represented by a rapidly decreasing function of h/l. The more pronounced the 3D state of a strained nucleus, the larger the contribution of elastic relaxation (a decrease in the strain in the regions of the nucleus that are the most remote from the substrate), and the smaller the additional contribution of the strain energy to the free energy of the nucleus. The surface energy of a system composed of the Ge film (with Ge island) and the Si substrate also depends on the Ge coating thickness (and the shape of the Ge island) [15, 17]. At present, it is generally believed that the key factor in the transition from the 2D (layer-by-layer) to the 3D (island-type) growth of pseudomorphous films is an energy gain due to a decrease in elastic stresses via their elastic relaxation. We note that, in the case of homoepitaxy on a fairly clean surface, the bulk islands are not formed for almost all semiconductors, and the film grows owing to either the motion of step (the step–layer growth) or the formation and coalescence of 2D islands. As will be clear from what follows, stresses also play an important role in the development of 3D islands and their distribution in size.

The determining role of elastic relaxation, which brings about the morphological instability of the film surface, was demonstrated by Asaro and Tiller (1972) [18] and by Grinfel'd (1986) [19]. The basic aspect of this model is the proposition that the rough surface of a strained layer has a lower total energy (the strain energy combined with the surface energy) as a result of elastic relaxation of stresses at the tops of asperities. An increase in the surface energy due to an increase in the rough-surface area is a factor that opposes the development of the film's surface relief; however, this factor reduces the energy gain via relaxation only in part [19]. The larger the mismatch between the film and substrate lattices, the smaller the thickness of the pseudomorphous film at which morphological stability is lost. The formation of islands is an extreme manifestation of morphological instability of strained films and is commonly observed in systems with large values of mismatch between the film and substrate lattices ($\varepsilon > 2\%$); the Ge–Si and InAs–GaAs structures are typical representatives of such systems. If the surface energy of a new phase is somehow reduced, the strained film can lose its morphological stability even for small values of mismatch. Thus, if the strained film is in contact with a liquid phase, in which case the surface energy of the film is appreciably lower than that of the film–vacuum (or film–vapor) interface, formation of islands is observed in a Ge_xSi_{1-x}–Si(001) system for low values of the mismatch $x \approx 0.05$ ($\varepsilon \approx 0.2\%$) [20]. The same small values of elastic strains brought about a branching in the shape of the island-type film in an $In_xGa_{1-x}As$–GaAs(111)*A* system formed also in contact with a liquid phase, and the splitting of this system into separate micrometer-sized islands [21]. In this paper, a a unique example of observing the dislocation-free islands that are formed on the substrate with (111) orientation and have a thickness exceeding the critical value for the introduction of misfit dislocations is reported; apparently, this result is a consequence of a decrease in the surface energy of the film that is in contact with the liquid phase.

According to classical notions (see, for example, [22]), formation of a new phase includes the following main stages: nucleation of the new-phase centers, their independent growth, and, finally, the development of these centers in interaction with each other (the so-called Ostwald ripening). This phenomenon represents the latest stage of evolution of the new-phase nuclei. If the objective of the study consists in producing an island-type film (as in the case under consideration), this stage of the Ostwald ripening may happen to be the main stage that defines the shape of the island distribution by size. Therefore, the applicability of the Ostwald-ripening model to the analysis of the self-organization of quantum-dimensional clusters in a Ge–Si system (and other systems) has received much attention in available publications.

The first comprehensive theory of Ostwald ripening to describe the formation of clusters (grains) in a volume of supersaturated solid solutions was developed by Lifshitz and Slyozov [23]. Later, this theory was modified by Chakraverty [24] so as to be applied to the surface. Recently, this theory has been widely used to interpret the processes observed at the semiconductor surface using modern high-resolution methods (see, for example, [25–29]). According to this model, the later stage in the development (ripening) of clusters is governed by the interaction of nuclei found within a saturated "sea" of adatoms via the Gibbs–Thomson effect (the equilibrium vapor pressure above the curvilinear surface of the nucleus should be higher than in other cases). The small-sized islands decrease in size owing to a more pronounced curvilinearity of the surface (or the pedestal of a cluster) and, ultimately, cease to exist, whereas the large islands grow. A characteristic feature of the Ostwald-ripening mechanism is a continuous

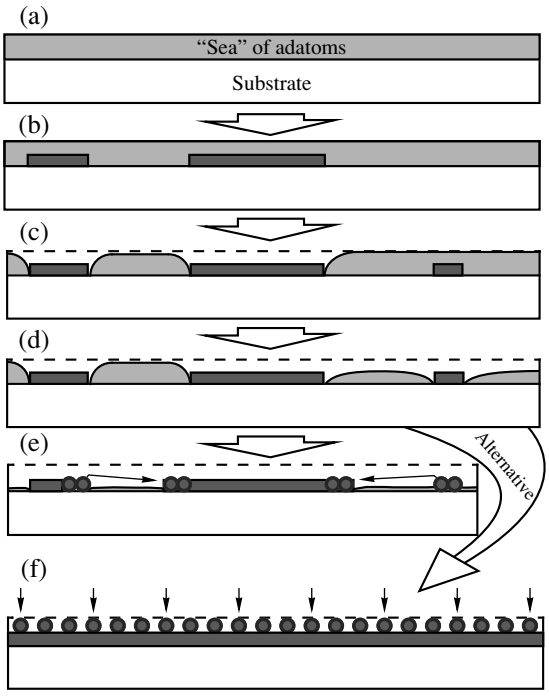

Fig. 3. Schematic representation of the initiation and formation of a new monolayer according to classical concepts forwarded by Kukushkin and Osipov [22] as applied to molecular epitaxy (for example, epitaxy of silicon on silicon). For details, see the text.

increase in the average island size with time and a broadening of the unnormalized distribution of islands in size.

Experimental observations of the development of 2D Si islands at the Si(100) surface are in close agreement with inferences from the Ostwald-ripening model (see, for example, [26]). Figure 3 illustrates schematically the formation and development of a new epitaxial monolayer according to classical concepts of the three stages [22]. In the initial state (representation a), there is a supersaturated adsorbate of Si atoms (a "sea" of adatoms) at the substrate surface, and, in the first stage, nucleation of 2D centers occurs (representation b). Following this comes the second stage consisting in the independent growth of the centers (representation c). During this stage, supersaturation around the centers is reduced; however, these centers do not yet interact with each other because their diffusion-source "feeding" fields do not yet overlap. Therefore, nucleation of new centers continues at the sites away from the islands that have been already formed (representation c, the center at the right). After the diffusion-source fields have overlapped (representation d) and the supersaturation between the islands has been reduced even more, there comes the third stage that consists in the correlated growth of the islands or the Ostwald ripening. According to Kukushkin and Osipov [22], the interaction between the islands occurs via a "generalized self-consistent diffusion-source field" (in the case under consideration, this field is represented by the Si adsorbate). Large islands grow, whereas the small islands cease to exist (representation e). This stage may span a long time if the system is closed and the number of adatoms amounts to less than a single monolayer [26]. The island-size distribution is a reproducible function that depends appreciably on the substrate orientation (see, for example, [30]). In the case of a continuous supply of atoms to the surface (an open system), the islands grow until they are in contact with each other; thus, a continuous monolayer is formed (representation f).

Lifshitz and Slyozov studied the ripening of grains and stated [23], in particular, that elastic strains in the grains may be taken into account, although this would not appreciably affect the shape of the final distributions, because the strains constitute a second-order correction. In fact, in the 3D case considered by Lifshitz and Slyozov, the strains in the 3D grains of a new material may be treated as an addition to the free energy of a cluster; this addition affects the nucleation and the growth rates of the cluster. Such an approach was used by Drucker [31] to evaluate the development of 2D islands at the substrate surface in the case of the Ostwald ripening. However, recent studies have shown that elastic strains in epitaxial films and nucleating 3D islands constitute a key and a multivalued factor that, in the majority of cases, changes radically the pattern of the classical phase-formation mechanisms. Thus, for the growth of Ge on Si and InAs on GaAs, it is the presence of these strains that induces the transition from layer-by-layer growth to the formation of 3D clusters at the surface of underlying Ge (or InAs) layer; as a result, the Stranski–Krastanov mechanism comes into effect. Significant nonuniformity of the elastic relaxation of an island over its height causes the energy gain to depend on the island shape. Several discrete shapes that are most favorable energetically (a "hut,", a "dome," and a "superdome") come into existence. Elastic strains at the cluster periphery increase with increasing cluster size, which affects the rules of attachment of adatoms to a cluster; as a result the growth rate of the clusters decreases [32–34]. It is believed that the emergence and heightening of the barrier related to the above constitute one of the main causes of the observation that the island-size distribution is narrower compared to theoretical predictions based on the Ostwald ripening (see, for example, [33]). Under certain conditions, the role of elastic strains and their relaxation in the islands becomes dominant until a quasi-equilibrium state is established. In this state, both the shape and the size-distribution of islands is time-independent; correspondingly, the ensemble of islands cannot be described in the context of the model based on the Ostwald ripening [29, 35–40].

Figure 4 illustrates schematically the main stages of formation of the strained-island ensemble and their difference from the classical variant. Similarly to what was shown in Fig. 3, there is initially a supersaturated

adsorbate at the surface (a); however, this adsorbate is now formed at the surface of underlying (wetting) layer from the deposited material (Ge). Nucleation of the 3D hut-shaped clusters (representation b) is caused by the elastic-strain relaxation (this is the first difference from the classical theory). Later (representation c), two distinct shapes ("hut" and "dome") come into existence. The energetic advantages of the first and second shapes depends on their volume; however, under certain conditions, the coexistence of these shapes is possible [35, 36] (the second difference from the classical theory). The flow of atoms to the islands with shapes that are more energetically favorable was observed [41] (representation d). In this case, the model of the Ostwald ripening is apparently valid (small islands cease to exist, and large islands grow); however, the island-size distribution is now bimodal rather than unimodal [36, 41]. A reverse transition from a dome shape to a hut shape was also observed (the third difference from the classical theory) [38, 40, 42]. A quasi-equilibrium state of the system is possible, in which case the sizes and shapes of the clusters are virtually time-independent if there is no external flux [39] (representation e) (the fourth difference from classical theory). Chiu [43] has demonstrated theoretically that the probability of the state of the ensemble being stable increases with increasing surface-energy anisotropy (as this energy increases at the facets of the islands). Under certain conditions (when the islands are closely spaced), the interaction of clusters via overlapping elastic-deformation fields in the substrate was substantiated theoretically [44, 45]; this interaction may be conducive to the ordering of spatial distribution of islands at the surface (the fifth difference from the classical theory). Consideration of elastic interaction via the substrate in a system of GeSi–on–Si islands made it possible to interpret the experimental results [46] correctly.

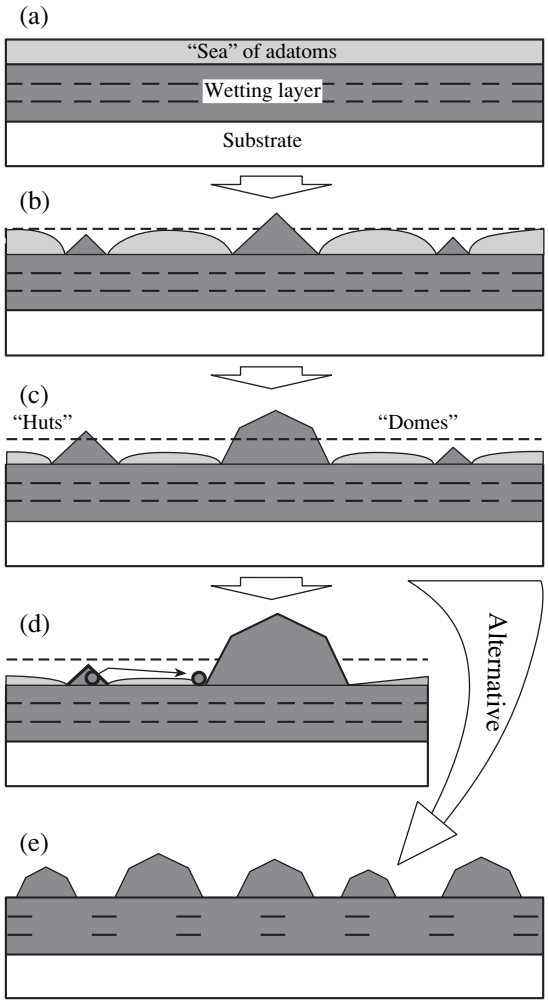

Fig. 4. Schematic representation of the stages of formation of three-dimensional islands in a Ge–Si(001) system. For details, see the text.

3. GROWTH AND SPECIAL FEATURES OF ORDERING IN THE ENSEMBLES OF Ge NANOCLUSTERS

3.1. Morphological Reconstructions

Several stages of the island evolution are observed experimentally in the Ge–Si systems. These stages differ for the substrates with (001) and (111) orientations. From the standpoint of producing quantum objects, the (001) surface is unique, because the compact 3D dislocation-free islands 10–100 nm in size were observed at this surface alone (Fig. 5). Emergence of such islands is observed after a continuous Ge film has been formed; the superstructure domains in this film are easily distinguished between the islands in Fig. 5. The onset of formation of the 3D clusters is accompanied by the emergence of strands in the patterns of high-energy electron diffraction (HEED); these strands are formed as a result of electron scattering by the {105} faces. Such islands are referred to as hut-clusters due to their shape [47]. As the average film thickness increases, the HEED patterns indicate the presence of {113} and {102} faces in addition to the {105} faces. It should be noted that the first study where the HEED method was used to reveal these faces of the Ge islands at the Si(001) surface was carried out the Institute of Semiconductor Physics (Siberian Division, Academy of Sciences of the USSR) as far back as 1987 [48]. The formation of the dome-shaped clusters is characteristic of this stage of growth. A transition from the hut-shaped clusters with sizes of 15–20 nm at the pedestal of the dome-shaped clusters (with average sizes of 50–100 nm) is accompanied with an increase in the degree of relaxation of stresses. According to the data obtained by Floro *et al.* [49], the material in the hut-shaped clusters is elastically relaxed by 20% on average, whereas in the dome-shaped clusters, the relaxation amounts to more than 50% due to a larger ratio between the height and the pedestal size; in this case, the islands remain coherently matched to the substrate. As follows from numerous experimental observations, the last stage in the development and

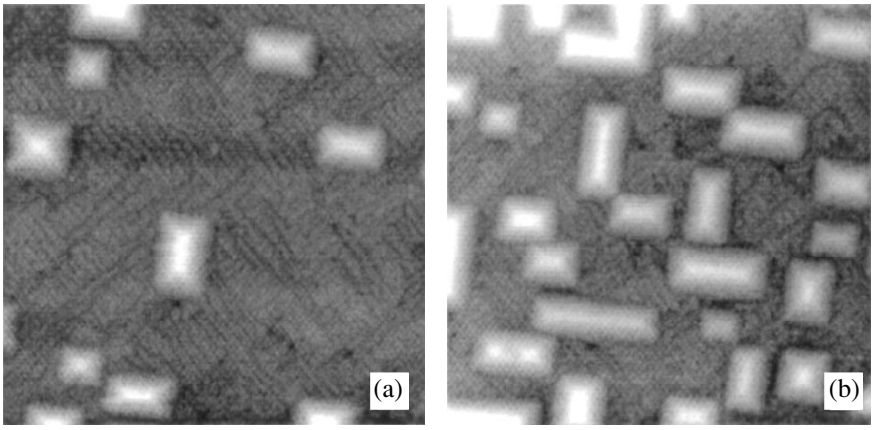

Fig. 5. An STM image of hut-shaped clusters on the Si(001) surface covered with a Ge sublayer with a thickness d_{eff} = (a) 4.6 and (b) 8 ML; T_g = 300°C. The side of the image amounts to 160 nm. STM stands for scanning tunneling microscopy.

structure of Ge_xSi_{1-x} islands on Si(001) and Si(111) consists in the formation of 3D plastically strained islands with misfit dislocations at the interface with the substrate, which is accompanied with a rapid increase in the island sizes (see, for example, [50–52]).

3.2. The Effects of Ordering

Ordering brings about the emergence of islands with preferential sizes, shapes, interisland distances, and relative positions in the system. This is a result of the minimization of the total free energy of the system. The existence of preferential characteristics should manifest itself in the scattering and diffraction spectra of electrons and X-rays interacting with the surface that contains the nanostructures and also in the electronic and optical spectra.

The distribution of Ge islands in size is given much attention in various publications because this parameter of the QD system is extremely important for practical applications. Typical island-size distributions and the range of normalized rms deviations $\sigma/\langle l\rangle$ ($\langle l\rangle$ is the average size) that define the broadening of the distributions are shown schematically in Fig. 6. According to the data reported elsewhere [29], narrower distributions are observed for the dome-shaped islands with average sizes of 50–100 nm (in [29], the Ge islands were grown by chemical deposition in an atmosphere of hydrogen that affects the mobility of Ge adatoms). The narrower distributions for the dome-shaped cluster are explained by the fact that an increase in elastic strain in the substrate, and in the cluster pedestal as the cluster size increases, reduces the growth rate of the cluster (in contrast with cluster development according to the mechanism of the Ostwald ripening). For the hut-shaped clusters obtained by the MBE [34], a similar pattern was observed; i.e., the growth rate of a hut-shaped Ge cluster decreased as its size increased (this phenomenon was studied in more detail in [34]). The above brings about an appreciable narrowing of the island-size distribution. An estimation of the broadening of the distributions for the Ge hut-shaped clusters (shown in Fig. 5) yields $\sigma/\langle l\rangle \sim 0.2$–$0.25$, which is appreciably smaller than for the hut-shaped clusters grown in the hydrogen atmosphere [29] (see Fig. 6, curve *a*). The most uniform Ge island-size distribution was reported in [53] ($\sigma/\langle l\rangle = 0.032$), and, with permission granted by the authors, such islands are shown in Fig. 7a. Such a narrow distribution, was obtained (according to the authors of [53]) owing to a thorough selection of the growth conditions.

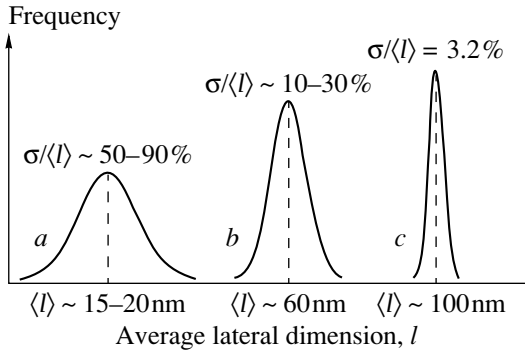

Fig. 6. Characteristic rms deviations ($\sigma/\langle l\rangle$) of the island sizes in a Ge–Si system: (*a*) for the hut-shaped islands, (*b*) for the dome-shaped islands (according to [29]); and (*c*) the distribution obtained by Jiang and coworkers [53]. The distributions are shown schematically.

The other following methods for enhancing the uniformity of the island sizes should be mentioned: (i) the use of tilted substrates, and (ii) the use of a special method for ensuring the simultaneous nucleation of the clusters [54]. The substantiation of these methods can be found in the following known facts and reasoning. In the publication by Goldfarb *et al.* [27], the details of transition from 2D to 3D growth and the initial stages of formation of the hut-shaped clusters were elaborated. The 3D islands appear at significantly different

points in time and are nucleated at imperfections of the 2D Ge layer, which confirms the generally accepted opinion that cluster nucleation is heterogeneous. Consequently, the preliminary formation of the sites that are preferential for the cluster nucleation may constitute a useful method for enhancing the ordering of these clusters. A preliminary ordering of steps at the surfaces that are disoriented with respect to (001) is widely used to form the QD arrays in an InAs–GaAs system (see, for example, one of the latest publications by Kim *et al.* [55] and the references therein). In the case of growing the Ge islands on Si, such an approach is used to a lesser extent; however, in order to enhance the ordering of steps at the 2D stage of growth, the authors of [56] not only used the steps' ordering related to the deviation of the substrate from the singular direction but also improved this ordering by preliminary overgrowth of the multilayered strained GeSi–Si superlattice. As a result [56], Ge islands having a uniformity of distribution both in height and in area of better than 10% with simultaneous significant spatial ordering were obtained (Fig. 7b).

According to the data obtained by Johansson and Seifert [57], the width of the island-size distribution (for InAs/InP) depends nonmonotonically on the growth rate. The distribution width decreases with increasing growth rate and reaches a minimum. As the growth rate increases further, the distribution broadens again. Such behavior verifies the importance of a single-moment heterogeneous nucleation. As the growth rate increases, the probability of the island nucleation at the onset of the process becomes higher; as a result, the islands grow for the same length of time and have almost the same dimensions. A further increase in the growth rate gives rise to the adatom supersaturation at the surface becoming so high that new islands are nucleated continuously. Because of this, the instant of nucleation again becomes spread, and the island-size distribution broadens.

It is possible to ensure an almost simultaneous nucleation of islands over the entire surface area of the substrate by providing an appreciable supersaturation of germanium adatoms at the initial instant of growth. This can be ensured, for example, by a short-term increase in the molecular-beam density or by a short-term decrease in the substrate temperature. The effect of synchronizing periodic short-term variations in the surface supersaturation on the 2D nucleation was observed by us previously in the case of homoepitaxy of silicon and germanium. On the basis of this effect, the MBE method with synchronization of nucleation was substantiated and implemented [54]. Later, an optimized method for the synthesis of quantum-dimensional structures such as the vertical superlattices, nanosystems consisting of quantum wires or dots, and the like, was suggested and substantiated theoretically for cyclic variation of supersaturation during the growth of each atomic layer of the film [58].

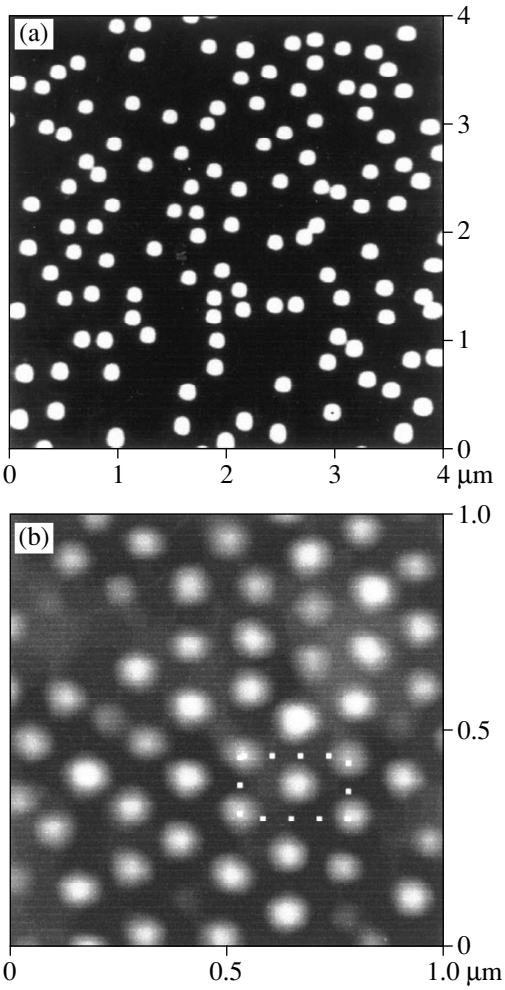

Fig. 7. Ge islands at the Si surface: (a) at a singular Si(001) face with the growth conditions specially selected (with permission given by the authors of [53]) and (b) at a vicinal Si(001) face with a preliminarily grown GeSi/Si superlattice [56] (with permission given by the authors of [56]).

Ordering with respect to the area is the weakest form of ordering, which is related to the fact that the islands interact weakly with each other at the initial stage of their formation. Therefore, the preliminary formation of ordered sites for the nucleation of nanoclusters is the most important method for ensuring their subsequent spatially ordered state. This statement is confirmed by an analysis of the two distributions of Ge islands over the singular (Fig. 7a) and vicinal (Fig. 7b) (100) Si faces. Figure 8 shows the spatial-ordering characteristics obtained by statistically processing the data shown in Fig. 7: the radial correlation functions that define the probability of finding the cluster at a certain distance from an arbitrarily chosen island (Figs. 8a, 8b). It can be seen that, in spite of an extremely small scatter in the parameters of the islands [53] whose microphotographs are shown in Fig.7a, their spatial distribution is almost unordered. A certain degree of

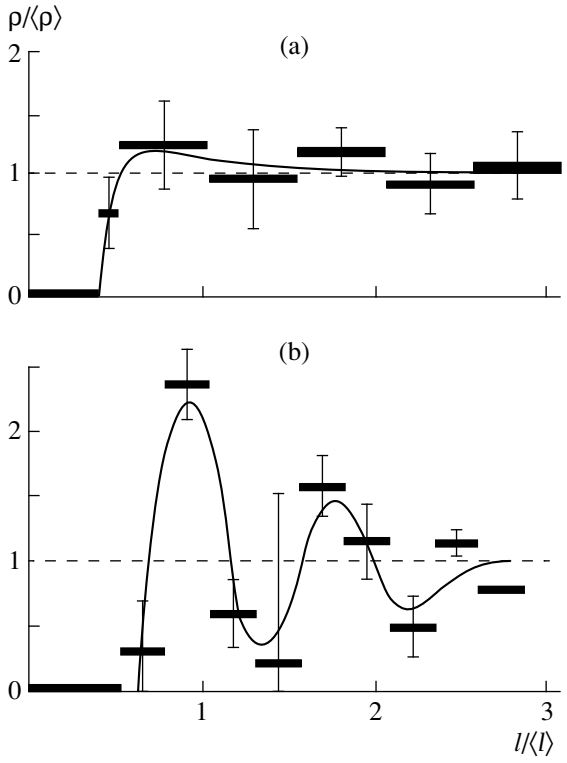

Fig. 8. Radial distributions of the normalized density of islands as a function of the normalized distance from an arbitrarily chosen particle for the above microphotographs (Figs. 8a and 8b correspond to Figs. 7a and 7b).

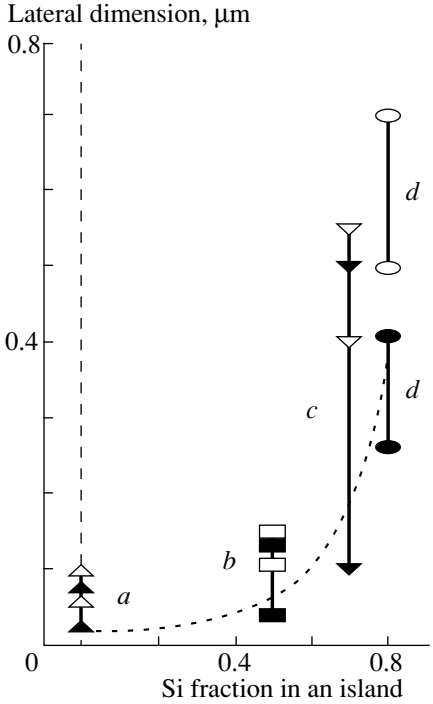

Fig. 9. Schematic representation of variations in the sizes of the hut- and dome-shaped clusters with increasing silicon fraction in an island on the basis of publications by (*a*) Kamins *et al.*, (*b*) Vostokov *et al.* [42], (*c*) Ross *et al.* [63], and (*d*) Floro *et al.* [49]. The dotted line represents the calculated waviness of the surface of a strained GeSi solid solution according to Obayashi and Shintani [64].

ordering is evidenced by the presence of a poorly pronounced preferential distance between the nearest neighbors and by the absence of 3D centers spaced at smaller than average intervals (Fig. 8a). Spatial distribution of the islands shown in Fig. 7b [56] may be considered as the most ordered among those observed in the Ge–Si system. The form of the correlation function shown in Fig. 8b is indicative of the presence of the short-range order in the first and second coordination shells. Spatial ordering of the islands becomes more pronounced with increasing coverage (the ratio between the total area of the islands and the substrate area), which is caused by minimization of repulsive forces of elastic interaction between neighboring islands [46, 59]. Because of this, the most highly spatially ordered arrays of islands occupy the largest fraction of the substrate area (see, for example, Fig. 7b, where the islands are nearly in contact with each other).

It was shown previously [13] that the sequential growth of layers with Ge islands overgrown with a material that is lattice-matched to the substrate (Si) causes the ordering (with respect both to the sizes and areas) to become more pronounced. The elastic-deformation fields are perturbed by clusters; these perturbations penetrate into the overgrown layer to different depths, depending on the volume of a specific island and on the degree of the island accumulation. The sites of preferential nucleation of new islands at the next level are formed at the surface of the overgrown layer. By varying the overgrown-layer thickness, one can suppress the influence of small islands. Corresponding studies have been performed both theoretically and experimentally, and we can cite several identical examples for III–V [14] and Ge–Si [13, 60] systems. Such multilayered heterostructures with QDs are of practical importance in relation to arising new possibilities (for example, the electron coupling of clusters in the vertical direction and the formation of 3D arrays consisting of islands–clusters that are often referred to as "artificial atoms" [61, 62]).

3.3. The Sizes and Density of the Islands: Methods for Control

Figure 9 shows the characteristic sizes of GeSi clusters of the hut and dome types; it can be seen that the sizes increase with an increasing Si fraction in the GeSi solid solution (the data reported in [29, 42, 49, 63] were used). Theoretical dependence of the period of the surface undulation for the GeSi/Si(100) film is also shown; this undulation is a result of the elastic relaxation of the strained solid solution (this dependence was derived by Obayashi and Shintani [64]). As the fraction of Si increases, strains in a cluster decrease and the neces-

sary gain in energy due to elastic relaxation in the islands occurs for the larger island sizes. Studies of GeSi solid solutions with a large Si content, convenient for simulation experiments, make it possible to easily clarify the main laws of the island formation due to their relatively large sizes [49]. However, the practical interest of researchers focuses on the systems that contain the islands of about 10 nm or less in size (pure Ge on Si), which is primarily due to the optical properties of such systems. The density of islands is also very important because the response of the system to external effects is directly related to the number of islands and, correspondingly, to their density. Both of these parameters (the size and density) depend on the growth conditions such as the substrate temperature and the growth rate. A decrease in the growth temperature, as well as an increase in the Ge flux, causes the diffusion length of Ge adatoms at the substrate to decrease. Correspondingly, the collection region of adatoms for a single island decreases, the island size also decreases, whereas the island density increases. Abstreiter and coworkers [65] regularly varied the island density to 10^{10} cm^{-2} by decreasing the growth temperature to 550°C and increasing the Ge flux. Further decrease in the growth temperature to 300°C made it possible to appreciably increase the density of Ge nanoclusters to $\sim 3 \times 10^{11}$ cm^{-2} [66]. Peng and coworkers [67] used antimony as a surfactant that reduced the surface diffusion length of Ge adatoms and managed to obtain an island density of $\sim 5 \times 10^{11}$ cm^{-2} (the highest so far).

3.4. A Comparison of the Si {001} and {111} Surfaces

The vast majority of theoretical and experimental studies of formation of Ge islands have been devoted to these processes at the Si(001) surface because it is this surface that is most favorable for the formation of high-density coherent nanoislands. Nevertheless, the problem of the influence of the substrate-surface orientation on the island formation in a strained heteroepitaxial film remains topical; therefore, in this section, we attempt to dwell briefly on the special features that distinguish the Ge/Si(001) and Ge/Si(111) systems with respect to morphological instability.

When Ge is deposited on the Si(001) surface, the formation of the wetting layer is followed by the emergence of the coherent (without misfit dislocations) hut-shaped clusters (Fig. 5) and then by the dome-shaped clusters whose height significantly exceeds the critical thickness that corresponds to the onset of the introduction of the misfit dislocations [10]. These dislocations appear in islands whose height exceeds 50 nm [10] (the so-called superdome clusters [39]). Thus, in a Ge/Si(001) system, there is an extended domain of conditions for the existence of Ge 3D coherent islands. The 3D Ge islands formed at the Si(111) surface differ appreciably in shape and constitute triangular pyramids with flat tops (Fig. 10) and {113} lateral faces [48, 68–70];

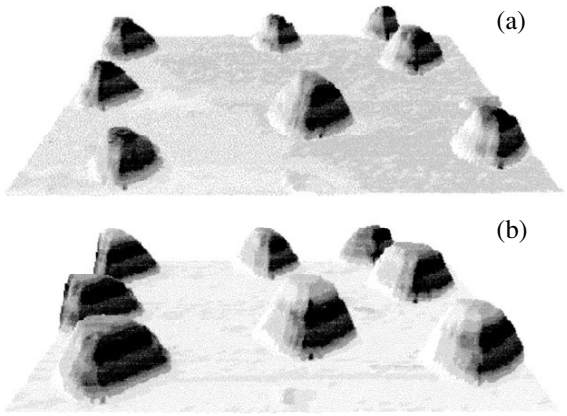

Fig. 10. A perspective STM image of typical Ge islands after the deposition of (a) 4.1 and (b) 6.8 Ge bilayers on the (111) surface of silicon. The image area is 330×330 nm^2. The average height of the islands in panel (b) is 8 nm. For details, see [68].

it is important that nanoislands contain the misfit dislocations even at the initial stages of island formation [71, 72].

As mentioned in Section 2, morphological instability of the strained-layer surface and the ultimate manifestation of this instability (the formation of the 3D coherent islands) develops if the gain in the free energy of the system due to elastic relaxation of stresses in the islands exceeds an addition to the surface energy due to an increase in the surface area and to the emergence of facets with a higher surface energy. We now compare the Ge/Si(001) and Ge/Si(111) systems taking into account the above considerations.

The facet closest to the (100) plane both for germanium [73, 74] and for silicon [75] is the (105) face and deviates by 11.3° from the (100) plane. According to the data reported elsewhere [76], this face consists of (100) terraces separated by steps. Formation of Ge–on–Si hut-shaped clusters faceted exactly by the {105} planes is due (according to the assumptions by Liu, Wu, and Lagally [77]) to an insignificant distinction between the surface energies of the {100} and {105} faces. On the other hand, the (113) face that facets the Ge 3D islands at the initial stage of their formation at the Si(111) plane [68] deviates from the basal plane by at least 29.5°. The surface energy (γ) of this face was determined experimentally for Si by Eaglesham and coworkers [78] and was found to be larger by a factor of 1.13 than the value of γ for the {111} plane. It was also experimentally demonstrated [78] that the step energy at the Si(111) surface is five times larger than that at the (001) surface, which is apparently the main factor conducive to the greater atomic smoothness of the (111) surface compared to the (001) surface and, correspondingly, to the greater morphological stability of this face. Barbezier and coworkers [72] also emphasize the deciding effect of the enhanced formation energy of the steps at the (111) surface compared to the

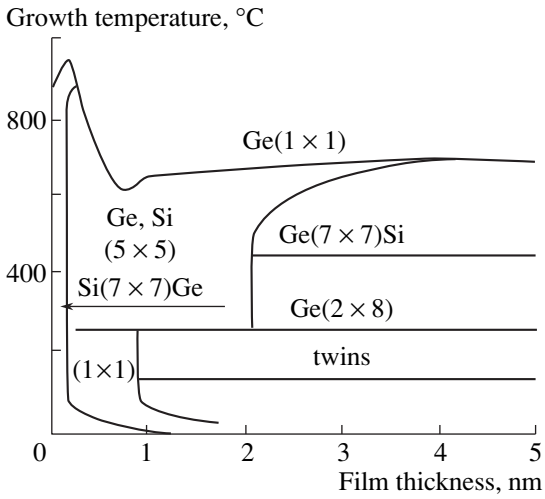

Fig. 11. Kinetic diagram of structural transitions at the film surface in the course of germanium heteroepitaxy onto the Si(111)–(7 × 7) surface.

(001) surface, which results in a higher morphological stability of the (111) face. Because of this, the 3D Ge islands at the Si(111) surface are shaped as truncated pyramids whose upper surface remains the same (111) plane and whose height is within 0.1–0.13 of their cross-sectional sizes [68]. We may assume that the clusters with such shapes are considerably less prone to stress relaxation due to elastic strains compared to the hut-shaped clusters at the (001) surfaces.

Thus, the Ge islands formed at the Si(111) surface are bound to gain less free energy due to elastic relaxation of stresses compared to the hut-shaped clusters at the (001) surface and should lose more surface energy due to a larger inclination angle of the nearest facet. We add to this comparison the fact that the (111) surface is the glide plane for dislocations, whereas the presence of an abrupt (111)–(113) step at the edge of a 3D island results in the so-called geometric enhancement of stresses, which reduces the energy barrier for the misfit-dislocation initiation. Correspondingly, such a shape of islands is conducive to the rapid onset of their plastic relaxation [79]. In our opinion, it is the combination of the aforementioned factors that gives rise to the fact that the existence domain for Ge 3D coherent islands in a Ge–Si(111) system is extremely narrow or is not present at all.

3.5. The Factors Influencing the Process of Ordering

It was mentioned above that the morphology of the surface at which the 3D islands are formed plays an important role and can be used as a controlling factor conducive to the ordering of the islands with respect to both their sizes and spatial distribution. The surface parameters may be controlled by the following methods:

(i) The use of the substrates that are tilted from the (001) surface and the various related methods for ordering the steps representing further the stencils for initiation of the islands [56, 80–86];

(ii) The use of surfactants that modify the surface characteristics (the surface energy and the diffusion length of adatoms) of both the substrate and the epilayer [67, 87–90];

(iii) The formation of microstressors at the substrate surface; these microstressors initiate the nucleation of islands at certain sites [91–93]; and

(iv) The use of lithography making it possible to form windows in the substrate; these windows restrict the region of collection of adatoms in the islands and separate the islands from each other [94, 95]. The photolithography-induced formation of facets that localize the initiation sites for the Ge islands [96, 97].

Each of these avenues of research are being developed; however, the studies are at the early stage. Because of this, we call the reader's attention to these avenues of research without analyzing them in detail.

3.6. The in situ Control

A strong dependence of the island parameters on the technological-process conditions makes it necessary to continuously control the growth surface of the substrate. A convenient method suitable for this purpose is the reflection high-energy electron diffraction (RHEED). As a typical example of a thorough study of the surface during heteroepitaxy, the RHEED was used [98] to plot the phase diagrams of structures that existed during epitaxy of Ge on the Si(111) and Si(001) substrates.

Figure 11 shows an example of such a diagram for the Si(111) surface. Two structures with a period multiple of 7 were observed during the epitaxy of Ge on Si(111). These structures are Si(111)–(7 × 7)Ge and Ge(111)–(7 × 7)Si. Here, the first chemical symbol indicates the material at whose surface a given superstructure was observed, whereas the second symbol indicates the material that stabilizes the given superstructure. The Si(111)–(7 × 7)Ge superstructure is formed at a high temperature if there is small amount of Ge at the Si surface. The highest temperature at which this superstructure was stable in the course of the film growth was 950°C. According to an estimate [98], the fluxes of adsorbing and desorbing Ge atoms are equal to each other at this temperature. As the temperature is increased further, the concentration of Ge atoms at the surface decreases rapidly.

After the critical thickness (corresponding to origination of the misfit dislocation) of the film has been attained, the Ge(111)–(7 × 7)Si superstructure is formed at the surface of Ge islands; this superstructure is stabilized by Si atoms that diffuse from the substrate. This conclusion is confirmed by the fact that the surface of the Ge film grown at a temperature below 350°C has

the Ge(111)–(2 × 8) superstructure, whereas the subsequent annealing of the film at 600–700°C gives rise to the Ge(111)–(7 × 7) superstructure. In addition to the aforementioned structures, the Ge(111)–(5 × 5) superstructure was also observed [99, 100]. The presence of the latter superstructure is related to the pseudomorphous state of the Ge film. After the pseudomorphism ceases to exist, this superstructure transforms either into Ge(111)–(7 × 7)Si or into Ge(111)–(2 × 8). The latter structure is characteristic of the atomically clean (111) surface of the bulk Ge. Consequently, the (5 × 5) structure is an indication that there are stresses in the film; relaxation of these may stimulate the formation of the islands.

Typically, the (2 × 1) and (2 × 8) superstructures are present at the surface during the growth of the Ge_xSi_{1-x} film on the Si(001) substrates. On the basis of the analysis of variations in the diffraction patterns in the course of the growth of Ge film on Si, we plotted [98] the phase diagram shown in Fig. 12. After the islands have been formed, the facets (Fig. 12) with the {105}, {118}, and {311} faces are observed [47, 101–103]. Correspondingly, in this case, the appearance of strands, which are related to the relevant crystal faces, at the RHEED pattern is an indication that the islands have been formed.

The shape of oscillations of a specular reflection in the electron-diffraction pattern observed during growth is also highly sensitive to morphological rearrangements at the surface of the growing film. This inherently high sensitivity of specular reflection to morphological features becomes even higher when the diffraction occurs under the conditions of surface resonance [104]. In these cases, the emergence of islands is accompanied by a drastic decrease in the specular-reflection intensity, which makes it possible to precisely determine the instant corresponding to the onset of the island formation.

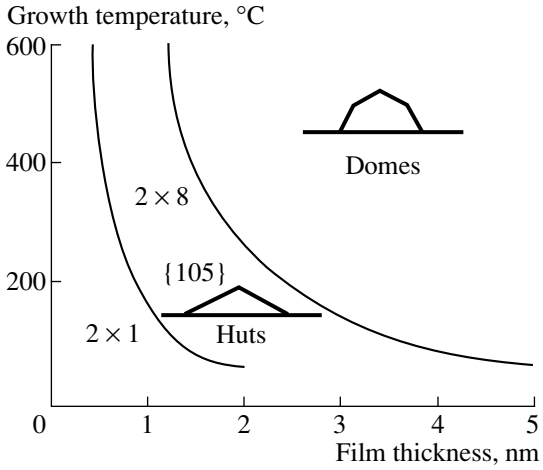

Fig. 12. Kinetic diagram of structural transitions at the film surface in the course of epitaxy onto the Si(001)–(2 × 1) substrate.

4. ELECTRONIC PROPERTIES OF SYSTEMS OF "ARTIFICIAL ATOMS"

Electronic properties of Ge–Si structures were studied by electron tunneling spectroscopy, capacitance spectroscopy, and conductance spectroscopy; in addition, the hopping conduction and the field effect were studied. The Ge–Si heterocombination belongs to heterostructures of the second type, in which the Ge islands constitute potential wells for holes. This fact governs the choice of the conduction type in the systems under consideration.

4.1. Electrical Properties

4.1.1. Electron tunneling spectroscopy. If the Fermi level in the emitter coincides with the allowed level of the charge carrier in a quantum well, a resonance enhancement of tunneling current should be observed. By changing the energy of the injected charge carrier by varying the voltage, one can obtain data on the energy spectrum of QDs. This spectroscopic method was first applied to the arrays of self-organized QDs in 1992 [6]. The structure studied included two parallel electrodes ($Ge_{0.3}Si_{0.7}$ layers doped heavily with boron) between which the Ge-nanocrystal layer [105] was confined, with potential barriers (Si interlayers) separating this layer from the electrodes. The dependence of differential conductance on the voltage is shown in Fig. 13. The upper panel corresponds to symmetric silicon barriers (both of them are 9 nm thick). The lower panel shows the conductance spectrum occurring in the situation when one of the barriers is thinner (the barrier thicknesses here are 9 and 6 nm); negative polarity of the voltage corresponds to the situation when a charge carrier (hole) first passes through the thin layer and then through the thick layer. In both cases, distinct oscillations of tunneling conductance of the structures are observed; these oscillations indicate that there exists a well-resolved discrete spectrum in the Ge islands. The oscillations in the vicinity of the zero bias are accompanied by the emergence of a region with negative differential conductance which is a characteristic feature of resonance tunneling. For the symmetric configuration of the barriers (see the upper panel in Fig. 13), the conductance oscillations are nearly symmetric with respect to the zero voltage and have a characteristic period of ~150 mV, which makes it possible to estimate the distance between the size-quantization levels at ~150/2 = 75 mV.

In the asymmetric structure, the conductance peaks are split into a series of oscillations with a smaller period in the region of negative biases. For this polarity of the voltage, accumulation of holes in the islands occurs as a result of a large difference between the coefficients of transit through the left and right barriers; thus, the processes of the charge-carrier Coulomb correlations caused by the carrier–carrier interaction

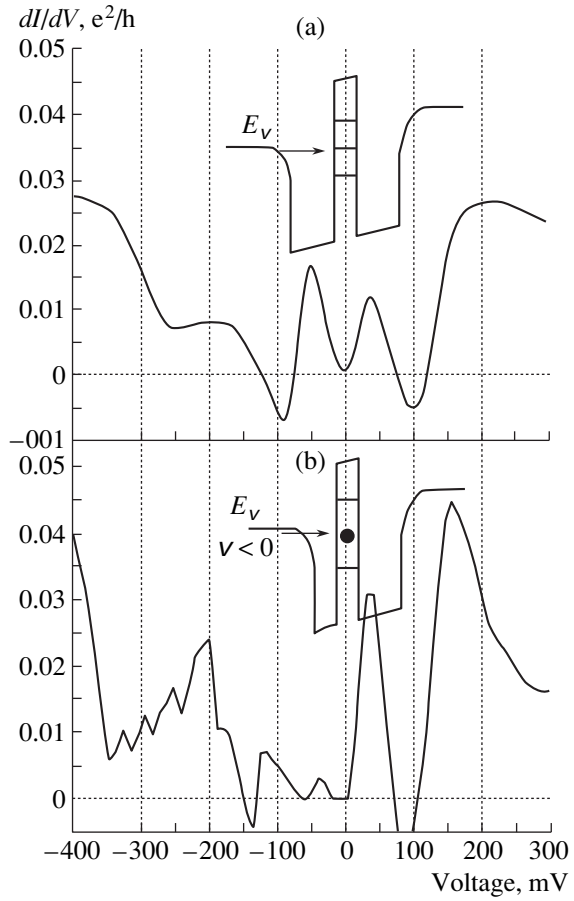

Fig. 13. Dependence of differential conductance of vertical two-barrier structures with Ge quantum dots for (a) a symmetric structure (the width of both Si barriers is 9 nm) and (b) an asymmetric structure (with barriers 6 and 9 nm wide).

become important. The Coulomb interaction removes the degeneracy of single-particle levels of size quantization since a hole overcomes the energy of electrostatic repulsion of charge carriers that are already present in the QD. Such an effect has been previously observed in the form of steplike current–voltage characteristics in tunneling transitions through metallic granules and has been named the "Coulomb staircase" [106]. The correlation energy of holes in the islands can be estimated from the distance between the conductance peaks at $E_C \approx 35$ meV in the ground state and at $E_C \approx 18$ meV in the first excited state.

4.1.2. Capacitance tunneling spectroscopy. The capacitance spectroscopy of QDs is based on the fact that the charge in zero-dimensional systems can change only discretely by a value of $\delta Q = eN$, where e is the elementary charge and N is the number of quantum dots in the sample [107]. The external voltage V_g at the gate electrode shifts the potential in the islands with respect to the Fermi level in the contact separated from the island-containing layer by a tunneling-transparent barrier and stimulates, either the capture of charge carriers from the contact by the QD levels, or the depopulation of these levels, depending on the polarity of V_g. If the Fermi level in the contact coincides with the bound-state energy in a QD, the differential capacitance $C(V_g) = dQ/dV_g$ is bound to feature a peak that is indicative of the presence of a discrete energy level. The total capacitance of the structure is a sum of two contributions: the first of these is due to the presence of a space-charge region in the material (in the case under consideration, this is silicon) that surrounds the islands, whereas the second contribution (C_{QD}) is related to the recharging of the QDs.

In the studied structures with the Schottky barrier, the effective layer thickness d_{eff} was varied [108]. The structures included the following sequence of layers beginning at the substrate: (i) the p^+-Si(100) substrate serving as the lower electrical contact; (ii) a $Si_{0.5}Ge_{0.2}$ layer having a thickness of $L = 10$ nm and ensuring an abrupt heteroboundary of the next Si tunneling barrier; (iii) a tunneling-transparent Si barrier ($p = 7 \times 10^{16}$ cm^{-3} and $L = 7$ nm); (iv) a layer containing the Ge nanocrystals; (v) a blocking Si layer ($p = 7 \times 10^{16}$ cm^{-3} and $L = 50$ nm); and (vi) an Al electrode controlling the occupancy of the islands and forming the Schottky barrier at the boundary with silicon. The area of the Al contact region was $\sim 8 \times 10^{-3}$ cm^2; a cylindrical mesastructure was etched off to a depth of about 5 μm according to the outline of this contact area.

The capacitance–voltage (C–V) characteristics of the structures without a Ge layer had a shape typical of a p-Si depletion layer (Fig. 14). In the case of $d_{eff} = 2$ monolayers (ML), a plateau appears in the C–V characteristics; this plateau is characteristic of a 2D charge-carrier gas. In the range of the effective Ge thicknesses of $8 \le d_{eff} \le 13$ ML, peaks appear in the C–V curves; the distance between these peaks, their width, and their position on the voltage scale (the energy scale) depends on d_{eff}: as d_{eff} increases, the peaks become narrower and their energy separation decreases. The energy distance between the levels corresponding to two capacitance peaks can be determined from the relationship $\Delta E = \Delta V_g b/L$ [109], where ΔV_g is the distance between the peaks in the C–V characteristic, b is the distance between a QD and the lower electrode, and L is the distance between the top and bottom electrodes. Calculations yield $\Delta E = 87$ ($d_{eff} = 8$ ML), 36 (for 10 ML), and 32 meV (13 ML) [108]. The value of $\Delta E = 36$ meV for the sample containing the amount of Ge that corresponds to $d_{eff} = 10$ ML is consistent with the recharging energy (E_C) of a QD in the ground state as was found in the experiments with resonance tunneling. Because of this, splitting of the peaks was attributed to the electrostatic Coulomb interaction.

The emergence of the capacitance oscillations is related to the formation of an array of Ge nanocrystals; this array is presumably rather uniform with respect to the island sizes, and the density of hole states in the array is a deltalike function of energy. For a large

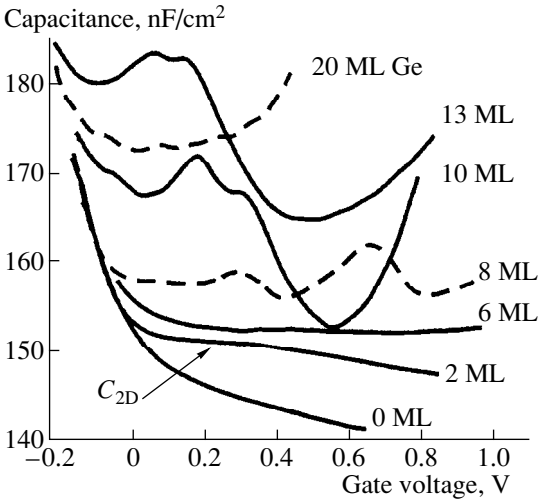

Fig. 14. The capacitance–voltage characteristics of Ge–Si(001) heterostructures with a different effective thickness (d_{eff}) of the Ge layer. The characteristics were measured at $T = 300$ K. Numbers at the curves indicate the value of d_{eff} measured in monolayers (ML).

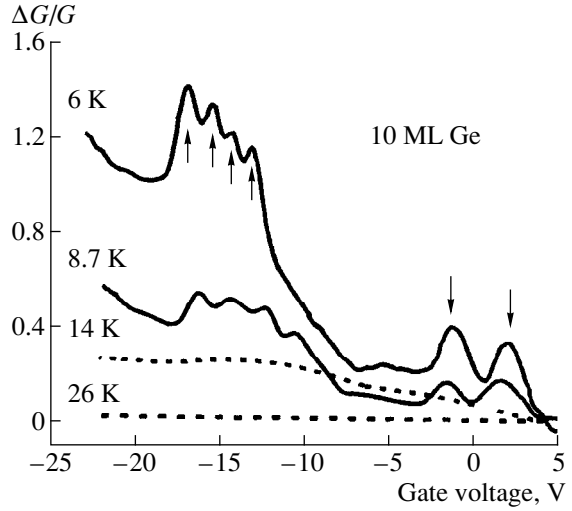

Fig. 15. Relative variation in the channel conductance of a field transistor that contains 10^9 quantum dots as a function of the gate voltage (the field effect) at different temperatures.

amount of deposited Ge (d_{eff} = 20 ML), plastic relaxation of elastic strains occurs and large (≈100 nm) islands with dislocations are formed. This is manifested by the disappearance of the capacitance peaks in the *C–V* characteristics. A large increase in the capacitance accompanied with a drastic increase in conductance for $d_{eff} > 20$ ML is apparently also related to the appearance of dislocations and the breakdown of the space-charge region.

The area under each peak (in the *C–V* characteristic) divided by the elementary charge was found to be almost exactly equal to the surface density of Ge islands ($2n_{QD} \approx 6 \times 10^{11}$ cm^{-2}). This means, first, that all Ge islands are involved in the process of recharging of the system and, second, that degeneracy in energy is removed owing to the Coulomb interaction.

Experimental verification of the Coulomb origin of splitting was found in the measurements of *C–V* characteristics for two layers of Ge islands with identical sizes [110]. In this case, the peak splitting caused by the Coulomb interaction increases.

4.1.3. The field effect. Variation in the conductance of MIS transistors, in which the conducting channel includes a layer of Ge nanocrystals, was found to be quite informative for studying the effects of electron correlations and quantum confinement [111]. Sequential population of the islands by charge carriers was accomplished by applying a voltage to the transistor gate. For the Ge-island density used (~3×10^{11} cm^{-2}), tunneling transitions between the states localized in different islands becomes important. The probability of a hole hopping between the QDs is defined by (I) the overlap of the wave functions for the occupied and empty states and (II) the occupancy of a given hole shell. If the relevant level is exactly half-occupied, the conductance is bound to be the largest and the activation energy for hops is bound to be defined by the electrostatic energy of interaction of a given hole with all charges in the nanocrystals. If the level is completely occupied, the charge carrier has to execute a transition to the excited states of the next shell. The activation energy increases by a value equal to the quantum-confinement energy, and the conductance decreases. As the occupancy of the excited state increases further, the activation energy required for the excitation of a charge carrier to the given level in other QDs decreases and again becomes a function of the electron–electron interaction, which brings about an increase in the contribution of the hopping conductivity, and so on. Thus, the hopping conductivity at a given temperature and also the activation energy for electrical conductivity are bound to oscillate with variations in the gate voltage, thus reflecting the structure of the spectrum of states. Such oscillations are inherent only in zero-dimensional systems where the electronic spectrum is discrete (atomlike).

Oscillations in the hopping conductivity under the conditions of the field effect were observed in MIS transistors that had a Ge layer with an effective thickness of more than 6 ML and contained up to 10^9 Ge islands [111]. A high-resistivity *n*-Si wafer was used as the substrate. In the low-temperature region ($T < 9$ K), oscillations were observed in the dependences of the channel conductance on the gate voltage; these oscillations corresponded to the occupation of the ground and excited states in a QD (Fig. 15).

In a MIS transistor with the QD layer formed on a silicon-on-insulator structure [separation by oxygen

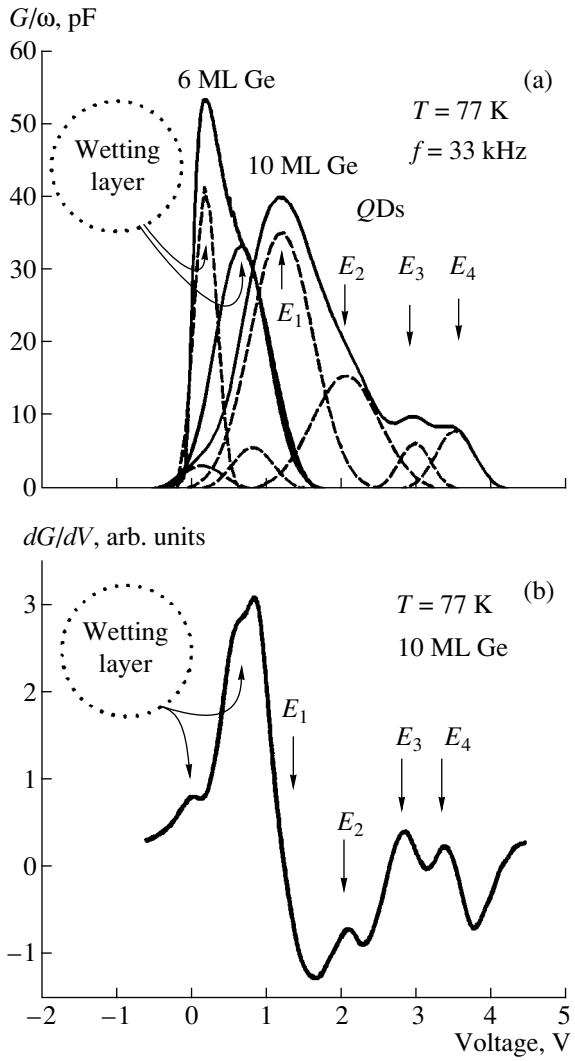

Fig. 16. (a) The admittance of the Schottky diode with quantum dots (10 ML of Ge) and with a continuous Ge layer (6 ML). The dashed lines represent the results of the decomposition of the experimental spectrum into Gaussians. The symbols E_1, E_2, E_3, and E_4 denote the response of discrete states in quantum dots. Figure 16b shows the derivative dG/dV.

implantation (SIMOX) technology was used] [112], the leakage currents through underlying Si layers were minimized; as a result, the conductance oscillations were observed at temperatures as high as ~150 K. The temperature dependence of conductance followed the Arrhenius law, which distinguishes the occurring processes from the resonance tunneling and substantiates the hopping mechanism of the charge transport over QDs.

4.1.4. Conductance spectroscopy. Measurements of admittance of the silicon Schottky barriers with a buried Ge-QD layer made it possible to gain additional information about the energy-spectrum structure of the QDs and the hole-state parameters [113]. In this case, the response of the QDs is equivalent to that of a capacitor with losses [114] and is characterized by the time constant $\tau = R_{QD}C_{QD}$. As the reverse bias increases in magnitude, the depletion layer penetrates deep into Si and, thus, brings about the depopulation of hole levels in a QD. Figure 16 shows the conductance (divided by the frequency of the periodic signal) as a function of the bias voltage for a structure with QDs (the sample with 10 ML of Ge) and a structure that contains only a wetting layer (6 ML of Ge). In the latter case, two peaks are observed at 0.1 and 0.6 V. Amplitudes of these peaks is frequency-independent in the range of 10–100 kHz; apparently, the peaks are related to the recharging of the wetting layer. For the sample with QDs, four additional peaks (denoted as E_1, E_2, E_3, and E_4 in Fig. 16) are observed. The temperature dependences of emission times made it possible to determine the activation energies (the depths of the corresponding levels): E_1 = (201 ± 7) meV, E_2 = (228 ± 7) meV, E_3 = (267 ± 12) meV, and E_4 = (288 ± 10) meV; the relevant capture cross sections were also determined (Fig. 17). The cross sections for the capture of holes by QDs increase with increasing level depths (Fig. 17) and exceed the known values for deep levels in Si by many orders of magnitude.

4.2. Optical Properties

Interest in the optical properties of QDs is caused by application-oriented considerations and by a number of advantages of such zero-dimensional objects compared to 2D QWs. Special features of QDs include, first, the possibility of controlling the spectral range of photoresponse by preliminarily populating the discrete states with the required transition energies; second, the presence of lateral quantization in zero-dimensional systems removes the forbiddenness of optical transitions polarized in the photodetector plane and, consequently, makes it possible to accomplish the absorption of light at a normal incidence of photons; and, third, an appreciable increase in the lifetime of charge carriers photogenerated in a QD due to the so-called "phonon bottleneck effect" [115].

4.2.1. Absorption in the infrared region of the spectrum. Absorption of light in the infrared (IR) region of the spectrum in Ge–Si multilayered heterostructures with self-organizing QDs has been studied previously [116, 117]. In both cases, the islands were ~40–50 nm broad at the base and were 2–4 nm in height. The density of the islands was ~10^8 cm^{-2}. The Ge islands were doped with boron [116] in order to populate the QD ground state with holes. A broad (~100 meV) line was observed in the absorption spectra within the wavelength range of 5–6 μm; the amplitude of this line decreased appreciably when the light with polarization perpendicular to the layer plane was used. This line was attributed to transitions between two lower levels of transverse quantization of heavy holes in a QD.

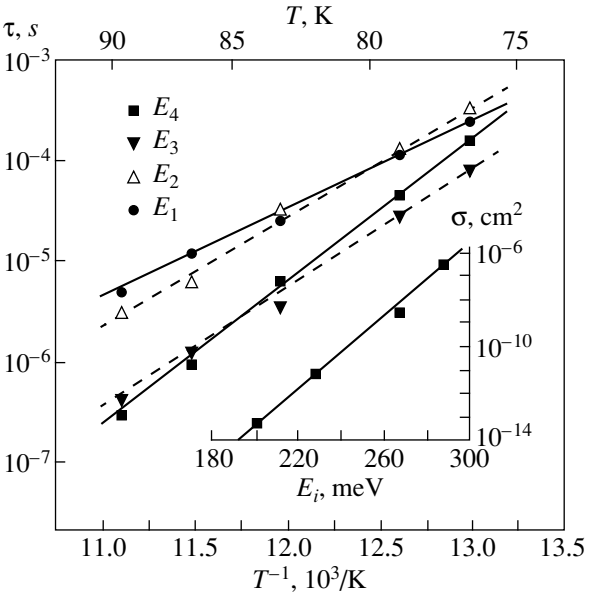

Fig. 17. Temperature dependence of the times of hole emission (τ) from excited state in quantum dots. Dependence of the cross section of the hole capture (σ) by the levels in quantum dots on the energy depth E_i of the levels is shown in the insert.

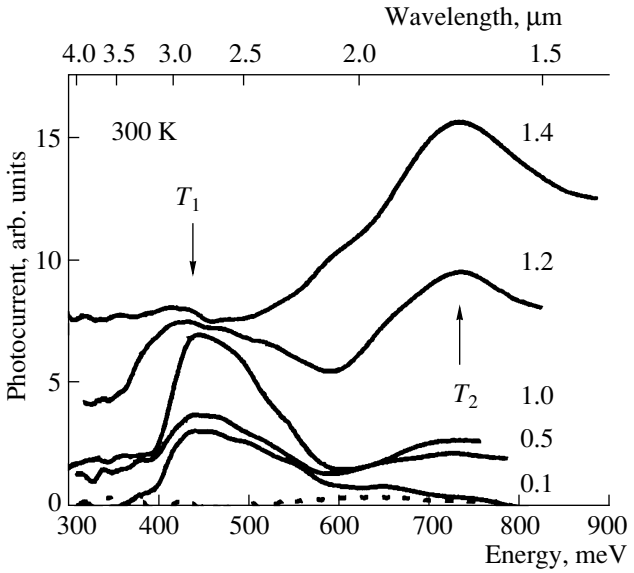

Fig. 18. The photocurrent spectra of a Si *p–i–n* diode with Ge quantum dots under a reverse bias indicated (in volts) at the corresponding curves. The dashed line demonstrates the absence of photoresponse in this range of photon energies in a structure with a continuous Ge layer (d_{eff} = 6 ML).

In order to activate optical transitions within an undoped QD, additional optical pumping was used [117]. The photoinduced absorption of light polarized parallel to the layer plane featured an asymmetric peak in the vicinity of 4.2 μm and was related to a transition of holes from the QD ground state to the valence-band delocalized states. The determined cross section for absorption [117] was unusually large (2×10^{-13} cm^2) and exceeded at least by an order of magnitude the known cross sections for photoionization of local centers in Si [118] and by three orders of magnitude the similar quantity for QDs in InAs–GaAs [119]. These data [117] indicate that a Ge–Si system has the potential to be used in IR photodetectors.

4.2.2. Photoconductivity. Observations of a photocurrent generated by photons with energy less than the band gap of silicon in Ge/Si heterostructures with QDs were first reported in [65, 120]. The possibility of developing a QD-containing photodetector tunable to the near- and medium-IR regions of the spectrum was demonstrated recently [66]. The photodetector was a silicon *p–i–n* diode, the base layer of which incorporated a 2D array of Ge nanoclusters. The average width of the QDs was 15 nm, and the height was 1.5 nm. The photocurrent spectra for various reverse-bias voltages are shown in Fig. 18. There was no photoresponse in the sample with continuous (d_{eff} = 6 ML) Ge film. In a structure with QDs, two peaks were observed at the wavelengths of 1.7 and 2.9 μm for photon energies lower than the energy corresponding to the fundamental-absorption edge in silicon (~1.12 eV). The heights of both peaks depended strongly on the reverse-bias voltage, with these dependences being correlated with each other. More specifically, as the magnitude of the bias was increased to 1.4 V, the photoresponse ceased to exist in the medium-IR region (at 2.9 μm, line T_1) and a signal in the near-IR region of the spectrum emerged (at 1.7 μm, line T_2). The photon energy corresponding to the peak of line T_1 (430 meV) coincides with the energy depth of the ground state of a hole in a QD [121]. Therefore, line T_1 was related to a transition of a hole from the ground state localized in a QD to delocalized states in the valence band. As the magnitude of the reverse bias increases, the hole levels in a QD are filled with electrons. In the region of voltages in the vicinity of 1.4 V, a QD becomes completely depleted of holes and transition T_1 turns out to be "forbidden." Starting from this moment, the band-to-band transitions of electrons between the valence and conduction bands become possible (process T_2). Since the system under consideration belongs to heterostructures of the second type (holes are localized in Ge regions, whereas these regions constitute potential barriers for electrons [122]), the band-to-band optical transition is indirect in the coordinate space and is accompanied with the transfer of electrons from Ge to Si. The energy of transition should be governed by the difference between the band gap of Si (1.12 eV) and the energy of the hole state in a Ge QD (0.43 eV); i.e., it should be equal to 700 meV, which is consistent with the experimental position of line T_2 (≈730 meV).

4.2.3. Photoluminescence. Conventionally, measurements of photoluminescence (PL) spectra are used to check the formation of the self-organizing QD lay-

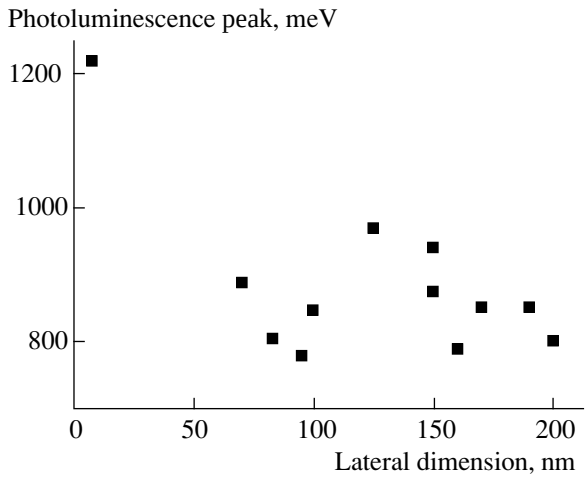

Fig. 19. The energy of the photoluminescence peak as a function of the lateral dimension of germanium islands in silicon.

ers; these measurements make it possible to determine the energies of the ground and excited states in a QD. For an InAs/GaAs system, the PL data were summarized and analyzed in [123]. In particular, it was shown [123] that the photon energy of the emission from QDs is controlled by the effective thickness of the deposited InAs layer and, as a result, by the QD size. The results of PL measurements as an illustration of the nucleation and evolution of QDs are also reported in many publications devoted to the epitaxy of Ge–Si structures. The appearance of a band in the vicinity of 800–900 meV in the PL spectra is related to the formation of Ge islands [13, 117, 120, 122–130]. The width of this band is tens of millielectronvolts; only once [124] were narrow (~2–10 meV) PL lines observed and attributed to the formation of an array of QDs that were uniform (to ~3%) in size. Nevertheless, in our opinion, the interpretation of the PL spectra for Ge–Si structures is somewhat contradictory. Figure 19 shows the position of a PL peak related previously to Ge islands as a function of the lateral size of nanoclusters. Here, we used the data reported in [13, 117, 120, 122–130]. In contrast with an InAs/GaAs system, a distinct dependence of the radiative-transition energies on the QD size is not observed; at the same time, it should be reasonable to expect that, as the QD size increases, the PL peak would shift to lower energies in the spectrum as a result of a decrease in the quantum-confinement energy in the islands. In addition, the observation of an emission with energy larger than the band gap of silicon [125] (the leftmost point in Fig. 19) seems surprising. All these circumstances have no generally accepted satisfactory explanation at present and will stimulate further thorough studies of mechanisms for PL in Ge–Si structures.

5. CONCLUSION

In this review, we analyzed scientific publications worldwide and noted the growing interest of scientists and technologists in the problems of the production and the application of nanostructures that are based on silicon and germanium and consist of Ge clusters of nanometer-scale size (quantum dots) embedded in the Si matrix. Elastic strain in epilayers and 3D Ge islands on Si is a key factor that not only initiates the morphological transition from a planar film to an island-containing film (the Stranski–Krastanov mechanism) but also influences the subsequent stages of evolution of the islands, including their shape, size, and spatial distribution. In many cases, this factor modifies substantially the classical stages of the phase-formation mechanisms and their sequence to the point of a quasi-equilibrium coexistence of 3D Ge nanoislands at the surface of Si substrate. In the considered systems of nanoclusters, we separated out various types of ordering: ordering with respect to the cluster shape, to its size, to the distance between islands and their mutual arrangement, and also ordering in the vertical direction (in the sequentially formed multilayered heterostructures with quantum dots). The method for enhancing the degree of ordering in nanostructures with arrays of quantum dots and attaining ultimately small sizes and a large density of distribution over the surface area was discussed.

In this review, we also cite the published data on the absorption of light in multilayered Ge–Si systems; these data are indicative of an anomalously large cross section of intraband absorption, which makes the class of nanostructures under consideration promising for the development of the IR-region photodetectors. Applying the tunneling, capacitance, and conductance spectroscopies, and also the field effect to the transistor structures that contained no less than 10^9 Ge nanoclusters, we observed well-resolved peaks related to a single-electron capture of up to six holes by each quantum dot. The main factors controlling the spectrum of states are the quantum confinement and Coulomb interaction between charge carriers. A new factor arising in the QD array and distinguishing it from the situation with a single QD is the Coulomb correlation between the islands.

Studies of the electrical and optical characteristics of arrays of Ge islands in Si make it possible to draw a conclusion regarding the formation of arrays of "artificial atoms" that feature a discrete energy spectrum; the latter is observed up to room temperature.

ACKNOWLEDGMENTS

This work was supported by the Russian Foundation for Basic Research (project nos. 00-02-17461, 00-02-17638, and 00-15-96806) and the Program of the Ministry of Science of Russian Federation "The Physics of Solid-State Nanostructures."

REFERENCES

1. R.A. Mezger, Compd. Semicond. **1**, 21 (1995).
2. U. Konig, Phys. Scr., T **68**, 90 (1996).
3. R. A. Soref, Thin Solid Films **294**, 325 (1997).
4. T. Tashiro, T. Tatsumi, M. Sugiyama, *et al.*, IEEE Trans. Electron Devices **44**, 545 (1997).
5. D. J. Paul, Thin Solid Films **321**, 172 (1998).
6. A. I. Yakimov, V. A. Markov, A. V. Dvurechenskiĭ, and O. P. Pchelyakov, Philos. Mag. B **65**, 701 (1992).
7. D. Leonard, M. Krishnamurthy, C.M. Reaves, *et al.*, Appl. Phys. Lett. **63**, 3203 (1993); D. Leonard, K. Pond, and P.M. Petroff, Phys. Rev. B **50**, 11687 (1994).
8. J.-M. Marzin, J.-M. Gerard, A. Izrael, and D. Barrier, Phys. Rev. Lett. **73**, 716 (1994).
9. L. N. Aleksandrov, R. N. Lovyagin, O. P. Pchelyakov, and S. I. Stenin, J. Cryst. Growth **24/25**, 298 (1974).
10. D. J. Eaglesham and M. Cerullo, Phys. Rev. Lett. **64**, 1943 (1990).
11. S. Guha, A. Madhukar, and K. C. Rajkumar, Appl. Phys. Lett. **57**, 2110 (1990).
12. R. Nötzel, Semicond. Sci. Technol. **11**, 1365 (1996).
13. F. Liu and M. G. Lagally, Surf. Sci. **386**, 169 (1997).
14. N. N. Ledentsov, V. M. Ustinov, V. A. Shchukin, *et al.*, Fiz. Tekh. Poluprovodn. (St. Petersburg) **32**, 385 (1998) [Semiconductors **32**, 343 (1998)].
15. P. Müller and R. Kern, J. Cryst. Growth **193**, 257 (1998).
16. A. A. Chernov, E. I. Givargizov, and Kh. S. Bagdasarov, in *Modern Crystallography*, Vol. 3: *Crystal Growth* (Nauka, Moscow, 1980; Springer-Verlag, Berlin, 1984).
17. F. Liu and M. G. Lagally, Phys. Rev. Lett. **76**, 3156 (1996).
18. R. J. Asaro and W. A. Tiller, Metall. Trans. **3**, 789 (1972).
19. M. A. Grinfel'd, Dokl. Akad. Nauk SSSR **290**, 1358 (1986) [Sov. Phys. Dokl. **31**, 831 (1986)].
20. W. Dorsch, H. P. Strunk, H. Wawra, *et al.*, Appl. Phys. Lett. **72**, 179 (1998).
21. Yu. B. Bolkhovityanov, V. I. Yudaev, and A. K. Gutakovsky, Thin Solid Films **137**, 111 (1986).
22. S. A. Kukushkin and A. V. Osipov, Usp. Fiz. Nauk **168**, 1083 (1998).
23. I. M. Lifshitz and V. V. Slyozov, J. Phys. Chem. Solids **19**, 35 (1961).
24. B. K. Chakraverty, J. Phys. Chem. Solids **28**, 2401 (1967).
25. M. C. Bartelt and J. W. Evans, Phys. Rev. B **46**, 12675 (1992).
26. N. C. Bartelt, W. Theis, and R. M. Tromp, Phys. Rev. B **54**, 11741 (1996).
27. I. Goldfarb, P. T. Hayden, J. H. G. Owen, and G. A. D. Briggs, Phys. Rev. Lett. **78**, 3959 (1997); Phys. Rev. B **56**, 10459 (1997).
28. B. A. Joyce, D. D. Vvedensky, A. R. Avery, *et al.*, Appl. Surf. Sci. **130–132**, 357 (1998).
29. T. I. Kamins, G. Medeiros-Ribeiro, D. A. A. Ohlberg, and R. Stanley Williams, J. Appl. Phys. **85**, 1159 (1999).
30. A. R. Avery, H. T. Dobbs, D. M. Holmes, *et al.*, Phys. Rev. Lett. **79**, 3938 (1997).
31. J. Drucker, Phys. Rev. B **48**, 18203 (1993).
32. Y. Chen and J. Washburn, Phys. Rev. Lett. **77**, 4046 (1996).
33. D. E. Jesson, G. Chen, K. M. Chen, and S. J. Pennycook, Phys. Rev. Lett. **80**, 5156 (1998).
34. M. Kästner and B. Voigtländer, Phys. Rev. Lett. **82**, 2745 (1999).
35. T. I. Kamins, E. C. Carr, R. S. Williams, and S. J. Rosner, J. Appl. Phys. **81**, 211 (1997).
36. G. Medeiros-Ribeiro, A. M. Bratkovski, T. I. Kamins, *et al.*, Science **279**, 353 (1998).
37. G. Medeiros-Ribeiro, T. I. Kamins, D. A. A. Ohlberg, and R. S. Williams, Phys. Rev. B **58**, 3533 (1998).
38. T. I. Kamins, G. Medeiros-Ribeiro, D. A. A. Ohlberg, and R. S. Williams, Appl. Phys. A: Solids Surf. **67**, 727 (1998).
39. R. S. Williams, G. Medeiros-Ribeiro, T. I. Kamins, and D. A. A. Ohlberg, J. Phys. Chem. B **102**, 9605 (1998).
40. T. I. Kamins, G. A. D. Briggs, and R. Stanley Williams, Appl. Phys. Lett. **73**, 1862 (1998).
41. F. M. Ross, J. Tersoff, and R. M. Tromp, Phys. Rev. Lett. **80**, 984 (1998); Microsc. Microanal. **4**, 254 (1998).
42. N. V. Vostokov, S. A. Gusev, I. V. Dolgov, *et al.*, Fiz. Tekh. Poluprovodn. (St. Petersburg) **34**, 8 (2000) [Semiconductors **34**, 6 (2000)].
43. C.-H. Chiu, Appl. Phys. Lett. **75**, 3473 (1999).
44. V. A. Shchukin and D. Bimberg, Appl. Phys. A: Solids Surf. **67**, 687 (1998); Rev. Mod. Phys. **71**, 1125 (1999).
45. P. Müller and R. Kern, J. Cryst. Growth **193**, 257 (1998).
46. J. A. Floro, V. B. Sinclair, E. Chason, *et al.*, Phys. Rev. Lett. **84**, 701 (2000).
47. Y.-W. Mo, D. E. Savage, B. S. Swartzentruber, and M. G. Lagally, Phys. Rev. Lett. **65**, 1020 (1990).
48. S. M. Pintus, S. M. Stenin, A. I. Toropov, *et al.*, Thin Solid Films **151**, 275 (1998).
49. J. A. Floro, E. Chason, L. B. Freund, *et al.*, Phys. Rev. B **59**, 1990 (1999).
50. F. K. LeGoues, M. C. Reuter, J. Tersoff, *et al.*, Phys. Rev. Lett. **73**, 300 (1994).
51. H. T. Johnson and L. B. Freund, J. Appl. Phys. **81**, 6081 (1997).
52. V. A. Markov, A. I. Nikiforov, and O. P. Pchelyakov, J. Cryst. Growth **175/176**, 736 (1997).
53. Z. Jiang, H. Zhu, F. Lu, *et al.*, Thin Solid Films **321**, 60 (1998).
54. V. A. Markov, O. P. Pchelyakov, L. V. Sokolov, *et al.*, Surf. Sci. **250**, 229 (1991).
55. Y. Kim, B. D. Min, and E. K. Kim, J. Appl. Phys. **85**, 2140 (1999).
56. J. Zhu, K. Brunner, and G. Abstreiter, Appl. Phys. Lett. **73**, 620 (1998).
57. J. Johansson and W. Seifert, Appl. Surf. Sci. **148**, 86 (1999).
58. O. P. Pchelyakov, I. G. Neisvestnyi, and Z. Sh. Yanovitskaya, Phys. Low-Dimens. Struct. **10/11**, 389 (1995).

59. J. A. Floro, E. Chason, M. B. Sinclair, *et al.*, Appl. Phys. Lett. **73**, 951 (1998).
60. H. Omi and T. Ogino, Appl. Surf. Sci. **130–132**, 781 (1998).
61. G. Springholz, V. Holy, M. Pinczolits, and G. Bauer, Science **282**, 734 (1998).
62. Y. W. Zhang, S. J. Xu, and C.-H. Chiu, Appl. Phys. Lett. **74**, 1809 (1999).
63. F. M. Ross, R. M. Tromp, and M. C. Reuter, Science **286**, 1931 (1999).
64. Y. Obayashi and K. Shintani, J. Appl. Phys. **84**, 3141 (1998).
65. G. Abstreiter, P. Schittenhelm, C. Engel, *et al.*, Semicond. Sci. Technol. **11**, 1521 (1996).
66. A. I. Yakimov, A. V. Dvurechenskiĭ, Yu. Yu. Proskuryakov, *et al.*, Appl. Phys. Lett. **75**, 1413 (1999).
67. C. S. Peng, Q. Huang, W. Q. Cheng, *et al.*, Appl. Phys. Lett. **72**, 2541 (1998).
68. B. Voigtländer and A. Zinner, Appl. Phys. Lett. **63**, 3055 (1993).
69. P. W. Deelman, L. J. Schawalter, and T. Thundat, J. Vac. Sci. Technol. A **15**, 930 (1997).
70. A. Shklyaev, M. Shibata, and M. Ichikawa, Surf. Sci. **416**, 192 (1998).
71. L. N. Aleksandrov, R. N. Lovyagin, O. P. Pchelyakov, and S. I. Stenin, in *Growth and Doping of Semiconductor Crystals and Films* (Nauka, Novosibirsk, 1977), Part II, p. 139.
72. I. Berbezier, B. Gallas, A. Ronda, and J. Derrien, Surf. Sci. **412/413**, 415 (1998).
73. B. Z. Ol'shanetskiĭ, V. I. Mashanov, and A. I. Nikiforov, Fiz. Tverd. Tela (Leningrad) **23**, 2567 (1981) [Sov. Phys. Solid State **23**, 1505 (1981)].
74. Z. Gai, R. G. Zhao, H. Ji, *et al.*, Phys. Rev. B **56**, 12308 (1997).
75. B. Z. Olshanetsky and V. I. Mashanov, Surf. Sci. **111**, 414 (1981).
76. B. Z. Olshanetsky, A. E. Solovyov, A. E. Dolbak, and A. A. Maslov, Surf. Sci. **306**, 327 (1994).
77. F. Liu, F. Wu, and M. G. Lagally, Chem. Rev. **97**, 1045 (1997).
78. D. J. Eaglesham, A. E. White, L. C. Feldman, *et al.*, Phys. Rev. Lett. **70**, 1643 (1993).
79. J. Walz, A. Greuer, G. Wedler, *et al.*, Appl. Phys. Lett. **73**, 2579 (1998).
80. M. Abdallah, I. Berbezier, P. Dawson, *et al.*, Thin Solid Films **336**, 256 (1998).
81. J. Zhu, K. Brunner, and G. Abstreiter, Appl. Phys. Lett. **72**, 424 (1998).
82. K. Sakamoto, H. Matsuhata, M. O. Tanner, *et al.*, Thin Solid Films **321**, 55 (1998).
83. H. Omi and T. Ogino, Appl. Surf. Sci. **130–132**, 781 (1998).
84. H. Omi and T. Ogino, Phys. Rev. B **59**, 7521 (1999).
85. D. Martou, P. Gentile, and N. Magnea, J. Cryst. Growth **201/202**, 101 (1999).
86. Y. Homma, P. Finnie, T. Ogino, *et al.*, J. Appl. Phys. **86**, 3083 (1999).
87. C. W. Oh, E. Kim, and Y. H. Lee, Phys. Rev. Lett. **76**, 776 (1996).
88. A. Nagashima, T. Kimura, and J. Yoshino, Appl. Surf. Sci. **130–132**, 248 (1998).
89. T. Tezuka and N. Sugiyama, J. Appl. Phys. **83**, 5239 (1998).
90. V. Le Thanh, Thin Solid Films **321**, 98 (1998).
91. X. Deng and M. Krishnamurthy, Phys. Rev. Lett. **81**, 1473 (1998).
92. O. G. Schmidt, C. Lange, K. Eberl, *et al.*, Thin Solid Films **321**, 70 (1998).
93. O. Leifeld, R. Hartmann, E. Müller, *et al.*, Nanotechnology **10**, 122 (1999).
94. E. S. Kim, N. Usami, and Y. Shiraki, Appl. Phys. Lett. **72**, 1617 (1998).
95. A. A. Shklyaev, M. Shibata, and M. Ichikawa, Appl. Phys. Lett. **72**, 320 (1998).
96. T. I. Kamins and R. S. Williams, Appl. Phys. Lett. **71**, 1201 (1997).
97. T. I. Kamins, R. S. Williams, and D. P. Basile, Nanotechnology **10**, 117 (1999).
98. O. P. Pchelyakov, V. A. Markov, A. I. Nikiforov, and L. V. Sokolov, Thin Solid Films **306**, 299 (1997).
99. L. V. Sokolov, M. A. Lamin, O. P. Pchelyakov, *et al.*, Poverkhnost' **9**, 75 (1985).
100. M. A. Lamin, O. P. Pchelyakov, L. V. Sokolov, *et al.*, Surf. Sci. **207**, 418 (1989).
101. N. Ohshima, Y. Koide, S. Zaima, and Y. Yasuda, J. Cryst. Growth **115**, 106 (1991).
102. Y. Koide, A. Furukawa, S. Zaima, and Y. Yasuda, J. Cryst. Growth **115**, 365 (1991).
103. C. Tatsuyama, T. Terasaki, H. Obata, *et al.*, J. Cryst. Growth **115**, 112 (1991).
104. K. Reginski, M. A. Lamin, V. I. Mashanov, *et al.*, Surf. Sci. **327**, 93 (1995).
105. A. I. Yakimov, V. A. Markov, A. V. Dvurechenskiĭ, and O. P. Pchelyakov, J. Phys.: Condens. Matter **6**, 2573 (1994).
106. U. Meirav and E. B. Foxman, Semicond. Sci. Technol. **10**, 255 (1995).
107. R. C. Ashoori, H. L. Stormer, J. S. Weiner, *et al.*, Phys. Rev. Lett. **68**, 3088 (1992).
108. A. I. Yakimov, A. V. Dvurechenskiĭ, A. I. Nikiforov, and O. P. Pchelyakov, Pis'ma Zh. Éksp. Teor. Fiz. **68**, 125 (1998) [JETP Lett. **68**, 135 (1998)].
109. G. Medeiros-Ribeiro, D. Leonard, and P. M. Petroff, Appl. Phys. Lett. **66**, 1767 (1995).
110. A. I. Yakimov, A. V. Dvurechenskiĭ, A. I. Nikiforov, and O. P. Pchelyakov, Thin Solid Films **336**, 332 (1998).
111. A. I. Yakimov, C. J. Adkins, R. Boucher, *et al.*, Phys. Rev. B **59**, 12598 (1999).
112. A. I. Yakimov, A. V. Dvurechenskiĭ, V. V. Kirienko, *et al.*, J. Phys.: Condens. Matter **11**, 9715 (1999).
113. A. I. Yakimov, A. V. Dvurechenskiĭ, A. I. Nikiforov, and O. P. Pchelyakov, Phys. Low-Dimens. Struct. **3/4**, 99 (1999).
114. S. Anand, N. Carlsson, M.-E. Pistol, *et al.*, J. Appl. Phys. **84**, 3747 (1998).

115. M. Sugawara, K. Mukai, and H. Shoji, Appl. Phys. Lett. **71**, 2791 (1997).
116. J. L. Liu, W. G. Wu, A. Balandin, *et al.*, Appl. Phys. Lett. **74**, 185 (1999).
117. P. Boucaud, V. Le Thanh, S. Sauvage, *et al.*, Appl. Phys. Lett. **74**, 401 (1999).
118. D. K. Schreder, in *Charge-Coupled Devices*, Ed. by D. Barbe (Springer-Verlag, Heidelberg, 1980; Mir, Moscow, 1982).
119. S. Sauvage, P. Boucaud, J.-M. Gerard, and V. Thierry-Mieg, Phys. Rev. B **58**, 10562 (1998).
120. P. Schittenhelm, C. Engel, F. Findeis, *et al.*, J. Vac. Sci. Technol. B **16**, 1575 (1998).
121. S. K. Zhang, H. J. Zhu, F. Lu, *et al.*, Phys. Rev. Lett. **80**, 3340 (1998).
122. V. Ya. Aleshkin, N. A. Bukin, N. G. Kalugin, *et al.*, Pis'ma Zh. Éksp. Teor. Fiz. **67**, 46 (1998) [JETP Lett. **67**, 48 (1998)].
123. M. Grassi Alessi, M. Capizzi, A. S. Bhatti, *et al.*, Phys. Rev. B **59**, 7620 (1999).
124. X. Wang, Z. Jiang, H. Zhu, *et al.*, Appl. Phys. Lett. **71**, 3543 (1997).
125. C. S. Peng, Q. Huang, Y. H. Zhang, *et al.*, Thin Solid Films **323**, 174 (1998).
126. P. Boucaud, V. Le Thanh, S. Sauvage, *et al.*, Thin Solid Films **336**, 240 (1998).
127. E. S. Kim, N. Usami, and Y. Shiraki, Appl. Phys. Lett. **72**, 1617 (1998).
128. E. Mateeva, P. Sutter, and M. G. Lagally, Appl. Phys. Lett. **74**, 567 (1999).
129. E. Palange, G. Capellini, L. Di Gaspare, and F. Evangelisti, Appl. Phys. Lett. **68**, 2982 (1996).
130. R. Apetz, L. Vescan, A. Hartmann, *et al.*, Appl. Phys. Lett. **66**, 445 (1995).

Translated by A. Spitsyn

Semiconductors, Vol. 34, No. 11, 2000, pp. 1248–1254. Translated from Fizika i Tekhnika Poluprovodnikov, Vol. 34, No. 11, 2000, pp. 1300–1306.

ATOMIC STRUCTURE AND NONELECTRONIC PROPERTIES OF SEMICONDUCTORS

Internal Microstrain and Distribution of Composition and Cathodoluminescence over Lapped $Al_xGa_{1-x}N$ Epilayers on Sapphire

A. S. Usikov, V. V. Tret'yakov, A. V. Bobyl', R. N. Kyutt, W. V. Lundin, B. V. Pushnyĭ, and N. M. Shmidt

Ioffe Physicotechnical Institute, Russian Academy of Sciences, Politekhnicheskaya ul. 26, St. Petersburg, 194021 Russia

Submitted April 12, 2000; accepted for publication April 13, 2000

Abstract—Structural properties and spatial inhomogeneity of MOCVD-grown $Al_xGa_{1-x}N$ layers on (0001) sapphire substrates were studied. A nonuniform distribution of Al across the epilayer was observed in layers grown at constant flux rates of precursors. The model of compositionally graded layer formation is proposed on the basis of cathodoluminescence and X-ray data. It is established that homogeneous samples can be obtained by increasing the flux rate of trimethylaluminum at the initial stage of epilayer growth compared with that in all further stages. Lowering the growth rate reduces strain in epitaxial $Al_xGa_{1-x}N$ layers. The influence of strain on the luminescence properties of the layers is discussed. *© 2000 MAIK "Nauka/Interperiodica".*

1. INTRODUCTION

Recently, epilayers of $Al_xGa_{1-x}N$ mixed solid solutions have attracted special attention in view of their potential application in optoelectronic devices for the UV spectral range [1, 2]. Currently, the most significant achievements have been made in the technology of III–N compounds on sapphire substrates [2]. $Al_xGa_{1-x}N$ layers grown directly on sapphire substrates can be used as wide-gap output windows for UV light emitted by the $Al_xGa_{1-x}N$/GaN active layer. Thick $Al_xGa_{1-x}N$ layers can also serve as buffer layers in the fabrication of the strain-compensated multilayer $Al_xGa_{1-x}N$/GaN structures [3]. However, both GaN and $Al_xGa_{1-x}N$ layers have been grown on sapphire substrates under large strain. In solid solutions, this leads to the formation of additional (compared with GaN) defects associated with deep centers and spatial compositional inhomogeneities in the layer [4–6]. Moreover, degradation of the $Al_xGa_{1-x}N$ layers doping efficiency [7] and a nonlinear dependence of the band gap on the solid solution composition have been noted [8–10], with the type of nonlinearity depending on the growth conditions. Thus, despite the fact that the chemical and transport processes in the growth chamber [11, 12] and growth and layer formation mechanisms for solid solutions $Al_xGa_{1-x}N$ [13, 14] have been studied in detail, investigations into the effect of growth conditions on structural, optical, and electrical properties of thick $Al_xGa_{1-x}N$ layers are still undoubtedly of interest.

The goal of this study was to gain insight into the spatial inhomogeneities of MOCVD-grown $Al_xGa_{1-x}N$ layers on (0001) sapphire substrates and into the correlation between the structural and luminescent properties of these layers, and to determine the growth conditions yielding $Al_xGa_{1-x}N$ layers with higher structural perfection.

2. SAMPLES AND EXPERIMENTAL PROCEDURES

The layers were grown in a horizontal reactor with inductive heating under lowered pressure (200 mbar) of a hydrogen flow [15]. Ammonia, trimethylgallium (TMG), and trimethylaluminum (TMA) were used as precursors. Monosilane (SiH_4) was employed for the silicon doping of the epilayers. The growth procedure included low-temperature (~510°C) deposition of a thin (about 300-Å-thick) AlGaN nucleation layer onto a (0001) sapphire substrate. Further, an epitaxial GaN sublayer and the main $Al_xGa_{1-x}N$ layer were successively grown at a higher temperature (~1040°C). Our experiments have shown that the epitaxial growth rate of GaN layers depends linearly on the TMG flow rate, and only weakly on temperature. In contrast to the epilayer, the nucleation layer grows in the diffusion mode at a growth rate independent of the TMG flow rate. The total thickness of epilayers was about 4–5 μm. The structures obtained were mirror-smooth. The technological, structural, and luminescence parameters of the samples studied are listed in the table. Samples A303 and A436 differed in the ratio of molecular flow rates TMA/(TMA + TMG) in the gaseous phase during growth of the $Al_xGa_{1-x}N$ solid solution layer. Sample A505 was grown after preliminary nitridation of the substrate surface in an ammonia flow at ~1000°C, with a doubled TMA/(TMA + TMG) ratio at the initial stage of the $Al_xGa_{1-x}N$ layer growth. The growth conditions

Parameters of $Al_xGa_{1-x}N$ epilayers on sapphire (for designations, see text)

Parameters	Sample				
	A303	A436	A505	A601	A602
$Al_xGa_{1-x}N$ layer thickness, μm	4.5	0.5	4.5	5.4	5.0
Doping	Undoped	Undoped	Si, top 3 μm	Si, top 3 μm	Undoped
GaN sublayer thickness, μm	0.5	3.5	0.0	0.0	0.0
Layer surface composition, x	0.1	0.081	0.069	0.123	0.114
$\langle\varepsilon_{zz}\rangle$	8.3	3.65	4.24	2.11	1.3
$\langle\varepsilon_{zx}\rangle$	20.4	10.05	11.6	14.8	16.1
$\langle\varepsilon_{xx}\rangle$	8.74	7.22	10.4	7.9	8.1
$\langle\varepsilon_{xz}\rangle$	13.3	3.64	3.2	4.7	4.4
t_z, nm	443	446	354	110	466
t_x, nm	140	240	215	180	193
I_{BB}	23000	26000	4000	18000	4000
$\langle I_{BB}\rangle$*	0.5	0.3	0.45	0.2	0.1
I_{DL}(~2.9 eV), arb. units	950	550	500	350	1200
$\langle I_{DL}\rangle$*	0.5	0.15	0.2	0.2	0.5
I_Y(~2.3 eV), arb. units	1300	100	800	1100	600
$\langle I_Y\rangle$*	0.4	0.1	0.15	0.2	0.4

Note: (*) Cathodoluminescence intensity variance over the initial sample surface. Excitation power ~350 W/cm^2.

for samples A601 and A602 differed from those for sample A505 in that a protective AlN coating was present on the graphite substrate holder.

The composition (x) distribution and luminescence spectra over the surface and angle lap of the samples were studied using X-ray spectral microanalysis (XRMA) and the microprobe-cathodoluminescence (MCL) technique. A Camebax microanalyzer was used, with a grating monochromator with spectral dispersion of ~2 nm/mm included in its optical system. Angle lapping was done with a Gatan dimple grinder device intended for sample preparation for transmission microscopy. The procedure included lapping at an oblique angle of 1°–2° to the sample plane with further polishing with 1-μm diamond paste. The layer composition was determined at a probe energy of 5–10 keV with 5% relative error.

MCL studies were performed with electron probe energies ranging from 2.5 to 10 keV and probe currents of 5–100 nA; the spatial resolution of the method was 5 μm. MCL spectra at 77–300 K were measured with a FEU-106 photomultiplier operating in the photon counting mode. Edge emission bands (*BB*) of excitonic nature were observed in the MCL spectra [2]. When plotted on a log–log scale, the excitation-power dependence of their intensities had a slope of about 1.0 ± 0.1. Also, two bands associated with recombination via deep levels in the band gap were observed: the so-called yellow (Y) band [6] peaked at ~2.3 eV (with a slope of the intensity–excitation-power dependence within 0.55 ± 0.05) and a band with an emission-energy peak of ~2.9 eV (DL) (with a slope of the intensity–excitation-power curve equal to that of the edge-emission band, 1.0 ± 0.1). For silicon-doped layers, a band due to donor–acceptor recombination was also observed at ~3.3 eV.

X-ray diffraction measurements were performed with a three-crystal diffractometer. Germanium single-crystals (111 reflection) were used as the monochromator and analyzer. The measurements were performed using three different configurations of diffraction from a sample: symmetric Bragg (0002 and 0004 reflections, CuK_α radiation), symmetric Laue (10–10 and 20–20, MoK_α), and grazing (11–20, CuK_α). Diffraction curves were measured for each reflection in two directions of sections through the reciprocal-lattice site: along the diffraction vector (θ–2θ-scans) and in the perpendicular direction (θ-scans). Since the diffraction peaks were broadened compared with the characteristic single-crystal half-width, expected on the basis of the dynamic theory of X-ray diffraction, the data obtained were analyzed in terms of the mosaic (block) model for GaN [16–18]. A structure of this kind also exists in the layers of $Al_xGa_{1-x}N$ solid solutions [4]. According to the model proposed in [17, 18], the strain state and the defect structure of an epilayer are characterized by components of the microdistortion tensor ε_{ij}, rms fluctuations of these components $\langle\varepsilon_{ij}\rangle \equiv \{\langle(\varepsilon_{ij})^2\rangle\}^{1/2}$, and effective dimensions of the coherent scattering regions (blocks) t_x and t_z along and across the layer. It was shown that, in most cases, the limited sizes t_x and t_z make

a much smaller contribution to the diffraction reflection broadening and, therefore, cannot be determined with a high precision (no better than 50 nm in our case).

Separate components of the microdistortion tensor describe different types of the crystal lattice distortions: $\langle\varepsilon_{zz}\rangle \equiv \{\langle(\delta c/c)^2\rangle\}^{1/2}$, $\langle\varepsilon_{xx}\rangle \equiv \{\langle(\delta a/a)^2\rangle\}^{1/2}$, $\langle\varepsilon_{xz}\rangle \equiv \{\langle(\delta\xi/\xi^2\rangle\}^{1/2}$, $\langle\varepsilon_{zx}\rangle \equiv \{\langle(\delta\gamma/\gamma)^2\rangle\}^{1/2}$, where c and a are the unit cell parameters for the wurtzite structure, ξ is the angle between the a-axis of a local region of the film and the substrate surface, and γ is the angle between the corresponding c-axis and the normal to the substrate surface. Edge dislocations normal to the heterointerface must make the main contribution to the components $\langle\varepsilon_{xx}\rangle$ and $\langle\varepsilon_{xy}\rangle$. The component $\langle\varepsilon_{xy}\rangle$, governed by the disorientation of atomic planes about the c-axis, is around 3×10^{-3} for all the samples and is not discussed further. Screw dislocations perpendicular to the heterointerface induce shear strain with the component $\langle\varepsilon_{zx}\rangle$ and distort only atomic planes parallel to the surface. Edge-type dislocations parallel to the heterointerface affect the components $\langle\varepsilon_{zz}\rangle$, $\langle\varepsilon_{xx}\rangle$, $\langle\varepsilon_{xz}\rangle$, and $\langle\varepsilon_{zx}\rangle$. The components $\langle\varepsilon_{zz}\rangle$ and $\langle\varepsilon_{xx}\rangle$ may also be affected by film-composition fluctuations. Investigations of GaN epilayers showed that, in most cases, the inequality $\langle\varepsilon_{zx}\rangle > \langle\varepsilon_{xz}\rangle$ holds, and $\langle\varepsilon_{xx}\rangle$ far exceeds $\langle\varepsilon_{zz}\rangle$ [16]. This gives reason to relate the $\langle\varepsilon_{zx}\rangle$ values to threading screw dislocations, and $\langle\varepsilon_{xx}\rangle$, to edge dislocations. Thus, the microstrain tensor allows the presence of different dislocations in the epilayer to be described in terms of the block (mosaic) model.

3. EXPERIMENTAL RESULTS AND DISCUSSION

Our investigations showed that $Al_xGa_{1-x}N$ layers obtained under different growth conditions show varied structure perfection and properties. The table characterizes the layers and lists their experimentally determined parameters (composition, microdistortion tensor components, relative intensities of main emission bands and the variances $\langle I\rangle = \{\langle(\delta I/I)^2\rangle\}^{1/2}$ over the sample surface). For all samples, the microdistortion component $\langle\varepsilon_{zx}\rangle$ was significantly larger than $\langle\varepsilon_{xz}\rangle$, and the sizes of the coherent-scattering regions were smaller in the transverse direction than along the normal, which verified columnar structure of the layers.

3.1. Layer Growth under Constant Flow Rate Ratio TMA/(TMA + TMG)

Sample A303, grown on a thin (~0.5 μm) GaN intermediate layer at a constant flow rate ratio TMA/(TMA + TMG), exhibits various inhomogeneities. Several separate peaks were observed in the edge MCL spectra, including bands with $E_{m1} \sim 3.56$ eV (corresponding to a composition $x \sim 7.5\%$) [8] and $E_{m2} \sim 3.59$ eV (corresponds to average composition of about 10% over the film surface) whose magnitude and position vary over the layer surface. The distribution of composition over the layer surface was uniform within the experimental error (±0.5%). XRMA studies of the composition over the angle lap revealed an increase in Al content from the substrate toward the layer surface (Fig. 1). Also, periodic fluctuations of the composition were detected in the obtained profile. The composition and integrated luminescence-intensity distribution across the sample thickness can be inferred from an analysis of Fig. 1. It can be seen that sublayers with correlated variations of the composition x and the luminescence intensity can be distinguished. Sample A303 also differs from other samples in X-ray diffraction characteristics. Figure 2 shows curves obtained in θ–2θ scans of the (0002) reflection for the studied samples. The peak positions on the 2θ scale are determined by the sample composition. Sample A303 is distinguished by a broader (about twofold) diffraction peak (Fig. 2) and greater microdistortion tensor components $\langle\varepsilon_{zz}\rangle$ and $\langle\varepsilon_{xz}\rangle$ (see table). These specific features must be associated with the composition variation across the film thickness. To verify this assumption, the intensity distribution was calculated for a reflection from an epilayer with composition gradient.

The nonuniform distribution of composition across the layer thickness was approximated by dividing the layer into n sublayers of the same thickness t with constant composition inside each sublayer. As a sublayer thickness t, was taken the effective coherent-scattering length along the normal to the surface (equal to 0.4 μm), determined from an analysis of $\Delta(2\theta)$ values for two orders of reflection. The diffraction from a single sublayer was calculated using the kinematic theory for a thin crystal, and the total intensity was obtained by the noncoherent summation of the intensities of all the n sublayers. Then the dependence of the intensity of a symmetric Bragg reflection I on the incidence angle θ can be represented as

$$I(\theta) = \sum_{k=1}^{n} \chi_{hk}^2 \frac{\sin^2[2\pi\cos\theta_k(\theta-\theta_k)t/\lambda]}{[(\theta-\theta_k)\sin 2\theta_k]^2} P_k. \quad (1)$$

Here, χ_{hk} is a Fourier component of polarizability (proportional to the corresponding structure factor); θ_k is the reflection center (Bragg angle) for the kth sublayer, determined by its average composition; $P_k = \exp(-\mu_k(2k-1)t)$ is the factor accounting for absorption in the upper layers; and μ_k is the photoelectric absorption coefficient. Consideration of the absorption in terms of this model (linear increase in the Al concentration from the heterointerface toward the surface) leads to asymmetry of the $I(\theta)$ curve (the effective contribution from deeper layers is smaller). However, the presence of structural defects (mainly dislocations) in the epilayer not only causes the effective dimensions of the coherent-scattering regions to decrease, but also gives rise to the additional broadening of the diffraction peak by local strain fields. Taking this effect into

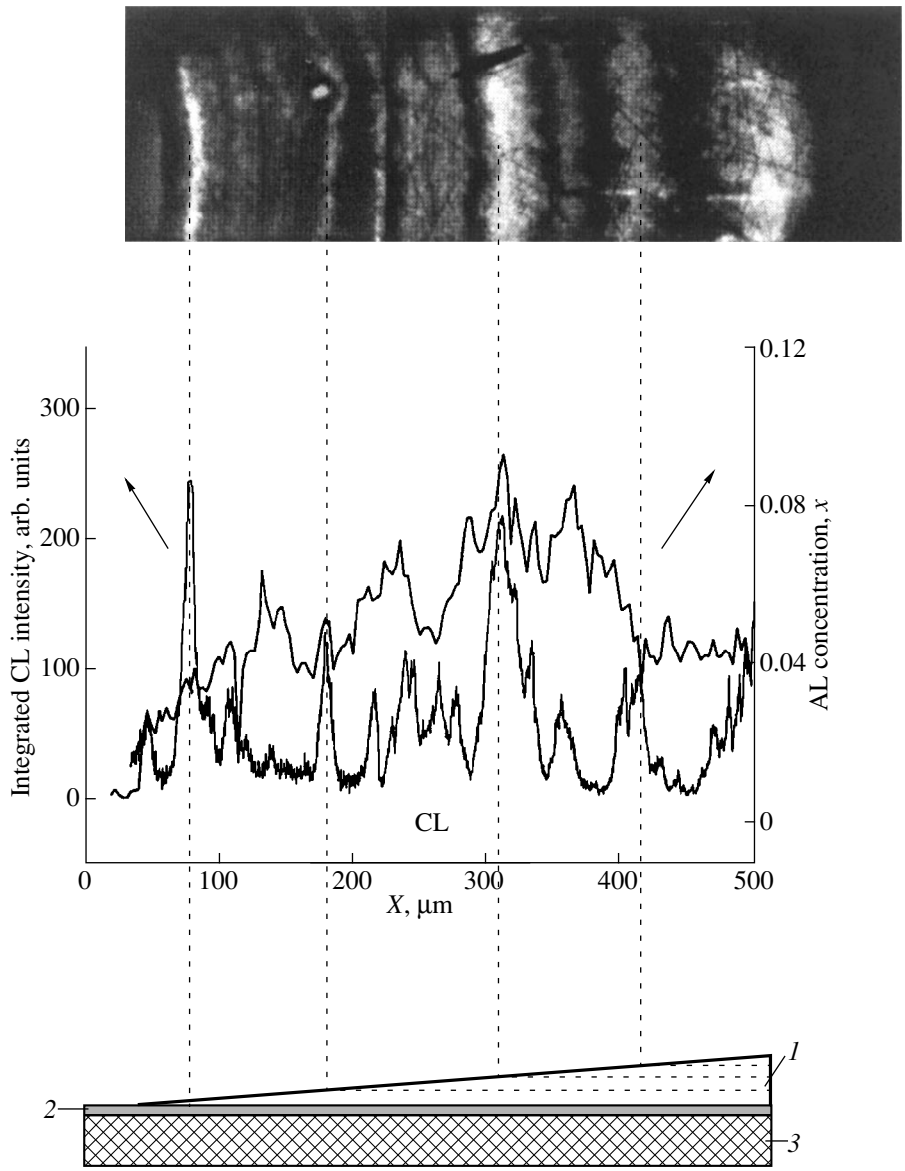

Fig. 1. Distributions of Al content (x) and integral luminescence intensity (CL) over angle lap of sample A303. (*1–3*) are $Al_xGa_{1-x}N$ and GaN layers and sapphire substrate, respectively. The CL intensities are obtained from a photographic image of luminescence from the lapped sample (above), excited by a defocused electron beam. Dashed lines: an example of dividing the structure into sublayers used to calculate the diffraction reflection curve for an epilayer with composition gradient.

account by convolving the intensity distribution $I(\theta)$ calculated by (1) with a Lorentz function with the half-width 2θ equal to the average broadening for other samples yields a resulting curve with insignificant asymmetry and close concordance with experimental data (points in Fig. 2).

The large value of $\langle \varepsilon_{xz} \rangle$ for sample A303 indicates the increased density of edge dislocations parallel to the layer–substrate interface. In this case, the formation of the epilayer can be represented as follows. During the initial stage of growth, the elastic strain field leads to the generation of dislocations and to the three-dimensional (3D) mechanism of $Al_xGa_{1-x}N$ layer growth, and gives rise to compositional inhomogeneities over the sample surface. During further layer growth, stress relaxation occurs, including that occurring via the generation of edge dislocations parallel to the layer–substrate interface. The decreasing strain in the layer leads to an abrupt transition to 2D layer growth, weaker spatial compositional inhomogeneities, and to a change in the average composition of the layer. Ultimately, such a change in the strain causes the formation of sublayers of varied composition, with different densities of defects and uncontrolled impurities

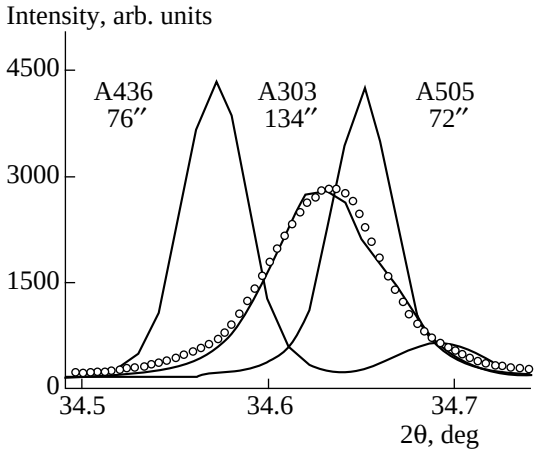

Fig. 2. Curves obtained by θ–2θ scanning of the (0002) reflection. Sample numbers correspond to those in the table; half-widths are indicated. The points represent calculations in terms of the sublayered structure model for sample A303.

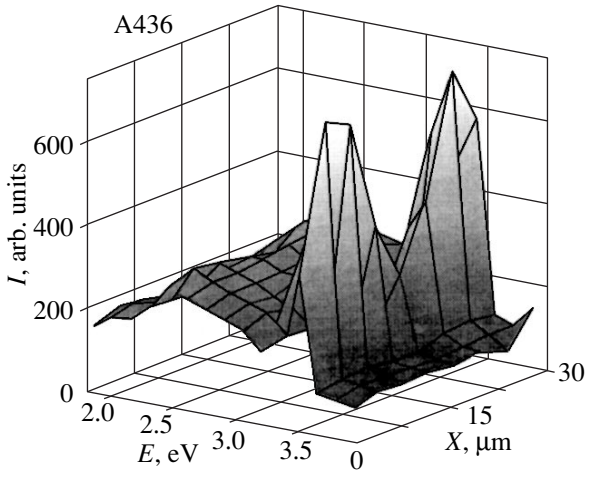

Fig. 3. Spectral distribution of the cathodoluminescence over the lapped surface of sample A436.

across the sample thickness, as shown in Fig. 1. MCL spectra measured from the surface of such layers are related to emission via localized states in different sublayers.

Previously, we have observed the depletion of the near-substrate region in Al and an increase in Al content toward the surface in thick $Al_xGa_{1-x}N$ layers grown under invariable growth conditions and different TMA/(TMG + TMA) ratios [19]. The effect of "composition tailing" has been observed in studying the In content distribution in epitaxial $In_xGa_{1-x}N$ layers [20]. An investigation of this effect in relation to substrate and layer parameters has attributed it to the presence of strain in the growing layer. Our experiments have also shown that the content of Al in a solid solution at the beginning of $Al_xGa_{1-x}N$ layer growth is governed both by the TMA/(TMG + TMA) flow-rate ratio and by the mismatch between layer and substrate parameters. All these factors allowed us to relate the Al content in a solid solution to the presence of strain during layer growth, as in [20].

To study the influence exerted by the strain on the composition distribution across the layer, a 0.5-μm-thick $Al_xGa_{1-x}N$ layer was grown on a 3.5-μm thick GaN sublayer (sample A436, see table). According to microanalysis data, the distribution of Al across the layer thickness is uniform; however, the scatter of values is beyond the limits of statistical measurement error. The thickness of the intermediate region between the GaN and $Al_xGa_{1-x}N$ layers, indicating the content of Al in the solid solution at the initial instant of $Al_xGa_{1-x}N$ layer growth, was no larger than 0.2 μm. Reflections from the $Al_xGa_{1-x}N$ layer were observable only in the θ–2θ scanning mode (in table, the parameters for sample A436 are given for the GaN layer). Therefore, it can be stated that the columnar structure of the $Al_xGa_{1-x}N$ layer inherits the *a* parameter of the GaN sublayer, and has a pseudomorphous character. An MCL study of the surface and angle lap of the sample revealed micrometer-size inclusions both in the solid solution layer and in the GaN sublayer. Some of these microinclusions were arranged along certain directions, manifesting hidden mechanical defects of the substrate. Figure 3 shows a 3D representation of MCL spectra measured from an angle-lapped sample at a 3-μm step. A pronounced decrease in the edge-luminescence intensity is observed in the middle part of the graph, which is due to the mosaic structure of the layer. However, only an insignificant decrease in the luminescence intensity is observed as compared with sample A303 (see table). On the whole, growing the $Al_xGa_{1-x}N$ layer of sample A436 on a thicker GaN buffer layer led to a considerable decrease in all the microdistortion tensor components and to smaller stresses throughout the structure. This favored, in our opinion, a more uniform distribution of composition across the layer. However, in this case the mosaic structure of the buffer layer affects the $Al_xGa_{1-x}N$ layer formation.

Decreasing the growth rate is known to be one of the methods for reducing strain in a growing layer. For epitaxial GaN layers, a linear dependence of the growth rate on the TMG flow rate is typical. Therefore, we may assume that, for $Al_xGa_{1-x}N$ layers with low Al content ($x < 0.2$), the growth rate is also governed by the TMG flow rate. Then, raising the TMA /(TMG + TMA) ratio by merely reducing the TMG molecular-flow rate will make it possible to decrease the $Al_xGa_{1-x}N$ layer growth rate. This should diminish strain, raise the amount of Al incorporated into the layer during the initial growth stage, and will eventually enable the fabrication of thick $Al_xGa_{1-x}N$ layers with a uniform Al distribution across their thickness.

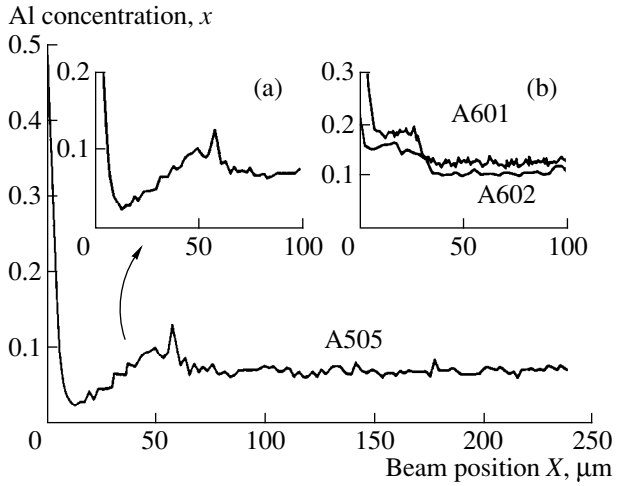

Fig. 4. Al distribution over the lapped surface of sample A505. Inserts: (a) interface between the sapphire substrate and the $Al_xGa_{1-x}N$ layer on larger scale and (b) the interfacial region for samples A601 and A602.

3.2. Growth of the $Al_xGa_{1-x}N$ Layer at a Varied Ratio of TMA/(TMA + TMG) Flow Rates during the Initial Stage of Layer Formation

The thick $Al_xGa_{1-x}N$ layer of sample A505 was grown at a doubled TMA/(TMA + TMG) flow rate ratio in the initial stage (0.5 μm) of layer growth. According to X-ray diffraction data, this layer has nearly the same microdistortion tensor as sample A436 (see table). In sample A505, the composition distribution across the layer was uniform, except for the initial section grown at a varied TMA/(TMA + TMG) flow-rate ratio (Fig. 4a). However, the edge-emission intensity I_{BB} from this sample is much lower; in addition, the sample contains macrodomains with varying defect density. MCL images taken with an unfocused beam showed growth defects in the form of hexahedral pyramids inside the $Al_xGa_{1-x}N$ layer, with a carrier concentration (determined from capacitance–voltage measurements) of $\sim 6 \times 10^{17}$ cm^{-3}. In the vicinity of these defects, the concentration decreased to 10^{17} cm^{-3}. For the spectra taken from the angle lap, the emission intensity for all the spectral lines increases toward the surface. Spectra taken in the vicinity of a pyramid of the above kind demonstrate low-intensity edge emission and enhanced intensity of the I_{DL} band. The growth of such hidden defects is probably associated with the pregrowth surface nitridation [21]. The decrease in the edge luminescence intensity may be due to a higher density of threading edge dislocations compared with other samples.

Samples A602 and A601 were grown with an increased TMA/(TMA + TMG) ratio at the initial growth stage and, as mentioned above, using a sample holder covered with AlN. This led to a higher Al content in the initial stage of growth (Fig. 4b) (see table).

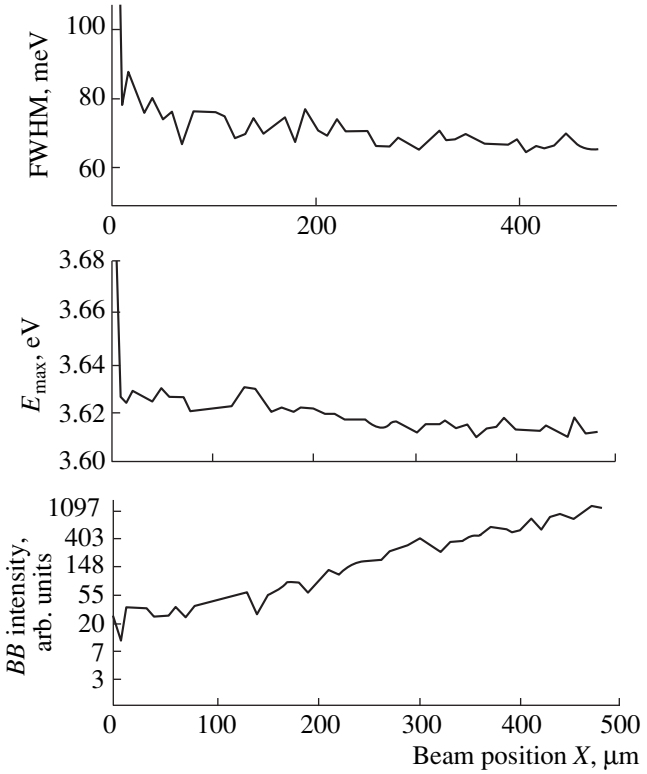

Fig. 5. The edge-luminescence intensity (*BB*), the full width at half-maximum (FWHM) of the edge-luminescence line, and the position of the luminescence peak (E_{max}) for different points on the angle lap of sample A601. The measurements were performed at 5-μm steps.

According to capacitance–voltage data, the carrier concentrations in samples A602 and A601 were $\sim 5 \times 10^{16}$ and 5×10^{17} cm^{-3}, respectively. An exponential increase in the edge-emission intensity across the layer thickness was observed. Also, the half-width of the edge-emission line and the energy E_{max}, at which the luminescence peak is observed, decreased (Fig. 5). X-ray data indicate an overall decrease in the number of layer imperfections, with the $\langle \varepsilon_{zx} \rangle$ component associated with the screw dislocations increasing somewhat. It may be assumed that, in this case, the growth conditions in the gaseous phase are improved through the elimination of undesired reactions at the holder surface and by an increase in the nitrogen flow rate, which results from the catalytic decomposition of ammonia. Consequently, these conditions appear optimal in diminishing the strain. On the whole, analysis of the microdistortion tensor components shows a tendency for the luminescence properties to improve with decreasing strain in the layers.

4. CONCLUSION

Correlation between microscopic properties (composition, cathodoluminescence) and structural charac-

teristics (microdistortion tensor components) were investigated for $Al_xGa_{1-x}N$ layers grown under varied conditions. The incorporation of Al into the solid solution during the initial stage of $Al_xGa_{1-x}N$ layer growth is governed both by the TMA/(TMA + TMG) flow-rate ratio and by the mismatch between the layer and substrate parameters. A reduction of strain in the $Al_xGa_{1-x}N$ layers leads to a more uniform Al distribution across the layer. The most compositionally homogeneous $Al_xGa_{1-x}N$ layers were obtained by growing them directly on the low-temperature nucleating layer with an increased (doubled) TMA/(TMA + TMG) ratio during the initial stage (0.5 μm) of growth of the layer deposited directly onto the sapphire substrate subjected to pregrowth nitridation. Lowering the growth rate reduces strain in the epitaxial $Al_xGa_{1-x}N$ layer. The reduction of strain improves the luminescence properties of the obtained layers. The investigation performed may provide a basis for fabrication of wide-gap windows for light-emitting diodes and photodetectors.

ACKNOWLEDGMENTS

This study was supported by the Russian Foundation for Basic Research, project no. 98-02-18109.

REFERENCES

1. F. Omnes, N. Marenco, B. Beaumont, *et al.*, J. Appl. Phys. **86**, 5286 (1999).
2. I. Akasaki and H. Amano, Jpn. J. Appl. Phys. **36**, 5393 (1997).
3. I. L. Krestnikov, W. V. Lundin, A. V. Sakharov, *et al.*, Phys. Status Solidi B **216**, 511 (1999).
4. T. J. Kistenmacher, D. K. Wickenden, M. E. Hawley, and R. P. Leavitt, Appl. Phys. Lett. **67**, 3771 (1995).
5. A. V. Polyakov, A. V. Govorkov, N. B. Smirnov, *et al.*, Solid-State Electron. **42**, 637 (1998).
6. A. V. Polyakov, M. Shin, J. A. Freitas, *et al.*, J. Appl. Phys. **80**, 6349 (1996).
7. C. G. van de Walle, C. Stampfl, J. Neugebauer, *et al.*, MRS Internet J. Nitride Semicond. Res. 4S1, G10.4 (1999).
8. H. Angerer, D. Brunner, F. Freudenberg, *et al.*, Appl. Phys. Lett. **71**, 1504 (1997).
9. A. S. Zubrilov, D. V. Tsvetkov, V. I. Nikolaev, and I. P. Nikitina, Fiz. Tekh. Poluprovodn. (St. Petersburg) **30**, 2051 (1996) [Semiconductors **30**, 1069 (1996)].
10. A. M. Tsaregorodtsev and A. N. Efimov, Pis'ma Zh. Tekh. Fiz. **22** (3), 86 (1996) [Tech. Phys. Lett. **22**, 130 (1996)].
11. G. Steude, T. Christmann, B. K. Meyer, *et al.*, MRS Internet J. Nitride Semicond. Res. 4S1, G3.26 (1999).
12. T. G. Mihopoulos, V. Gupta, and K. F. Jensen, J. Cryst. Growth **195**, 733 (1998).
13. S. Ruffenach-Clur, O. Briot, B. Gil, and R.-L. Aulombard, MRS Internet J. Nitride Semicond. Res. **2**, article 27 (1997).
14. F. Nukamura, S. Hashimoto, M. Hara, *et al.*, J. Cryst. Growth **195**, 280 (1998).
15. J. Christen, T. Hempel, F. Bertram, *et al.*, Physica E (Amsterdam) **2**, 557 (1998).
16. D. Kapolnek, X. H. Wu, B. Heying, *et al.*, Appl. Phys. Lett. **67**, 1541 (1995).
17. A. V. Bobyl', R. N. Kyutt, and V. V. Tretyakov, Semicond. Sci. Technol. **14**, 589 (1999).
18. A. S. Usikov, V. V. Ratnikov, R. Kyutt, *et al.*, MRS Internet J. Nitride Semicond. Res. **3**, 42 (1998).
19. W. V. Lundin, A. S. Usikov, B. V. Pushnyĭ, *et al.*, in *Proceedings of the 7th International Conference on Silicon Carbide, III–Nitrides and Related Materials-97, Stockholm, 1997*, Part 2, p. 1315.
20. K. Hiramatsu, Y. Kawaguchi, M. Shimizu, *et al.*, MRS Internet J. Nitride Semicond. Res. **2**, article 6 (1997).
21. I. Akasaki, H. Amano, Y. Koide, *et al.*, J. Cryst. Growth **98**, 209 (1989).

Translated by D. Mashovets

Semiconductors, Vol. 34, No. 11, 2000, pp. 1255–1258. Translated from Fizika i Tekhnika Poluprovodnikov, Vol. 34, No. 11, 2000, pp. 1307–1310.

ATOMIC STRUCTURE AND NONELECTRONIC PROPERTIES OF SEMICONDUCTORS

Epitaxial Deposition of InGaAsP Solid Solutions in the Miscibility Gap

L. S. Vavilova, V. A. Kapitonov, A. V. Murashova, and I. S. Tarasov*

Ioffe Physicotechnical Institute, Russian Academy of Sciences, Politekhnicheckaya ul. 26, St. Petersburg, 194021 Russia

** e-mail: tarasov@hpld.ioffe.rssi.ru*

Submitted May 17, 2000; accepted for publication May 18, 2000

Abstract—Liquid-phase epitaxy of InGaAsP solid solutions isoperiodic with (001)GaAs substrates was studied in the miscibility gap. At the initial stage of deposition (first 1–2 s), thin (up to 0.15 μm) planar layers of homogeneous InGaAsP solid solutions are formed. This is aided by pronounced supercooling of the melt (by 10–15°C) and the resulting high growth rates. In further stages, growth becomes slower and a natural nanoheterostructure starts to form owing to decomposition of the solid solution. The formation of a nanoheterostructure comprising domains of different compositions with different lattice constants is accompanied by the appearance of an undulating relief on the sample surface, with the undulation magnitude increasing as the layer grows. Under the technological conditions employed, the thickness of InGaAsP solid solution layers containing a nanoheterostructure is limited to 0.5 μm. © *2000 MAIK "Nauka/Interperiodica".*

INTRODUCTION

It has been established theoretically [1–7] and experimentally [8–11] that, in certain ranges of temperatures and compositions, homogeneous InGaAsP solid solutions are unstable and decompose into periodic structures with modulated composition. The decomposition of solid solutions results from the fact that a composition-modulated solid solution has lower free energy compared with the homogeneous material.

In our previous studies, when growing InGaAsP solid solutions in the miscibility gap, we obtained structures with modulated composition and studied their properties. Investigations of such structures by transmission electron microscopy (TEM) [12, 13] and photoluminescence (PL) and electroluminescence (EL) techniques [14] have shown that they have the form of periodically alternating, in the directions [100] and [010] of the easiest compression, domains of two solid solutions of different compositions with different band gaps (E_{g1} and E_{g2}) and lattice parameters (a_1 and a_2). Therefore, the PL and EL spectra of the structures include short- and long-wavelength bands associated with radiative recombination in two different kinds of domains. The domain sizes are in the range of 200–600 Å for different structures. Comparison of experimental results with theoretical data [13] suggested that in all probability we observed decomposition of InGaAsP solid solutions in our samples. It is this phenomenon that gives rise to the above natural nanoheterostructures, hereinafter named spontaneously forming periodic (SFP) InGaAsP structures. A schematic of a structure of this kind is shown in Fig. 1.

In this paper, we report the results of studying the specific features of growth of the SFP InGaAsP structures under various technological conditions and compare this process with the growth of homogeneous InGaAsP solid solutions outside the miscibility gap.

EXPERIMENTAL SAMPLES

Epitaxial layers of InGaAsP solid solutions were obtained by liquid phase epitaxy (LPE) on (001) substrates. InGaAsP solid solutions were grown both within and outside the miscibility gap. Those $In_{1-x}Ga_xAs_{1-y}P_y$ solid solutions, isoperiodic with GaAs, whose compositions lie within the ranges x = 0.6–0.82 and y = 0.95–0.48 are unstable at the growth temperature used in this study (750°C). An experimental sample with an epitaxial InGaAsP layer grown within the miscibility gap is shown schematically in Fig. 1. Experimental samples were grown in a sliding graphite boat by the method of forced cooling at the rates V_c = 0.8 and 2.0°C/min. It should be noted that InGaAsP solid solution growth did not vary significantly between these two cases.

The growth of InGaAsP layers was studied under various technological conditions. The layer growth duration t_G and the amount of supercooling ΔT of the melt from which the layer was grown were varied. The melt supercooling $\Delta T = T^L - T_G$ (T^L is the liquidus temperature, the same in all the technological processes, and T_G is the temperature of the layer growth onset) was varied from 1 to 15°C at fixed melt cooling rates and layer growth duration. In another experimental series, the layer growth duration was varied, all other parameters remaining the same.

The obtained samples were studied by the PL technique. A CamScan S4-90FE scanning electron micro-

1063-7826/00/3411-1255$20.00 © 2000 MAIK "Nauka/Interperiodica"

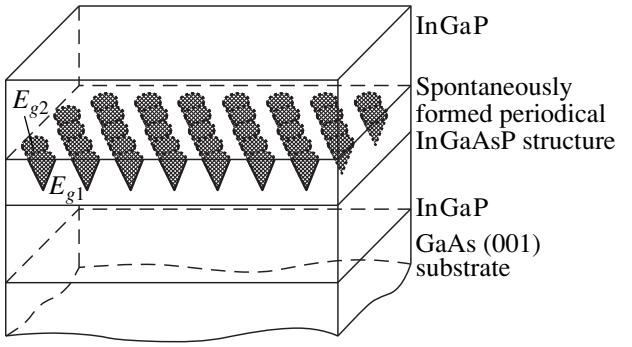

Fig. 1. Experimental sample.

scope was used to examine the sample surfaces and cleaved cross sections lying in one of the (110) planes. The cleaved cross sections were preliminarily etched in a sulfuric acid etchant $H_2SO_4 : H_2O_2 : H_2O$ (1 : 1 : 50) for 1 min.

EXPERIMENTAL RESULTS AND DISCUSSION

In the miscibility gap, we studied the growth of InGaAsP solid solutions from three different liquid phases. Epilayers thicker than 0.2 μm contained InGaAsP SFP structures composed of two solid solution domains, and their PL spectra measured at room and liquid-nitrogen temperatures showed two emission bands. At 300 K, the short-wavelength bands had peaks at around 0.70, 0.72, and 0.76 μm (for three different structures), and the long-wavelength bands, at 0.78, 0.82, and 0.85 μm, respectively.

Outside the miscibility gap, we studied the growth of a homogeneous $In_{0.21}Ga_{0.79}As_{0.68}P_{0.32}$ solid solution. The PL spectrum of this solid solution exhibited at room and liquid-nitrogen temperatures a single emission band peaked at 0.8 μm at 300 K. The half-width of the band is 70 meV, which indicates that there is no composition gradient in the layer.

The main specific feature of InGaAsP solid solutions grown in the miscibility gap was the limited epilayer thickness. The maximum thickness of ~0.5 μm was attained for the melt supercooling by ΔT = 5–15°C and the layer growth times t_G = 10–20 s. On reaching a layer thickness of ~0.5 μm, a further increase in the duration of its growth made impossible the melt removal from the sample surface. Growth from saturated liquid phases failed to produce thicker layers.

No difficulties of this kind were encountered in growing an $In_{0.21}Ga_{0.79}As_{0.68}P_{0.32}$ homogeneous solid solution. An increase in the layer growth duration resulted in progressively thicker layers whose surface remained specular. For example, a 1.6-μm-thick layer of a homogeneous $In_{0.21}Ga_{0.79}As_{0.68}P_{0.32}$ solid solution was obtained in 80 s from a liquid phase supercooled by 10°C.

In order to gain insight into the reasons why the thickness of InGaAsP solid solution layers is limited in the miscibility gap, we investigated cross sections and the surface of experimental samples by scanning electron microscopy (SEM). It was found that layers containing SFP InGaAsP structures are not planar, and their surface is not flat and shows an undulating relief.

This conclusion is illustrated by cross-sectional SEM images (Fig. 2) of several experimental samples. The samples had multilayered structure comprising a (001)GaAs substrate, an InGaP buffer layer, an InGaAsP solid-solution layer under study, and an InGaP cap layer deposited for better observability of the upper boundary of the preceding layer. This set of micrographs corresponds to an InGaAsP solid solution whose PL spectrum at 300 K includes short- and long-wavelength bands at 0.76 and 0.85 μm, respectively. In these samples, InGaAsP layer growth started at T_G = 754°C (ΔT = 6°C) and proceeded at a cooling rate V_c = 0.8°C/min for various times: t_G = 10 s (Fig. 2a), 30 s (Fig. 2b), and 10 min (Fig. 2c). As can be seen from Fig. 2, the InGaAsP layer almost ceases to grow with increasing growth duration, and its upper boundary becomes increasingly rough, which hinders the growth of the succeeding InGaP layer in the single-crystal form and results in the poor removal of the melt from the sample surface. Poor melt removal was already observed when the growth duration of the InGaAsP layer exceeded 20 s. This is clearly seen in Fig. 2b, where most of the cap InGaP layer, resembling a set of pyramids after etching-off indium from its surface, is within the image frame.

The most characteristic state of the surface of the epilayers of InGaAsP solid solutions grown within the miscibility gap is illustrated by Fig. 3. The sample shown in Fig. 3 was grown without a cap InGaP layer. The growth of the InGaAsP solid solution started at T_G = 748°C (ΔT = 12°C) and proceeded at a cooling rate of V_c = 0.8°C/min for t_G = 5 s. The PL spectrum of the obtained InGaAsP layer at room temperature included two emission bands peaked at 0.76 and 0.85 μm. It can be seen from Fig. 3 that the open surface of the InGaAsP layer (0.2 μm thick) has an undulating relief in the form of pits and hillocks several hundred nanometers in size. A similar relief can be seen in the cross-sectional SEM images of the samples (Fig. 2). In addition, most InGaAsP layers grown within the miscibility gap have a surface relief in the form of a grid whose lines are oriented along the directions [100] and [010]. This is clearly seen on the sample surface (Fig. 3).

It should be noted that the homogeneous $In_{0.21}Ga_{0.79}As_{0.68}P_{0.32}$ solid solutions grown under any of the technological conditions used in this study had flat, specular surfaces.

The appearance of a relief on the surface of InGaAsP epilayers grown in the miscibility gap can be explained as follows. As mentioned above, SFP

InGaAsP structures contain domains of two solid solutions with different lattice constants (a_1 and a_2). According to TEM data, the difference between the lattice constants of the two kinds of domains is ~1% for the structures studied. Thus, alternating dilated and compressed regions are present on the surface of a growing layer. Then, in accordance with the kinetic theory of decomposition of solid solutions [15], a flat surface may become unstable against macroscopic surface undulations. The appearance of a macroscopic profile is accompanied by a decrease in the elastic energy of the SFP InGaAsP structure and, consequently, may be energetically favorable for the growing layer despite the simultaneous increase in its surface energy. The magnitude of the profile will increase in the course of layer growth. Under actual conditions, the surface curvature becomes, at a certain stage of the growth process, sufficient for hindering melt removal from the sample surface.

The appearance of a relief may also be due to growth features at the liquid–solid-phase interface (such as, local etch undercutting of an already grown layer) during growth of a solid solution containing domains of different compositions.

When studying the growth of InGaAsP solid solutions in the miscibility gap, we noticed another phenomenon. It was found that certain technological conditions allow growth of thin (up to 0.15 μm thick) planar layers of InGaAsP solid solutions even in the miscibility gap. Such layers have the room- and liquid-nitrogen-temperature PL spectra with a single (short-wavelength) narrow emission band and, therefore, can be considered to be composed of homogeneous solid solutions.

Homogeneous InGaAsP solid solutions can be obtained in the miscibility gap only in the initial growth stage. With melt supercooled by 10–15°C and growth times of 1–2 s, ~0.15-μm-thick planar layers of homogeneous solid solutions could be grown. A further increase in layer-growth duration leads to the appearance of an SFP InGaAsP structure with all its characteristic features. At low liquid-phase supercooling (1–3°C), ~0.05-μm-thick planar layers of homogeneous InGaAsP solid solutions could be grown in 5 s. An increase in the growth duration led to the formation of an SFP InGaAsP structure, with melt removal from the layer surface becoming impossible at layer thickness of ~0.2 μm. A further increase in the growth duration led to etch undercutting of the grown layer by the liquid phase. This etching rendered an InGaAsP solid solution layer highly nonuniform in thickness and occasionally caused in to rupture.

Thus, layers of homogeneous InGaAsP solid solutions can be obtained in the miscibility gap only in a narrow range of technological conditions, namely, at high growth rates. It can be stated that layer growth from a heavily supercooled melt (ΔT = 10–15°C) occurs in two stages. In the first stage, at high layer

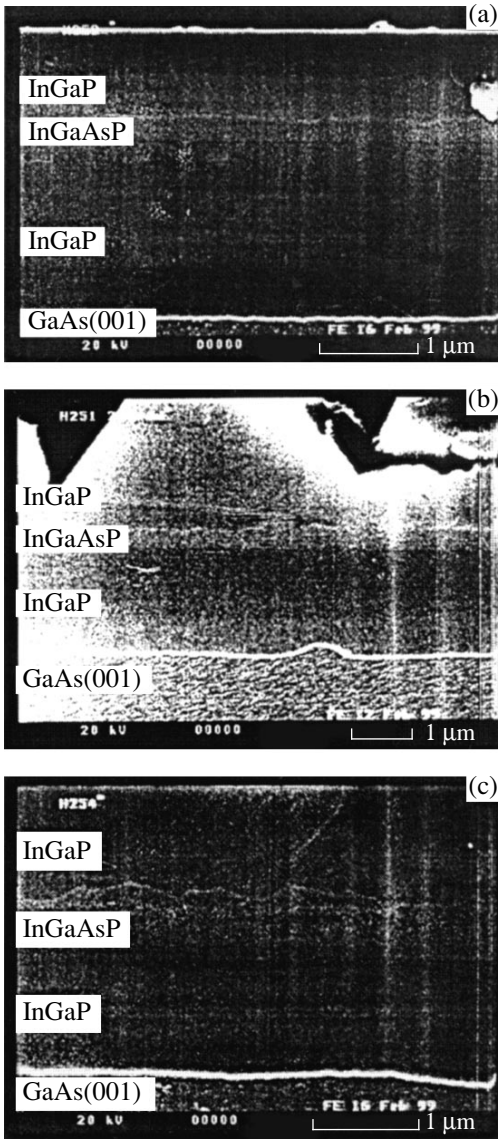

Fig. 2. SEM images of cleaved surfaces of experimental samples. InGaAsP layer growth duration: (a) 10 s, (b) 30 s, and (c) 10 min.

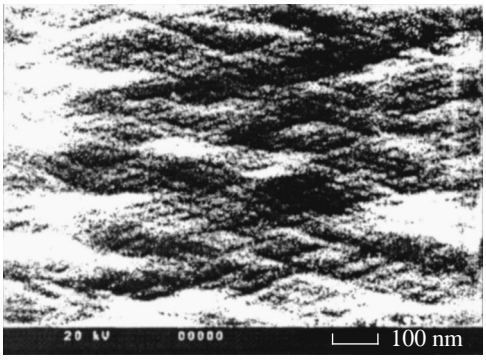

Fig. 3. Plan-view SEM image of InGaAsP epilayer grown in the miscibility gap.

growth rates, a ~0.15-μm-thick layer of a homogeneous InGaAsP solid solution can be obtained in a sufficiently short time (1–2 s). Then the layer growth rate decreases, since the melt adjacent to the growing surface is depleted of component atoms (Ga, As, P) and an SFP InGaAsP structure starts to form. It was shown previously [15] that high growth rates hinder formation of an SFP InGaAsP structure, since the layer is formed fast and phase separation has no time to occur.

CONCLUSION

Having studied epitaxial precipitation of InGaAsP solid solutions in the miscibility gap, we determined the technological conditions which allow the growth of thin (up to 0.15 μm) layers of homogeneous solid solutions and demonstrated the possibility of obtaining natural nanoheterostructures (SFP InGaAsP structures) characterized by the uniform size of nanoclusters.

PL and EL properties of SFP InGaAsP structures are of interest for optoelectronic devices. Lasers based on anisotype double heterostructures with an active region in the form of an SFP InGaAsP heterostructure were studied previously [14]. According to theoretical calculations, the presence of domains in a wide-gap solid solution surrounding the narrow-gap material in the active region of a laser allows the threshold current densities of laser diodes to be reduced to 20 A/cm^2 at 77 K and to 90 A/cm^2 at 300 K. However, at present, it is only possible to achieve threshold current densities of 70 A/cm^2 at 77 K and 700 A/cm^2 at 300 K owing to specific features of SFP InGaAsP structure fabrication by LPE. Moreover, at characteristic growth temperatures used in LPE, it is impossible to obtain thick (>0.15 μm) layers of homogeneous $In_{1-x}Ga_xAs_{1-y}P_y$ solid solutions isoperiodic with GaAs and having compositions in the ranges $x = 0.6$–0.82 and $y = 0.95$–0.48.

Possibly, fabrication of SFP InGaAsP structures by MOCVD will obviate difficulties, such as melt removal from a grown layer, hindered by surface relief, and will allow much easier control over the growth of various layers in a single technological run. By taking advantage of these growth opportunities, it would be possible to easily obtain thick layers of homogeneous solid solutions even within the miscibility gap and grow thicker layers containing SFP InGaAsP structures.

ACKNOWLEDGMENTS

We thank V.M. Busov for SEM analysis of the experimental samples and his helpful participation in discussions.

This study was supported by the Russian Foundation for Basic Research (project no. 97-02-18105) and State Scientific Program "Physics of Solid-State Nanostructures."

REFERENCES

1. B. de Cremoux, J. Phys. (Paris) **43** (C5), 19 (1982).
2. K. Onabe, Jpn. J. Appl. Phys. **21**, L323 (1982).
3. G. B. Stringfellow, J. Cryst. Growth **65**, 454 (1983).
4. A. G. Khachaturyan, *Theory of Structural Transformations in Solids* (Wiley, New York, 1983).
5. I. P. Ipatova, V. G. Malyshkin, A. Yu. Maslov, and V. A. Shchukin, Fiz. Tekh. Poluprovodn. (St. Petersburg) **27** (2), 285 (1993) [Semiconductors **27**, 158 (1993)].
6. I. P. Ipatova, V. G. Malyshkin, and V. A. Shchukin, Philos. Mag. **70**, 557 (1994).
7. D. Bimberg, I. P. Ipatova, P. S. Kop'ev, *et al.*, Usp. Fiz. Nauk **167** (3), 552 (1997) [Phys. Usp. **40**, 529 (1997)].
8. O. Ueda, S. Isozumi, and S. Komiya, Jpn. J. Appl. Phys. **23** (4), L241 (1984).
9. R. Kudela and M. Morvic, Phys. Status Solidi A **95**, K1 (1986).
10. S. Mukai, J. Appl. Phys. **54** (5), 2635 (1983).
11. A. Zunger and S. Mahajan, in *Handbook on Semiconductors*, Ed. by T. S. Moss and S. Mahajan (Elsevier, Amsterdam, 1994), Vol. 3, p. 1399.
12. A. A. Sitnikova, N. A. Bert, A. V. Murashova, *et al.*, in *Proceedings of the 14th International Symposium on Electron Microscopy, Cancun, Mexico, 1998*, p. 199.
13. N. A. Bert, L. S. Vavilova, I. P. Ipatova, *et al.*, Fiz. Tekh. Poluprovodn. (St. Petersburg) **33** (5), 544 (1999) [Semiconductors **33**, 510 (1999)].
14. L. S. Vavilova, V. A. Kapitonov, D. A. Livshits, *et al.*, Fiz. Tekh. Poluprovodn. (St. Petersburg) **34** (3), 325 (2000) [Semiconductors **34**, 319 (2000)].
15. V. A. Shchukin and A. N. Starodubtsev, in *Abstracts of the 26th International Symposium on Compound Semiconductors, Berlin, 1999.*

Translated by M. Tagirdzhanov

Semiconductors, Vol. 34, No. 11, 2000, pp. 1259–1263. Translated from Fizika i Tekhnika Poluprovodnikov, Vol. 34, No. 11, 2000, pp. 1311–1315.

ELECTRONIC AND OPTICAL PROPERTIES OF SEMICONDUCTORS

Influence of Heat Treatment on Luminescence of Semi-Insulating Undoped GaAs Crystals

K. D. Glinchuk*, N. M. Litovchenko, A. V. Prokhorovich, and O. N. Stril'chuk

Institute of Semiconductor Physics, National Academy of Sciences of Ukraine, Kiev, 252028 Ukraine

** e-mail: ria@isp.kiev.ua*

Submitted February 21, 2000; accepted for publication April 24, 2000

Abstract—Variations in the spectra of edge-emission photoluminescence of semi-insulating undoped GaAs crystals as a result of heat treatment for 20–90 min at 900°C were studied. It is shown that heat treatment substantially affects (transforms) the excitonic component of the spectrum. The observed changes in the spectra are related to variations in the impurity composition of the crystals studied. These variations are shown to be caused by heat treatment. *© 2000 MAIK "Nauka/Interperiodica".*

1. INTRODUCTION

Heat treatment of semi-insulating (SI) undoped *n*-GaAs crystals at temperatures of T_a = 800–1100°C is widely used to enhance the uniformity of distribution of various impurities and defects in these crystals (see, for example, review [1] and the relevant references therein). Obviously, in the course of such a treatment, not only the homogeneity of the SI undoped GaAs crystals increases but also appreciable changes in their impurity and defect composition occur.

This paper reports the results of studying the influence of heat treatment at T_a = 900°C on luminescent properties of SI undoped GaAs crystals. Variations in the photoluminescence (PL) spectra induced by heat treatment in the SI undoped GaAs crystals make it possible to assess the changes in the impurity–defect composition of gallium arsenide (most of the lines in the GaAs PL spectra are positively identified; i.e., the impurities and defects responsible for these lines are known [1]).

2. EXPERIMENTAL

In the studies, we used SI undoped *n*-GaAs crystals (with the resistivity of $\rho \approx 10^8\ \Omega$ cm at a temperature of $T \approx 293$ K and $\rho \longrightarrow \infty$ at $T \le 200$ K) that were 50 mm in diameter and were obtained by the Czochralski method in pyrolitic boron-nitride crucibles with B_2O_3 liquid-flux encapsulation in an inert atmosphere under a pressure of P = 3 atm. The crystals were grown under conditions close to stoichiometric; the equilibrium concentration of electrons was $n_0 \approx 10^7$ cm^{-3} at T = 293 K ($n_0 \longrightarrow 0$ for $T \le 200$ K with $n_0 \propto \exp(-0.75\ \text{eV}/kT)$, and the dislocation density was (3.2–4.8) × 10^4 cm^{-2}. Dark conductivity of the studied crystals was controlled by deep donors, i.e., the *EL*2 defects (the energy position of the levels is 0.75 eV; the corresponding concentration was 1.6×10^{16} cm^{-3}). The main background impurity in these crystals were the carbon-related acceptors with a concentration of 6×10^{15} cm^{-3}; these acceptors compensated for the *EL*2 defects.

Heat treatment of SI undoped GaAs crystals (~12 mm × 4 mm × 2 mm in size) was performed at T = 900°C for 20–90 min in evacuated and sealed quartz ampules with subsequent rapid cooling in atmospheric air (at the rate of 100–200°C/min). The heating did not affect the conductivity type of the crystal, somewhat reduced (by a factor of 1.5 at most) the value of n_0, and did not result in significant changes [exceeding the accuracy of measurements (~15%) and the spread over the cross section of the crystal (~10%)] in both the concentrations of *EL*2 defects and the carbon atoms in them.[1] However, the thermal treatment brought about appreciable changes in the concentration of the centers of nonradiative recombination of nonequilibrium charge carriers.

The PL spectra measured at T = 4.2 and 77 K for SI undoped GaAs crystals were analyzed in the energy range of $h\nu$ = 1.4–1.6 eV using an MDR-23 spectrometer with a resolution of 0.3 meV or better. The signal was detected with a cooled FEU-62 photomultiplier. Luminescence was excited with highly absorbed He–Ne-laser radiation with an intensity of $L = 10^{18}$–10^{20} photon/(cm^2 s) and the light propagating along the *y* direction. The source of the recombination emission was a

[1] Heating caused a degradation of the crystal surface (a low-resistivity near-surface layer was formed [2]) as a result of evaporation of As atoms. This layer was removed before measuring the luminescence characteristics.

1063-7826/00/3411-1259$20.00

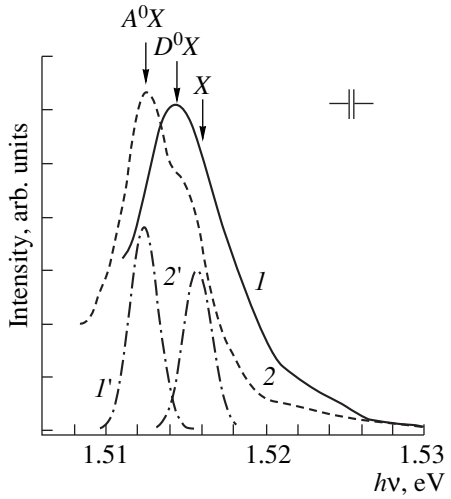

Fig. 1. The edge-emission PL spectra at $T = 4.2$ K of (*1*) initial SI undoped GaAs crystals and (*2*) the crystals subjected to a heat treatment for 90 min at $T_a = 900$°C. Curves *1*' and *2*' represent the specific PL bands related to annihilation of the bound excitons (A^0X) in initial crystals and the free excitons (X) in the heat-treated crystals, respectively. The method for decomposition of the spectra was described elsewhere [5].

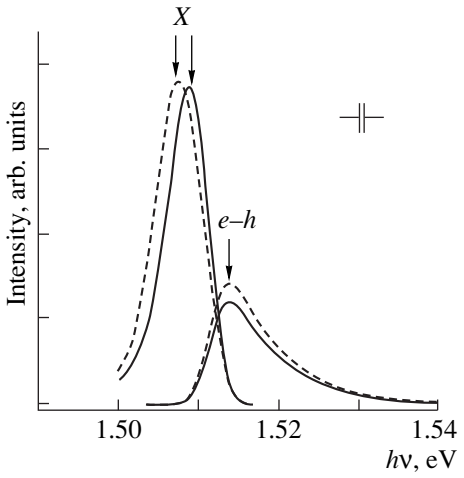

Fig. 2. The results of decomposition of the edge-emission PL spectrum (measured at $T = 77$ K) into elementary components (excitonic X and the interband e–h) of initial SI undoped GaAs crystals (continuous line) and the crystals heat-treated for 30 min at $T_a = 900$°C (the dashed line). For the details of the method for decomposition, see [5].

thin (several micrometers thick) region near the GaAs surface. The shape of PL spectra (position of the peaks and widths of PL bands and the ratio of their intensities) was almost independent of L. Therefore, we report below the PL spectra and the intensities of corresponding bands measured in the case of $L = 10^{19}$ photon/(cm^2 s). Undoubtedly, the excess holes and electrons (with concentrations of δp and δn, respectively) generated by laser radiation control the electrical conductivity of GaAs crystals (obviously, δp, $\delta n \gg n_0$ and, to a large extent, the PL intensity $I = \varphi(\delta n, \delta p)$). In order to eliminate the trivial PL-intensity variations related to changes in the concentrations of the centers of nonradiative-recombination centers for the charge carriers (correspondingly, the quantities δn and δp) as a result of heat treatment, normalized the PL-band intensity using the intensity of the band of luminescence caused by annihilation of free excitons as the reference [3, 4]. As a result, the PL-intensity variations caused by heat treatment and evident in the PL spectra reported below may be regarded as completely related to the corresponding changes in the luminescence-center concentrations.

Prior to measurements, the crystals were treated in a $H_2SO_4 : H_2O_2 : H_2O = 3 : 1 : 1$ polishing-etchant solution. Preliminarily (as was mentioned above), the low-resistivity surface layer was removed by grinding in order to circumvent the spectrum distortions related to degradation of the crystal surface during heat treatment. Thus, the annealing-stimulated variations in luminescent properties of the SI undoped GaAs crystals were completely caused by the processes that occurred in their bulk.

3. RESULTS

The most interesting variations in luminescent properties of the SI undoped GaAs crystals subjected to heat treatment were observed in the edge-emission PL spectrum (in the exciton portion). Therefore, in what follows, we restrict ourselves to the consideration of the edge-emission PL spectra alone.

Figures 1 and 2 show the spectra of edge-emission luminescence of the initial crystals and those heat-treated at $T_a = 900$°C; the spectra were measured at $T =$ 4.2 and 77 K.

At $T = 4.2$ K, the shape of the spectrum of initial crystals is mainly controlled by radiative annihilation of free excitons X (the emission band is peaked at $h\nu_m =$ 1.5158 eV; the corresponding PL intensity is denoted by I_X) and also by annihilation of excitons bound to shallow-level neutral acceptors A^0 and donors D^0 (the bound excitons A^0X and D^0X; the PL bands are peaked at $h\nu_m = 1.512$ and 1.514 eV; and the corresponding intensities are denoted as I_{A^0X} and I_{D^0X}). At this temperature, the intensity of PL related to recombination of free electrons and holes is low.[2] At 77 K, the shape of the edge-emission PL spectrum of initial crystals is mainly governed by annihilation of free excitons (band X peaked at $h\nu_{mX} = 1.5088$ eV with the half-width of

[2] See [5, 6] for identification of various lines in the edge-emission PL spectrum of gallium arsenide.

w_X = 6 meV). At this temperature, the intensities of PL caused by annihilation of bound excitons A^0X and D^0X and also by recombination of free electrons e and holes h are rather low [5].[3]

Heat treatment of SI undoped GaAs crystals at T_a = 900°C induces the following changes in the PL spectra. (I) The intensity of the A^0X band increases substantially, whereas that of the D^0X band decreases considerably. Consequently, the PL band caused by annihilation of bound excitons D^0X (its intensity exceeds that of the A^0X band) is dominant in the PL spectra of initial crystals at 4.2 K, whereas, in heat-treated crystals, the PL band caused by annihilation of the bound excitons A^0X becomes dominant (its intensity is higher than that of the D^0X band). (II) In the spectra measured at 77 K, the heat treatment caused the PL band related to annihilation of free excitons to significantly shift to lower energies (from 1.5088 to 1.5070 eV); simultaneously, the half-width of this band increased from 6 to 7 meV.

Figures 4 and 5 show the intensities of the PL bands related to bound excitons A^0X and D^0X and also the position of the peak and the half-width of the PL band related to annihilation of free excitons X in relation to the duration t of heat treatment of the SI undoped GaAs crystals at T_a = 900°C. As can be seen, an increase in the duration of heat treatment results in a steady increase in the A^0X-band intensity and in nonmonotonic changes in the intensity of the band D^0X (this intensity first decreases and then increases). In addition, an increase in the duration of heat treatment brings about a nonmonotonic shift to lower energies of the PL band related to annihilation of free excitons (the peak of this band first shifts from 1.5088 to 1.507 eV and then shifts from 1.507 to 1.508 eV); simultaneously, the half-width of this band also changes nonmonotonically (it increases first from 6 to 7 meV and then decreases from 7 to 6 meV).

4. DISCUSSION OF THE RESULTS

We now discuss the above data. It is necessary to take into account two facts. First, heat treatment does not bring about any significant variations in the carbon concentration. Second, the annealing-stimulated changes in the intensities I_{A^0X} and I_{D^0X} (normalized to the value of I_X) are governed only by the corresponding variations in the concentrations of the shallow-level acceptors N_A and donors N_D.[4] Then the following explanations can be given to the above experimental data.

—The annealing-induced increase in the intensity of PL caused by annihilation of bound excitons A^0X and a decrease in the intensity of PL related to annihilation of bound excitons D^0X (Fig. 1) is explained by an increase in the concentration of shallow-level acceptors (most probably, the zinc atoms) and a decrease in the concentration of shallow-level donors (most probably, the silicon atoms) as a result of their activation and passivation, respectively, during the thermal treatment.

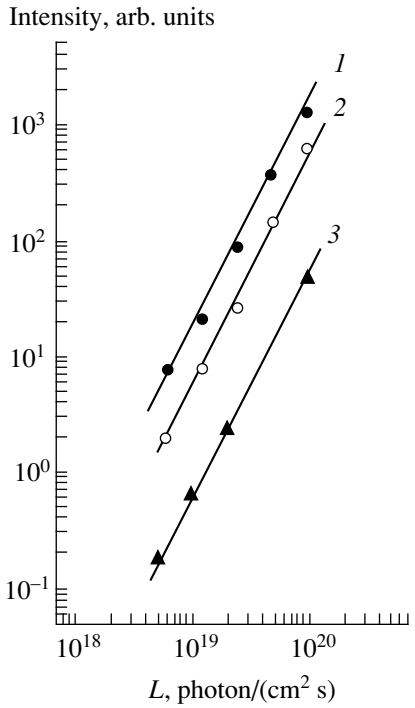

Fig. 3. The intensities of PL bands in relation to the intensity of illumination: (*1*) the A^0X band, T = 4.2 K, $h\nu_m$ = 1.512 eV; (*2*) the D^0X band, T = 4.2 K, $h\nu_m$ = 1.514 eV; and (*3*) the X band, T = 77 K, $h\nu_m$ = 1.5088 eV. The straight lines correspond to theoretical dependences I_{A^0X}, I_{D^0X}, $I_X \propto L^2$.

[3] For the high excitation levels used (δn, $\delta p \gg n_0$ and δn, $\delta p \propto L$), the intensities of excitonic luminescence bands I_{A^0X}, I_{D^0X}, and I_X increased with increasing intensity of illumination in proportion to L^2 (Fig. 3). In particular, it follows from the above that, for T = 4.2 K and L = 10^{18}–10^{20} photon/(cm^2 s), the acceptors and donors are mainly in the neutral state (A^0 and D^0), whereas, for T = 4.2 K and L = 0, they are mainly charged (A^- and D^+) [7, 8].

[4] Obviously, in the general case, we have $I_{A^0X} \propto \int_0^\infty N_a^0 n_e dy$, $I_{D^0X} \propto \int_0^\infty N_D^0 n_e dy$, and $I_X \propto \int_0^\infty n_e dy$, where N_A^0 and N_D^0 are the concentrations of neutral acceptors and donors to which excitons are bound [7]. Consequently, the above statement is true if N_A^0, $N_D^0 \neq \varphi(L)$, in particular, for $N_A^0 \approx N_A$ and $N_D^0 \approx N_D$ (the latter approximate equalities held in the experiment, see above). In this case, $I_{A^0X} \propto N_A^0 \int_0^\infty n_e dy$ and $I_{D^0X} \propto N_D^0 \int_0^\infty n_e dy$, whereas the intensities (normalized to I_X) $I_{A^0X}/I_x \propto N_A$ and $I_{D^0X}/I_x \propto N_D$ (see also [3, 7]).

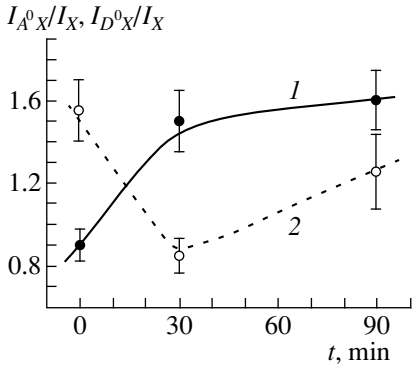

Fig. 4. The dependences of normalized intensities of the PL bands related to bound excitons (*1*) A^0X and (*2*) D^0X on the duration t of heat treatment of the SI undoped GaAs crystals at T_a = 900°C. The intensities I_{A^0X} and I_{D^0X} were measured at T = 4.2 K.

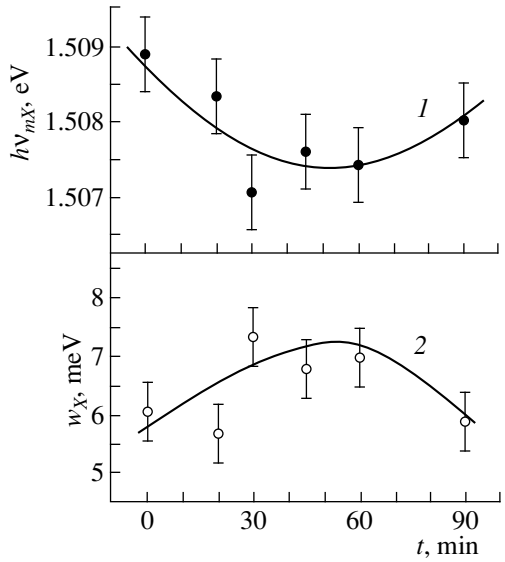

Fig. 5. Dependences of the (*1*) position of the peak $h\nu_{mX}$ and (*2*) the half-width w_X of the PL band related to annihilation of free excitons in relation to the duration t of heat treatment of the SI undoped GaAs crystals at 900°C. The quantities $h\nu_{mX}$ and w_X were measured at 77 K.

—The annealing-stimulated shift of the excitonic PL band to lower energies and an increase in the half-width of this band (Fig. 2) is related to an increase in the concentration of electrically active impurities (in particular, the shallow-level acceptors) during heat treatment of the SI undoped GaAs crystals (for more details, see [5]).

—The steady increase in the A^0X-band intensity (Fig. 4) with increasing duration of heat treatment is related to the annealing-stimulated activation of the shallow-level background acceptors. The simultaneously observed nonmonotonic variation in the intensity of the D^0X band (Fig. 4) is related first to gradual deactivation and then to activation of background donors

—A nonmonotonic change in the position of the peak and the half-width of the band X (Fig. 5) by increasing duration of the heat treatment is caused by the annealing-stimulated variations in the total concentration of electrically active background impurities (for more details, see [5]).

The aforementioned variations in the concentrations of shallow-level donors and acceptors during heat treatment of the SI undoped GaAs crystals may be caused by the following processes (occurring with differing rates):

(i) Interaction of interstitial shallow-level impurities with arsenic and gallium vacancies formed in the course of heat treatment [9, 10]. Such an interaction results in an increase in the concentration of shallow-level impurities at the lattice sites, i.e., in the electrically active state.

(ii) Interaction of interstitial arsenic and gallium atoms formed during the heat treatment with substitutional shallow-level impurities [10]. As a result of this interaction, the shallow-level impurities are pushed out from the lattice sites into interstices; i.e., these impurities become electrically inactive.

(iii) The annealing-stimulated exchange of sites of the shallow-level impurities B and D of Group IV, one of which ($\mathcal{B}_{Ga}$) initially resides in the gallium sublattice of gallium arsenide and is a donor, whereas the other impurity ($\mathcal{D}_{As}$) resides in the arsenic sublattice and is an acceptor (the corresponding reaction can be written as $\mathcal{B}_{Ga} + \mathcal{D}_{As} \longrightarrow \mathcal{B}_{As} + \mathcal{D}_{Ga}$) [11]. Such a process causes an obvious transformation of donors $\mathcal{B}_{Ga}$ into acceptors $\mathcal{B}_{As}$ and of acceptors $\mathcal{D}_{As}$ into donors $\mathcal{D}_{Ga}$. Undoubtedly the consequences are a decrease in the concentrations of donors $\mathcal{B}_{Ga}$ and acceptors $\mathcal{D}_{As}$ and an increase in the concentrations of acceptors $\mathcal{B}_{As}$ and $\mathcal{D}_{Ga}$.

(iv) The annealing-induced processes of generation and destruction of electrically inactive complexes that consist of a shallow-level impurity and an intrinsic defect in the lattice [10, 12]. An obvious result of such a process is a decrease (in the case of generation) or an increase (in the case of destruction) in the concentrations of shallow-level donors or acceptors.

Direct measurements of concentrations of the shallow-level donors and acceptors in the SI undoped GaAs crystals confirm the opinion that heat treatment can indeed result in significant variations in their concentrations [9, 12].

5. CONCLUSION

Heat treatment of the SI undoped GaAs crystals for 20–90 min at T_a = 900°C significantly affects the shape

of the excitonic PL spectrum; namely, the intensity of PL band A^0X related to annihilation of bound excitons increases steadily, the intensity of the luminescence band D^0X related to annihilation of bound excitons varies nonmonotonically, the peak of the band related to annihilation of free excitons shifts nonmonotonically to lower energies, and the half-width of the latter band also varies nonmonotonically. The aforementioned changes in the excitonic PL spectra as a result of heat treatment are related to nonmonotonic variation in the impurity composition of the samples with increasing duration of annealing. In fact, the above changes in the spectra may be due to (i) an increase in the concentration of shallow-level acceptors (most likely, zinc atoms) involved in the bound excitons A^0X as a result of activation of these acceptors in the course of heat treatment; (ii) first a decrease and then an increase in the concentration of shallow-level donors (most likely, silicon atoms) involved in the bound excitons D^0X as a result of activation and deactivation of these donors during heat treatment; and (iii) an enhancement of exciton–impurity interaction as a consequence of an increase in the total impurity content in the crystal in the course of thermal treatment.

REFERENCES

1. K. D. Glinchuk, V. I. Guroshev, and A. V. Prokhorovich, Optoélektron. Poluprovodn. Tekh. **24**, 66 (1992).
2. I. F. Aĭbazov, S. B. Mikhrin, and B. E. Samorukov, Fiz. Tekh. Poluprovodn. (St. Petersburg) **29**, 162 (1995) [Semiconductors **29**, 85 (1995)].
3. A. S. Kaminskiĭ, L. I. Kolesnik, B. M. Leĭferov, and Ya. E. Pokrovskiĭ, Zh. Prikl. Spektrosk. **36**, 745 (1982).
4. K. D. Glinchuk, N. M. Litovchenko, A. V. Prokhorovich, and O. N. Stril'chuk, Fiz. Tekh. Poluprovodn. (St. Petersburg) **34** (5), 530 (2000) [Semiconductors **34**, 514 (2000)].
5. K. D. Glinchuk, N. M. Litovchenko, A. V. Prokhorovich, and O. N. Strilchuk, Phys. Status Solidi B **213**, 233 (1999).
6. L. Pavesi and M. Guzzi, J. Appl. Phys. **75**, 4779 (1994).
7. T. Schmidt, K. Lischka, and W. Zulehner, Phys. Rev. B **45**, 8989 (1992).
8. K. D. Glinchuk, N. M. Litovchenko, A. V. Prokhorovich, and O. N. Strilchuk, in *Proceedings of the 43rd International Scientific Colloquium, Technical University of Ilmenau, Germany, 1998*, Vol. 2, p. 588.
9. M. Suemitsu, K. Terada, M. Nishijima, and N. Miyamoto, J. Appl. Phys. **70**, 2594 (1991).
10. Chen Chao, V. A. Bykovskiĭ, and M. I. Tarasik, Fiz. Tekh. Poluprovodn. (St. Petersburg) **28**, 35 (1994) [Semiconductors **28**, 19 (1994)].
11. J. van de Ven, W. J. Hartmann, and L. J. Giling, J. Appl. Phys. **60**, 3735 (1986).
12. O. Ka, O. Oda, Y. Makita, and A. Yamada, Appl. Phys. Lett. **61**, 1095 (1992).

Translated by A. Spitsyn

Semiconductors, Vol. 34, No. 11, 2000, pp. 1264–1269. Translated from Fizika i Tekhnika Poluprovodnikov, Vol. 34, No. 11, 2000, pp. 1316–1321.

ELECTRONIC AND OPTICAL PROPERTIES OF SEMICONDUCTORS

Basic Principles of Postgrowth Annealing of CdTe:Cl Ingot to Obtain Semi-Insulating Crystals

O. A. Matveev* and A. I. Terent'ev

Ioffe Physicotechnical Institute, Russian Academy of Sciences, ul. Politekhnicheskaya 26, St. Petersburg, 194021 Russia

** e-mail: Oleg.matveev@pop.ioffe.rssi.ru*

Submitted April 26, 2000; accepted for publication April 28, 2000

Abstract—The process of annealing of a CdTe:Cl ingot during its cooling after growth was studied. The annealing was performed in two stages: a high-temperature stage, with an approximate equality of chlorine and cadmium vacancy concentrations established at the thermodynamic equilibrium between the crystal and vapors of volatile components, and a low-temperature stage, with charged defects interacting to form neutral associations. The chlorine concentrations necessary to obtain semi-insulating crystals were determined for various ingot cooling rates in the high temperature stage. The dependence of the chlorine concentration $[Cl_{Te}^{+}]$ in the ingot on the temperature of annealing in the high-temperature stage was found. The carrier lifetimes and drift mobilities were obtained in relation to the temperature and cadmium vapor pressure in the postgrowth annealing of the ingot. © *2000 MAIK "Nauka/Interperiodica"*.

As is known, the low conductivity of CdTe crystals and the high free-carrier lifetimes and mobilities, needed for nuclear radiation detectors [1, 2], can be achieved in a chlorine-doped material owing to the self-compensation of charged atomic defects [3–6].

Previously [7, 8], we have studied the self-compensation in annealing of $3 \times 3 \times 12$ mm^3 CdTe:Cl samples under controlled pressure of Cd and Te vapors, simulating the cooling of an ingot after crystal growth at $T \lesssim 980$°C. The annealing produced semi-insulating samples with a conductivity of $\sigma \approx 10^{-10}$ Ω^{-1} cm^{-1} and low free-carrier concentration $p(n) = (10^7–10^8)$ cm^{-3}. However, the mobility–lifetime products for electrons and holes in the annealed samples, $\mu_e\tau_e \approx 10^{-4}$ cm^2 V^{-1}, $\mu_h\tau_h \approx 10^{-5}$ cm^2 V^{-1}, were much smaller than those in the as-grown ingot: $\mu_e\tau_e \approx 10^{-3}$ cm^2 V^{-1}, $\mu_h\tau_h \approx 10^{-4}$ cm^2 V^{-1}. Unfortunately, the annealing could not be performed in these studies at the highest temperatures, where postgrowth annealing sets in, nor at low cadmium vapor pressure $P_{Cd} \longrightarrow P_{Cd}^{min}$. This was due to the fact that under these conditions the sublimation and transfer of the material into the cold part of an ampule caused changes not only at the surface, but also in the bulk of the sample, indicated by its nonuniform electrical conductivity.

In this paper, we report the results obtained by studying self-compensation in the annealing of an ingot immediately after its growth, with the annealing practically beginning with the compound crystallization temperature.

CdTe:Cl ingots weighing 0.5–1.0 kg are grown by horizontal planar crystallization under controlled cadmium vapor pressure [9]. During the growth, the material is doped with N(Cl) of chlorine. During the postgrowth cooling, the ingot is annealed, which enables the self-compensation of charged atomic crystal defects beginning with the highest temperatures. The self-compensation occurs in two annealing stages. In the first stage, there occurs high temperature annealing (T_{ann} = 1070–800°C) when the solubility of intrinsic atomic defects is high [10] and a high concentration of cadmium vacancies $[V_{Cd}^{-2}] + [V_{Cd}^{-1}] \gtrsim [Cl_{Te}^{+}]$ can be obtained, which also should exceed the concentration of unintentional impurities. At this temperature, the association of donors and acceptors is weakly pronounced and can be neglected [3, 10]. The second stage consists in low-temperature annealing (T_{ann} = 800–400°C). This stage is dominated by the interaction of charged defects to form uncharged associations: $(V_{Cd}^{-2}2Cl_{Te}^{+})^0$, $(V_{Cd}^{-}Cl_{Te}^{+})^0$, $(A^-D^+)^0$. Primary defects, not bound into neutral associations, remain in the crystal: V_{Cd}^{-2}, $(V_{Cd}^{-2}Cl_{Te}^{+})^-$ and other defects, e.g.,$(V_{Cd}^{-2}D^+)^-$, $(A^{-2}Cl_{Te}^{+})^-$ (here D and A are the background donor and acceptor impurities), giving rise to energy levels in the band gap: E_v + 0.9 eV, E_v + 0.14 eV, and E_v + (0.5–0.9) eV [11]. The carrier mobilities and lifetimes are determined by the concentrations of these crystal defects. Hereinafter, no mention is made of the vacancy V_{Cd}^{-1}, present in much lesser amount compared with the V_{Cd}^{-2} vacancy. The predominance of the V_{Cd}^{-2} defect governs the self-compensation in CdTe [6, 10].

1063-7826/00/3411-1264$20.00

Let us consider the self-compensation conditions in the high-temperature stage of the ingot annealing. When an ingot is kept at a constant temperature at thermodynamic equilibrium between CdTe and cadmium vapor with the pressure P_{Cd} in the ampule for a long time (t = 5–15 h), the crystal composition corresponding to the vapor pressure and the related concentration of cadmium vacancies are established. The main condition for self-compensation is that V_{Cd} be soluble at the annealing temperature. T_{ann} = 800°C is the lowest temperature that allows a sufficiently high defect concentration $[V_{Cd}^{-2}] \gtrsim [Cl_{Te}^{+}]$ to be obtained. At lower T_{ann}, the solubility of acceptor defects V_{Cd}^{-2} at the crystal–gas equilibrium is not sufficiently high to enable the self-compensation of charged defects even at very low vapor pressures $P_{Cd} \approx P_{Cd}^{min}$.

Another condition for self-compensation is that the ratio of donor and acceptor concentrations $[V_{Cd}^{-2}] \gtrsim [Cl_{Te}^{+}]$ be maintained constant during cooling at the high-temperature stage. It was found experimentally that the obtainment of a semi-insulating self-compensated material depends on the chlorine concentration. If the concentration of $[Cl_{Te}^{+}]$ defects exceeds the cadmium vacancy concentration during the ingot cooling, we obtain a high-conductivity material with $n \approx 10^{16}$ cm^{-3}. The solubility of chlorine and cadmium vacancies decreases as the CdTe crystal temperature becomes lower [12, 13]. Consequently, two possibilities exist in ingot cooling. First, if the $[V_{Cd}^{-2}]$ and $[Cl_{Te}^{+}]$ concentrations decrease in approximately the same manner, the relation $[V_{Cd}^{-2}] \gtrsim [Cl_{Te}^{+}]$ remains valid and a semi-insulating material is obtained. The second possibility is that the relation between the concentrations varies in such a way that $[Cl_{Te}^{+}]$ starts to exceed $[V_{Cd}^{-2}]$ and we obtain a high-conductivity material.

Either semi-insulating or high-conductivity CdTe can be obtained depending on N(Cl) and the ingot cooling rate (v_{CdTe}) at the high-temperature stage (see Fig. 1). The N(Cl) concentration includes chlorine dissolved in the CdTe ingot, i.e., electrically charged chlorine (Cl_{Te}^{+}), chlorine at grain boundaries, and also chlorine filling the gas space of the ampule and adsorbed by the graphite coating of the ampule and the container, etc. It seems reasonable that, the experimental conditions being the same, changes in N(Cl) will lead to the corresponding changes in the chlorine content in the crystal itself. We used N(Cl) concentrations no lower than 2×10^{18} cm^{-3}, the minimal value necessary for crystal self-compensation to occur in CdTe growth from the melt [14], to N(Cl) $\approx 2 \times 10^{19}$ cm^{-3}, at which $CdCl_2$ precipitates at the grain boundaries [15]. To

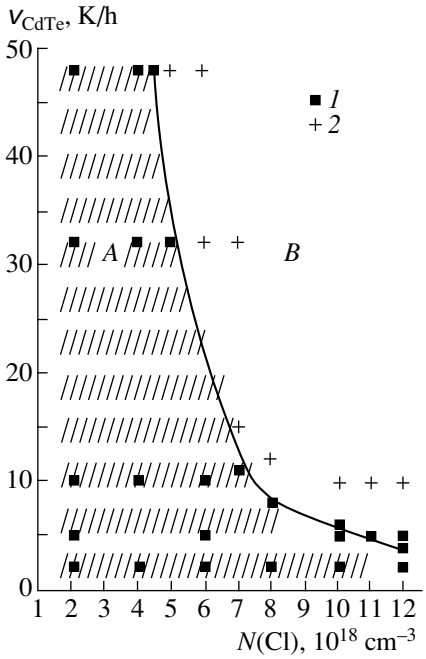

Fig. 1. Regions of low (*A*) and high (*B*) conductivities of CdTe:Cl crystals in the diagram showing the rate of ingot cooling (v_{CdTe}) in the temperature range 1070–900°C against the chlorine concentration. Regions *A* and *B* correspond to concentrations: (*A*) $p \approx 10^8$ cm^{-3} and (*B*) $n \approx 10^{16}$ cm^{-3}. Designations: (*1*) semi-insulating and (*2*) high-conductivity CdTe.

obtain semi-insulating crystals, the ingot cooling rate should be chosen so that the defect concentrations $[Cl_{Te}^{+}]$ and $[V_{Cd}^{-2}]$ are approximately the same during the entire high-temperature annealing stage. The curve in Fig. 1 divides its area into two regions corresponding to the two possible relations between the defect concentrations: $[V_{Cd}^{-2}] \geq [Cl_{Te}^{+}]$ and $[Cl_{Te}^{+}] > [V_{Cd}^{-2}]$. A semi-insulating material is obtained over the entire range of dopant concentrations N(Cl) = 2×10^{18}–2×10^{19} cm^{-3} when v_{CdTe} = 2 K/h (see Fig. 1). For higher ingot cooling rates, this region becomes narrower at the expense of high chlorine concentrations, when a high-conductivity material (region *B* in Fig. 1) is obtained. At the highest cooling rates v_{CdTe} = 48 K/h, a semi-insulating crystal is obtained only at the lowest concentrations N(Cl) = (2–4) $\times 10^{18}$ cm^{-3}.

Under the annealing conditions represented by the high-conductivity region *B* (unshaded field in Fig. 1), high cooling rates at a high chlorine content in the ingot make it impossible to maintain equal concentrations of chlorine and cadmium vacancies [13, 16]. This is associated with the fact that, in fast cooling, the $[Cl_{Te}^{+}]$ concentration has no time to attain the value corresponding to the equilibrium solubility of chlorine owing to its low diffusion coefficient, compared with that for the

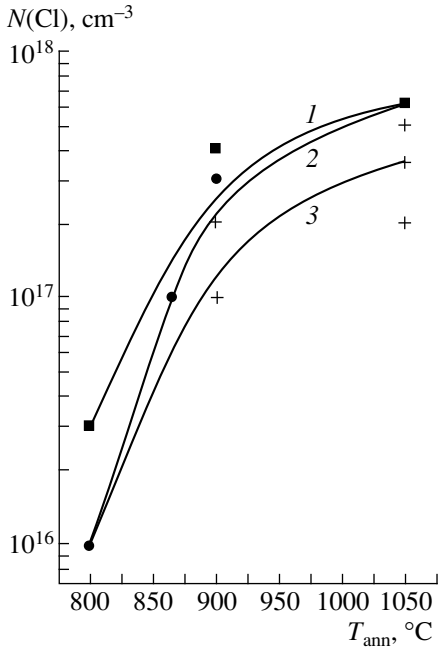

Fig. 2. Chlorine concentration N(Cl) in the CdTe:Cl ingot, determined (*1*) by mass-spectral analysis, (*2*) by atomic sorption analysis, (*3*) from Hall data, vs. the annealing temperature T_{ann}.

cadmium vacancies. Consequently, the Cl_{Te}^{-} impurity concentration in the crystal may exceed the concentration of V_{Cd}^{-2} vacancies, thus giving rise to a material with $n \approx 10^{16}$ cm^{-3}.

Thus, the conditions for self-compensation in CdTe:Cl by high-temperature annealing of an ingot are determined for the entire high-temperature stage cooling after crystal growth in a wide range of doping levels and cooling rates.

The ingot annealing at the low-temperature stage is also performed satisfying the requirements that self-compensation should occur. In this stage, the ingot is cooled at an experimentally selected rate v = 50–80 K/h, which is sufficiently fast to prevent the attainment of a low cadmium vacancy concentration corresponding to these temperatures (800–400°C) [17, 18]. Thus, the charged-defect concentration balance achieved in the high-temperature stage is not disturbed. At the same time, this cooling rate is quite sufficient to ensure the formation of associations of Cl_{Te}^{+} donors with V_{Cd}^{-2} acceptors, so that the crystal becomes "self-purified" [5]. The associations are formed as a result of defects migrating toward one another. The probability of association formation is evaluated using the theory of random walks [19]. The probability that the motion of a defect results in its arrival at a "sink" (association formation) nearly equals the probability that the lattice site at which the defect finds itself is a sink. This probability is equal to the atomic fraction of sinks C. In the case under consideration,

$$C \approx \frac{[Cl_{Te}^{+}]}{N_0} \approx \frac{[V_{Cd}^{-2}]}{N_0} \approx \frac{10^{16}\ \text{cm}^{-3}}{10^{22}\ \text{cm}^{-3}} = 10^{-6},$$

where N_0 is the atomic concentration per cubic centimeter. Therefore, the average number of hops necessary for arriving at a sink is approximately $\bar{n} \approx 1/C = 10^6$. To determine the time necessary for association formation to be complete, we need to evaluate the time constant for the reduction in the concentration of defects $\bar{\tau}$. This constant can be calculated in terms of diffusion theory: $\bar{n} = z\bar{\nu}\bar{\tau}$, where $z = 4$ is the coordination number and $\bar{\nu} = D/a^2\gamma$ is the average frequency of jumps in the direction toward the sink, corresponding to the diffusion coefficient D for a moving defect; $\gamma = 1$ for a cubic lattice; $a = 2.5 \times 10^{-8}$ cm is the interatomic distance in CdTe. Thus, we have $\bar{\tau} \approx 1.6 \times 10^{-10}/D$. For the extreme temperatures in the second stage of annealing, 400 and 800°C, we have the following diffusion coefficients for the moving defects [13, 16]:

$$D(\text{Cl}) = 10^{-11}\ \text{cm}^2\ \text{s}^{-1}, \quad D(V_{Cd}) = 10^{-10}\ \text{cm}^2\ \text{s}^{-1},$$

and

$$D(\text{Cl}) = 10^{-9}\ \text{cm}^2\ \text{s}^{-1}, \quad D(V_{Cd}) = 2 \times 10^{-8}\ \text{cm}^2\ \text{s}^{-1},$$

respectively. The cooling time of 6 h, chosen for our experiment, is $\sim 10^3\bar{\tau}$ even for the smallest diffusion coefficient D, and, as a result, the process of defect association can be considered complete.

To obtain semi-insulating crystals, the relation $[Cl_{Te}^{+}] \approx [V_{Cd}^{-2}]$ should be fulfilled during both annealing stages. Therefore, it is important to know the chlorine concentration, and its temperature variation, directly in the crystal in order to specify in a substantiated way the necessary $[V_{Cd}^{-2}]$ concentration by maintaining the P_{Cd} pressure.

The chlorine content in the ingot at varied annealing temperatures was determined by mass-spectrometric and atomic sorption analyses and, indirectly, by measuring the Hall constant of specially annealed single-crystal samples (Fig. 2). The free-carrier concentration corresponding to the chlorine (shallow donor) concentration, $n = [Cl_{Te}^{+}]$, was found from the Hall voltage [10]. The chlorine was transformed from bound states $(V_{Cd}^{-2}\,2Cl_{Te}^{+})^0$, $(A^{-}Cl_{Te}^{+})^0$ into a donor state by annealing at a high pressure P_{Cd} [7]. The results obtained by using both direct and indirect methods indicate that the chlorine concentration behaves in the same way in the CdTe ingot with the annealing temperature under postgrowth cooling conditions. The chlorine concentration determined from the Hall voltage is the lowest, compared

with the values produced by other analytical methods, because it includes only electrically charged isolated Cl_{Te}^{+} defects.

Figure 3 shows the carrier concentrations n and p in relation to pressure P_{Cd} for two annealing temperatures. For high P_{Cd}, n reaches values of 10^{16} cm^{-3}, since the relation $[Cl_{Te}^{+}] > [V_{Cd}^{-2}]$ is valid under these conditions. The Cl_{Te}^{+} defect gives rise to a shallow donor level in the band gap $E_c = 0.01$ eV, so its excess leads to a fast rise in n in the crystal. The V_{Cd}^{-2} defect and its associations give rise to deep levels at $E_v + (0.5–0.9)$ eV; therefore, p also grows with decreasing P_{Cd}, but this process is much slower and p increases only to 10^9 cm^{-3}. The dependences of n and p on P_{Cd} for annealing at 900 and 1070°C are surprisingly alike in shape at practically the same free-carrier concentrations. The minima in the dependences of n and p on pressure P_{Cd} reliably characterize the maximum degree of self-compensation, $p(n)/[Cl_{Te}^{+}]$, when the donor and acceptor concentrations are equal, $[Cl_{Te}^{+}] = [V_{Cd}^{-2}]$. The defect concentrations $[Cl_{Te}^{+}]$, $[V_{Cd}^{-2}]$ are not the same at different annealing temperatures in the high-temperature stage and after the association of the majority of defects in the low-temperature stage. This must manifest itself in carrier scattering in drift-mobility measurements and in carrier recombination in the measurement of lifetime.

Therefore, we studied the crystal parameters μ_e, μ_h, τ_e, and τ_h, the most sensitive to the extent to which the annealing process is complete, in relation to the ingot annealing temperature and P_{Cd}. These dependences were obtained for crystals with hole concentrations $p = (10^8–10^9)$ cm^{-3} and with the largest $\mu\tau$ product for carriers, such crystals being characterized by a low content of unassociated V_{Cd}^{-2} vacancies giving rise to a deep level in the band gap [11].

Figure 4 shows the drift mobility of electrons and holes as a function of the ingot annealing temperature. It can be seen that electrons and holes attain high mobility at relatively low annealing temperatures $T_{ann} =$ 800–900°C; i.e., the mobility practically reaches its limiting value at the lower temperature in the interval corresponding to the high-temperature stage of ingot annealing. In semi-insulating CdTe:Cl, the carrier mobility is also determined by strains and inhomogeneities limiting the conducting part of the crystal or causing additional scattering [20]. At lower annealing temperatures, the solubility of charged atomic defects decreases. This diminishes the number of inhomogeneities and neutral associations of impurities and structural defects responsible for carrier scattering. The τ_e value also increases when the crystal annealing temperature is lowered (Fig. 5, curve *1*), similarly to $\mu_{e,h}$, and

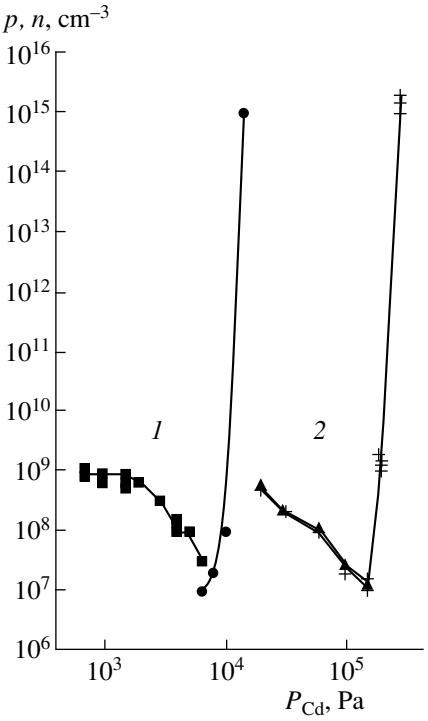

Fig. 3. Free carrier concentrations (n, p) vs. the cadmium vapor pressure (P_{Cd}) for two temperatures T_{ann} of CdTe:Cl ingot annealing: (*1*) 900 and (*2*) 1070°C.

presumably does so for the same reason. It can be seen from curve *2* in Fig. 5 that the hole lifetime grows with increasing crystal annealing temperature. Raising the temperature T_{ann} leads to an increase in V_{Cd}^{-2} solubility, both in absolute value and relative to that of the V_{Cd}^{-1} vacancies [6, 10]. The latter favors more complete association of these defects in the form of $(V_{Cd}^{-2}\,2Cl_{Te}^{+})^0$ [3]. Such a decrease in the content of V_{Cd}^{-2} defects in the crystal leads to a lower concentration of deep levels in the band gap and, correspondingly, to a longer hole lifetime. Presumably, the decrease in the $[V_{Cd}^{-2}]$ concentration exerts a stronger influence on the hole lifetime τ_h than the dependence of the distribution of the defects determining τ_e on strains and inhomogeneities does.

Thus, attainment of the necessary τ_e and τ_h values requires some tradeoffs in the choice of ingot annealing temperatures in the high-temperature annealing stage. This criticality (see Fig. 5) demands a very careful choice of the ingot annealing temperatures, depending on specific requirements to the τ_e and τ_h values in the crystal, not only in the high-temperature stage, but also in the low-temperature annealing stage, when the V_{Cd}^{-2} defects are eliminated via their association with donors. In connection with this, it is worth studying the τ_e, τ_h,

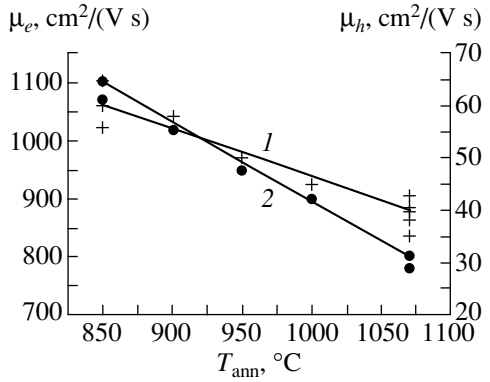

Fig. 4. Drift mobility of (*1*) electrons and (*2*) holes vs. the CdTe:Cl ingot annealing temperature T_{ann}.

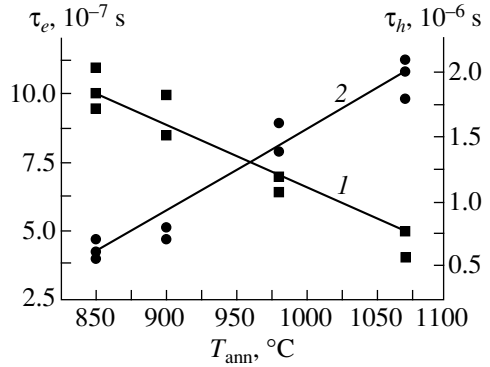

Fig. 5. Lifetimes of electrons (τ_e, *1*) and holes (τ_h, *2*) vs. the CdTe:Cl ingot annealing temperature T_{ann}.

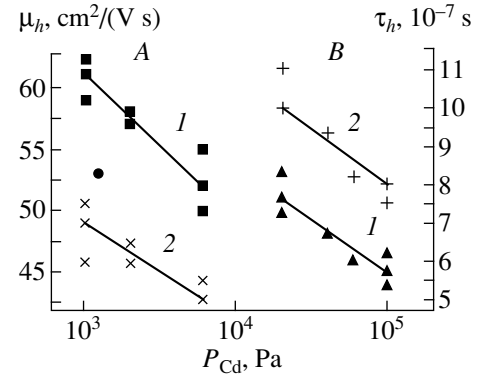

Fig. 6. (*1*) Drift mobility and (*2*) lifetime of holes vs. the cadmium vapor pressure P_{Cd} in annealing of CdTe:Cl ingot at annealing temperatures T_{ann} of (*A*) 900 and (*B*) 1070°C.

μ_e, and μ_h dependences on the vacancy concentration determined by the vapor pressure P_{Cd} in the ampule during ingot annealing. The maximum concentration of cadmium vacancies in the crystal is specified by the pressure $P_{Cd} \longrightarrow P_{Cd}^{min}$. With increasing P_{Cd}, this concentration decreases to values corresponding to *p*-type conduction (see Fig. 3, left-hand portions of curves *1* and *2*, for ingot annealing temperatures T_{ann} = 900 and 1070°C, respectively). Figure 6 shows the dependences of τ_h and μ_h on P_{Cd} at the same annealing temperatures. The tendency for these charge transport parameters of the crystal to decrease with increasing P_{Cd} during annealing is also seen. This dependence of τ_h and μ_h on P_{Cd} is explained as follows. The decrease in the V_{Cd}^{-2} concentration in the ingot (with increasing P_{Cd}) in the high-temperature stage of annealing leads to a lower extent of V_{Cd}^{-2} and Cl_{Te}^{+} association in the low temperature stage. As a result, the V_{Cd}^{-2} and Cl_{Te}^{+} defects remaining unassociated after annealing contribute to a decrease in hole lifetime and mobility.

The influence of the ingot annealing temperature on the hole lifetime and mobility, illustrated in Figs. 4 and 5, can be also inferred from Fig. 6. For crystals annealed at T_{ann} = 1070°C (interval *B* of P_{Cd} variation in Fig. 6) the lifetime is about 1.5 times longer than that for crystals annealed at T_{ann} = 900°C (interval *A* in Fig. 6). For crystals annealed at T_{ann} = 900°C, the hole mobility is about 1.2 times higher.

Thus, the annealing temperature is a key factor. Indeed, high τ_h values are attained only at high temperatures owing to the high solubility of V_{Cd}^{-2}. Raising the $[V_{Cd}^{-2}]$ concentration by decreasing the pressure P_{Cd} affects τ_h, but to a smaller extent, precluding achievement of such high τ_h values. At low temperatures, high τ_h, μ_e, and μ_h are obtained owing to a decrease in the concentration of charged and neutral defects and the lower nonuniformity of their distribution.

No influence of P_{Cd} on τ_e and μ_e was observed. This is explained by the fact that the changes in the V_{Cd}^{-2} concentration, to which the quantities τ_h and μ_h for holes are sensitive, are insufficient for exerting a noticeable influence on τ_e and μ_e.

Thus, we described here a procedure for two-stage postgrowth annealing of a CdTe:Cl ingot with programmed cooling to a low temperature (400°C). In the high-temperature stage of annealing, we studied the factors governing the relation between atomic defect concentrations $[Cl_{Te}^{+}] \approx [V_{Cd}^{-2}]$. This relation is the condition for sufficient self-compensation of charged defects in CdTe:Cl in the low-temperature annealing stage by way of defect association into neutral complexes. The rates of ingot cooling corresponding to different levels of chlorine doping were established, ensuring self-compensation. We determined the manner in which the chlorine solubility decreases as temperature becomes lower in the course of ingot cooling. In the process, exact self-compensation and, conse-

quently, large $\mu\tau$ products for carriers in the crystal are achieved by adjusting the concentration $[V_{Cd}^{-2}] \gtrsim 0.5[Cl_{Te}^{+}]$. A tendency was observed for μ_e, μ_h and τ_e to increase as the ingot annealing temperature is lowered, which is explained by a decrease in the content of charged defects in the crystal at low temperature. An opposite tendency was observed for the hole lifetime, τ_h, which becomes longer with increasing annealing temperature. This may be due to a decrease in the vacancy concentration $[V_{Cd}^{-2}]$ in the process of their association into neutral complexes $(V_{Cd}^{-2}\,2Cl_{Te}^{+})^0$, occurring to a greater extent during high-temperature annealing.

To conclude, the proposed two-stage postgrowth annealing of the ingot allows extremely precise control over the self-compensation and "self-purification" processes and enables growth of CdTe:Cl semi-insulating crystals with good transport properties. We believe that an analogous two-stage annealing will make it possible to produce other II–VI compounds and their solid solutions with desirable characteristics by horizontal planar crystallization, since in these materials the self-compensation mechanism is known to be clearly pronounced, similarly to CdTe crystals.

ACKNOWLEDGMENTS

This study was supported by INTAS, grant no. 99-01456.

REFERENCES

1. L. V. Maslova, O. A. Matveev, S. M. Ryvkin, *et al.*, Rev. Phys. Appl. **12**, 291 (1977).
2. E. N. Arkad'eva, L. V. Maslova, O. A. Matveev, *et al.*, Dokl. Akad. Nauk SSSR **225**, 77 (1975) [Sov. Phys. Dokl. **20**, 211 (1975)]; O. A. Matveev and A. I. Terent'ev, in *Proceedings of the 11th Workshop on Room Temperature Semiconductor X- and Gamma-ray Detectors and Associated Electronics, Vienna, 1999*, p. 56.
3. R. O. Bell, F. V. Wald, C. Canaly, *et al.*, IEEE Trans. Nucl. Sci. **NS-21**, 331 (1974).
4. R. Triboulet, Iv. Marfaing, A. Cornet, and P. Siffert, J. Appl. Phys. **45**, 2759 (1974).
5. O. A. Matveev, E. N. Arkad'eva, and L. A. Goncharov, Dokl. Akad. Nauk SSSR **221**, 325 (1975) [Sov. Phys. Dokl. **20**, 220 (1975)].
6. K. Zanio, in *Semiconductors and Semimetals* (Academic, New York, 1978), Vol. 13, p. 230.
7. O. A. Matveev and A. I. Terent'ev, Fiz. Tekh. Poluprovodn. (St. Petersburg) **27**, 1894 (1993) [Semiconductors **27**, 1043 (1993)].
8. O. A. Matveev and A. I. Terent'ev, Fiz. Tekh. Poluprovodn. (St. Petersburg) **32**, 159 (1998) [Semiconductors **32**, 144 (1998)].
9. O. A. Matveev and A. I. Terent'ev, Fiz. Tekh. Poluprovodn. (St. Petersburg) **29**, 378 (1995) [Semiconductors **29**, 191 (1995)].
10. F. Kröger, *The Chemistry of Imperfect Crystals* (North-Holland, Amsterdam, 1964; Mir, Moscow, 1969).
11. E. N. Arkadyeva and O. A. Matveev, Rev. Phys. Appl. **12**, 239 (1977).
12. H. H. Woodbury and R. B. Hall, Phys. Rev. **157**, 641 (1967).
13. *Physics and Chemistry of II–VI Compounds*, Ed. by M. Aven and J. S. Prener (North-Holland, Amsterdam, 1967; Mir, Moscow, 1970).
14. E. N. Arkad'eva, O. A. Matveev, E. N. Mel'nikova, and A. I. Terent'ev, Fiz. Tekh. Poluprovodn. (Leningrad) **14**, 1415 (1980) [Sov. Phys. Semicond. **14**, 839 (1980)].
15. T. J. Magee, J. Peng, and J. Bean, Phys. Status Solidi A **27**, 557 (1975).
16. H. H. Woodbury, in *Proceedings of the International Conference on Defect Characterization: Diffusivity and Electrical Measurement in II–VI Semiconducting Compounds* (W. A. Benjamin, New York, 1967), p. 244.
17. H. R. Vydyanath, J. Ellsworth, J. J. Kennedy, *et al.*, J. Vac. Sci. Technol. B **10**, 1476 (1992).
18. J. H. Greenberg, V. N. Guskov, V. B. Lazarev, and O. V. Shekershneva, J. Solid State Chem. **102**, 382 (1993).
19. A. C. Damask and G. J. Dienes, *Point Defects in Metals* (Gordon and Breach, New York, 1963; Mir, Moscow, 1966).
20. M. V. Alekseenko, E. N. Arkad'eva, and O. A. Matveev, Fiz. Tekh. Poluprovodn. (Leningrad) **4**, 414 (1970) [Sov. Phys. Semicond. **4**, 349 (1970)].

Translated by D. Mashovets

Semiconductors, Vol. 34, No. 11, 2000, pp. 1270–1274. Translated from Fizika i Tekhnika Poluprovodnikov, Vol. 34, No. 11, 2000, pp. 1322–1326.

ELECTRONIC AND OPTICAL PROPERTIES OF SEMICONDUCTORS

A Quasi-Linear Photorefractive Effect in Silicon

A. L. Filatov

Institute of Radio Engineering and Electronics, Russian Academy of Sciences (Fryazino Branch), pl. Vvedenskogo 1, Fryazino, Moscow oblast, 141120 Russia

e-mail: fil288@ire.216.msk.ru

e-mail: a.filatov@ms.ire.rssi.ru

Submitted May 11, 2000; accepted for publication May 11, 2000

Abstract—Nonlinearities of the photorefractive effect that arise if the intensity of the pump radiation is increased are studied. Phenomena related to the Auger recombination and variations in the contribution of ambipolar diffusion were analyzed. The possibilities of using the results of studying the quasi-linear photorefractive effect to determine the transport parameters of semiconductors are considered. © *2000 MAIK "Nauka/Interperiodica".*

INTRODUCTION

Noncontact methods for measuring the electronic [2] and thermal [3] parameters of silicon with high spatial resolution have been developed recently. These methods were based on the photorefractive effect in semiconductors [1] and were used with good results. The essence of this effect consists in the fact that the gradients of the photogenerated-carrier concentration and temperature arise periodically in the case of absorption of intensity-modulated pump radiation in the bulk of the sample (in the vicinity of the site of absorption). In turn, these gradients give rise to periodic emergence of photoinduced optical inhomogeneity. The amplitude and phase dependences of the angle of deflection of the probe beam due to this inhomogeneity on the modulation frequency of the pump radiation and on the distance between the beams carry the information about the parameters of the medium.

Schematic representation of the passage of beams in photorefractive experiments is shown in Fig. 1. The intensity-modulated pump beam passes at a distance z from the sample surface and is absorbed weakly in the medium. The probe beam passes perpendicularly to the pump beam at a distance x from the latter and is periodically deflected by optical inhomogeneity by an angle Θ that has two components; one of these (Θ_x) is perpendicular to the pump beam and the other (Θ_z) is parallel to this beam. The amplitude of Θ_x is mainly controlled by the gradients of the free-carrier concentration and temperature. The amplitude of Θ_z is mainly governed by attenuation of the pump beam when it propagates deep into the sample. An analysis [1] showed that Θ_x is severalfold larger than Θ_z in the case of silicon. Both angle components carry almost the same amount of information. Therefore, it is typical that the dependences of amplitude and phase of only the angle component Θ_x on the distance between the beams and the modulation frequency of the pump beam are studied.

The main distinction of photorefractive effect from the related effects consists in the fact that the former is three-dimensional. In the interference, photodeformation, and mirage effects, one-dimensional [4, 5] or two-dimensional [6, 7] models are used. A lowered dimensionality yields a higher signal-to-noise ratio because a larger length of interaction between the probe beam and optical inhomogeneity is ensured.

Small deflection angles related to small size of the interaction region in the photorefractive method result almost inevitably in a poor signal-to-noise ratio. Attempts to solve this problem by increasing the pump-radiation intensity give rise to nonlinear effects. It was reported [2, 3] that the photorefractive signal deviated from the calculated values with increasing pump-radiation intensity in high-resistivity silicon samples. For such samples, it was recommended to choose the pump-radiation intensity in such a way that the concentration of photogenerated charge carriers would be much lower than the concentration of the equilibrium charge carriers. In this paper, we report the results of theoretical and experimental studies of the photorefractive effect in the situation when the pump-radiation intensities are such that the concentration of photogenerated charge carriers is comparable to or higher than the concentration of the equilibrium charge carriers.

THEORY

The theory of photorefractive effect in the situation when the transport parameters of semiconductor are independent of the pump-radiation intensity has been developed previously [1]. The derived formula for the dependence of the component Θ_x of the photorefractive deflection angle on the circular frequency ω of the pump-radiation modulation and on the distance x between the probe and heating (pump) beams generally was rather cumbersome. However, it was demonstrated

1063-7826/00/3411-1270$20.00

[1] that this formula can be simplified significantly, if several assumptions were made. If the radius of the pump beam is smaller than the characteristic diffusion lengths for charge carriers and heat, the region under consideration is away from the illuminated surface, the characteristic absorption length for the pump radiation exceeds all other characteristic lengths, and, in addition, the measurements are performed at high frequencies (in which case, the influence of electronic parameters of the sample on the index of refraction becomes predominant), then the formula is substantially simplified and takes the form

$$\Theta_x(\omega, x) = C\exp(-x/L_{\text{eff}} + ix/L_\varphi),$$

where

$$L_\varphi = \sqrt{2D\tau/(-1 + \sqrt{1+\Omega^2})},$$

$$L_{\text{eff}} = \sqrt{2D\tau/(1 + \sqrt{1+\Omega^2})}, \quad \Omega = \omega\tau,$$

C is a coefficient that depends on the sample parameters, depends linearly on the pump-radiation power, and is independent of the parameters ω and x; D is the coefficient of ambipolar diffusion; and τ is the lifetime of charge carriers.

In the context of the formulated problem [1], the pump-power dependence of photorefractive signal (which is proportional to the angle Θ_x) should be linear. In addition, at high frequencies, the amplitude and phase of the signal should almost exponentially decrease with increasing distance between the beams. Experimentally, such behavior is not necessarily observed [2, 3]. Nevertheless, for all samples, the power ranges can be chosen in such a way that the above dependences hold. Departures from the linear model can be most easily explained by the fact that the lifetime and diffusion coefficient of charge carriers generally depend on the concentration of photogenerated charge carriers and, consequently, on the pump-radiation power. In order to gain qualitative insight into the role of concentration, it is convenient to divide the range of variations in transport parameters into four zones.

The first zone corresponds to the photogenerated-carrier concentration higher than 10^{18} cm^{-3}. In this zone, the Auger recombination of charge carriers occurs. As is known, the rate of such recombination depends quadratically on concentration, and, consequently, in this zone, the lifetime of charge carriers varies significantly with increasing distance from the pump beam. In order to assess whether our concept of the existence of this zone is valid, we estimate the concentration of photogenerated charge carriers Δn as the number of carriers generated within the lifetime τ in a volume into which the carriers diffuse during this time; thus, we have

$$\Delta n = P\tau\beta/(h\nu\pi D\tau),$$

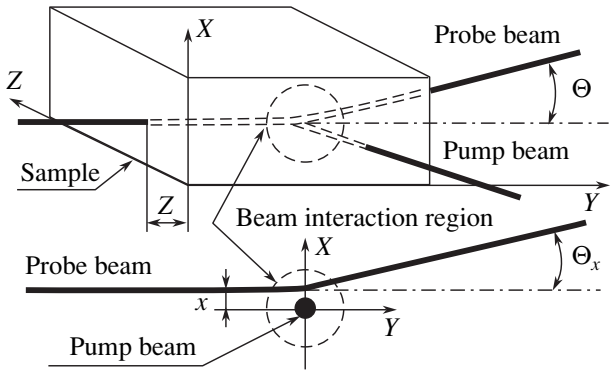

Fig. 1. Schematic illustration of passage of laser beams in experimental studies of photorefractive effect.

where P is the power of absorbed pump radiation, $h\nu$ is the energy of a photon, β is the absorption coefficient, and D is the diffusion coefficient for the charge carriers. In the experiments, we have $h\nu = 1.17$ eV, $\beta = 10$ cm^{-1}. $D = 18$ cm^2/s, and $P < 1$ W; as a result, the concentration of photogenerated carriers is lower than 10^{18} cm^{-3}. Thus, the Auger recombination should not affect the photorefractive signal. However, in other photoacoustic methods (e.g., those based on the laser-induced generation of the free-carrier and temperature gratings), such a type of recombination should be taken into account [8].

The second zone corresponds to the case when the concentration of photogenerated charge carriers far exceeds the equilibrium-carrier concentration but is lower than the level necessary for activation of the Auger recombination. In this case, the diffusion coefficient depends only slightly on the concentration of photogenerated carriers and corresponds to combined diffusion of electrons and holes. Generally, the lifetime in this region depends on the concentration of charge carriers. However, if this dependence is weak, we may use the linear model.

In the third zone, the concentration of photogenerated carriers becomes approximately equal to the equilibrium-carrier concentration. The behavior of the diffusion coefficient is described now in terms of conventional ambipolar model in which this coefficient is defined as

$$D = D_n D_p(n_e + n_p)/(D_n n_p + D_p n_e),$$

where D_n and D_p are the diffusion coefficients for electrons and holes, and n_e and n_p are the corresponding concentrations. Taking into account that the concentrations of photogenerated electrons and holes are equal to each other, we can rewrite the above expression (for example, for a p-type sample) as

$$D = \frac{2D_nD_p}{D_n + D_p}\left(1 + \frac{N_p(D_n - D_p)}{2\Delta n(D_n + D_p) + 2N_pD_p}\right),$$

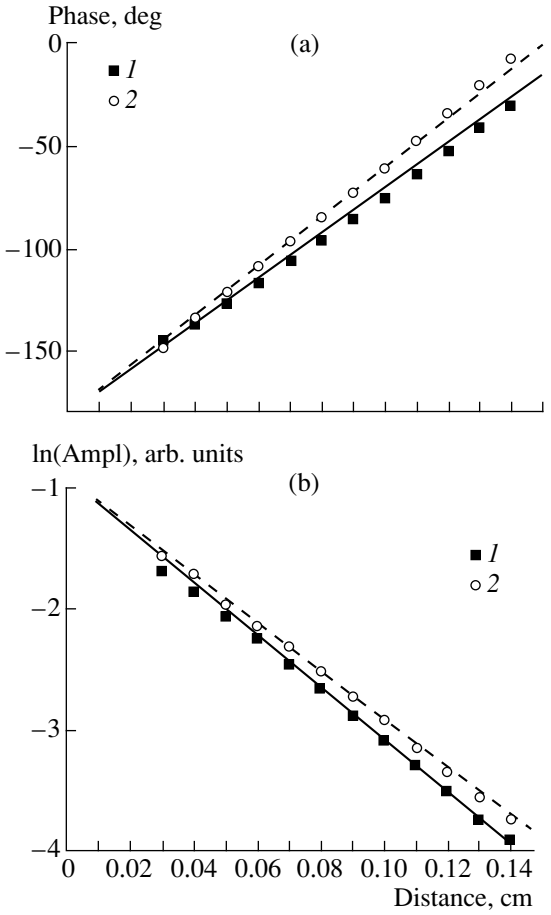

Fig. 2. Dependences of the photorefractive-signal parameters on the distance between the pump and probe beams for an *n*-Si sample with resistivity of 5 Ω cm: the dependences of (a) the phase and (b) the logarithm of amplitude are shown. Experimental dependences were obtained using the laser-radiation power of (*1*) 0.7 and (*2*) 0.08 W. Theoretical dependences were calculated for τ = 0.4 ms and D = 12 cm^2/s (the solid lines) and τ = 1.2 ms and D = 12 cm^2/s (the dashed lines).

where Δn is the concentration of photogenerated charge carriers and N_p is the concentration of equilibrium holes.

In the fourth zone, the equilibrium-carrier concentration far exceeds the concentration of photogenerated charge carriers. In this zone, the diffusion coefficient is controlled by the diffusion of the minority charge carriers. This coefficient, as well as the lifetime, is nearly independent of the concentration of photogenerated charge carriers.

Thus, it is only in the fourth zone that the angle of deflection of the probe beam can be calculated according to the linear model [1]. Nonlinear phenomena should be taken into account in the second and third zones. These phenomena are related to the variations in the lifetime and diffusion coefficient during an experiment. An introduction of additional parameters required for such calculations renders the model excessively complex and makes the fit of theoretical and experimental results ambiguous. However, as a rule, if the concentrations change only slightly, the lifetime and diffusion coefficient vary, insignificantly. Furthermore, the transport parameters are averaged over the diffusion length. Therefore, even in a nonlinear case, theoretical and experimental results for the dependences $\Theta_x(x)$ can be fitted to each other using the linear model for the distances (from the spot of the pump-radiation absorption) smaller than the diffusion length. We verified this assumption experimentally.

EXPERIMENT

In order to study in detail the nonlinear modes of photorefractive effect, we used the same setup as was employed previously [1–3]. As the pump-beam source, we used a YAG laser with the highest emission power of 1 W and a wavelength of 1.06 μm. The sample was probed with a beam of a He–Ne laser at a wavelength of 1.15 μm. The diameters of the probe and pump beams were about 50 μm in the region of their interaction. Mutual arrangement of the beams was varied by changing the position of a lens used to focus the pump beam. A mechanical chopper ensured the pump-beam modulation with frequencies from 1 Hz to 2 kHz. Deflection of the probe beam was sensed by a position-sensitive detector. The main factor restricting the sensitivity of the setup was related to fluctuations of the angle of the probe-beam deflection. These fluctuations amounted to about 10^{-8} rad/$\sqrt{\text{Hz}}$ on an average.

We performed experiments with a number of *p*- and *n*-Si samples with various resistivities using the intensities of the pump-laser radiation in the range from 1 mW to 1 W. We measured the dependences of the amplitude and phase of photorefractive signal on the distance between the probe and pump beams for a fixed laser power. The frequency of modulation of the pump radiation was 1600 Hz in all experiments, which ensured that the influence of electronic properties of the sample on photorefractive signal was predominant compared with the effect of thermal properties. All the measurements were performed away from the surface of the samples in order to eliminate the influence of surface recombination on the effect under consideration.

Almost in all experiments, variations in the phase and amplitude dependences were observed as the pump-radiation intensity was changed. For a fraction of dependences obtained in several experiments with the same sample using different pump-radiation intensities, we succeeded in performing a conventional procedure for fitting the experimental data to the linear theoretical model. The fitting was carried out by the method described elsewhere [1, 2]; i.e., by adjusting the values of two parameters: the lifetime τ and the coefficient of diffusion D of photogenerated charge carriers.

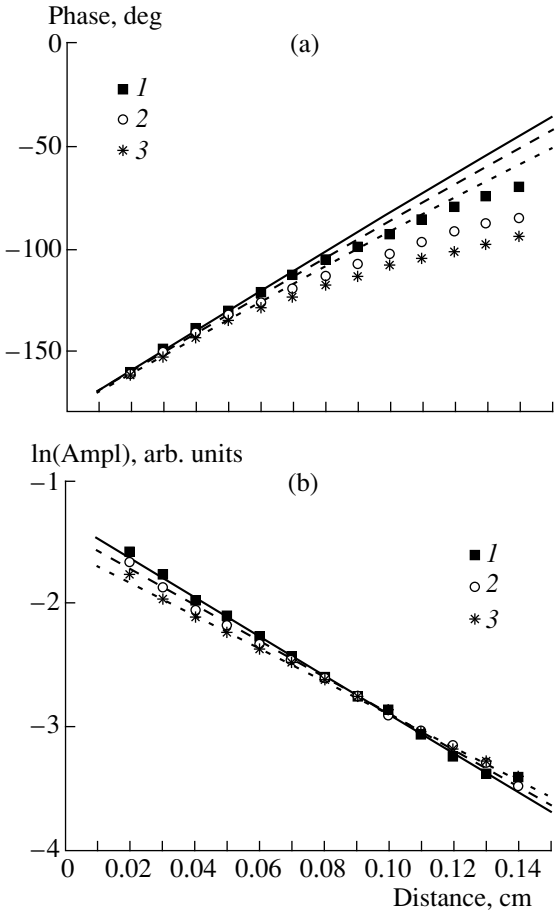

Fig. 3. Dependences of the photorefractive-signal parameters on the distance between the pump and probe beams for a *p*-Si sample with resistivity of 20 kΩ cm: the dependences of (a) the phase and (b) the logarithm of the amplitude are shown. Experimental dependences were obtained for the laser-radiation power of (*1*) 0.9, (*2*) 0.26, and (*3*) 0.06 W. Theoretical dependences were calculated for $\tau = 0.75$ ms and $D = 18$ cm^2/s (the solid lines), $\tau = 0.75$ ms and $D = 20$ cm^2/s (the dashed lines), and $\tau = 0.75$ ms and $D = 23$ cm^2/s (the dotted lines).

As an illustration, Fig. 2 shows the experimental and calculated dependences obtained for an *n*-Si sample with resistivity of 5 Ω cm. Experimental results obtained for the values of the YAG-laser radiation power of 0.7 and 0.08 W are shown by the symbols indicated by *1* and *2*, respectively. Calculated dependences are represented by the continuous line for the parameters $\tau = 400$ μs and $D = 12$ cm^2/s and by the dashed for $\tau = 1200$ μs and $D = 12$ cm^2/s, respectively. It can be seen that there is good quantitative agreement between experimental and calculated values of the phase and amplitude of photorefractive signal at distances that exceed the diffusion length of charge carriers, which is equal to about 0.1 cm in the case under consideration. The charge-carrier lifetime determined from the decay of photoconductivity (450 μs) coincides with the value of $\tau = 400$ μs derived by analyzing the data obtained by photorefractive method for high intensity of radiation. The value of the diffusion coefficient corresponds to that of the coefficient of diffusion of holes in silicon that are the minority charge carriers in the *n*-type sample. This corresponds to the case when the concentration of intrinsic carriers far exceeds the concentration of photogenerated charge carriers. Consistency of experimental data for these samples with the linear model of photorefractive effect indicates that the sample parameters vary insignificantly during each experiment.

For certain experimental dependences obtained with the same sample for various intensities of the pump radiation, it was found impossible to perform the fitting for all values of the distance between the pump and probe beams. In this case, the fitting was performed over the region closest to the radiation-absorption spot. It is these calculated dependences obtained for a *p*-Si sample with resistivity of 20 kΩ cm that are shown in Fig. 3. Experimental data obtained for the laser powers of 0.9, 0.26, and 0.06 W are shown by the symbols indicated by *1*, *2*, and *3*, respectively. The parameters of calculated dependences are given in the caption of Fig. 3. It can be seen from the plots that there is a good agreement between experimental and calculated values only to a distance of about 0.06 cm between the pump and probe beams. This distance corresponds to the diffusion length which is equal to about 0.1 cm in the cases under consideration. The obtained value of the lifetime ($\tau = 750$ μs) is in good agreement with $\tau = 800$ μs determined for the same sample from the photoconductivity decay. Variation in the value of the diffusion coefficient from 18 to 23 cm^2/s corresponds to a gradual transition from simultaneous diffusion of electrons and holes to the predominance of the diffusion of the minority charge carriers (electrons).

CONCLUSION

The linear theory of photorefractive effect [1] is based on the assumption that the transport parameters of semiconductors are constant. However, experiments have shown that, even when the equilibrium-carrier concentration far exceeds the concentration of photogenerated charge carriers, discrepancies can be observed between the calculated and experimental data if the latter are obtained for different pump-radiation powers. Furthermore, it has been found that, for high-resistivity silicon samples, attempts to increase the signal-to-noise ratio in photorefractive by increasing the pump-radiation power gives a rapid rise to a situation in which it is no more possible to fit the curves calculated on the basis of linear theory to experimental data.

The observed discrepancies can be consistently accounted for by the known facts that the lifetime and diffusion coefficient depend on the concentrations of both photogenerated and equilibrium charge carriers. We performed a theoretical analysis with subsequent experimental test and demonstrated that it is possible to

use the linear model of photorefractive effect (when this model is applied to distances smaller than the diffusion length of charge carriers) to determine the transport parameters of charge carriers even if the diffusion coefficient varies during the experiment.

The results make it possible to extend the range of applicability of photorefractive method to samples with higher resistivity. In addition, on the basis of analysis of the dependence of the diffusion coefficient on the radiation intensity, it is possible to develop a noncontact method for determining the electrical conductivity in the bulk of the samples with high spatial resolution.

REFERENCES

1. A. L. Filatov, V. I. Mirgorodsky, and V. A. Sablicov, Semicond. Sci. Technol. **8**, 694 (1993).
2. A. L. Filatov, V. I. Mirgorodsky, and V. A. Sablicov, Eng. Opt., 321 (1993).
3. A. L. Filatov, Zh. Tekh. Fiz. **68** (9), 115 (1998) [Tech. Phys. **43**, 1111 (1998)].
4. A. Skumanich, D. Fournier, A. C. Boccara, and N. M. Amer, Appl. Phys. Lett. **47**, 402 (1985).
5. D. Fournier, A. C. Boccara, A. Skumanich, and N. M. Amer, J. Appl. Phys. **59**, 787 (1986).
6. H. Dersch and N. Amer, Appl. Phys. Lett. **47** (3), 292 (1985).
7. N. M. Amer, J. Phys. (Paris) **44**, C6-185 (1983).
8. H. J. Eichler, F. Massmann, E. Biselli, *et al.*, Phys. Rev. B **36** (6), 3247 (1987).

Translated by A. Spitsyn

Semiconductors, Vol. 34, No. 11, 2000, pp. 1275–1280. Translated from Fizika i Tekhnika Poluprovodnikov, Vol. 34, No. 11, 2000, pp. 1327–1332.

ELECTRONIC AND OPTICAL PROPERTIES OF SEMICONDUCTORS

Fabrication and Photoelectronic Properties of ZnTe Single Crystals and Schottky Diodes

G. A. Il'chuk*, V. I. Ivanov-Omskiĭ, V. Yu. Rud'***, Yu. V. Rud'**, R. N. Bekimbetov**, and N. A. Ukrainets***

** Lviv Polytechnical State University, Lviv, 79013 Ukraine*

*** Ioffe Physicotechnical Institute, Russian Academy of Sciences, Politekhnicheskaya ul. 26, St. Petersburg, 194021 Russia*

**** St. Petersburg State Technical University, Politekhnicheskaya ul. 29, St. Petersburg, 195021 Russia*

Submitted April 28, 2000; accepted for publication May 11, 2000

Abstract—*n*- and *p*-ZnTe single crystals were grown by the method of the gaseous-phase reactions using various halogen-containing agents (NH_4Cl, NH_4Br, and NH_4I) as the carrier gases. Luminescent properties of the crystals were studied in relation to the type of the carrier gas. In/ZnTe Schottky barriers were formed. The photovoltaic effect was studied in the obtained structures for cases of natural and linearly polarized radiation. It was ascertained that the induced photopleochroism of the Schottky barriers is controlled by the angle of incidence of radiation and remains unchanged in the region of high photosensitivity. It is concluded that the obtained barriers may be used as broadband photosensors of linearly polarized radiation. © *2000 MAIK "Nauka/Interperiodica".*

INTRODUCTION

Interest in II–VI compounds and the corresponding solid solutions has been growing recently. This is due to the fact that these materials are being used in the fabrication of quantum-well structures and semiconductor lasers [1]. Zinc telluride (ZnTe) is among the relatively poorly studied direct-gap II–VI semiconductor compounds and attracts an interest from the standpoint of expanding the component base of modern photoelectronics and luminescent electronics [2, 3]. In the vast majority of studies of this promising material, the crystals grown from ZnTe melts whose composition was almost stoichiometric were used [2]. In this study, ZnTe single crystals were grown for the first time by the gaseous-phase process in which case the material is transported by compounds containing a halogen and having the common formula NH_4X, where X = Cl, Br, or I. This basically opens new possibilities of uniform doping of ZnTe with halogens [4]. In this paper, we consider the results of the first studies of the physical properties of homogeneous ZnTe single crystals and ZnTe-based surface-barrier structures.

EXPERIMENTAL

ZnTe single crystals were grown by the method of chemical transport reactions using NH_4Cl, NH_4Br, or NH_4I as the carrier gases. Preliminarily, we theoretically analyzed the equilibrium composition of the gaseous phase in a ZnTe–NH_4X system (X = Cl, Br, or I) [5] in the ranges of temperatures of 1000–1400 K and total pressures of 1.01×10^3–1.01×10^5 Pa, which made it possible to calculate the temperature dependences of the partial pressures of the main components in the gaseous medium and choose a temperature–concentration range that ensured the crystal growth. Theoretical simulation of the mass transport and comparison of the obtained results with measurements of the amount of transported material made it possible to infer that this transport has a diffusion-related origin [6]. The amount of ZnTe charged into the growth ampule was equivalent to 60 kg/m^3. As a result, under the conditions of free growth, we obtained ZnTe single crystals that have a natural specular faceting and sphalerite structure, as in the case of crystallization of ZnTe from the melt [2]. The crystal-lattice parameter coincided with that known for ZnTe from the available publications [3, 7]. For the process duration equal to 100 h, the maximal dimensions of single crystals were as large as ~2 mm × 4 mm × 4 mm. As the measurements of the thermoelectric-power sign showed, all the obtained ZnTe samples had electron type of conduction if NH_4I and NH_4Br carrier gases were used, whereas the crystals of both *n*- and *p*-type conductivity occurred in the case of using NH_4Cl (Table 1). Consequently, we may assume that, if NH_4I and NH_4Br are used, the chosen conditions of crystallization ensure the predominant formation of donor defects, whereas, in the case of NH_4Cl, the ratio between the donor and acceptor concentrations may vary over a wide range which is determined by specific conditions of the process.

Spectral dependences of the intensity of steady-state photoluminescence (PL) I_{PL} were studied at $T \approx 77$ K for the obtained ZnTe single crystals. The PL was excited by the focused radiation of a helium–cadmium laser (with a wavelength of $\lambda_{exc} \approx 0.44$ μm and a power

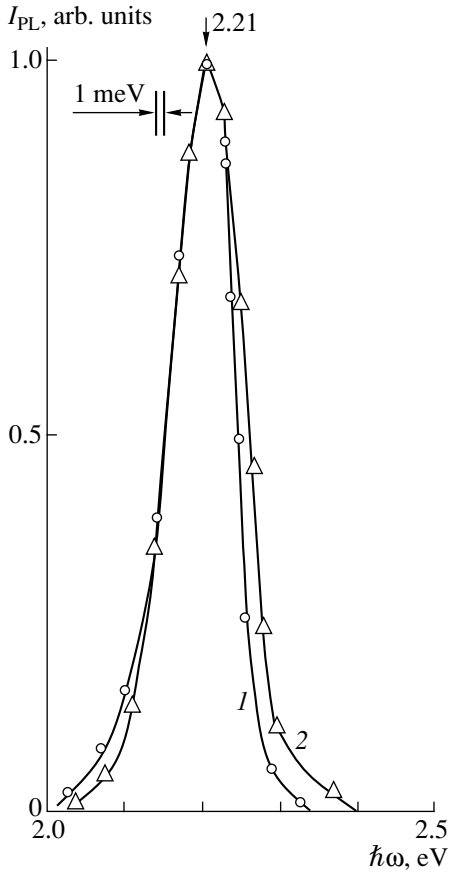

Fig. 1. Spectral dependences of intensity of the steady-state photoluminescence (at T = 77 K) of ZnTe single crystals grown by the method of chemical transport reactions. The carrier gas was (*1*) NH_4I and (*2*) NH_4Br.

of $P \approx 10$ mW) and was observed from the same side onto which the excitation radiation was incident.

The Schottky barriers (SBs) were formed on the grown ZnTe single crystals by depositing thin (~1 μm) In layers onto the natural specular surface. There was no need of any thermal treatment of the samples. The latter is very important in studying the variable-composition compounds, because, in forming the In/ZnTe SBs, there are no actual reasons for changes in the composition of ZnTe crystals after their growth. Thin In layers were deposited by thermal sputtering in vacuum.

EXPERIMENTAL RESULTS AND DISCUSSION

In the case of ZnTe single crystals grown using NH_4I and NH_4Br, the zone of PL emission was homogeneous and had a bright-orange coloring. If the ZnTe crystals were grown using NH_4Cl, the PL intensity decreased by several orders of magnitude. In Table 1, the PL intensities I_{PL} of typical ZnTe single crystals under identical conditions of excitation are compared. It can be seen that the most intense PL is characteristic of the crystals grown using NH_4I. If NH_4Br or NH_4Cl are used, this intensity is reduced by a factor of 4–5 or by 2–3 orders of magnitude, respectively, compared to the case of ZnTe samples grown in the presence of NH_4I.

Typical spectral dependences of PL of ZnTe crystals are shown in Fig. 1. It can be seen that the PL spectra of the crystals fabricated using different carrier gases are almost the same. These spectra involve a single, rather broad band peaked at the photon energy of $\hbar\omega_{PL}^{m} = 2.21$ eV at $T = 77$ K.

In view of the fact that the value of $\hbar\omega_{PL}^{m}$ was found to be smaller than that of the ZnTe band gap ($E_g \approx 2.36$ eV at $T \approx 77$ K [2]), there are grounds to relate the observed PL to radiative transitions to the levels of the predominant lattice defects. These levels are separated by ~0.15 eV from one of the free bands. This inference is also supported by fairly large values of the full-widths of the observed PL bands at the half-height $\hbar\omega_{1/2}$ = 100–110 meV. As a whole, the fact that the determined values of $\hbar\omega_{PL}^{m}$ and $\hbar\omega_{1/2}$ are almost the same for the crystals grown using different carrier gases (NH_4I and NH_4Br) may indicate that the energy spectrum of dominant lattice defects in ZnTe crystals

Table 1. Luminescent characteristics of ZnTe single crystals at T = 77 K

The carrier gas	Sample no.	The conduction type	$\hbar\omega_{PL}^{m}$, eV	$\hbar\omega_{1/2}$, meV	I_{PL}, arb. units
NH_4Cl	A62	*n*			~10^{-2}
	A27	*p*			~10^{-3}
	A30	*n*			~10^{-2}
NH_4Br	A53-1	*n*	2.21	110	0.20
	A53-2	*n*	2.21	105	0.25
NH_4I	A14-1	*n*	2.21	100	1.0
	A14-2	*n*	2.21	97	0.95
	A67	*n*	2.21	98	0.98

under consideration is nearly insensitive to a change of the carrier gas. At the same time, the observed dependence of the PL intensity on the type of the carrier gas may be related to variations in the concentration of the formed lattice defects that control the nonradiative recombination channel in the obtained ZnTe crystals.

Typical steady-state current–voltage characteristics $I(U)$ for such structures are shown in Fig. 2, and certain parameters of these structures are listed in Table 2. It can be seen that the rectification effect is clearly pronounced in all structures formed on the crystals grown using different carrier gases. The forward direction corresponds to negative polarity of external bias voltage applied to the *n*-ZnTe substrate. The forward portion of the SB current–voltage characteristics obeys the relation

$$U = U_{c0} + R_{\text{res}} I, \tag{1}$$

where the residual resistance $R_{\text{res}} \approx 10^4$–$10^6$ Ω and the cutoff voltage $U_{c0} \approx 0.2$–0.8 V in different structures (Table 2). It is worth noting that a reproducible decrease in R_{res} and U_{c0} occurs when the ZnTe substrates grown in the presence of NH_4Cl (instead of other carrier gases) are used in the SBs. As the reverse bias voltage increases, current through the formed barriers increases according to the power law $I \propto U^{\alpha}$, where $\alpha \approx 0.8$–1.0 for different structures, which may be indicative of imperfections at the periphery of these structures. The lowest reverse currents ($\sim 2 \times 10^{-8}$ A for $U \approx 2$ V) were observed in the SBs formed on the crystal grown using NH_4Br. On the whole, the observed correlation of electrical characteristics of the In/ZnTe SBs with the nature of carrier gas demonstrates the possibility of controlling the ensemble of electrically active lattice defects in ZnTe crystals in the course of their growth from a gaseous phase.

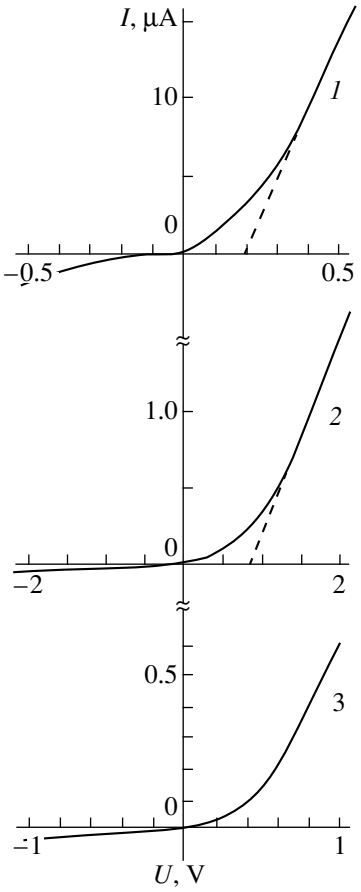

Fig. 2. Steady-state current–voltage characteristics $I(U)$ of the In/*n*-ZnTe surface-barrier structures. The carrier gases were (*1*) NH_4Cl (sample A62), (*2*) NH_4Br (sample A53-1); and (*3*) NH_4I (sample A14-2). The forward direction corresponds to negative polarirty of external bias applied to the *n*-ZnTe substrate.

Under irradiation with unpolarized light, the formed In/ZnTe SBs exhibit a pronounced photovoltaic effect that typically has larger magnitude if the active region is illuminated from the barrier-contact side. The sign of the photovoltaic effect was found to be independent of both the energy of incident photons and the position of the optical-beam spot (with diameter of ~0.2 mm) at the surface of the In/ZnTe SBs and corresponded to the rectification direction in such structures. Under the conditions of irradiation with unfocused light of an incandescent lamp (~80 W), the open-circuit photovoltage was as high as 30–40 mV and the short-circuit photocurrent was 0.2–0.5 μA in the best SBs at $T = 300$ K. The highest voltage photosensitivity was $S_U^m \approx 10$ V/W (Table 2).

Typical spectral dependences of the voltage photosensitivity S_U for SBs formed on ZnTe crystals that are grown using different carrier gases are shown in Fig. 3 for the case of illumination of the structures from the barrier-contact side. In such barriers, the spectral profile of S_U did not exhibit any pronounced dependence on the type of the carrier gas. As can be seen from Fig. 3, the S_U spectra are broadband and cover the range

Table 2. Photoelectric properties of the In/ZnTe surface-barrier structures at $T = 300$ K

The carrier gas	Sample no.	U_{c0}, V	R_{res}, Ω	$\hbar\omega_{\text{ph}}^m$, eV	$\delta_{1/2}$, meV	S, eV^{-1}	S_U^m, V	P_I, % ($\theta \approx 80°$)
NH_4Cl	A62	0.2	4.2×10^4	2.34	0.40	23	0.2	66
NH_4Br	A53-1	0.8	1.5×10^6	2.34	0.58	46	1	66
NH_4I	A14-2	0.4	1.7×10^6	2.27	0.66	38	10	68

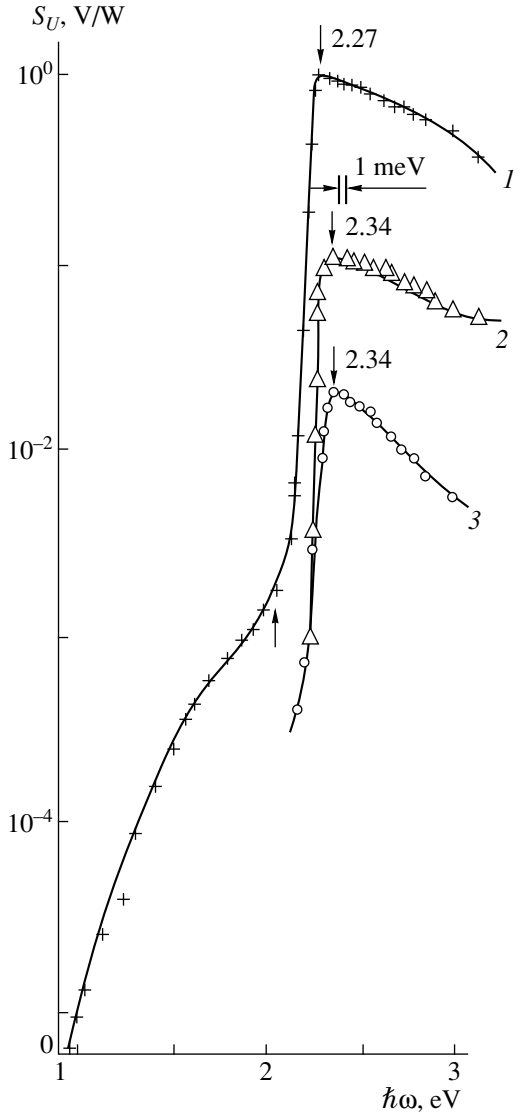

Fig. 3. Spectral dependences of the voltage photosensitivity of the In/ZnTe structures at T = 300 K. The carrier gas was (*1*) NH_4I (sample A14-1), (*2*) NH_4Br (sample A53-1), and (*3*) NH_4Cl (sample A62). The samples were illuminated from the In-contact side.

of 1–3 eV, if the structures are illuminated from the barrier-contact side. The long-wavelength exponential edge of photosensitivity is observed in a narrow spectral range of 2.10–2.25 eV and exhibits a large slope $S = \delta(\ln S_U)/\delta(\hbar\omega) \approx 23$–$46$ eV^{-1}, which corresponds to direct band-to-band transitions in the ZnTe electron spectrum [2]. The energy position of the peak of photosensitivity $\hbar\omega_{\mathrm{ph}}^m$ is nearly equal to the ZnTe band gap [2, 7] only for the barriers based on the crystals grown using NH_4I (Fig, 3, curve *1*), whereas, in the case of NH_4Br and NH_4Cl carrier gases, the peak $\hbar\omega_{\mathrm{ph}}^m$ shifts slightly to shorter wavelengths, $\hbar\omega_{\mathrm{ph}}^m > E_g$ (Fig. 3, curves *2*, *3*). The observed short-wavelength falloff of S_U for $\hbar\omega > \hbar\omega_{\mathrm{ph}}^m$ may indicate that the obtained In/ZnTe barriers are not yet sufficiently perfect and the influence of the surface recombination is important. In the case when the same barriers are illuminated from the ZnTe-substrate side, the steep short-wavelength falloff of photosensitivity shifts to longer wavelengths and typically occurs for $\hbar\omega_{\mathrm{ph}}^m > 2.1$ eV for wafers 0.1–0.2-mm thick. This falloff reflects the effect of the radiation absorption in the ZnTe bulk and, thus, occurs for $\hbar\omega_{\mathrm{ph}}^m < E_g$ in all the barriers.

It can also be seen from Table 2 that, in the case of illuminating the In/ZnTe barriers from the indium-contact side, the full width of the photosensitivity spectra at their half-width $\delta_{1/2}$ is found to be rather large and exhibits a tendency to decrease from 0.66 to 0.40 eV as the carrier gas is changed in the sequence $NH_4I \longrightarrow NH_4Br \longrightarrow NH_4Cl$. Therefore, there are no good reasons to attribute completely the short-wavelength falloff of S_U in SBs for $\hbar\omega_{\mathrm{ph}}^m > E_g$ and illumination from the indium-contact side to the effect of surface recombination because all the barriers were formed by the same method and the properties of the crystals are controlled only by the type of the carrier gas used.

It also follows from Fig. 3 that, if the carrier gas is changed in a sequence $NH_4I \longrightarrow NH_4Br \longrightarrow NH_4Cl$, the spectral profile of S_U remains unchanged but the voltage photosensitivity decreases (Table 2). As a result, the $S_U(\hbar\omega)$ spectra shift to lower values along the vertical axis. The observed variations in the value of the slope S (Table 2) in this case is may be due to a fluctuation in the charged lattice-defect potential.

In the range of 1–2 eV, spectral dependences of photosensitivity of the SBs formed on ZnTe crystals grown using NH_4I carrier gas obey the Fowler law (Fig. 4). The height of the surface potential barrier estimated from these dependences is φ_B = 1.24 eV at T = 300 K.

In the case of irradiating the SB with linearly polarized light, the polarization sensitivity arises in all structures only if the angle of incidence (θ) of radiation onto the surface is different from the zero angle. Under the condition that $\theta = 0°$, the spectral dependences $S_U(\hbar\omega)$ are insensitive to the direction of the vector **E** of the optical-wave electric field and coincide with those considered for unpolarized light (Fig. 3). For $\theta \neq 0°$, the short-circuit photocurrent (i_φ) of the SB begins to depend on the azimuthal angle φ between **E** and the plane of incidence (PI) of radiation. For θ = const, this dependence is given by

$$i_\varphi = i^p \cos^2\varphi + i^s \sin^2\varphi, \qquad (2)$$

where i^p corresponds to the polarization **E** || PI and i^s, to the polarization **E** $\perp$ PI. The inequality $i^p > i^s$ is characteristic of the entire photosensitivity range, which is consistent with the Fresnel formulas for amplitude

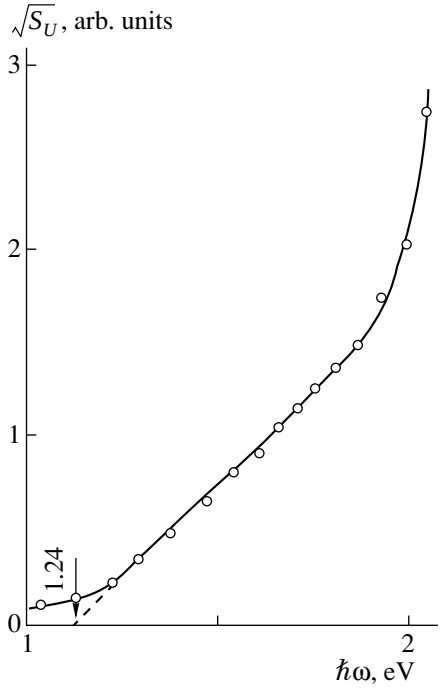

Fig. 4. Spectral dependence of $\sqrt{S_U}$ for an In/ZnTe structure in the long-wavelength region of the spectrum at T = 300 K. The carrier gas was NH_4I (sample A14-2). The sample was illuminated from the In side.

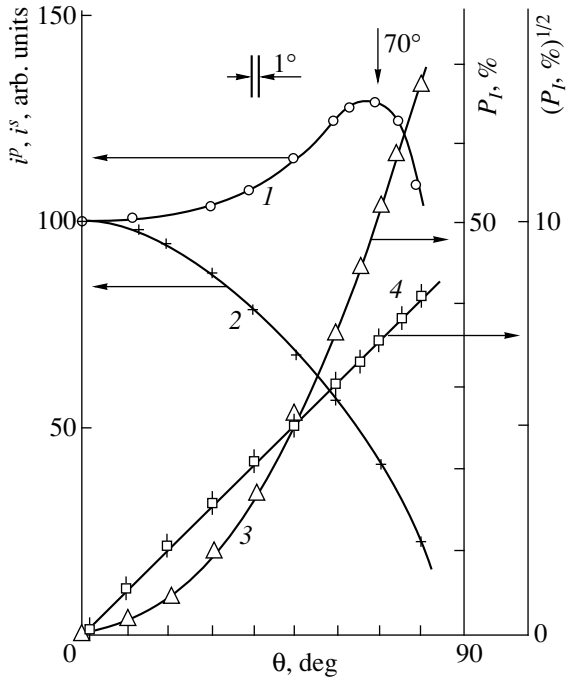

Fig. 5. Dependences of (*1*, *2*) the short-circuit photocurrent for radiation with polarizations (*1*) **E** ∥ PI and (*2*) **E** ⊥ PI and (*3*, *4*) the photopleochroism coefficient on the angle of incidence of radiation on the In/ZnTe-structure surface from the barrier-contact side at T = 300 K. Sample A12-2, $\hbar\omega$ = 2.3 eV.

coefficients of transmission of linearly polarized radiation through the air–semiconductor interface [8]. This behavior is also reproduced in the spectral dependences of S_U for the *s* and *p* polarizations (S_U^s and S_U^p, respectively). As a result, the spectral profiles of photosensitivity for different polarizations coincide with each other and are similar to the spectral dependence $S_U(\hbar\omega)$ for unpolarized radiation. For this reason, the transition from the **E** ∥ PI polarization to **E** ⊥ PI is accompanied with a shift of the spectral curve S_U^s to lower values compared to S_U^p, with the polarization-induced difference in photosensitivity increasing with θ.

Figure 5 shows typical dependences of the short-circuit photocurrents and the induced-photopleochroism coefficient P_I on θ for an SB irradiated with linearly polarized light from the barrier-contact side. In the case where the radiation-polarization plane coincides with the plane of incidence of radiation, the photocurrent i^p first increases with increasing angle of incidence, attains a maximum, and then starts to decrease for θ > 70°. An increase in i^p may be as high as ~30%, which may be a result of maximal reduction of losses by reflection in the vicinity of the pseudo-Brewster angle θ ≈ 70° (Fig. 5 curve *1*). In contrast with i^p, the photocurrent i^s exhibits a steady decrease with increasing θ (Fig. 5, curve *2*). The similar form of angular dependences of i^p and i^s is retained in the entire range of photosensitivity of BSs based on ZnTe crystals obtained using the above carrier gases. This is consistent with an analysis of the process of transmission of linearly polarized radiation through the air/ZnTe interface on the basis of the Fresnel formulas [8] and makes it possible [9, 10] to infer that there is a high structural perfection of the planes of natural faceting in the obtained ZnTe crystals. For all SBs, angular dependences of induced-photopleochroism coefficient (Fig. 5, curves *3*, *4*) follow the quadratic law $P_I \sim \theta^2$, which is consistent with the theory in the absence of the interference phenomena [10, 11]. For all obtained SBs and the angles of incidence of θ ≈ 80°, the coefficient of induced photopleochroism was almost the same and was as high as 66–68%. Estimation of the refractive index on the basis of the measurements of P_I yields $n \approx 3.5$, which is consistent with the known value for ZnTe [7].

A typical spectral dependence P_I of $n \approx 3.5$ for one of the formed SBs for θ ≈ 80° is shown in Fig. 6. It can be seen that, within the entire range of high photosensitivity, the induced-photopleochroism coefficient of the In/ZnTe structures remains virtually constant, which is consistent with the statements of the theory in the absence of the interference phenomena for a linearly polarized radiation [10].

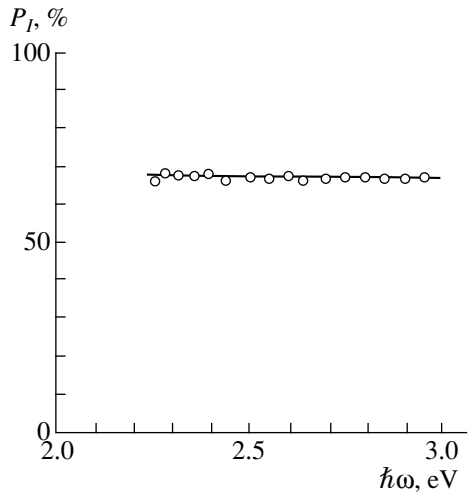

Fig. 6. Spectral dependence of the photopleochroism coefficient for an In/ZnTe structure at $T = 300$ K. The ZnTe crystal was grown using the NH_4I carrier gas, sample A14-2, $\theta \approx 80°$. The structure was illuminated from the side of the In barrier contact.

The highest azimuthal photosensitivity (~15 V/(W K) for $T = 300$ K) was observed for the best SBs in the case of using the NH_4I carrier gas to grow the ZnTe single crystals. Evidently, the proper choice of composition of the $Cd_xZn_{1-x}Te$ solid solution makes it possible to develop polarimetric photodetectors designed for the spectral range between the values of E_g of CdTe and ZnTe [7].

Thus, the method of gaseous-phase reactions makes it possible to grow the *n*- and *p*-ZnTe single crystals, whereas a change of the type of the carrier gas ensures a control over electrical and luminescent properties of these crystals, which may find application in developing the photodetectors of natural and linearly polarized radiation on the basis of these structures. We observed and studied the photovoltaic characteristics of the In/ZnTe Schottky barriers that can be used as broadband photodetectors of natural and polarized radiation.

REFERENCES

1. M. Strassburg, V. Kutzer, U. Pohl, *et al.*, Appl. Phys. Lett. **72**, 942 (1998).
2. *Physics and Chemistry of II–VI Compounds*, Ed. by M. Aven and J. S. Prener (North-Holland, Amsterdam, 1967; Mir, Moscow, 1970).
3. *Physics of II–VI Compounds*, Ed. by A. N. Georgobiani and M. K. Sheĭnkman (Nauka, Moscow, 1986).
4. G. A. Il'chuk, N. A. Ukrainets, V. I. Ivanov-Omskiĭ, *et al.*, Fiz. Tekh. Poluprovodn. (St. Petersburg) **33**, 553 (1999) [Semiconductors **33**, 518 (1999)].
5. G. A. Il'chuk, Neorg. Mater. **35** (7), 812 (1999).
6. G. A. Il'chuk, Neorg. Mater. **36** (7), 805 (2000).
7. *Physicochemical Properties of Semicoductors: A Reference Book* (Nauka, Moscow, 1978).
8. G. S. Landsberg, *Optics* (Nauka, Moscow, 1976).
9. V. Yu. Rud', Yu. V. Rud', and H. W. Schock, Solid State Phenom. **67/68**, 421 (1999).
10. F. P. Kesamanly, V. Yu. Rud', and Yu.V. Rud', Fiz. Tekh. Poluprovodn. (St. Petersburg) **33** (5), 513 (1999) [Semiconductors **33**, 483 (1999)].
11. G. A. Medvedkin and Yu. V. Rud', Phys. Status Solidi A **67**, 333 (1981).

Translated by A. Spitsyn

Semiconductors, Vol. 34, No. 11, 2000, pp. 1281–1286. Translated from Fizika i Tekhnika Poluprovodnikov, Vol. 34, No. 11, 2000, pp. 1333–1338.

ELECTRONIC AND OPTICAL PROPERTIES OF SEMICONDUCTORS

Quasi-localized States and Resonance Scattering of Particles by Defects in Semiconductor Crystals with Band Spectrum Structure

S. E. Savotchenko

Belgorod State University, Belgorod, 308007 Russia

e-mail: savotchenko@bsu.edu.ru

Submitted February 22, 2000; accepted for publication May 14, 2000

Abstract—The interaction of particles with planar defects in semiconductor crystal was studied on the basis of a model of the band energy-spectrum structure. Generalized localized states are shown to exist in the vicinity of defects. It is also shown that nonquadratic dispersion law gives rise to quasi-localized states. Particle scattering by the semiconductor boundary was analyzed. The condition for the total reflection from the interface is formulated as follows: the incident-particle energy should be equal to the energy of a quasi-localized state. It was found that a weak dissipation of particle energy in the crystal causes instability of the resonance condition for the total reflection. © *2000 MAIK "Nauka/Interperiodica".*

1. Recently, considerable attention has been focused on scattering of waves by planar and point defects in crystals. Elastic scattering of waves by a thin passive (devoid of internal degrees of freedom) layer in an isotropic medium was investigated elsewhere [1, 2]. It was demonstrated that, if the phase velocity of an incident wave falls within the range between longitudinal and transverse velocities of sound ($c_t < c < c_l$), the total transmission and the total reflection are both possible. A similar problem was studied previously [3] by the methods of the crystal-lattice dynamics on the basis of a simple model of planar defect in fcc crystal and in [4], where the effect of interaction between atoms (not necessary neighboring) in a linear chain was investigated. A theory providing explanation of the related resonance effects and, specifically, unexpected total reflection was proposed in [5].

The above-mentioned studies dealt with elastic-displacement vector fields containing two partial terms. If the phase velocity of a wave falls within the range $c_t < c < c_l$, one of the partial terms accounts for a longitudinal wave localized in the vicinity of a defect and the other, for a bulk transverse wave. This type of oscillations is referred to as quasi-localized [6, 7]. Resonance scattering is possible because of the interaction between transverse and longitudinal modes at a defect. These waves do not interact and propagate independently in the bulk of an ideal crystal. The resonance occurs provided the phase velocity (or frequency) of incident wave coincides with the phase velocity (or frequency) of quasi-localized oscillation.

Ambiguous frequency spectrum may arise for a field describing the electron and hole motion in special semiconductor crystals with band energy-spectrum structure. For example, the generalized model of energy spectrum was used [8] to explain a variety of CdSb and ZnSb properties. The key point of this model is the presence of two energy valleys near the Brillouin zone edge in the valence band and two valleys in the conduction band. Detailed study [9, 10] indicates that the dependence of energy ε on either electron or hole quasi-momentum $\mathbf{k}$ in nondegenerate bands of In_4Se_3 crystal can be described by the dispersion law

$$\varepsilon(\mathbf{k}) = E_0 - \alpha_x k_x^2 - \alpha_y k_y^2 - \alpha_z k_z^2 + \beta_x k_x^4 + \beta_y k_y^4 + \beta_z k_z^4 \quad (1)$$

in the vicinity of a band gap, which has multiple valleys and is non-parabolic with negative curvature at the minimal wave vectors; as $\mathbf{k}$ increases, the parabolicity is restored. Such an atypical dispersion law (1) obtained regardless of spin–orbit interaction is valid in the vicinity of the Brillouin zone center in In_4Se_3 and results from the interaction of close subbands in the valence and conduction bands.

In this paper, we analyze stationary eigenstates and scattering of quasiparticles by a planar defect; the particles are described by two-partial scalar field in semiconductor with the band spectrum structure. The assumptions that follow and concern the parameters of the dispersion law (1) actually allow us to treat the problem as one-dimensional, which makes it possible to obtain analytical results easily and reveal some special features of the two-partial field dynamics. In semiconductor crystal with band energy-spectrum structure, dispersion law is not quadratic but biquadratic, like (1). The wave function of such a state will consist of partial components. This may result in a total reflection from the planar interface between the media under the following nontrivial conditions: the parameter of defect

1063-7826/00/3411-1281$20.00 © 2000 MAIK "Nauka/Interperiodica"

(interface) is nonzero, and the incident particle energy does not coincide with the edge of the bulk state continuum.

In the studied system, both localized and quasi-localized states can exist. Spatial dispersion in the medium where the wave propagates leads to a nonquadratic dependence of energy on quasi-momentum. Consideration of the spatial dispersion will obviously lead to a change in the system properties. Specifically, the localized states will become extended [11, 12], which means that the amplitudes of their wave functions decrease with distance in oscillating manner (similar to the generalized Rayleigh waves). The localized states appearing in the vicinity of defects are also thoroughly studied for models implying biquadratic dispersion law [13]. However, no consideration has been given to quasi-localized states characterized by a scalar field, especially for nonsymmetrical stationary eigenstates with energy belonging to a defect-free medium continuum; therefore, these states are currently of interest in theory and applications.

It was recently shown [14] that, in a more realistic model, the anomalous total reflection from a passive defect is absent when dissipation in crystal is taken into account. It is of interest to ascertain the conditions under which the anomalous total reflection from interface in crystals is possible. In this paper, we analyze the effect of scattering-particle energy dissipation on the condition for the reflection resonance.

2. Let us consider a planar defect, for example, an interface between two similar semiconductor crystals with dispersion law given by (1), where $\alpha_j > 0$ and $\beta_j > 0$ ($j = x, y, z$). We assume that the crystal exhibits a strong spatial dispersion only in one direction, to be precise, in the direction perpendicular to the plane of the defect (this assumption can be validated by choosing an appropriate anisotropy type). Let us choose the coordinates in such a way that yOz plane coincides with the plane of defect and let us align the Ox axis with normal to this plane. Then, denoting $\alpha = \alpha_x$, $\beta = \beta_x$, $\alpha_\perp = \alpha_y = \alpha_z$ and assuming that $\beta_x \gg \beta_y$ and $\beta_x \gg \beta_z$, we obtain the dispersion law as

$$\varepsilon(\mathbf{k}) = E_0 - \alpha k^2 - \alpha_\perp k_\perp^2 + \beta k^4, \tag{2}$$

where $k = k_x$ and $k_\perp^2 = k_y^2 + k_z^2$. The dispersion law (2) corresponds to a time-independent Schrödinger equation:

$$\varepsilon\Psi = E_0\Psi + \alpha\frac{\partial^2\Psi}{\partial x^2} + \alpha_\perp\left(\frac{\partial^2\Psi}{\partial y^2} + \frac{\partial^2\Psi}{\partial z^2}\right) + \beta\frac{\partial^4\Psi}{\partial x^4} + U(x)\Psi, \tag{3}$$

where the interface between crystal half-spaces is simulated by the potential $U(x) = U_0\delta(x)$. Assuming that crystal is uniform over the interface, let us seek a solution of (3) in the form $\Psi(x, y, z) = \psi(x)\exp(ik_y y + ik_z z)$. With this assumption, Eq. (3) is reduced to one-dimensional equation for ψ function:

$$E\psi = E_0\psi + \alpha\frac{\partial^2\psi}{\partial x^2} + \beta\frac{\partial^4\psi}{\partial x^4} + U(x)\psi, \tag{4}$$

where we introduced $E = \varepsilon + \alpha_\perp k_\perp^2$. As follows from (4), the stationary homogeneous states $\psi(x) = \psi_0\exp(ikx)$ are characterized by the dispersion law

$$E(k) = E_0 - \alpha k^2 + \beta k^4. \tag{5}$$

Integrating (2) in the vicinity of interface $x = 0$ yields the boundary condition

$$\alpha\left(\frac{\partial\psi(+0)}{\partial x} - \frac{\partial\psi(-0)}{\partial x}\right) + \beta\left(\frac{\partial^3\psi(+0)}{\partial x^3} - \frac{\partial^3\psi(-0)}{x^3}\right) + U_0\psi(0) = 0. \tag{6}$$

For $\beta = 0$, condition (6) coincides with the well-known boundary condition for the Schrödinger equation with a quadratic dispersion law. We will concentrate on the case $\beta \neq 0$. The system of boundary conditions should also include the requirement of continuity of the wave function $\psi(x)$ and its second derivative at $x = 0$, which implies the continuity of its first derivative as well. Then, we obtain the following system of boundary conditions:

$$\psi(+0) = \psi(-0), \quad \frac{\partial\psi(+0)}{\partial x} = \frac{\partial\psi(-0)}{\partial x}, \quad \frac{\partial^2\psi(+0)}{\partial x^2} = \frac{\partial^2\psi(-0)}{\partial x^2}, \quad \frac{\partial^3\psi(+0)}{\partial x^3} - \frac{\partial^3\psi(-0)}{\partial x^3} = \eta\psi(0), \tag{7}$$

where $\eta = -U_0/\beta$.

Depending on energy E, the solutions to Eq. (4) correspond to homogeneous, localized, or quasi-localized states.

As follows from the dispersion law (5), each particular state is defined by two different quasi-momenta. Within the continuum range $E_m < E < E_0$, where $E_m = E_0 - \alpha^2/4\beta$, there are two pairs of real quasi-momenta:

$$k_{1,2}^2 = k_m^2 \pm \sqrt{\frac{E - E_m}{\beta}}. \tag{8}$$

Obviously, wave function of the homogeneous wave with quasi-momenta (8) comprises two terms with different amplitudes and oscillation frequencies:

$$\psi(x) = A_1 e^{ik_1 x} + A_2 e^{ik_2 x}. \tag{9}$$

The more interesting point, in the context of condensed-state physics, is the origin of localized states in the vicinity of a defect. Let us consider the case of $E < E_m$ in more detail. In this spectral range, each state is

defined by two complex quasi-momenta: $\kappa_1 = \gamma - iq$ and $\kappa_2 = \gamma + iq$, where

$$q^2 = \frac{1}{2}\left\{\sqrt{\frac{E_0 - E}{\beta} + k_m^2}\right\},$$
$$\gamma^2 = \frac{1}{2}\left\{\sqrt{\frac{E_0 - E}{\beta} - k_m^2}\right\}, \quad (10)$$

and $k_m^2 = \alpha/2\beta$. With the boundary conditions (7), a solution to Eq. (4) can be written as

$$\psi(x) = A\sin(q|x| + \vartheta)e^{-\gamma|x|}, \quad (11)$$

where phase is given by $\sin 2\vartheta = \sqrt{(E_m - E)/(E_0 - E)}$, and A is an arbitrary constant. Wave function (11) describes the so-called generalized localized state [11, 12], which decays in oscillatory manner with increasing distance from defect. The boundary conditions (4) provide a dispersion relationship for localized energy levels

$$4\gamma(\gamma^2 + q^2) = \eta, \quad (12)$$

which exist only if the defect parameter satisfies the condition $U_0 < 0$.

The prerequisites for the formation of a localized state similar to (11) in the vicinity of planar defect were studied elsewhere [13] for domain wall in ferromagnetic superconductor. In uniform magnetic field, at sufficiently low temperature, an inhomogeneous superconducting state is possible. The wave function of this state has the meaning of the order parameter and obeys the linearized Ginzburg–Landau equation for the fourth space derivative, since the effective exchange field in the vicinity of domain wall is considerably decreased. Solution similar to (11) in the vicinity of point defect was obtained in [13] for three-dimensional spherically symmetric case of dependence of energy on wave vector.

3. Now we discuss the case of $E > E_0$, when one of the quasi-momenta is real $k_1 = k$ and the other is pure imaginary $k_2 = i\kappa$:

$$k^2 = \sqrt{\frac{E - E_0}{\beta} + k_m^4} + k_m^2,$$
$$\kappa^2 = \sqrt{\frac{E - E_0}{\beta} + k_m^4} - k_m^2. \quad (13)$$

The dependences $E(k) = E_0 - \alpha k^2 + \beta k^4$ and $E(\kappa) = E_0 + \alpha\kappa^2 + \beta\kappa^4$ show (Fig. 1) that each energy value has two corresponding quasi-momenta (13).

In the case under study, quasi-localized state [6, 7] is formed within the continuum; its wave function consists of two partial components, one of which governs a standing wave along the entire Ox axis and the other

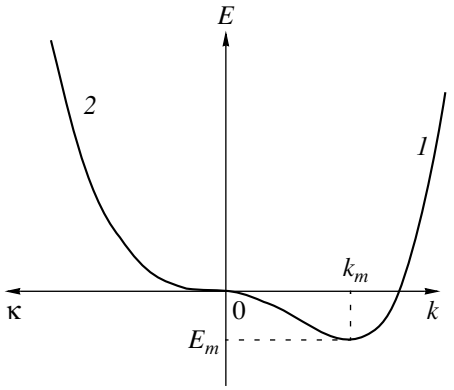

Fig. 1. Quasiparticle energy versus quasi-momentum (*1*) real and (*2*) imaginary components.

corresponds to an oscillation localized in the vicinity of defect:

$$\psi(x) = \begin{cases} A\sin(kx - \varphi_1) + Me^{-\kappa x}, & x < 0, \\ B\sin(kx - \varphi_2) + Me^{-\kappa x}, & x > 0. \end{cases} \quad (14)$$

Solution (14) incorporates five parameters: the amplitudes A, B, and M and phases φ_1 and φ_2. Substituting (14) into the boundary conditions (7), we obtain a set of algebraic homogeneous equations for quasi-localized state amplitudes A, B, and M:

$$\begin{cases} A\sin\varphi_1 - B\sin\varphi_2 = 0, \\ Ak\cos\varphi_1 - Bk\cos\varphi_2 + 2\kappa M = 0, \\ A(\eta\sin\varphi_1 + k^3\cos\varphi_1) - Bk^3\cos\varphi_2 - M(\eta + 2\kappa^3) = 0. \end{cases} \quad (15)$$

Equating the determinant of system (15) to zero, we obtain a relationship between φ_1 and φ_2, where one of the phases may be considered as a free parameter:

$$\{\eta + 2\kappa(k^2 + \kappa^2)\}k\sin(\varphi_1 - \varphi_2) = 2\kappa\eta\sin\varphi_1\sin\varphi_2. \quad (16)$$

The following special feature of quasi-localized states is worth noting. It turns out that there exists a stationary eigenstate $\psi_N = \psi_S + \psi_L$, such that standing wave exists only in one of half-spaces

$$\psi_S(x) = \begin{cases} A\sin kx, & x < 0, \\ 0, & x > 0, \end{cases} \quad (17)$$

whereas a localized state may exist on either side of the defect $\psi_L(x) = M\exp(-\kappa|x|)$. Actually, if $B = 0$ in (15), it follows from (16) that $\varphi_1 = 0$ and the localized-state amplitude is uniquely defined as $M = -(k/2\kappa)A$. The energy of these quasi-localized states is determined from the relationship

$$\eta = -2\kappa(k^2 + \kappa^2). \quad (18)$$

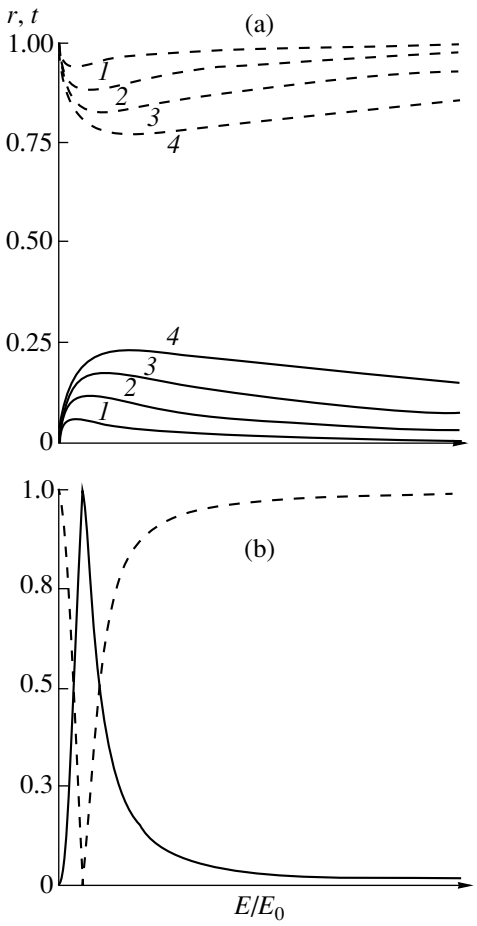

Fig. 2. Typical behavior of reflection coefficient $r = |R|^2$ (solid lines) and transmission coefficient $t = |T|^2$ (dashed lines) for (a) nonresonance case, $U_0 < 0$, for defect parameter $U_0 = U_j$ (j = 1, 2, 3, 4, curves *1–4*, respectively), where $|U_1| < |U_2| < |U_3| < |U_4|$; and (b) resonance case, $U_0 > 0$, where $\varepsilon_R = E_R/E_0$ is given by (18).

Quasi-localized state ψ_N exists only if $U_0 > 0$. In the next section we will show that the existence condition for nonsymmetrical ($B = 0$) quasi-localized state coincides with the condition for total resonance reflection from the defect.

We note that the quasi-localized state accounting for the single standing wave along the entire Ox axis ($A = B$) with non-zero local amplitude M is possible only for $\kappa = 0$, which corresponds to the edge of energy spectrum $E = E_0$.

4. Let us now consider scattering of a quasiparticle by crystal interface. We assume that the incident-particle energy falls within the range where quasi-localized states exist $E > E_0$. Then, we seek solution to Eq. (4) in the form

$$\psi(x) = \begin{cases} e^{ikx} + Re^{-ikx} + Me^{\kappa x}, & x < 0, \\ Te^{ikx} + Ne^{-\kappa x}, & x > 0, \end{cases} \qquad (19)$$

where R, T, M, N stand for the amplitudes of the reflected, transmitted, and localized on either side of defect waves, and k and κ are defined by (13). Substituting (19) into the boundary conditions (7), we readily obtain the corresponding amplitudes. The reflection and transmission coefficients are of our prime interest:

$$|R(E)|^2 = \frac{\left|\Delta_R^0(E)\right|^2}{\left|\Delta_R^0(E)\right|^2 + \left|\Delta_T^0(E)\right|^2}, \qquad (20)$$

$$|T(E)|^2 = \frac{\left|\Delta_T^0(E)\right|^2}{\left|\Delta_R^0(E)\right|^2 + \left|\Delta_T^0(E)\right|^2}, \qquad (21)$$

where

$$\left|\Delta_R^0(E)\right|^2 = 4\eta^2\kappa^2, \qquad (22)$$

$$\left|\Delta_T^0(E)\right|^2 = 4k^2\{\eta + 2\kappa(\kappa^2 + k^2)\}^2. \qquad (23)$$

Clearly, the quantum-mechanics conservation law

$$|R(E)|^2 + |T(E)|^2 = 1 \qquad (24)$$

holds in the medium, if the wave-energy absorption in the crystal volume is disregarded.

The reflection coefficient is proportional to the defect intensity $|R|^2 \sim U_0^2$, which leads to $|R|^2 = 0$ and $|T|^2 = 1$ for $U_0 \longrightarrow 0$; i.e., quasiparticle is insensitive to the interface and may pass freely from one half-space into another. For nonzero defect parameter U_0, total transmission may occur if the incident particle has the energy of the spectrum edge $E = E_0$. For high-energy quasiparticles, the interface is almost transparent (Fig. 2a). However, the discussed conditions are trivial, and they also hold in the case of quadratic dispersion law.

The fascinating fact is that, under nontrivial conditions, the total reflection of quasiparticle from interface is possible, i.e., $|R|^2 = 1$ and $|T|^2 = 0$ (Fig. 2b). Analysis of expressions (20) and (21) shows that the total reflection occurs if the incident quasiparticle energy $E_R(\eta)$ satisfies the condition $2\kappa(k^2 + \kappa^2) = -\eta$, which coincides with (18).

It is well known that the density of states exhibits sharp peaks for energies giving rise to singularities of the reflection or transmission coefficients. Because of this, the energy levels where the total reflection or transmission occurs are referred to as resonance levels.

In the system under study, a resonance (total reflection, to be precise) arises when the incident quasiparticle energy coincides with the energy level of a quasi-localized nonsymmetrical eigenstate. Resonance is conditioned by interaction at the interface of the media of wave-function partial components, one accounting for spatially localized state and the other, for traveling wave. These conclusions are in agreement with the results reported in publications [2–5], though they were

concerned with resonance effects in quite different physical fields (the acoustic Rayleigh waves).

5. In order to find out if the anomalous reflection from the passive defect analyzed in the previous section is observable in experiment, we should account for dissipation in crystal. Following [14], we will show that the condition for total reflection may be unstable in relation to small perturbations. Energy absorption in medium can be treated as such a perturbation. To account for dissipation in crystal volume, we should add a term in the form $i\nu\psi$ to Eq. (4). Then, the equation for scalar field in the studied model becomes

$$E\psi = E_0\psi + \alpha\frac{\partial^2\psi}{\partial x^2} + \beta\frac{\partial^4\psi}{\partial x^4} - i\nu\psi + U(x)\psi. \quad (25)$$

Solution to the scattering problem based on Eq. (25) can be written in the form

$$\psi(x) = \begin{cases} e^{ipx} + Re^{-ipx} + Me^{\lambda x}, & x < 0, \\ Te^{ipx} + Ne^{-\lambda x}, & x > 0, \end{cases} \quad (26)$$

where the quasi-momenta p and λ are complex quantities. Assuming that dissipation of quasiparticle energy is rather weak, we obtain

$$p = k + \frac{i\nu}{2k\Omega} \quad \text{and} \quad \lambda = \kappa + \frac{i\nu}{2\kappa\Omega}, \quad (27)$$

where $\Omega(E) = 2\sqrt{\beta(E - E_m)}$, and k and κ are still defined by (13). Then, the reflection and transmission coefficients take the following forms:

$$|R(E, \nu)|^2 = \frac{|\Delta_R(E, \nu)|^2}{|\Delta(E, \nu)|^2}, \quad (28)$$

$$|T(E, \nu)|^2 = \frac{|\Delta_T(E, \nu)|^2}{|\Delta(E, \nu)|^2}, \quad (29)$$

where

$$|\Delta_R(E, \nu)|^2 = |\Delta_R^0(E)|^2 + \frac{\nu^2\eta^2}{\kappa^2\Omega^2}, \quad (30)$$

$$|\Delta_T(E, \nu)|^2 = |\Delta_T^0(E)|^2\left(1 + \frac{\nu^2}{16k^4\Omega^2}\right) + \frac{2\nu^2}{\kappa\Omega}\left\{\frac{2k^4(5\kappa^2 + k^2)^2}{\kappa\Omega} - |\Delta_T^0(E)|\frac{5(\kappa^2 + k^2)}{k}\right\}, \quad (31)$$

$$|\Delta(E, \nu)|^2 = |\Delta_R(E, \nu)|^2 + |\Delta_T(E, \nu)|^2 + \frac{\nu^2}{\kappa\Omega^2}|\Delta_T^0(E)|(5\kappa^2 + k^2) + \frac{2\nu\eta}{\Omega}\left\{|\Delta_T^0(E)|\frac{2k^2 - \kappa^2}{2\kappa k^2} - 4k(5\kappa^2 + k^2)\right\}, \quad (32)$$

and the determinants $|\Delta_R^0(E)| = |\Delta_R(E, \nu = 0)$ and $|\Delta_T^0(E)| = |\Delta_T(E, \nu = 0)|$ are defined by (22) and (23). The consideration of dissipation in crystal naturally breaks the conservation law (24).

Let us consider the case when the incident-wave frequency is close to the resonance frequency E_R given by (18). In that event, $|\Delta_T^0(E_R)| = 0$, as was pointed above. The reflection and transmission (28), (29) coefficients can be written as

$$|R(E_R)|^2 = \frac{d^2}{d^2 + \gamma^2 + 2\gamma d}, \quad (33)$$

$$|T(E_R)|^2 = \frac{\gamma^2}{d^2 + \gamma^2 + 2\gamma d}, \quad (34)$$

where the following dimensionless quantities were introduced: $\gamma = \nu/\Omega\kappa_R^2 \ll 1$ is effective length of quasiparticle energy absorption, $d = U_0/\beta k_R(k_R^2 + 5\kappa_R^2)$ is an effective defect thickness, and $\kappa_R = \kappa(E_R)$ and $k_R = k(E_R)$.

If the effective defect thickness considerably exceeds the effective absorption length, $d \gg \gamma$, which is the case of a strong interaction between quasiparticle and interface, one can see from (33) and (34) that the total-reflection resonance is almost not disturbed.

In the case of a weak interaction between quasiparticle and interface, i.e., when $d \ll \gamma \ll 1$, expressions (33) and (34) yield $|T|^2 = 1$ and $|R|^2 = 0$, which indicates that the total transmission of wave through a defect is possible. If the energy of incident quasiparticle is close to the resonance energy of reflection in crystal without dissipation, then consideration of weak energy absorption leads to a reversed situation of resonance total transmission under the condition of weak interaction between quasiparticle and defect. Therefore, singularities in the reflection and transmission coefficients $|R|^2 = 1$ and $|T|^2 = 0$ prove to be unstable in relation to small perturbations, which can lead to $|T|^2 = 1$ and $|R|^2 = 0$ if quasiparticle interaction with defect is much weaker than the energy absorption in the crystal. These are the conclusions made in [14], where dissipation effect on elastic wave scattering in crystals was analyzed.

6. We considered the model of a semiconductor crystal with the band structure of quasiparticle spectrum when the dependence of energy on quasi-momentum is ambiguous. The main point of the model is consideration of spatial derivatives of the order higher than second in Schrödinger equation, i.e., inclusion of spatial dispersion. As a result, we managed to get insight

into several fundamentally new effects conditioned by the fact that quasiparticles follow nonquadratic dispersion law, even in the simplest one-dimensional case. In conclusion, we would like to point out the role of spatial dispersion in studying the resonance wave scattering by crystal defects.

Consideration of spatial dispersion via nonquadratic dependence of energy on quasi-momentum enables, with nontrivial initial parameters, the total reflection of the wave $\psi(x) \sim \exp(ikx)$ (quasiparticle) from dispersive media interface. In the case of quadratic dispersion law $E(k) = E_0 + \alpha k^2$, the reflection and transmission coefficients have the forms

$$|R|^2 = \frac{U_0^2}{U_0^2 + 4\alpha(E - E_0)}, \qquad |T|^2 = \frac{4\alpha(E - E_0)}{U_0^2 + 4\alpha(E - E_0)}. \tag{35}$$

The total reflection is evidently possible only if $E = E_0$. Therefore, as the analysis of the reflection (20) and transmission (21) coefficients indicates, resonance properties of interface in dispersive and dispersion-free media differ considerably.

Quasi-localized states also exhibit new features in dispersive medium. Specifically, spatial decay of the wave function of localized states is oscillatory. In contrast, for the quadratic dispersion law, at $E < E_0$, the wave function of a localized state decreases steadily $\psi(x) = \psi(0)\exp(-\kappa|x|)$, where $\kappa^2 = (E_0 - E)/\alpha > 0$. The energy of this localized state is defined by explicit formula $E_l = E_0 - (U_0^2/4\alpha)$.

We note that quasi-localized states governed by scalar field do not arise in media with quadratic dispersion law.

In media with spatial dispersion of the opposite sign ($\beta < 0$), the described above scattering features and quasi-localized states do not change. Substituting $\beta = -|\beta|$ in all the expressions above, one can see that the states interchange their energy-dependent types. Now, quasi-localized states exist for $E < E_0$ and localized, for $E > E_0$. Moreover, for $E_0 < E < E_0 + (\alpha^2/4\beta)$, localized states are conventional (their amplitudes decrease exponentially with distance from defect) and, for $E > E_0 + (\alpha^2/4\beta)$, localized states are generalized. Therefore, for $\beta < 0$, a change in the defect parameter may lead to a conversion of conventional localized states to generalized states. The effect is similar to that described in [11, 12].

It may be shown that the results obtained in Sections 1 and 2 depend only slightly on particular boundary conditions and equation of motion that cause nonquadratic dispersion of quasiparticles in many-valley (two-valley, in our case) semiconductor. Consequently, the main results are applicable not only to systems with uniformly distributed field, but to discrete models as well.

ACKNOWLEDGMENTS

I am grateful to A.M. Kosevitch and E.S. Syrkin for their valuable comments and fruitful participation in discussions.

REFERENCES

1. A. N. Darynskii and G. A. Maugin, Wave Motion **23**, 363 (1996).
2. A. M. Kosevich and A. V. Tutov, Phys. Lett. A **248**, 271 (1998).
3. A. M. Kosevich, D. V. Matsokin, and S. E. Savotchenko, Fiz. Nizk. Temp. **25**, 63 (1999) [Low Temp. Phys. **25**, 48 (1999)].
4. A. M. Kosevich and S. E. Savotchenko, Fiz. Nizk. Temp. **25**, 737 (1999) [Low Temp. Phys. **25**, 550 (1999)].
5. A. M. Kosevich, Zh. Éksp. Teor. Fiz. **115**, 306 (1999) [JETP **88**, 168 (1999)].
6. A. M. Kosevich and A. V. Tutov, Fiz. Nizk. Temp. **19**, 1273 (1993) [Low Temp. Phys. **19**, 905 (1993)].
7. A. M. Kosevich, D. V. Matsokin, and S. E. Savotchenko, Fiz. Nizk. Temp. **24**, 992 (1998) [Low Temp. Phys. **24**, 748 (1998)].
8. D. M. Bercha, O. B. Mitin, and I. M. Rarenko, Fiz. Tekh. Poluprovodn. (St. Petersburg) **28**, 1249 (1994) [Semiconductors **28**, 711 (1994)].
9. D. M. Bercha, O. B. Mitin, L. Yu. Kharkhalis, and A. I. Bercha, Fiz. Tverd. Tela (St. Petersburg) **37**, 3233 (1995) [Phys. Solid State **37**, 1778 (1995)].
10. D. M. Bercha, L. Yu. Kharkhalis, A. I. Bercha, and M. A. Sznajder, Phys. Status Solidi B **203**, 427 (1997).
11. S. V. Tarasenko, Fiz. Nizk. Temp. **24**, 219 (1998) [Low Temp. Phys. **24**, 164 (1998)].
12. S. V. Tarasenko, Fiz. Nizk. Temp. **24**, 832 (1998) [Low Temp. Phys. **24**, 624 (1998)].
13. A. I. Buzdin, V. N. Men'shov, and V. V. Tugushev, Zh. Éksp. Teor. Fiz. **91**, 2204 (1986) [Sov. Phys. JETP **64**, 1310 (1986)].
14. Yu. A. Kosevich and E. S. Syrkin, Phys. Lett. A **251**, 378 (1999).

Translated by A. Sidorova-Biryukova

Semiconductors, Vol. 34, No. 11, 2000, pp. 1287–1289. Translated from Fizika i Tekhnika Poluprovodnikov, Vol. 34, No. 11, 2000, pp. 1339–1341.

ELECTRONIC AND OPTICAL PROPERTIES OF SEMICONDUCTORS

Magneto-Optical Study of Bismuth at 80–280 K

V. M. Grabov*, K. G. Ivanov, and A. A. Zaĭtsev*****

** Hertzen Russian State Pedagogical University, St. Petersburg, 191186 Russia*

*** St. Petersburg State University of Technology and Design, St. Petersburg, 191186 Russia*

**** Elets State Pedagogical Institute, Elets, 399740 Russia*

Submitted May 17, 2000; accepted for publication May 17, 2000

Abstract—Infrared transmission ($\lambda = 10.6$ μm) of samples consisting of two symmetric plane-parallel halves of a Bi single crystal separated by a gap were studied in a pulsed magnetic field. Oscillations associated with interband optical transitions involving Landau levels were observed at 80–280 K. The temperature dependences of the energy gap, effective masses, and relaxation time of carriers were determined. © *2000 MAIK "Nauka/Interperiodica".*

The transmission of infrared (IR) laser radiation ($\lambda = 10.6$ μm) by a symmetric strip line comprising two halves of a bismuth single crystal separated by a gap of the order of the wavelength [1, 2] was studied. The measurements were performed in a pulsed magnetic field of up to 25 T in the temperature range $T = 80$–280 K.

The transmission-coefficient oscillations are due to interband optical transitions involving the Landau levels [3]. The positions of resonances in a magnetic field were analyzed in terms of the Lax model [3]. The effective masses of carriers and the energy gap of bismuth were determined. The results agree satisfactorily with the previous data [4]; however, the latter were obtained, for only three fixed temperatures. Simulation of the transmission of a symmetric strip line made it possible to determine the temperature dependence of the magneto-optical time of carrier relaxation.

The transmission of a bismuth symmetric strip line was studied using an experimental setup described previously [1]. IR radiation from a cw laser was directed into the gap of the strip line during a short time interval synchronized with the magnetic field pulse. The maximum magnetic field induction was 25 T at 80 K and 4.5 T at $T = 280$ K.

The measurements were carried out with the magnetic field directed parallel to the binary or bisector axes of the single crystal, and also with a number of intermediate orientations. The samples were prepared by electrical-erosion cutting, and the working surfaces, by chemical polishing.

Figure 1 shows the spectra taken for the binary orientation of the magnetic induction vector at $T = 80$ and 140 K. The magnetic-field positions of the oscillations due to optical interband transitions are enumerated in accordance with the numbers of Landau levels from which the transitions occur. Since the maximum field strength for these spectra is limited by 3.5 T, the interband transition from the level $j = 1$ at $T = 140$ K is not shown. Comparison of the spectra indicates a significant shift of the transitions to higher fields with increasing temperature.

Figure 2 shows the spectra obtained on further sample heating to 230 and 280 K. It is worth noting here that the oscillation amplitude decreases substantially. The signal-to-noise ratio for these spectra is on the order of unity. As a result, the observed oscillations decrease significantly in number.

According to [3], the interband optical transitions involving the Landau levels are periodic in the reciprocal magnetic field, with the period given by

$$\Delta\left(\frac{1}{H}\right) = \left(4E_G\frac{e\hbar}{m_c c}\right)/(E_{PH}^2 - E_G^2). \qquad (1)$$

For a fixed radiation-quantum energy E_{PH} the oscillation period is proportional to the ratio of the band gap to the cyclotron mass at the band bottom, E_G/m_c.

The period of transmission oscillations as a function of the reciprocal magnetic field was determined from the spectra obtained for different orientations and varied temperatures. The following temperature dependences were obtained for light binary $(E_G/m_c)_1$, light bisector $(E_G/m_c)_2$, and heavy bisector $(E_G/m_c)_3$ masses of L-electrons in bismuth:

$$\begin{aligned}(E_G/m_c)_1 &= 7.329 - (9.5\times10^{-3})T - (5.0\times10^{-6})T^2,\\ (E_G/m_c)_2 &= 8.199 - (8.4\times10^{-3})T\\ &\quad - (1.7\times10^{-5})T^2,\\ (E_G/m_c)_3 &= 4.237 - (2.9\times10^{-3})T - (1.7\times10^{-5})T^2,\end{aligned} \qquad (2)$$

where the band gap E_G is given in meV, and the cyclotron mass m_c, in free-electron mass units. The decrease in the E_G/m_c ratio with increasing temperature agrees satisfactorily with the results obtained in [4].

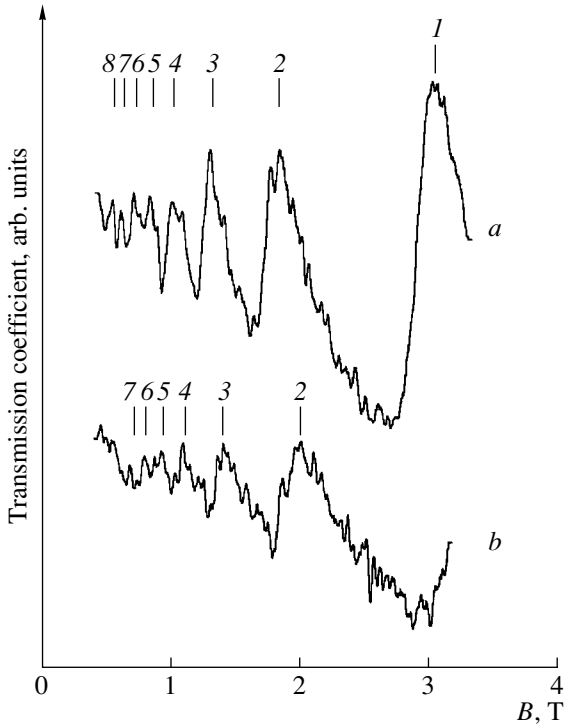

Fig. 1. Magnetotransmission oscillations due to interband transitions in bismuth at (*a*) 80 and (*b*) 140 K. The magnetic-field induction vector is parallel to the binary axis.

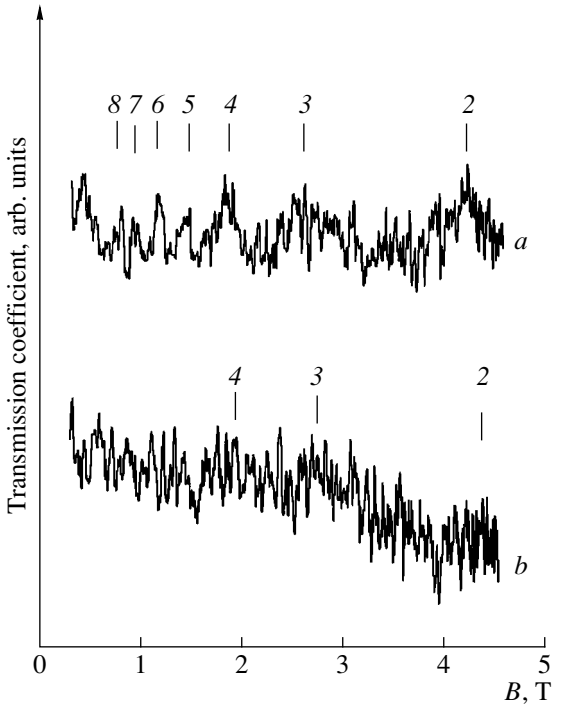

Fig. 2. Magnetotransmission oscillations caused by interband transitions in bismuth at (*a*) 230 and (*b*) 280 K. The magnetic field induction vector is parallel to the binary axis.

From an analysis of the transitions involving the Landau levels $j = 0$, band gap at the L-point $E_G = 20 \pm 2$ meV at 140 K was obtained. Previously, a value $E_G = 17 \pm 2$ meV was obtained for $T = 80$ K [2, 5]. The increase in E_G with temperature is of interest. The $E_G(T)$ dependence is a sum of two terms:

$$\frac{\partial E_G}{\partial T} = \left(\frac{\partial E_G}{\partial T}\right)_P + \left(\frac{\partial E_G}{\partial T}\right)_V. \quad (3)$$

The first term characterizes the thermal expansion under constant pressure, and the second, the influence of lattice vibrations for a fixed volume. The first term in the right-hand side of (3) was obtained using the pressure measurement results reported in [6]:

$$\left(\frac{\partial E_G}{\partial T}\right)_P \approx -3 \times 10^{-5} \text{ eV/K}, \quad (4)$$

and the derivative below was found in the experiment reported here:

$$\left(\frac{\partial E_G}{\partial T}\right)\Bigg|_{80\text{ K}} \approx 5 \times 10^{-5} \text{ eV/K}. \quad (5)$$

Thus, the band gap increases with increasing temperature despite the negative contribution from the pressure-related component. Consequently, the phonon contribution to the E_G variation in bismuth prevails at liquid nitrogen temperature over that associated with the thermal expansion of the lattice. On the whole, the increase in E_G with temperature is untypical of conventional semiconductors and is observed only in semimetals and narrow-gap semiconductors [7].

A simulation of the symmetric strip line transmission [2] allowed the carrier relaxation time τ to be determined in the temperature range 80–280 K. The obtained dependence is shown in Fig. 3, where the

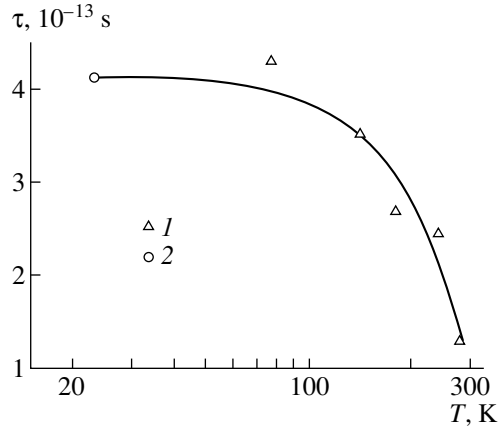

Fig. 3. Temperature dependence of the relaxation time for interband transitions between Landau levels in bismuth: (*1*) this study and (*2*) [5].

value of τ at $T = 22$ K [5] is also shown. We note that the relaxation time is practically constant ($\sim 4 \times 10^{-13}$ s) in the temperature range 22–80 K.

Figure 3 demonstrates a pronounced decrease in τ at temperatures higher than 100 K. According to [8], the characteristic temperatures for acoustic and optical phonons in bismuth are 43 and 130 K, respectively. Thus, scattering by optical phonons is the most effective in the observed magneto-optical effects in bismuth.

The reported results demonstrate the high efficiency of magneto-optical methods for investigating carrier parameters in semimetals and narrow-gap semiconductors in a wide temperature range.

REFERENCES

1. K. G. Ivanov, O. V. Kondakov, S. V. Brovko, and A. A. Zaĭtsev, Fiz. Tekh. Poluprovodn. (St. Petersburg) **30**, 1585 (1996) [Semiconductors **30**, 831 (1996)].
2. S. V. Brovko, A. A. Zaĭtsev, K. G. Ivanov, and O. V. Kondakov, Fiz. Tekh. Poluprovodn. (St. Petersburg) **31**, 416 (1997) [Semiconductors **31**, 350 (1997)].
3. R. N. Brown, J. G. Mavroides, and B. Lax, Phys. Rev. **129**, 2051 (1963).
4. M. P. Vecchi and M. S. Dresselhaus, Phys. Rev. B **10**, 771 (1974).
5. M. P. Vecchi, J. R. Pereira, and M. S. Dresselhaus, Phys. Rev. B **14**, 298 (1976).
6. E. E. Mendez, A. Misu, and M. S. Dresselhaus, Phys. Rev. B **24**, 639 (1981).
7. Yu. I. Ravich, B. A. Efimova, and I. A. Smirnov, *Semiconducting Lead Chalcogenides* (Plenum, New York, 1970); *Methods for Researching Semiconductors as Applied to Lead Chalcogenides PbTe, PbSe, and PbS* (Nauka, Moscow, 1968).
8. F. E. Macfarlane, J. Phys. Chem. Solids Suppl. **32** (1), 989 (1971).

Translated by D. Mashovets

Semiconductors, Vol. 34, No. 11, 2000, pp. 1290–1294. Translated from Fizika i Tekhnika Poluprovodnikov, Vol. 34, No. 11, 2000, pp. 1342–1346.

ELECTRONIC AND OPTICAL PROPERTIES OF SEMICONDUCTORS

Stimulation of Luminescence in Graded-Gap $Al_xGa_{1-x}As$ Semiconductors

K. Požela, R.-A. Bendorius, J. Požela, and A. Šilenas

Semiconductor Physics Institute, A. Goštauto 11, Vilnius, 2600 Lithuania

Submitted May 17, 2000; accepted for publication May 17, 2000

Abstract—The stimulation of photoluminescence in a graded-gap $Al_xGa_{1-x}As$ semiconductor was studied. It is shown that stimulation by external illumination makes it possible to increase the internal quantum yield of luminescence and specify the direction in which stimulated emission propagates. A method is proposed for measuring the internal quantum efficiency. *© 2000 MAIK "Nauka/Interperiodica".*

1. INTRODUCTION

Detectors of ionizing radiation with optical output signal, fabricated on the basis of $Al_xGa_{1-x}As$ structures, have many advantages over silicon and GaAs detectors with current-signal output [1, 2]. $Al_xGa_{1-x}As$ optical-output structures can convert an ionizing radiation pattern into an optical pattern with a high resolution, without the necessity of constructing an array of small-area detectors with a complex system for charge information transfer and reading, which has to be done in the case of current-output detectors [3]. An optical-output detector needs no power supply. It is based on a low-resistivity doped $Al_xGa_{1-x}As$ semiconductor in contrast to the high-resistivity high-purity material (GaAs, Si, or Ge) with extremely low defect concentration, used in current-output detectors.

However, the acquisition of information about the number of electron–hole pairs generated by external radiation in the volume of an optical-output detector is less efficient than that in the current-output devices. In the latter, the high quality and purity of the material ensure a very long lifetime of nonequilibrium electron–hole pairs. This makes it possible to collect with small losses most of the charges (almost 100%) generated in the detector volume by the external radiation under sufficiently high bias applied to the detector (commonly several hundred volts).

In optical-output detectors, the information about electron–hole pairs generated in the bulk is acquired optically. Photons emitted in electron–hole recombination in the bulk emerge from the sample through the wide-gap surface of the graded-gap semiconductor. The efficiency of the optical response (crystal luminescence) is mainly determined by two parameters: internal quantum yield η and efficiency of emission extraction from the crystal γ. The internal quantum yield η is determined by the fraction of electron–hole pairs generated in the bulk that recombines radiatively:

$$\eta = \frac{1}{1 + \tau_r/\tau_{nr}}, \quad (1)$$

where τ_r and τ_{nr} are electron–hole pair lifetimes for radiative and nonradiative recombination, respectively. The nonradiative lifetime is rather short in doped crystals $Al_xGa_{1-x}As$: $\tau_{nr} \approx 10^{-9}$ s. The graded-gap semiconductor $Al_xGa_{1-x}As$ is doped with Zn^+ acceptor impurity to improve the quantum yield. This brings the rate of radiative recombination to a level characteristic of a nonradiative recombination. In this way η can be raised to 60–80%. An additional decrease in τ_r, and the corresponding increase in the internal quantum yield η, can be achieved by stimulating the radiative recombination by means of an external optical source.

The stimulation of the radiative recombination can also be conducive to solving the problem of emission output from the sample. The angle of total internal reflection at the GaAs–air interface is only 16° because of the high refractive index of $Al_xGa_{1-x}As$. Therefore, only a very small fraction of photons generated in the crystal emerge outwards ($\gamma \approx 2$–3%). However, the output efficiency γ can be raised manifold by concentrating photons generated in the crystal into a solid angle of 16°, thereby avoiding the total reflection from the crystal surface. This can be achieved by stimulating radiative recombination with an external optical beam perpendicular to the interface. It can be shown that, in this case, the stimulated photon has the same frequency, phase, polarization, and propagation direction as those of the stimulating photon [4]. A parallel optical beam with a divergence angle less than 16° stimulates the radiative recombination with emission into this angle, thus ensuring high emission output from the crystal.

1063-7826/00/3411-1290$20.00

In this paper, we consider the possibility of raising both the internal and external quantum yields of photoluminescence (PL) from the $Al_xGa_{1-x}As$ structure by stimulating the radiative recombination with an additional external optical source.

2. STIMULATION OF EMISSION

We examine (in terms of a simple two-level model) the photon emission from a semiconductor wafer of thickness L where N_2 electron–hole pairs per unit volume are generated by some ionizing agent. We assume the energy spacing between the two levels and, therefore, the energy of emitted photons $\hbar\omega_{21}$ to be close to the band gap in GaAs, i.e., 1.5 eV. We also assume that, in thermal equilibrium, the electron population of the upper level n_{20} is zero, and that of the lower level is n_{10}.

In a steady state, the rate of electron–hole pair generation by ionizing radiation is equal to the rate of the carrier recombination

$$\left(\frac{dN_2}{dt}\right)_{\text{gen}} = N_2\left(\frac{1}{\tau_{nr}} + \frac{1}{\tau_r}\right) + B(N_2 - N_1)I_{\nu 21}, \quad (2)$$

where τ_{nr} and τ_r are the relaxation times of nonradiative and radiative spontaneous recombination, respectively; $I_{\nu 21}$ is the intensity of radiation with photon energy $\hbar\omega_{21}$; and B is the Einstein coefficient governing the rate of stimulated recombination

$$B = \left(\frac{c}{n_r}\right)^2 \frac{1}{8\pi\nu_{21}^2\tau_r}. \quad (3)$$

Here, c/n_r is the speed of light in a medium with refraction index n_r.

The relaxation time of stimulated recombination equals

$$\tau_i^{-1} = BI_{\nu 21}. \quad (4)$$

In the case of GaAs, $\nu_{21} \approx 4 \times 10^{14}$ s^{-1}, $n_r = 3.54$, and $B\tau_r \approx 0.54$ cm^3/s. Assuming the rate of generation by ionizing radiation to be BN_1I_1, where I_1 is the intensity of ionizing radiation, we use (2)–(4) to obtain the following relation between the populations of the second level with N_2^{i} and without N_2 stimulation

$$N_2 \approx N_2^{\text{i}}\left(1 + \frac{I_{\nu 21}}{I_1}\right). \quad (5)$$

The stimulating radiation does not affect the number of electron–hole pairs when its intensity is much lower than that of the ionizing radiation.

For $I_1 \gg I_{\nu 21}$, the ratio of the stimulated emission intensity $I_m^{\text{i}} \sim N_2^{\text{i}}\eta_i/\tau_i$ to that of spontaneous radiation $I_m^{sp} \sim N_2\eta/\tau_r$ is given by

$$\frac{I_m^{\text{i}}}{I_m^{sp}} = \frac{\eta_i\tau_r}{\eta\tau_i}, \quad (6)$$

where

$$\eta_i = \frac{1}{1 + \tau_i/\tau_{nr}} \quad (7)$$

determines the fraction of electron–hole pairs involved in radiative recombination in the presence of stimulation, and η, without stimulation [see (1)]. Relation (6) shows that the radiation intensity can be considerably raised by stimulating the electron–hole recombination.

Let us determine the luminescence intensity from a semiconductor wafer of thickness L in which N_2 electron–hole pairs per unit volume are generated by ionizing radiation.

The flux of photons $N_{\nu 21}$ with energy $\hbar\omega_{21}$ in the z-direction normal to the semiconductor wafer surface is given by

$$J_{21} = \frac{c}{n_r}N_{\nu 21}\hbar\omega_{21}. \quad (8)$$

The change in the photon flux density in the interval dz due to absorption and stimulation of radiation is equal to

$$dJ_{21} = kJ_{21}dz, \quad (9)$$

where the stimulation and absorption coefficient has the form

$$k = \frac{n_r}{c}B(N_2 - N_1). \quad (10)$$

We note that $N_1 = n_{10} - N_2$. The negative component of the coefficient k corresponds to radiation absorption

$$k_a = -\frac{n_r}{c}Bn_{10}, \quad (11)$$

and the positive component

$$k_i = \frac{n_r}{c}B(2N_2) \quad (12)$$

amounts for both the effect of radiation stimulation and the decrease in the absorption of the stimulating radiation absorption in the generation of N_2 electron–hole pairs. The intensity of the "primary" radiation coming to the wafer surface (with coordinate L) from a plane with coordinate z_1 is given by

$$j(z_1)e^{k(L-z_1)}dz_1. \quad (13)$$

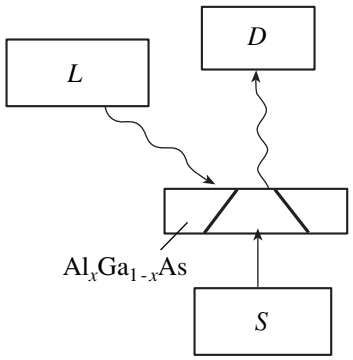

Fig. 1. Schematic of the experiment. The PL excited by modulated beam of laser *L* (wavy arrow) is synchronously detected by detector-spectrometer *D*. Unmodulated white-light illumination from source *S* (straight arrow) stimulates radiative transitions in graded-gap $Al_xGa_{1-x}As$ wafer. The trapezium across the plate shows the spatial change of the band gap: the small and large bases of the trapezoid correspond, respectively, to the narrow- and wide-gap sides of the graded-gap crystal.

The total photon flux through the wafer surface L is equal to the sum of fluxes coming from all the planes z_1 within the wafer

$$I_L = \int_0^L j(z_1)dz_1. \quad (14)$$

Assuming for simplicity that the generation of N_2 electron–hole pairs is uniform across the wafer, we obtain the following expression for the intensity of spontaneous luminescence from the wafer:

$$I_L^{sp} = j_{spo}\frac{e^{kL}-1}{k}. \quad (15)$$

Here,

$$j_{spo} = \frac{N_2}{\tau_r}\hbar\omega_{21}\frac{c}{n_r}. \quad (16)$$

For stimulation by external photon flux j_{021} incident on the crystal plane $z = 0$, the flux across the plane z_1 is written as

$$j(z_1) = j_{spo} + j_{021}e^{k^i z_1} \quad (17)$$

and, correspondingly, the intensity of stimulated luminescence from the wafer is given by

$$I_L^i = I_L^{spi} + j_{021}Le^{k^i L}. \quad (18)$$

Here, the superscripts i at I_L^{spi} and k^i correspond to a change of N_2 for N_2^i [see equality (5)] in the case of stimulation.

It can be seen that the stimulated luminescence consists of two components: spontaneous luminescence with pair concentration N_2^i instead of N_2 and modulated absorption of stimulating radiation.

We note that the spontaneous luminescence is isotropic and emitted within a solid angle 4π. Only a minor fraction of the emission, falling within the solid angle

$$\Omega(\theta) = 4\pi\sin^2\frac{\theta}{2}\left(1 + \cos^2\frac{\theta}{2}\right), \quad \sin\theta = \frac{1}{n_r}, \quad (19)$$

where θ is the angle of total internal reflection, emerges from the crystal.

The stimulating radiation is directed and is conducive to the exit of the stimulated emission from the crystal, guiding it into the solid angle $\Omega(\theta)$. If the stimulating radiation is directed into the solid angles outside $\Omega(\theta)$, it cannot leave the crystal at all, together with the stimulated emission.

3. EXPERIMENTAL DETERMINATION OF THE POSSIBILITY OF STIMULATING THE PL IN $Al_xGa_{1-x}As$ CRYSTALS

Since the stimulated emission leaves the crystal together with the stimulating radiation, a locked-in detection was used to separate them experimentally. Figure 1 shows an outline of the experiment. An argon laser ($\lambda = 488$ nm) was employed for electron–hole pair generation. Its radiation was modulated by a chopper determining the synchronizing frequency (~130 Hz) of the luminescence signal detection. An MDR-12-LOMO monochromator and a FEU-157 photomultiplier sensitive to IR luminescence from GaAs were used to measure the luminescence intensity spectrum.

Thus, only the modulated luminescence component was measured, excluding the unmodulated component of stimulating radiation.

As can be seen from Fig. 1, carriers are generated by a laser beam in a layer about 1 μm thick on the narrow-gap side of the crystal and luminescence is observed from the same side. The stimulating radiation with a continuous spectrum in the range of 600–900 nm is directed from an incandescent lamp with a stabilized power supply in the direction normal to the crystal surface from the wide-gap side. Owing to the graded-gap structure of the crystal, the stimulating radiation passes without being absorbed by the narrow-gap side of the sample where photons with energies corresponding to radiative transitions of nonequilibrium electrons are selected automatically from the white-light spectrum. Radiative transitions were stimulated in this way.

The layer where the radiation interacts with generated carriers is thin ($L \approx 1$ μm); therefore, we may assume that $\tilde{k}L < 1$, where $\tilde{k} = B(\tilde{N}_2 - \tilde{N}_1)n_r/c$. Tildes indicate the ac components of the absorption coefficient. Further, in accordance with (15) and (18), the

modulated ac components of luminescence detected by the locked-in detector equal

$$\tilde{I}^{sp} \approx \tilde{j}_{spo} L \tag{20}$$

for spontaneous emission and

$$\tilde{I}^{i} \approx j_{021} e^{-k_a L} \tilde{k} L^2 + \tilde{j}^{i}_{spo} L, \tag{21}$$

for the stimulated emission.

The first term in (21) may be smaller in comparison with the second term owing to the large value of the absorption coefficient [see (11)]. Then we have

$$\frac{\tilde{I}^{i}}{\tilde{I}^{sp}} \approx \frac{\eta_i}{\eta}. \tag{22}$$

Since the band gap decreases toward the surface of the graded-gap crystal, the absorption of the stimulating radiation decreases in the red spectral region for small thicknesses L. A decrease in $k_a L$ enhances the contribution of the first term in the right-hand side of (21) to the intensity of the stimulated emission. This causes a corresponding rise in the ratio between the stimulated- and spontaneous-radiation intensities.

The experimental spectra of modulated components of the spontaneous and stimulated emission are shown in Fig. 2 for an $Al_xGa_{1-x}As$ sample with composition varying across the sample thickness (d = 50 μm) from x = 0 to x = 0.3. The results obtained for this sample were typical of the entire set of $Al_xGa_{1-x}As$ samples with different compositional gradients and doping levels. The samples were doped with Zn^+ acceptor to $N_{Zn} > 10^{17}$ cm^{-3}. No luminescence was observed in undoped samples.

As was expected, once the stimulating light is switched on, the emission intensity in the range of the spontaneous-emission line increases. This corresponds to an increase in the quantum yield η_i with growing intensity of the stimulating light. For a sufficiently high stimulating-light intensity, an increase in I^i tends to level off in the short-wavelength part of the emission band, which means that $\eta_i \longrightarrow 1$. This occurs in the case shown in Fig. 2. Therefore, the $\tilde{I}^{i}/\tilde{I}^{sp}$ ratio near the emission-line peak furnishes an opportunity to use (22) to estimate the internal quantum yield at $\eta \approx 0.7$. We note that the $\tilde{I}^{i}/\tilde{I}^{sp}$ ratio is somewhat larger (see Fig. 2) in the red part of the emission band, as would be expected from (21).

The locked-in detection enables elimination of the dc component of the stimulating radiation. Without laser excitation, but with stimulating illumination, the background radiation was much weaker than both the spontaneous luminescence signal under laser excitation and the luminescence enhancement under stimulation (Fig. 2). However, as can be seen from Fig. 2, significant radiation-intensity fluctuations were observed in

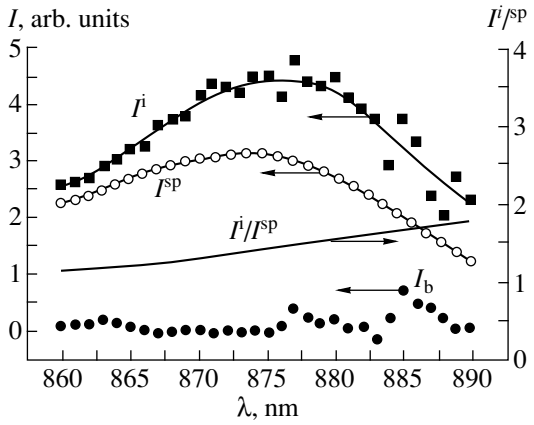

Fig. 2. Spectra of spontaneous I^{sp} and stimulated I^i luminescence from $Al_xGa_{1-x}As$ wafer and the ratio of their intensities I^i/I^{sp} for the experimental configuration shown in Fig. 1. Curve I_b shows the background radiation in the absence of laser generation of electron–hole pairs.

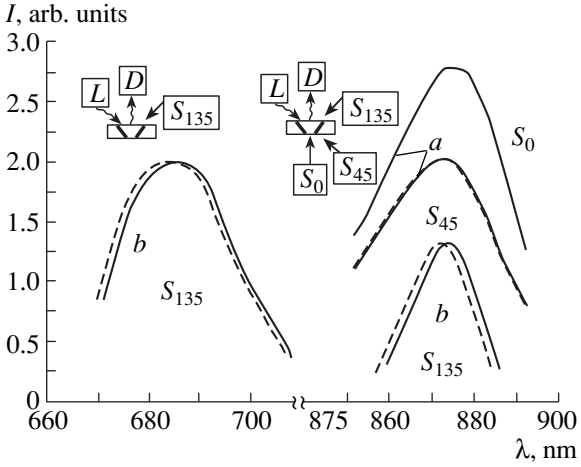

Fig. 3. Spectra of averaged experimental luminescence intensities for $Al_xGa_{1-x}As$ structures with (a) x = 0.2 and d = 55 μm and (b) x = 0.32 and d = 70 μm for different directions of the stimulating illumination. The experimental configuration is shown in notations of Fig. 1. Numbers designating the illumination source S correspond to the angle between the illuminating light and detected luminescence directions. Dashed lines correspond to spontaneous luminescence in the absence of illumination.

the long-wavelength part of the spectrum, becoming more pronounced with increasing illumination intensity. We relate these fluctuations to those of the stimulating signal intensity. The fluctuations imposed a restriction on the stimulating light intensity used in the experiment.

The stimulated luminescence intensity depends on the direction of the stimulating illumination. The stimulating radiation filling an external solid angle $d\Omega$ is refracted at the surface of the semiconductor wafer with

high n_r and finds itself within a narrow solid angle inside the semiconductor

$$d\Omega(\theta) = \frac{d\Omega}{n_r^2}. \quad (23)$$

Thus, the stimulating radiation in the semiconductor is always within the solid angle corresponding to the angle of the total internal reflection, which ensures its emergence from the crystal. In order to ensure the output of the stimulated emission within the solid angle $d\Omega_{det}$ corresponding to the angular aperture of the luminescence detector, the stimulating radiation incident on the wafer should be concentrated within the same solid angle $d\Omega = d\Omega_{det}$ in accordance with (23).

The dependence of PL spectra of a graded-gap crystal on the direction of a parallel beam of stimulating light is shown in Fig. 3. The angular aperture of the luminescence-detector lens is less than 30°. From Fig. 3 it is evident that a clearly pronounced stimulated luminescence component is observed in the detected output signal when the incidence angle $\varphi < 30°$. However, this component disappears at $\varphi > 30°$, which indicates a directed effect of the stimulating illumination on the stimulated luminescence. The stimulated part of the luminescence from the narrow-gap side of the crystal disappears completely if the stimulating illumination is incident on the same side. In this case, the stimulating radiation was directed from the emitting surface inside the crystal bulk where it was re-emitted with a red shift in the radiation spectrum (Fig. 3).

4. CONCLUSION

It is shown that stimulation of the recombination of nonequilibrium electron–hole pairs in a graded-gap $Al_xGa_{1-x}As$ semiconductor by external radiation causes a rise in the internal quantum yield of PL. This manifests itself in the fact that the intensity of stimulated luminescence is $1/\eta$ stronger, compared with the spontaneous emission, which makes it possible to determine experimentally the external quantum yield η of the spontaneous electron–hole recombination.

Stimulating illumination governs the direction of the stimulated emission. This permits the radiation to be directed within a solid angle smaller than the angle of the total internal reflection and thus be extracted from the crystal.

REFERENCES

1. J. Požela, V. Jucienė, and K. Požela, Nucl. Instrum. Methods Phys. Res. A **410**, 111 (1998).
2. J. Požela, K. Požela, A. Šilėnas, *et al.*, Lith. Phys. J. **39**, 139 (1999).
3. J. Požela, K. Požela, A. Šilėnas, *et al.*, Nucl. Instrum. Methods Phys. Res. A **434**, 169 (1999).
4. P. A. M. Dirac, *The Principles of Quantum Mechanics* (Clarendon Press, Oxford, 1958; Fizmatizdat, Moscow, 1960).

Translated by S. Ktitorov

Semiconductors, Vol. 34, No. 11, 2000, pp. 1295–1300. Translated from Fizika i Tekhnika Poluprovodnikov, Vol. 34, No. 11, 2000, pp. 1347–1352.

SEMICONDUCTOR STRUCTURES, INTERFACES, AND SURFACES

Photoelectric Properties of Isotype and Anisotype Si/GaN:O Heterojunctions

S. E. Aleksandrov, T. A. Gavrikova, and V. A. Zykov

St. Petersburg State Technical University, ul. Politekhnicheskaya 29, St. Petersburg, 195251 Russia

Submitted March 2, 2000; accepted for publication April 28, 2000

Abstract—Results of a comprehensive study of electrical and photoelectric properties of isotype (*p*-Si/*p*-GaN:O) and anisotype *n*-Si/*p*-GaN:O) heterojunctions are reported. The structures were fabricated by chemical vapor deposition of thin films of GaN:O solid solutions on silicon substrates by pyrolytic decomposition of gallium monoammine chloride in the presence of water vapor. Total and spectral photosensitivity and photoresponse kinetics in the current mode under forward and reverse biases, current–voltage characteristics, and saturation open-circuit photovoltage were studied. It was found that in both kinds of heterojunctions the charge distribution near the contacts is mainly governed by carrier capture into interface states (with density estimated to be ~10^{14}–10^{15} cm^{-2}) with the formation of depletion layers on both sides of the interface. Photosensitivity mechanisms are analyzed for anisotype and isotype heterojunctions. It is shown that the differential nature of the photoresponse kinetics is related to the recharging of interface states, and the strong rise in the photoresponse signal of a biased anisotype heterojunction is attributed to the phototransistor effect. The proposed energy band models of the heterojunctions consistently describe the observed effects. © *2000 MAIK "Nauka/Interperiodica".*

The wide band gap (E_g = 3.4 eV) accounts for the interest in gallium nitride as a promising material for the fabrication of detectors and light-emitting devices for the short-wavelength region of the visible spectral range. The introduction of oxygen into gallium nitride is accompanied by the formation of oxynitride solid solutions GaN:O and leads to the widening of the band gap to as much as 3.9 eV [1]. This fact gives reason to believe that detectors of UV light can be fabricated on the basis of oxynitrides. The use of gallium oxynitride as a heterojunction (HJ) component and the fabrication of a device on its basis combining advantages of a HJ and the possibilities of the oxynitride enhance the prospects for practical application of this material. First attempts to develop a photodetector on the basis of a Si/GaN:O demonstrated that the device shows photosensitivity in a wide spectral range [1].

In this paper (a continuation of [1]), we report the results obtained in a comprehensive study of electrical and photoelectric properties of isotype (*p*-Si/*p*-GaN:O) and anisotype (*n*-Si/*p*-GaN:O) HJs. An attempt is made to analyze the photosensitivity mechanisms with regard to the energy band diagrams of isotype and anisotype Si/GaN:O HJs.

The heterostructures were fabricated on *n*- and *p*-type (100) Si substrates KEF-7.5 (*n*-Si:P, ρ = 7.55 Ω cm) and KDB-10 (*p*-Si:B, ρ = 10 Ω cm, respectively). GaN:O films with varied content of oxygen were grown by the chemical vapor deposition method in the chloride-hydride system, using the pyrolytic decomposition of gallium monoammine chloride (gallium trichloride ammonia complex, GTAC) [1]. The carrier (hole) concentration in the films was, $p = 5 \times 10^{17}$–5×10^{18} cm^{-3}, depending on the oxygen content.

The total photosensitivity, photoresponse kinetics, and spectral photosensitivity of the obtained heterostructures were measured and their current–voltage (*I*–*V*) characteristics were measured. The photoresponse signal U_{ph} was measured in the short-circuit mode with varied bias *U* applied to a HJ. All measurements were done with HJ illuminated from the wide-gap side. The photoresponse kinetics was studied by recording the photoresponse oscillograms on illuminating the HJ with 2–10-ms rectangular light pulses. As a source of light, we used a GaAs LED with emission wavelength λ = 0.85 μm. The measurements were performed in the linear portion of the photocurrent–illuminance characteristic.

All the HJs studied, both isotype (*p*–*p*) and anisotype (*n*–*p*), showed photosensitivity under zero bias. The measurement results are listed in the table. The photoresponse signal of anisotype HJs far exceeds (by nearly three orders of magnitude) the corresponding values for isotype HJs. Such an excess of the photosensitivity of anisotype HJs over that of isotype heterojunctions was observed for all oxygen concentrations in the oxynitride film, characterized by the vapor pressure ratio P_{H_2O}/P_{GTAC} of water and GTAC vapors in the course of deposition. Under reverse bias (with GaN positive for isotype HJ), the photoresponse signal increased for both anisotype and isotype HJs. A rise in the signal was observed with an increase in the bias voltage and reached the maximum value of photoresponse achieved at $U \approx -(3–4)$ V. The ratio of the max-

1063-7826/00/3411-1295$20.00

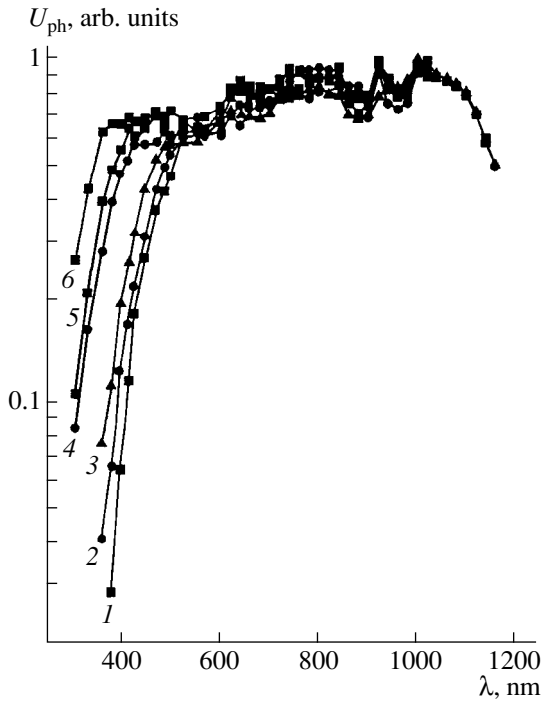

Fig. 1. Spectral characteristics of anisotype *n*-Si/*p*-GaN:O heterojunctions obtained at various partial pressures of water vapor P_{H_2O}/P_{GTAC} = (*1*) 0, (*2*) 0.150, (*3*) 0.267, (*4*) 0.464, (*5*) 0.55, and (*6*) 0.725.

imum photoresponse signals for anisotype HJs to the values at zero bias was no larger than 2–5 (depending on oxygen content of the films). The same ratio for isotype HJs was as large as 10^2–10^3 (see table). Furthermore, for isotype HJs, a rise in photoresponse signal (with respect to the zero-bias value) was observed not only under reverse, but also under forward bias (with GaN negative).

The zero-bias spectral characteristics of anisotype HJs (Fig. 1) are typical of HJs (similar dependences measured in the open-circuit mode were reported for anisotype HJs in [1]). The photoelectric threshold is determined by the band gap of the narrow-gap semiconductor, i.e., Si. The position of the short-wavelength photosensitivity falloff depends on the oxygen content, being shifted to shorter wavelengths with increasing oxygen concentration in the film. Under reverse bias, the shape of the spectral characteristics of anisotype HJs remained practically unchanged. On applying reverse bias, the spectral characteristics of isotype HJs showed changes in the photoresponse signal only in the short-wavelength region of the spectrum. With an increase in the oxygen content of a gallium nitride film, the current sensitivity in this spectral region decreased. A similar behavior was observed on forward-biasing of isotype HJ.

Measurements of the photoresponse kinetics for an anisotype HJ demonstrated that the photoresponse variation with time t has a differential nature, irrespective of the oxygen content of the film. Once the HJ is illuminated (t = 0), the photocurrent rises fast, reaching maximum value. After that the signal decays slowly. The time constants of the fast and slow processes are $\sim 5 \times 10^{-5}$ and $\sim 3 \times 10^{-3}$ s, respectively. On switching the light off, a sharp signal overshoot with sign reversal was observed, with subsequent slow decay to the zero value. Figure 2 shows characteristic time dependences of photoresponse relaxation $U_{ph}(t)$ for an anisotype HJ under varied bias. With an increase in the reverse bias, the photoresponse curves are smoothed and become

Photoelectric parameters of anisotype and isotype Si/GaN:O HJ

Sample no.	P_{H_2O}/P_{GTAC}	HJ type Si/GaN:O	Photoresponse signal U_{ph}, mV (U = 0 V)	Photoresponse signal U_{ph}, mV (U = –3 V)
1	0	*n–p*	13	38
		p–p	0.09	–
2	0.138	*n–p*	11	30
		p–p	0.062	50
3	0.150	*n–p*	50	40
		p–p	0.03	55
4	0.267	*n–p*	35	60
		p–p	0.26	65
5	0.464	*n–p*	32	75
		p–p	0.02	90
6	0.550	*n–p*	30	80
		p–p	0.058	150
7	0.725	*n–p*	0.12	50
		p–p	0.022	65

monotonic at $U \approx -(0.2–4)$ V. Under forward bias, the photoresponse kinetics remains qualitatively the same, with the signal sign preserved. However, with an increase in the forward bias, the relaxation curves become increasingly nonmonotonic, and the photoresponse-signal intensity markedly decreases.

The differential nature of the photoresponse signal relaxation is also characteristic of isotype HJs (Fig. 3). However, in contrast to the case considered above, here, the relaxation curves are smoothed with increasing bias for both the reverse and forward biases. In addition, the photoresponse signals have different signs for forward- and reverse-biased HJs.

All isotype and anisotype HJs exhibit rectification [1]. At small biases, forward *I–V* characteristics of anisotype HJs (Fig. 4a) show an exponential dependence of the type $I \propto \exp(eU/\beta kT)$ with $\beta = 2–3$. At higher voltages the forward current $I \propto \exp(AU)$. The reverse *I–V* characteristics are characterized by a power-law dependence of the current on voltage $I = A(T)U^m$.

For isotype HJs, the forward and reverse currents are described by power-law dependences of the type $I = A(T)U^m$. The slope of the forward characteristics varies, depending on the voltage, between $m \approx 1.5$ at $U < 2$ V to $m \approx 2.5$ at higher voltages (Fig. 5a). In reverse characteristics, two linear portions can also be distinguished, with different slopes at small and high biases (Fig. 5b).

Energy band diagrams were constructed to analyze the photosensitivity mechanisms, for both types of HJs under study. Since no data on the electron affinity of gallium oxynitride are available in the literature, the basic parameters of the diagrams (band offsets ΔE_c and ΔE_v) were determined from the experimentally found diffusion potentials V_{D1} and V_{D2} with regard to the Fermi energies and band gaps of the HJ components. The diffusion potentials were found from the saturation open-circuit voltage on illuminating a HJ with high-intensity light pulse, and also from *I–V* characteristics. Figures 6a and 6b show energy band diagrams (T = 300 K) for isotype and anisotype Si/GaN:O HJs with oxygen content in the wide-gap material corresponding to $P_{H_2O}/P_{GTAC} = 0.55$. In the diagrams, the band gaps of silicon and gallium oxynitride are, respectively, E_{g1} = 1.12 eV and E_{g2} = 3.85 eV [1]; ΔE_c = 2.75 eV, ΔE_v = 0.18 eV, V_{D1} = 0.30 eV, and V_{D2} = 0.11 eV for anisotype HJ and ΔE_c = 2.92 eV, ΔE_v = 0.27 eV, V_{D1} = 0.32 eV, and V_{D2} = 0.09 eV for isotype HJ.

A specific feature of Si/GaN:O HJs, and also of many other actual HJs with pronounced lattice mismatch, is the high concentration of surface states at the Si–GaN:O interface. An estimation taking into account the lattice mismatch between the two components yields, depending on the oxygen content in the oxynitride film, surface state densities of ~10^{14}–10^{15} cm^{-2}. Interacting with carriers, surface states modify the spatial distribution of charge at the interface and thereby affect characteristics of nonequilibrium processes [2]. The presence of surface states at the Si–GaN:O interface is confirmed by the data on the open-circuit voltage sign for isotype HJ. The different signs of photovoltage in exciting the electron–hole pairs in silicon (by photons with energy $E_{g1} < h\nu < E_{g2}$) and in oxynitride ($h\nu < E_{g2}$) indicate that the contact electric fields in these semiconductors are oppositely directed. Conse-

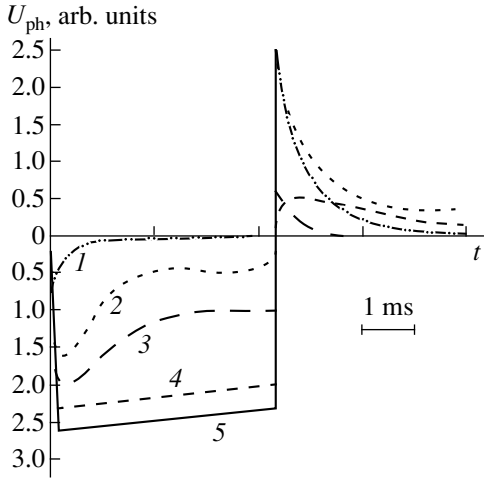

Fig. 2. Photoresponse kinetics of anisotype *n*-Si/*p*-GaN:O heterojunction under various forward (+) and reverse (–) biases U = (*1*) +0.25, (*2*) 0, (*3*) –0.1, (*4*) –0.2, and (*5*) –3 V.

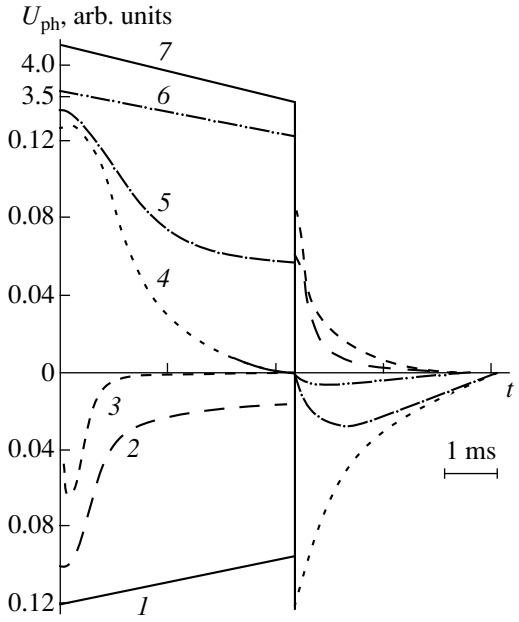

Fig. 3. Photoresponse kinetics of isotype *p*-Si/*p*-GaN:O heterojunction under various forward (+) and reverse (–) biases. U: (*1*) –0.2, (*2*) –0.1, (*3*) 0, (*4*) +0.1, (*5*) +0.2, (*6*) +0.4, and (*7*) +3.5 V.

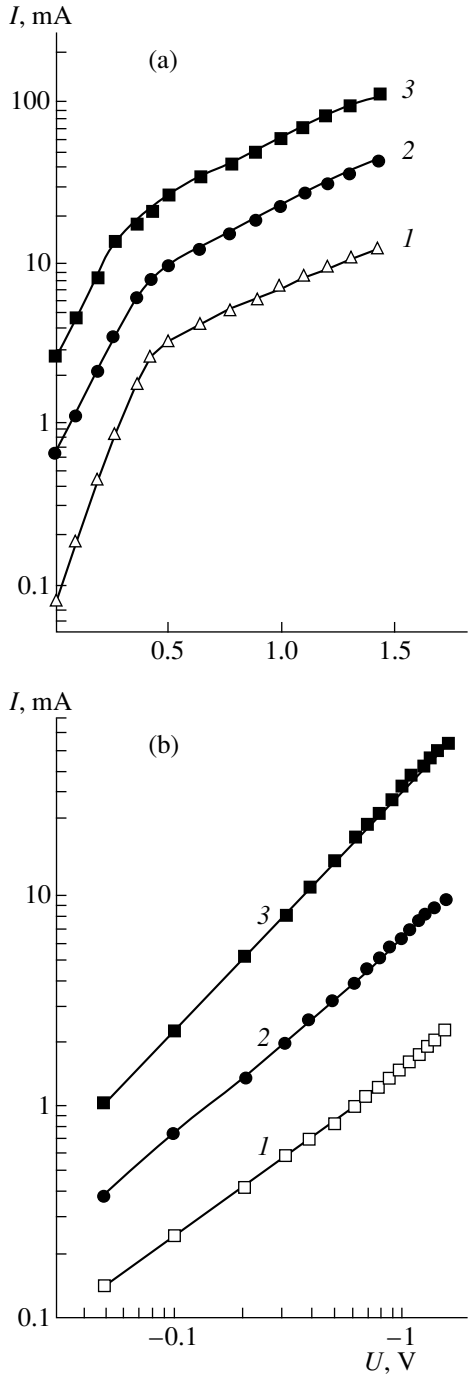

Fig. 4. Forward (a) and reverse (b) *I–V* characteristics of anisotype *n*-Si/*p*-GaN:O heterojunction at different temperatures *T*: (*1*) 200, (*2*) 250, and (*3*) 300 K.

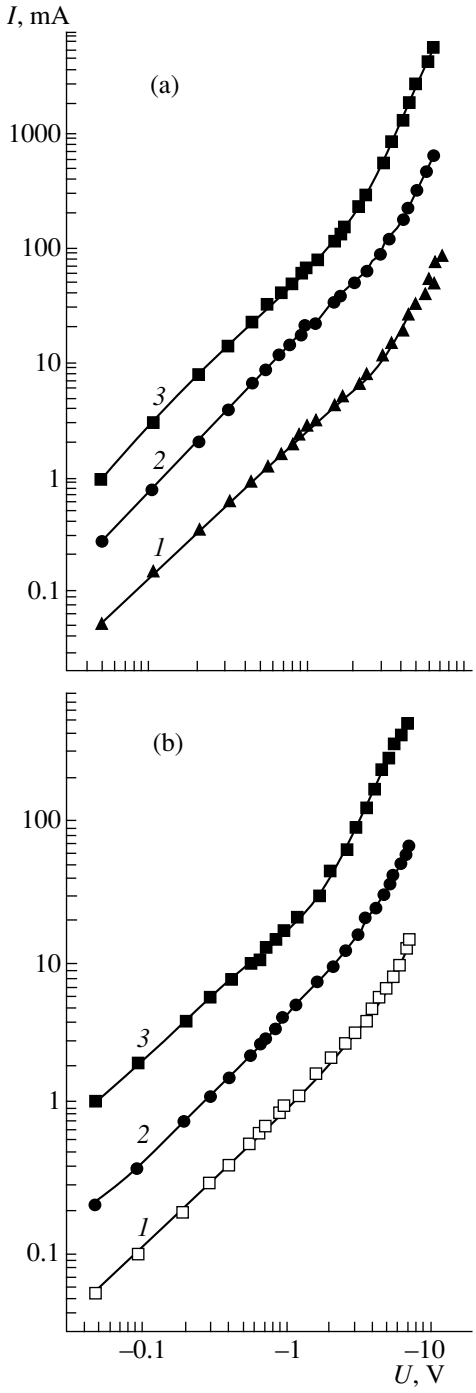

Fig. 5. Forward (a) and reverse (b) *I–V* characteristics of isotype *p*-Si/*p*-GaN:O heterojunction at different temperatures *T*: (*1*) 150, (*2*) 250, and (*3*) 300 K.

quently, the surface states change the space charge regions (SCRs) in gallium oxynitride and silicon, forming depletion layers on both sides of the interface. The presence of surface states is also evidenced by the coefficient $\beta \approx 2$ in the forward *I–V* characteristic of the anisotype HJ, $I \propto \exp(eU/\beta kT)$, pointing to the participation of recombination processes at the interface in the charge transport [2]. In anisotype HJs, surface states redistribute the diffusion potentials between the components, resulting in higher V_{D2} values in the heavily doped oxynitride. (Without taking into account the surface states, the values of V_{D2} would be expected to be much lower than those observed in the experiment for the existing carrier concentrations in GaN:O.)

Let us consider the obtained results taking into account the effect of surface states at the HJ interface. An especially profound effect is exerted on the photoresponse kinetics and photosensitivity of the heterojunction.

Describing the photoresponse of an anisotype HJ, we noted its differential form. The nonmonotic run of photoresponse curves has been observed previously in studying the photoresponse kinetics of anisotype *n*-Si/*p*-PbS [3], isotype *n*-CdS/*n*-CdSe [4], and other HJs [5–7]. Despite the qualitative similarity of the results, such a behavior may have a different origin. In [3], the differential type of the photoresponse kinetics was related to the presence of an insulating layer at the interface between the HJ components. In [8], it was demonstrated theoretically that a nonmonotonic photoresponse kinetics is likely to occur if a certain relation exists between parameters of semiconducting materials and capacitance of the depletion regions at the HJ interface, with such a situation possible both in ideal and nonideal HJs. The model proposed in [5–7] explains the nonmonotonic behavior with the occurrence of two competing processes. The first of these is associated with the separation of nonequilibrium carriers in the electric field of the near-interface barrier and leads to a rise in photoresponse amplitude. The second is related to the recharging of the surface states. The decrease in photoresponse is explained by the capture of nonequilibrium carriers by surface states and their subsequent recombination. The changing sign of the photoresponse on switching off the light is attributed to a loss of charge from surface states, with the barrier height decreasing. In [4], the differential behavior of the photoresponse of an isotype *n*-CdS/*n*-CdSe HJ was related to the surface states and a conclusion was made that illumination causes the height of the equilibrium barrier (formed through capture of carriers by surface states) to decrease, rather than increase as in [5–7]. This is due to the accumulation of photogenerated holes in the near-interface potential well and their recombination with electrons in surface states. The recombination and a decrease in the barrier height result in an increased carrier flux to surface states, and the photoresponse signal decreases. After the illumination is switched off, the barrier height is restored to the equilibrium value via capture of electrons from the bulk by surface states.

Analyzing the photoresponse kinetics for the HJs under study, we come to a conclusion that the photosensitivity mechanisms in isotype and anisotype Si/GaN:O HJs are different (despite the fact that the SCRs in both types of HJ are determined by surface states). In isotype HJs the photosensitivity mechanism is associated with two competing processes: carrier separation in the near-interface field, resulting in higher photocurrent, and recharging of the surface states, leading to a decrease in photocurrent. Since in illumination through the wide-gap material (GaN:O) nonequilibrium carriers are generated in Si near the interface, there is a high probability that photogenerated electrons will be captured by surface state and then recombine with holes. The carrier separation efficiency grows when the internal accelerating field becomes stronger, which occurs with increasing reverse bias. In this case, capture of carriers and their recombination via surface states decrease with the result that the photoresponse increases and its time dependence is smoothed, retaining its maximum value during the entire light pulse. However, an increase in the bias causes the photoresponse signal to become only several times larger.

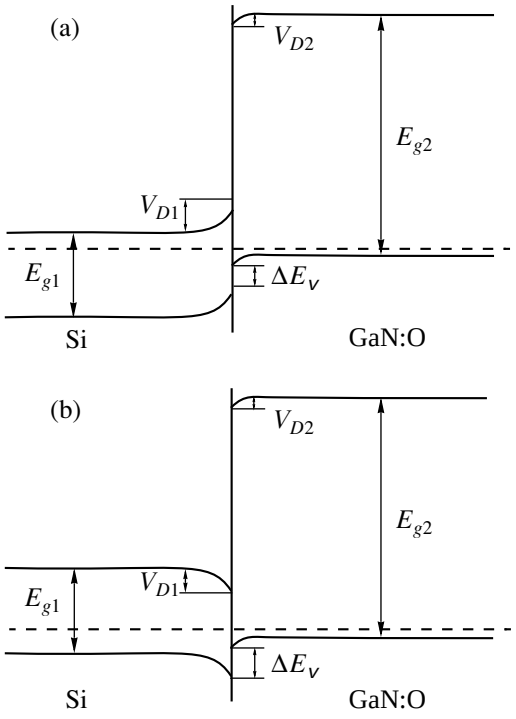

Fig. 6. Energy band diagrams: (a) anisotype *n*-Si/*p*-GaN:O and (b) isotype *p*-Si/*p*-GaN:O HJs.

In isotype HJs, as also in anisotype heterojunctions, the kinetics of photoresponse relaxation has a differential form. However, the kinetics of the isotype HJ shows some specific features. First, the photoresponse at zero bias is very weak. A bias, positive or negative, applied to the HJ results in stronger photoresponse. Second, the photoresponse of a forward-biased HJ has a sign opposite to that for zero and reverse biases. Third, a bias applied to the HJ raises the photocurrent by several orders of magnitude. It should be noted that the different signs of the photoresponse under forward and reverse biases and its increase in intensity in both cases can serve as an additional argument in favor of the conclusion that we are dealing with an isotype HJ having depletion regions on both sides of the heterointerface.

The strong rise in photoresponse on applying a bias cannot be attributed only to the efficiency of photocarrier separation by accelerating near-interface field. The observed rise in photoresponse of a HJ with high den-

sity of surface states under both bias polarities may be due to a phototransistor effect. On illuminating a HJ, nonequilibrium carriers (electrons) generated in the narrow-gap semiconductor are directed into the well by the near-interface field. The accumulation of minority carriers at the interface and their recombination with the charge in the surface states reduce the height of the potential barrier. This, in turn, leads to an increasing flow of majority carriers across the interface. Thus, the change in the current flowing through the HJ may exceed manyfold the flow of photocarriers generated directly by the incident light. Such an increase in photosensitivity owing to the modulation of the through current has been observed in *n*-CdS/*n*-CdSe [4] and *n*-Ge/*n*-Si [9] structures. Another specific feature of the photoresponse curves of isotype HJs is to be noted: the photoresponse signal has different signs under forward and reverse biases. This can be explained by the different flow directions of the majority carriers in these two cases. As a result, the photoresponse sign reversal can be observed on applying biases of different polarities. Thus, the fact that the photosensitivity of isotype HJs is governed by the mechanism of through current modulation makes it possible to obtain strong photoresponse signals in structures with high density of surface states.

REFERENCES

1. S. E. Aleksandrov, T. A. Gavrikova, and V. A. Zykov, Fiz. Tekh. Poluprovodn. (St. Petersburg) **34**, 297 (2000) [Semiconductors **34**, 291 (2000)].
2. A. G. Milnes and D. L. Feucht, *Heterojunctions and Metal-Semiconductor Junctions* (Academic, New York, 1972; Mir, Moscow, 1975).
3. L. G. Bakueva, V. I. Il'in, S. F. Musikhin, *et al.*, Fiz. Tekh. Poluprovodn. (Leningrad) **16**, 1416 (1982) [Sov. Phys. Semicond. **16**, 907 (1982)].
4. M. G. Ermakov, V. I. Polyakov, P. I. Perov, and M. I. Elinson, Fiz. Tekh. Poluprovodn. (Leningrad) **18**, 115 (1984) [Sov. Phys. Semicond. **18**, 69 (1984)].
5. S. C. Dehlberg and W. Orr, Surf. Sci. **67**, 226 (1977).
6. S. C. Dehlberg, J. R. Chelikowsky, and W. Orr, Phys. Rev. B **15**, 3163 (1977).
7. A. J. Steckl, H. Elabd, K. Y. Tam, *et al.*, IEEE Trans. Electron Devices **ED-27**, 126 (1980).
8. A. Ya. Shik, Fiz. Tekh. Poluprovodn. (Leningrad) **16**, 1411 (1982) [Sov. Phys. Semicond. **16**, 904 (1982)].
9. S. Yawata and R. L. Anderson, Phys. Status Solidi **12**, 297 (1965).

Translated by M. Tagirdzhanov

Semiconductors, Vol. 34, No. 11, 2000, pp. 1301–1304. Translated from Fizika i Tekhnika Poluprovodnikov, Vol. 34, No. 11, 2000, pp. 1353–1356.

SEMICONDUCTOR STRUCTURES, INTERFACES, AND SURFACES

Nanorelief of a GaN Surface: the Effect of Sulfide Treatment

V. N. Bessolov*, Yu. V. Zhilyaev*, E. E. Zavarin*, M. E. Kompan*, E. V. Konenkova*, A. S. Usikov*, and V. A. Fedirko**

** Ioffe Physicotechnical Institute, Russian Academy of Sciences, Politekhnicheskaya ul. 26, St. Petersburg, 194021 Russia*

*** Stankin Moscow State University of Technology, Moscow, 101472 Russia*

Submitted April 26, 2000; accepted for publication April 28, 2000

Abstract—Atomic-force microscopy and photoluminescence were used for studying the nanorelief of a (0001)GaN surface treated in sodium-sulfide solutions. The small-scale surface relief of the layer was shown to be largely smoothed after the sulfide treatment. © *2000 MAIK "Nauka/Interperiodica".*

In recent years, the investigations of the properties of gallium-nitride surfaces and of ways to modify their electronic structure have acquired a special importance in the development of electronics (surface-emitting lasers, ultraviolet photodetectors, etc.) [1]. As is known, gallium-nitride single crystals are chemically inert with respect to the majority of etchants used for III–V semiconductors [2]. Recently, it was found that alkaline etchants based on NaOH and KOH can be used successfully in the chemical treatment of a GaN surface [3, 4]. However, low etch rates and a strong anisotropy of the crystal result, as a rule, in the emergence of roughness on the gallium-nitride surface [5].

Currently, the technology of III–V semiconductors (GaAs, InP, InAs, etc.) includes the chalcogenide passivation of a surface using solutions. For example, this method of treatment made it possible to substantially reduce the density of the GaAs surface states and, as a result, to enhance the performance of transistors, lasers, and a number of other devices [6].

Attempts are undertaken to use this technology for modifying the electronic structure of a GaN surface as well. The treatment of the *n*-GaN surface in $(NH_4)_2S$ solutions has already made it possible to increase the photoluminescence (PL) intensity [7], to reduce the resistance of nonrectifying contact to *p*-GaN [8, 9], and to reduce the height of the near-surface barrier in GaN [10].

The purpose of this study is to clarify the feasibility of using the sulfide solutions for smoothing the nanorelief of the (0001)GaN surface.

GaN layers, 2 mm thick with an electron concentration $n = 10^{17}$ cm^{-3}, were grown by gaseous-phase epitaxy from organometallic compounds on sapphire substrates with the (0001) orientation [11].

The chemical treatment of the GaN surface was achieved by the immersion of a layer for 1 min in a boiling water solution of sodium sulfide ($Na_2S : 9H_2O$) with simultaneous illumination with a 200-W incandescent lamp.

The PL was excited by a pulsed nitrogen laser (emission wavelength $\lambda = 337$ nm) similar to [12] and measured at room temperature. The PL was excited and detected through the sapphire substrate (Fig. 1).

The surface of the layers grown has both a large-scale roughness associated with the sapphire-substrate relief and a nanoscale irregularity associated with the interaction of gallium atoms with oxygen and carbon. Atomic-force microscopy (AFM) under atmospheric conditions was used for investigating the nanometer-scale fluctuations of the relief in the area of $\sim 200 \times 200$ nm^2, a linear size of the scanned area amounting to approximately a half-wavelength of the PL emission.

The experimental results are as follows.

At a temperature $T = 300$ K, we observed two emission bands in the PL spectrum of the *n*-GaN layers with energies $h\nu_1 = 3.4$ eV and $h\nu_2 = 2.8$ eV and half-widths of 0.05 and 0.25 eV, respectively (Fig. 2a). As has been shown in previous studies, the low-energy band ($h\nu_2$) corresponds to the donor–acceptor recombination, while the band with the peak at $h\nu_1$ belongs to the so-called edge luminescence (see, for example, [13]).

Unexpected results were obtained in the measurements of the luminescence passing through a sapphire substrate. For this variant of detection, it turns out that the chemical treatment of the GaN surface in sulfide solutions leads to a marked, almost double, increase in the intensity of the donor–acceptor-recombination band (Fig. 2b). The intensity of the edge-luminescence band remains virtually unchanged. The detection of the spectra from the free-surface side revealed no such effect.

The comparison between the treated and untreated small areas of the GaN surface (200×200 nm^2) by means of AFM showed that the chemical treatment results in decreasing both the amplitude of the

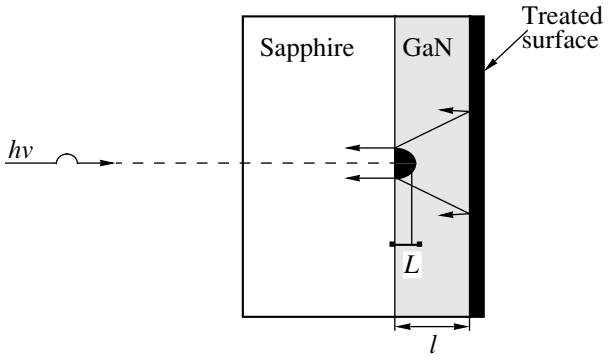

Fig. 1. Schematic representation of a GaN/sapphire structure under PL conditions.

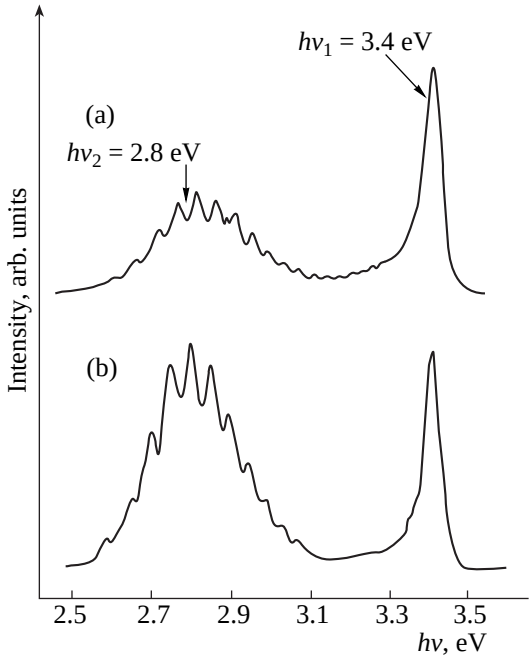

Fig. 2. PL spectra from the GaN layer (a) untreated and (b) treated in a Na_2S water solution.

GaN-surface roughness (by the factor of 3) and the size of fluctuations in the surface roughness (by a factor of 5).

As is known, GaN interacts with KOH and NaOH solutions according to the reaction

$$GaN + OH^- + 3H_2O \longrightarrow Ga(OH)_4^- + NH_3 \qquad (1)$$

with subsequent dissolution of gallium hydroxide in water. However, this process does not result in the chemical polishing of the GaN surface because the rate of the hydroxide formation is higher than the rate of its removal, and the oxides are removed only slightly [5]. When using sodium-sulfide water solutions, the interaction between GaN and HS^- ions proceeds according to the reaction

$$2GaN + 3HS^- + 5H_2O \longrightarrow Ga_2S_3 + 2NH_3 + 5OH^- + H_2. \qquad (2)$$

In this case, as with the chalcogenide passivation of III–V semiconductors [6], the removal of oxides from the GaN surface and the formation of a sulfur-containing layer must take place. In fact, when the GaN surface is treated in $(NH_4)_2S$ solutions, the amount of oxides on the surface decreases [10]. Since the GaN etching according to reaction (2) must occur with a substantially higher rate than that for reaction (1), the GaN-surface sulfidizing must result in more efficient polishing.

Based on the above concept of chemical modification of a gallium-nitride surface by sulfide solutions, we may assume that a change in the ratio between intensities of the bands is caused by a change in the free-surface state of these samples during their treatment.

In fact, when the GaN layer with a thickness l = 2 μm is illuminated from the sapphire-substrate side, the absorption of the light occurs at a distance L_0 = 0.05 μm [14] from the sapphire–GaN interface. In this case, the diffusion length for the minority charge carriers amounts to $L_* = 0.2 \pm 0.05$ μm [15]. Because the thickness of the photoactive region $L = L_0 + L_* \approx$ 0.3 μm remains significantly less than l, the emission associated with the interband recombination emerges partially through the sapphire window and is partially absorbed in the GaN layer bulk without reaching the surface. The emission associated with the donor–acceptor recombination also emerges partially through the sapphire window; however, it partially reaches the surface of the GaN layer and, virtually without absorption, reflects from this surface, emerging through the sapphire window only after this. A change in the relief of the GaN surface affects only the photons that emerge through the sapphire window and are associated with the donor–acceptor recombination. The modulation of the donor–acceptor recombination band (periodic peaks) (Figs. 2a, 2b) caused by the interference of the emission in the GaN layer confirms unambiguously that the light reflected by the GaN-layer surface actually reaches the substrate and emerges through it.

We detect experimentally an intensity of the PL component that emerges through the sapphire window and is associated with the donor–acceptor recombination. After the chemical treatment, it is the GaN surface region that is modified to an insignificant depth (of the order of nanometers), and, in this case, the intensity in the donor–acceptor-recombination band increases. Under these conditions, it is reasonable to relate the effect observed to a change in the coefficient of reflection of the donor–acceptor emission from the layer free

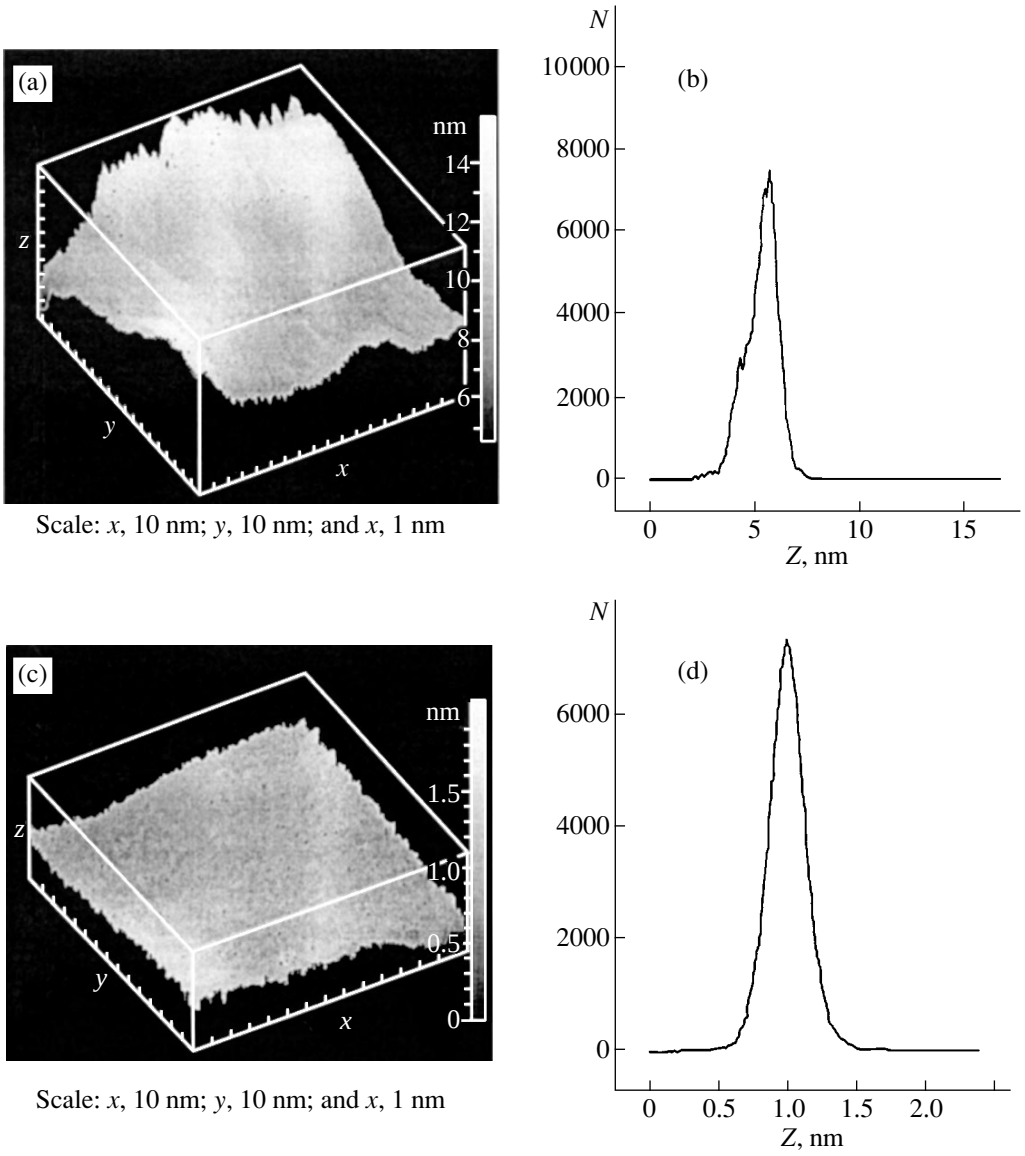

Fig. 3. (a, c) Surface profile and (b, d) the magnitude of the fluctuation of the surface inhomogeneities for GaN (a, b) untreated and (c, d) treated in a Na_2S water solution. *N* is the number of points with the given height *Z* of the relief.

surface. Since the intensity of the edge-luminescence band remains unchanged, the ratio between the intensities of the donor–acceptor recombination and the edge recombination changes towards the increase of the former (Fig. 2b).

Certain details of the spectra observed remain unexplained. In particular, it is not quite clear why the depth of the interference modulation of the donor–acceptor band does not change with increasing reflected-light intensity. A qualitative explanation for this fact can be found by assuming that the interference contrast is determined by the phase loss of the light wave when it passes through an inhomogeneous medium (the GaN layer). However, the data available are insufficient for the qualitative justification of such an assumption.

It may appear that a change in the nanometer-scale surface relief should not influence the passage of the light. Indeed, since a PL wavelength amounts to 0.5 μm, and so the light waves cannot be reflected and refracted by nanometer inhomogeneities of the surface. In this case, the light wave propagates as if in a continuum, and the parameters of individual inhomogeneities influence only the averaged parameters of the medium in which the wave propagates. However, when the light passes through the sample surface (the media interface), the presence of the nanorelief on the surface means that there is a transition layer with the refractive index changing from a value characteristic for the crystal to unity. Thereby, the developed surface relief in the nanometer scale is a natural antireflection layer for the emerging PL emission. The treatment of the surface

leading to smoothing the relief on this scale and, thereby, to improving the quality of the surface, at the same time, removes an oxidized near-surface layer and forms a sulfidized layer that results in changing the refractive index and in increasing the intensity of the light reflected from this near-surface layer.

The comparison and analysis of the AFM-images of surface areas, both untreated and treated in a sulfide solution, show that the chemical treatment leads to an appreciable decrease in the amplitude of nanoscale fluctuations of the relief over an area of 200×200 nm^2 difference between the peaks and valleys in the relief decreases approximately by a factor of 3 (Figs. 3a, 3c), while the rms value of the relief fluctuation decreased almost by the factor of 5 (Figs. 3b, 3d). As the analysis of the AFM-images of the surface and the results of the PL investigation show, the treatment in the sulphur-containing solutions leads to an appreciable decrease in the nanoscale fluctuations of the GaN surface layer.

Thus, the following results were obtained in this study:

We discovered the effect of reducing the inhomogeneities of a GaN surface when using the sulphur-containing solutions.

We assumed that the change in the nanorelief of the GaN surface can occur owing to the removal of the oxidized layer and the formation of a sulfidized layer at a higher rate of reaction.

ACKNOWLEDGMENTS

This study was supported in part by the program "Surface atomic structures" (project no. 5-4-99) and by the Russian Foundation for Basic Research (project no. 00-02-16989).

REFERENCES

1. M. S. Shur and M. A. Khan, in *Semiconductors and Semimetals* (Academic, New York, 1999), Vol. 57, Chap. 10, p. 407.
2. *Gmelin Handbook of Inorganic and Organometallic Chemistry*, Ed. by H. Katscher and B. Mohsin (Springer-Verlag, Berlin, 1996), Suppl. Vol. C2, p. 181.
3. M. S. Minsky, M. White, and E. L. Hu, Appl. Phys. Lett. **68**, 1531 (1996).
4. N. V. Edwards, M. D. Bremser, T. W. Weeks, Jr., *et al.*, Appl. Phys. Lett. **69**, 2065 (1996).
5. J. L. Weyher, S. Muller, I. Grzegory, and S. Porowski, J. Cryst. Growth **182**, 17 (1997).
6. V. N. Bessolov and M. V. Lebedev, Fiz. Tekh. Poluprovodn. (St. Petersburg) **32**, 1281 (1998) [Semiconductors **32**, 1141 (1998)].
7. Yu. V. Zhilyaev, M. E. Kompan, E. V. Konenkova, and S. D. Raevskiĭ, MRS Internet J. Nitride Semicond. Res. 4S1, G6.14 (1998).
8. J. K. Kim, J. L. Lee, J. W. Lee, *et al.*, J. Vac. Sci. Technol. B **17** (2), 497 (1999).
9. J. S. Jang, S.-J. Park, and I. Y. Seong, J. Vac. Sci. Technol. B **17** (6), 2667 (1999).
10. X. A. Cao, S. J. Pearton, G. Dang, *et al.*, Appl. Phys. Lett. **75** (26), 4130 (1999).
11. W. V. Lundin, A. S. Usikov, B. V. Pushnyi, *et al.*, Mater. Sci. Forum **264**, 1125 (1998).
12. M. E. Kompan and I. Yu. Shabanov, Fiz. Tverd. Tela (St. Petersburg) **39** (7), 1030 (1997) [Phys. Solid State **39**, 1030 (1997)].
13. S. Strie and H. Morkoc, J. Vac. Sci. Technol. B **10** (4), 1237 (1992).
14. N. Dyakonova, A. Dickons, M. S. Shur, *et al.*, Appl. Phys. Lett. **72**, 2562 (1998).
15. Z. Z. Bandic, P. M. Bridger, E. C. Piquette, and T. C. McGill, Appl. Phys. Lett. **73** (22), 3276 (1998).

Translated by V. Bukhanov

Semiconductors, Vol. 34, No. 11, 2000, pp. 1305–1310. Translated from Fizika i Tekhnika Poluprovodnikov, Vol. 34, No. 11, 2000, pp. 1357–1362.

SEMICONDUCTOR STRUCTURES, INTERFACES, AND SURFACES

The Dislocation Origin and Model of Excess Tunnel Current in GaP *p–n* Structures

V. V. Evstropov*, M. Dzhumaeva, Yu. V. Zhilyaev*, N. Nazarov**, A. A. Sitnikova*, and L. M. Fedorov***

** Ioffe Physicotechnical Institute, Russian Academy of Sciences, Politekhnicheskaya ul. 26, St. Petersburg, 194021 Russia*

*** Physicotechnical Institute, Academy of Sciences of Turkmenistan, Ashkhabad, 744000 Turkmenistan*

Submitted April 26, 2000; accepted for publication April 28, 2000

Abstract—An excess tunnel current in GaP epitaxial nondegenerate *p–n* junctions on GaP and Si substrates was studied. An important experimental result is that the slope of exponential current–voltage (*I–V*) characteristic (in ln*I–V* coordinates) is independent of the width of the space-charge region, i.e., on *n*- and *p*-region doping levels. This fact is unexplained by existing models. A dislocation shunt model based on multihop tunneling through a dislocation line, which may be considered as a chain of parabolic potential barriers, is proposed. The density of dislocations predicted by this model is in agreement with the transmission electron microscopy (TEM) observations. © *2000 MAIK "Nauka/Interperiodica".*

1. INTRODUCTION

A topical problem of micro- and optoelectronics is the determination of dislocation density in homo- and heterostructures (*p–n* junctions and metal–semiconductor junctions), which considerably affects both the operating parameters and the stability of semiconductor devices. Specifically, dislocations are known to cause the so-called excess tunneling component of the forward current in tunnel diodes [1], i.e., in degenerate *p–n* junctions. The tunneling component of forward current was observed also in nondegenerate heterojunctions [2–4] and homojunctions [4], where it can also be considered as excess tunneling component. Numerous experiments have shown that this component arises as a result of intentional introduction of defects: electron radiation [1, 5, 6], neutron radiation [7], high doping [5, 6], and a mismatch in the heterocombination lattices [2, 3, 8] are some examples. In accordance with the existing models [3, 5, 9], the defects induced in a space-charge region, produce levels within the band gap, thus considerably facilitating the tunneling.

It is believed that dislocations threading through the space-charge region are the defects that promote the tunneling and cause the excess tunnel current. Actually, a dislocation is a linear extended defect that can provide a series of localized states spaced at a characteristic tunneling length (~1 nm). For a similar result, the concentration of randomly distributed point defects should be as high as 10^{21} cm^{-3}, which is sufficient for giving rise to an excess tunnel current even in lightly doped and noncompensated semiconductor structures.

In this paper, we use GaP *p–n* junctions to demonstrate that an excess tunnel current can be attributed to dislocations. A model of tunneling through a space-charge region (SCR) along a dislocation line (tube) is suggested.

First, we compare the values of excess tunnel current in epitaxial GaP *p–n* structures that were grown on GaP substrate and foreign Si substrate, owing to which they had appreciably different dislocation density (a foreign substrate is known to cause an increase in the dislocation density in the epilayer).

Second, we used the current–voltage characteristics to determine the dislocation density in an active region of GaP *p–n* junction assuming that the excess tunnel current is governed by dislocations that thread through the SCR and compared the result with the transmission electron microscopy (TEM) observations.

2. EXPERIMENTAL

Two types of *p–n* structures, on Si and GaP substrates, were grown by the same procedure, with the aim of assessing the effect of additional defects resulting from replacement of GaP substrate with an extraneous one.

The epitaxial GaP *p–n* junctions on *n*-Si substrate were produced by gaseous epitaxy in a chloride system Ga(GaP)–PCl_3–H_2 [10, 11] and had *n*- and *p*-regions of 3–4 and 2–3 μm thick, respectively.

The epitaxial *p–n* junctions on *n*-GaP substrate were produced simultaneously with *p–n*-GaP/*n*-Si structures (by the same procedure) and had the same thickness of epitaxial *n*- and *p*-regions. The equilibrium majority-carrier densities in *n*- and *p*-GaP regions were 10^{17} cm^{-3} and (3–5) × 10^{16} cm^{-3}, respectively. Polished *n*-Si waters (*n*-Si:P, ρ = 0.001 Ω cm) oriented in (100) plane with a disorientation of 4°–6° in [110] direction and polished *n*-GaP waters oriented in (100) plane with a

1063-7826/00/3411-1305$20.00 © 2000 MAIK "Nauka/Interperiodica"

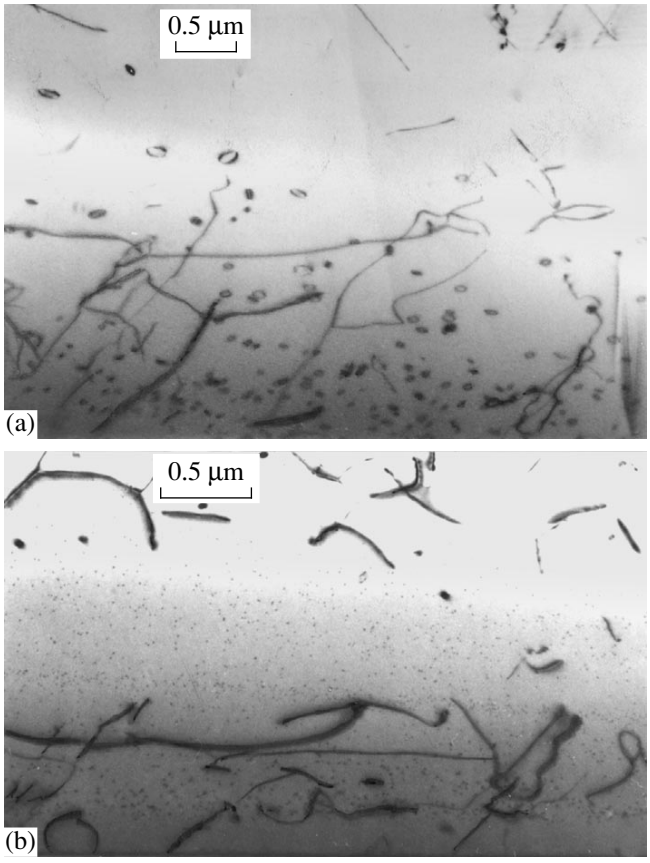

Fig. 1. The TEM images of cross sections of (a) *p*–*n*-GaP/*n*-Si and (b) *p*–*n*-GaP/*n*-GaP structures.

disorientation of 4° in [110] direction were used for substrates. The equilibrium majority-carrier density in *n*-GaP waters was (5–8) × 10^{17} cm^{-3}. The junction areas for the studied *p*–*n*-GaP/*n*-Si and *p*–*n*-GaP/*n*-GaP structures were 1–3 mm^2.

To form nonrectifying contacts, In + 2.5%Zn was alloyed into *p*-GaP epitaxial layer and In + 2.5%Te, into the *n*-Si and *n*-GaP substrates; the alloying temperature was 600–650°C in all the cases.

3. TRANSMISSION ELECTRON MICROSCOPY (TEM)

Density of dislocations affecting the current through the barrier structures was determined by transmission electron microscopy. The samples were prepared conventionally, with the use of ion etching.

The images of cross sections of *p*–*n*-GaP/*n*-Si and *p*–*n*-GaP/*n*-GaP samples are shown in Fig. 1. The GaP *p*-region is in the upper panel and the *n*-region is in the lower panel; i.e., the barrier is horizontal. Both regions contain plenty of defects (various dislocations, dislocation loops, precipitates, etc.). However, the statistical processing of the data yields the linear density of dislocations crossing *p*–*n* junction at angles close to 90° as 1.2 × 10^4 cm^{-1} for *p*–*n*-GaP/*n*-Si and 10^3 cm^{-1} for *p*–*n*-GaP/*n*-GaP (counted per unit boundary length). These values correspond to dislocation densities in the plane of junction $\rho \approx 10^8$ and 10^6 cm^{-2}.

4. DISLOCATION TUNNEL SHUNTING: MAIN CONSEQUENCES OF THE MODEL

According to the model of dislocation tunnel shunting [4], the modulus of direct tunnel current and the dependences of current I on voltage V and temperature T can be expressed as

$$I = I_0(\exp eV/\varepsilon - 1), \tag{1}$$

$$I_0 = e\rho\nu_D \exp(-eV_c/\varepsilon), \tag{2}$$

$$eV_c = E_g - kT\ln\frac{N_c}{n_n} - kT\ln\frac{N_v}{p_p}, \tag{3}$$

where ε is the characteristic energy, e is the elementary charge, ν_D is the Debye frequency, ρ is the dislocation density, k is the Boltzmann constant, V_c is the contact potential difference between *p*- and *n*-regions, E_g is the band gap linearly depending on temperature in the considered temperature range as

$$E_g = E_g(0) - \alpha T \tag{4}$$

(for GaP, $E_g(0)$ = 2.35 eV and α = 3.2 meV/K); N_c and N_v are effective densities of states in the conduction and valence band, respectively (for GaP at 293 K, $N_c = N_v = 8 \times 10^{18}$ cm^{-3}); and n_n and p_p are the free electron and hole densities in *n*- and *p*-regions, respectively (in the studied case, n_n = (1–3) × 10^{17} cm^{-3} and p_p = (2–5) × 10^{17} cm^{-3} for *p*–*n*-GaP/*n*-Si; n_n = (1–3) × 10^{17} cm^{-3} and p_p = (1–2) × 10^{18} cm^{-3} for *p*–*n*-GaP/*n*-GaP).

As follows from (3) and (4), the contact potential difference V_c decreases linearly with increasing temperature, and the proportionality factor β can be written as

$$e\beta = \alpha + k\ln\frac{N_c}{n_n} + k\ln\frac{N_v}{p_p}. \tag{5}$$

As follows from (2)–(4), $\ln I_0$ increases linearly with increasing temperature, and the proportionality factor can be expressed as

$$a = e\beta/\varepsilon. \tag{6}$$

It may be noted that the dependences of excess tunnel current on voltage and temperature reflects its tunnel origin and is well-known [2]. A new aspect provided by the model [4] is the expression for the preexponential factor, which is rather simple and has a clear physical meaning.

Using the model [4], and knowing ε and I_0 from experimental current–voltage characteristic as well as

knowing V_c, we can determine the dislocation density from (2) as

$$\rho = \frac{I_0}{e\nu_D}\left(\frac{n_n p_p}{N_c N_v}\right)^{kT/\varepsilon} \exp\frac{E_g}{\varepsilon}. \quad (7)$$

Using the values of $I_0(0)$ and $\varepsilon(0)$ obtained by extrapolating the dependences $I_0(T)$ and $\varepsilon(T)$ to zero temperature, we obtain

$$\rho = \frac{I_0(0)}{e\nu_D}\exp\frac{E_g(0)}{\varepsilon(0)}. \quad (8)$$

5. CURRENT–VOLTAGE (*I–V*) AND CAPACITANCE–VOLTAGE (*C–V*) CHARACTERISTICS

The forward current–voltage (*I–V*) characteristics for GaP *p–n* junction on Si substrate at different temperatures are shown in Figs. 2 and 3. First of all it may be noted that, from near-room temperature and above, the portions of current–voltage characteristic can be approximated by the exponential function (1). The higher is the temperature, the more valid is the exponential approximation. At lower temperatures, the *I–V* curve becomes hump-shaped. Close to the liquid-nitrogen temperature, the humps are already pronounced; this is the reason that we did not use the exponential approximation in this region.

Referring to Fig. 2, the current in the *p–n* junctions on Si substrate is larger than that in the structures on GaP substrate, and the same is true for I_0. The slopes of ε curves are nearly equal, suggesting a similar origin of the current component in both cases.

It has been found experimentally that ε is almost independent of temperature (Fig. 4b). The preexponential factor I_0 exhibits an exponential temperature dependence (see Fig. 4a):

$$I_0 \propto \exp aT, \quad (9)$$

where the experimental value of a is consistent with that obtained from (5) and (6) with the use of the experimental values of ε.

Temperature independence of ε and exponential temperature dependence of I_0 point to the tunneling origin of the current, unlike thermal-injection current in GaP junctions observed in [12] and similar to excess tunnel current observed in [13]. In the latter case, however, the excess tunnel component was not initially present but arose and increased as a result of current degradation. The fact that I_0 is larger in the junctions on foreign Si substrates having higher dislocation densities points to the possible dislocation origin of the excess tunnel current. The *I–V* curve humpy structure, especially pronounced at low temperatures, is indicative of the crowding of levels in the band gap; hence, it does not contradict but even supports the model based on dislocation tunnel shunting.

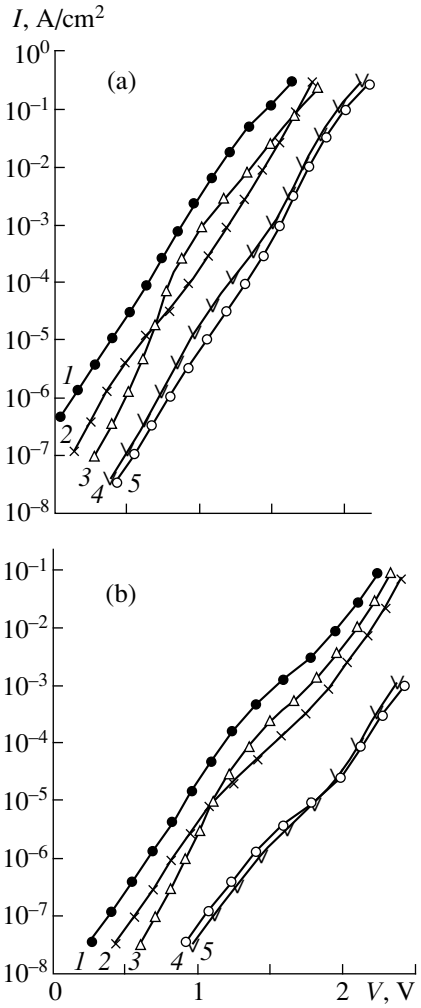

Fig. 2. The forward current–voltage characteristics of GaP junctions on (*1–3*) Si and (*4*, *5*) GaP substrates at T = (a) 300 and (b) 77 K.

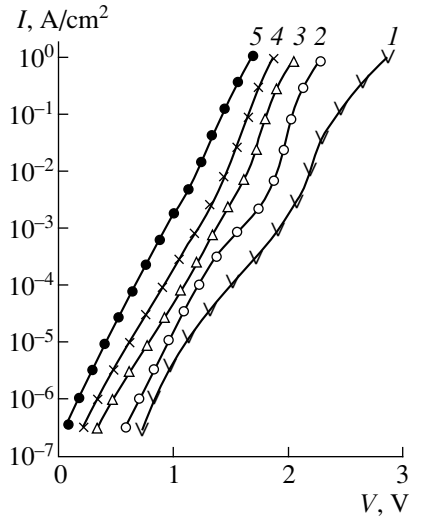

Fig. 3. The forward current–voltage characteristics of GaP junction on Si substrate at T = (*1*) 80, (*2*) 140, (*3*) 210, (*4*) 293, and (*5*) 373 K.

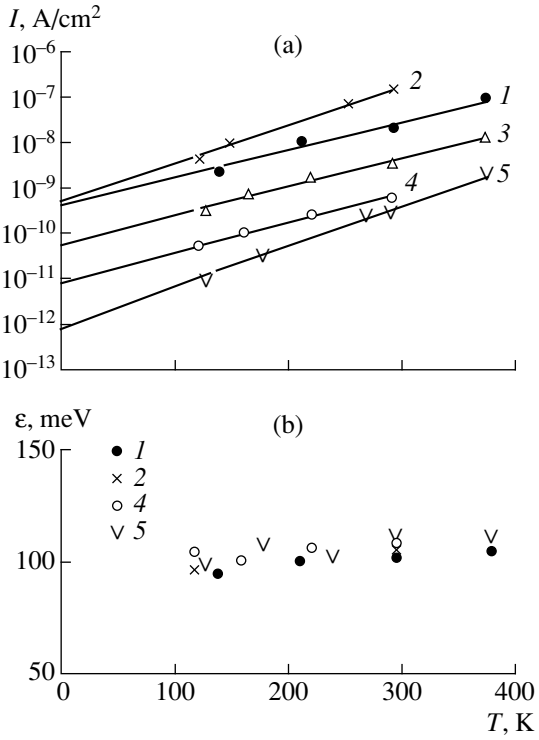

Fig. 4. Temperature dependences of (a) pre-exponential factor I_0 and (b) characteristic energy ε in GaP junctions on (*1–3*) Si and (*4*, *5*) GaP substrates.

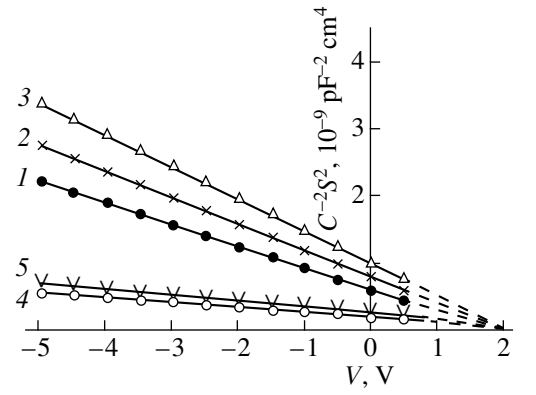

Fig. 5. Voltage (*V*) dependences of the inverse squared capacitance (C^{-2}) in GaP junctions on (*1–3*) Si and (*4*, *5*) GaP substrates for N_{eff} = (*3*) 2.5×10^{16} and (*4*, *5*) 1.7×10^{17} cm^{-3}.

Taking into account the linear dependence of reciprocal square capacitance (C^{-2}) on voltage (V) makes it possible to obtain the effective density

$$N_{\text{eff}} \approx \frac{n_n p_p}{(n_n + p_p)}.$$

We note that the effective charge-carrier density in *p–n* junctions on Si substrates is 3–5 times lower than that in the junctions on GaP substrates (Fig. 5).

6. DISCUSSION

The whole body of experimental data presented in this paper indicates an excess-tunnel character of the forward current. The following facts support its dislocation origin: First, at equal voltages, the current through the Si-substrate junction exceeds the current through the GaP-substrate junction (see Figs. 2a, 2b). This is due, in particular, to the preexponential factor.

Second, the dislocation density determined using expressions (7) and (8) appears to be of the same order of magnitude as the value obtained from the TEM measurements. For *p–n*-GaP/*n*-Si, it is 5×10^7 cm^{-2} (we take 10^{12} s^{-1} for the Debye frequency in GaP).

Expressions (1)–(4) describe well the dependences of forward current on voltage and temperature and yields a reasonable dislocation density. However, the experiment demonstrated that the original model of dislocation tunnel shunting [4] needs some further correction to describe the concentration dependence of ε more accurately. Specifically, from the capacitance–voltage (*C–V*) characteristics shown in Fig. 5 one can infer that, for the two types of structures under study, the quantities N_{eff} differ by a factor of 3–5. According to the model [4], this yields a 1.5–2 times difference in values of ε, since $\varepsilon \propto 1/W \propto \sqrt{N_{\text{eff}}}$ (where W is the SCR width). However, the experimental values of ε obtained from the current–voltage characteristics (Fig. 4) are nearly equal for both types of structures.

From the above follows that the model [4] needs correction. An attempt to do so is made in the next section. The suggested changes do not affect the procedure used in [4] for calculating the dislocation density from (7) and (8), since the calculation involves only an empirically determined ε.

7. CORRECTED MODEL OF A DISLOCATION SHUNT: MULTIHOP TUNNELING ALONG A DISLOCATION LINE

To explain the independence of ε from $\sqrt{N_{\text{eff}}}$ observed experimentally, we propose a model of multihop tunneling over a dislocation line.

We proceed from treating a dislocation line as a chain of localized centers represented as funnel-shaped potential wells with a set of allowed levels at the edge of each well. Peaks of the interwell barriers are approximated by parabolas. This representation is illustrated in Fig. 6. Each of the barriers can be surmounted as a result of an isoenergetic tunnel hop.

In the symmetrical nondegenerate *p–n* junction (Fig. 6), the most probable scenario of electron and hole motion is the following: they move towards each other making a series of hops up to the center of junction, where annihilation occurs. The highest barrier that limits the carrier motion is in the center of a *p–n* junction, with a height of $E_{b\max} = e(V_c - V)/2$, where V_c is

the contact potential difference (for definiteness, electron hop is considered).

Tunnel hops are initiated by phonons; therefore, the limiting hop rate (probability per unit time) $\nu = \nu_D P$, where ν_D is the Debye frequency and P is the highest barrier transparency.

For a parabolic barrier,

$$P = \exp\left(-\frac{2\pi E_{b\max}}{\hbar\omega}\right), \quad (10)$$

where $\omega = \sqrt{r/m_e^*}$, m_e^* is the effective electron mass and r is the curvature of the peak of the limiting parabolic barrier. The current along a dislocation line is $i = e\nu$; then, the current density is $I = i\rho$, where ρ is the density of dislocations intersecting the space-charge region of the p–n junction. Therefore,

$$I = I_0 \exp\frac{eV}{\varepsilon}. \quad (11)$$

Here, I_0 is given by (2), as before. Using (10), we obtain

$$\varepsilon = \frac{\hbar}{\pi}\sqrt{\frac{r}{m_e^*}}, \quad (12)$$

which differs radically from the well-known [2, 4] expression

$$\varepsilon = \frac{\hbar e}{2}\sqrt{\frac{N_{\text{eff}}}{\xi_0 \xi m_e^*}} \propto \frac{1}{W},$$

where ξ_0 is the permittivity of free space, and ξ is the relative permittivity of semiconductor (GaP, in our case).

In the considered model of multihop tunneling over a dislocation line, ε depends on the phenomenological parameter r (barrier curvature); i.e., ε is actually a characteristic of dislocation type. Experimental quantity $\varepsilon = 105$ meV implies $r = 0.25$ J/m^2 and limiting barrier width (when its height is $E_{b\max} = eV_c/2 = 1.1$ eV, i.e., at zero bias $V = 0$) $d = 2$ nm.

In contrast to many other models dealing with excess tunnel current [2–5], the model of dislocation shunt implies independence of the current–voltage characteristic slope ε from the SCR width W, and consequently, from the effective density N_{eff} defined by n- and p-region doping level. This independence is the essential distinguishing feature of the dislocation-shunt model and can serve as a decisive experimental criterion that governs the model choice. From an experimental point of view, an important advantage of the dislocation-shunt model [4] is the analytical expression for preexponential factor I_0, which is rather simple and has a clear physical meaning.

As compared to some other models, the dislocation-shunt model has a wider field of application that is not restricted to the Schottky-barrier and an abrupt p–n junction, i.e., the structures with a parabolic dependence $W \propto (V_c - V)^{1/2}$, which leads to an exponential current–voltage characteristic. Actually, in the other models, $P \propto e^{-W/\lambda}$, where $\lambda \propto (V_c - V)^{-1/2}$ is the tunnel de Broglie wavelength, and hence, $I \propto P \propto \exp(eV/\varepsilon)$. In contrast, in the dislocation-shunt model, I depends exponentially on V not only for the steplike but for any other distribution of impurities in the p–n junction, because, in this case, the probability P depends on the width of an individual link (barrier) in the chain of parabolic barriers simulating a dislocation line, $P \propto \exp(-d/\lambda)$ rather than on the SCR width W. This width (at the tunneling height) is $d \propto (V_c - V)^{1/2}$, yielding an exponential $I(V)$ dependence for any barrier structure threaded by a dislocation. This is also true, in particular, for a gradient p–n junction (where $W \propto (V_c - V)^{1/3}$) and is well supported by experimental data.

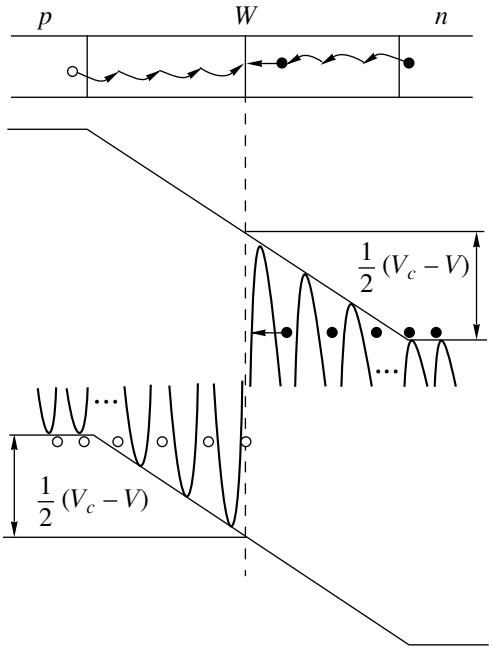

Fig. 6. Dislocation-shunt model (multihop tunneling along dislocation line) for p–n junction. Straight arrow indicates the limiting tunnel hop.

8. CONCLUSION

Exponential forward current–voltage characteristics were studied in GaP p–n junctions grown by chloride gaseous epitaxy on GaP substrates and extraneous Si substrates, thus having essentially different dislocation density.

The typical features of a tunnel current (I_0 temperature dependence is weak and ε is nearly independent of temperature) were observed; i.e., the current is found to be of excess tunneling origin.

Preexponential factor I_0 obtained for the junctions on extraneous Si substrates is found to be considerably (from 1.5 to 2 orders of magnitude) larger than that for

the junctions on GaP substrates, whereas the characteristic energies ε are nearly equal. It may be concluded that the excess tunnel current has a dislocation origin.

The slope (ε) of the current–voltage characteristic plotted in ln*I*–*V* coordinates is independent of the SCR width (i.e., of N_{eff} governed by *n*- and *p*-region doping level). This experimental fact suggests that model [4] should be corrected.

The dislocation-shunt model implying multihop tunneling along a dislocation line that threads the SCR of a *p*–*n* junction is proposed. According to this model, dislocation line is represented as a chain of parabolic potential barriers, which can be surmounted through a series of isoenergetic tunnel hops initiated by phonons. The current through the dislocation line is controlled by the rate of the most improbable (limiting) hop. This is an electron tunnel hop through the highest barrier located in the center of *p*–*n* junction.

The suggested model enables an estimation of the dislocation density in active (space-charge) region of a junction. In structures on Si and GaP substrates, the dislocation density is estimated at 10^7–10^8 and 10^5–10^6 cm^{-2}, respectively.

REFERENCES

1. R. P. Nanavati, *An Introduction to Semiconductor Electronics* (McGraw-Hill, New York, 1963; Svyaz, Moscow, 1965).
2. B. L. Sharma and R. K. Purohit, *Semiconductor Heterojunctions* (Pergamon, Oxford, 1974; Sov. Radio, Moscow, 1979).
3. A. G. Milnes and D. L. Feucht, *Heterojunctions and Metal-Semiconductor Junctions* (Academic, New York, 1972; Mir, Moscow, 1975).
4. V. V. Evstropov, Yu. V. Zhilyaev, M. Dzhumaeva, and N. Nazarov, Fiz. Tekh. Poluprovodn. (St. Petersburg) **31**, 152 (1997) [Semiconductors **31**, 115 (1997)].
5. S. Sze, *Physics of Semiconductor Devices* (Wiley, New York, 1981; Mir, Moscow, 1984).
6. C. T. Sah, in *Tunneling Phenomena in Solids*, Ed. by E. Burstein and S. Lundqvist (Plenum, New York, 1969; Mir, Moscow, 1973).
7. V. V. Evstropov and A. M. Strel'chuk, Fiz. Tekh. Poluprovodn. (St. Petersburg) **30**, 92 (1996) [Semiconductors **30**, 52 (1996)].
8. A. T. Gorelenok, V. G. Gruzdov, V. V. Evstropov, *et al.*, Fiz. Tekh. Poluprovodn. (Leningrad) **18**, 1413 (1984) [Sov. Phys. Semicond. **18**, 885 (1984)].
9. A. G. Chynoweth, W. L. Feldman, and R. A. Logan, Phys. Rev. **121**, 684 (1961).
10. V. V. Evstropov, Yu. V. Zhilyaev, N. Nazarov, *et al.*, Fiz. Tekh. Poluprovodn. (St. Petersburg) **27**, 668 (1993) [Semiconductors **27**, 369 (1993)].
11. V. V. Evstropov, Yu. V. Zhilyaev, N. Nazarov, *et al.*, Zh. Tekh. Fiz. **63** (12), 41 (1993) [Tech. Phys. **38**, 1057 (1993)].
12. V. V. Evstropov, B. N. Kalinin, and B. V. Tsarenkov, Fiz. Tekh. Poluprovodn. (Leningrad) **17**, 599 (1983) [Sov. Phys. Semicond. **17**, 373 (1983)].
13. V. D. Vedenin, V. V. Evstropov, B. N. Kalinin, and B. V. Tsarenkov, Fiz. Tekh. Poluprovodn. (Leningrad) **9**, 1976 (1975) [Sov. Phys. Semicond. **9**, 1294 (1975)].

Translated by A. Sidorova-Biryukova

Semiconductors, Vol. 34, No. 11, 2000, pp. 1311–1315. Translated from Fizika i Tekhnika Poluprovodnikov, Vol. 34, No. 11, 2000, pp. 1363–1367.

LOW-DIMENSIONAL SYSTEMS

Photoresistance of Si/Ge/Si Structures with Germanium Quantum Dots

O. A. Shegaĭ*, K. S. Zhuravlev, V. A. Markov, A. I. Nikiforov, and O. P. Pchelyakov

Institute of Semiconductor Physics, Siberian Division, Russian Academy of Sciences, pr. Akademika Lavrent'eva 13, Akademgorodok, Novosibirsk, 630090 Russia

**e-mail: shegai@thermo.isp.nsc.ru*

Submitted March 27, 2000; accepted for publication April 21, 2000

Abstract—An exponential decrease in the resistance of a Si/Ge/Si structure containing germanium quantum dots with an increase in the band-to-band optical excitation intensity is observed at 4.2 K. Two different exponential regions in the dependence of structure resistance on the optical excitation intensity are observed in elastically strained structures, but only one such region is observed in unstrained structures. The experimental results obtained are explained within the model of the hopping conduction of nonequilibrium electrons, which are localized at and between quantum dots in the strained structures, but are localized only between quantum dots in the unstrained structures. *© 2000 MAIK "Nauka/Interperiodica".*

INTRODUCTION

Studies of self-organizing quantum dots (QDs) have evolved recently into a rapidly developing field of semiconductor physics; this field is important both from the fundamental and applied points of view. A major concept of the method for self-organizing QD formation consists in the growth of a thin layer of one semiconductor with several monolayers in a matrix of another semiconductor with highly mismatched lattice parameters. Owing to the mechanical strains appearing for a definite critical layer thickness, formation of the islands becomes energetically favorable (the Stranski–Krastanov mechanism) [1–8]. The properties of Si/Ge/Si-structures are studied most actively by the methods of electron and atomic-force microscopy [9–13], photoluminescence [10–16], and Raman scattering [4, 5, 10, 17]. The transverse tunneling transport of charge carriers was studied previously [3], and the transport over the QD layers was studied in [8]. In this study, the dependence of planar resistance of Si/Ge/Si structures with QDs on the band-to-band optical excitation intensity was measured and analyzed for the first time.

EXPERIMENTAL

The structures studied were synthesized by molecular-beam epitaxy (MBE) using a Katun' S MBE system. A buffer layer of about 40–100 nm thick was grown on the silicon substrates (*n*-Si:P, ρ = 5–7.5 Ω cm) with (100) orientation; then, a thin layer of germanium was grown, which was covered by a surface silicon layer 20–40 nm thick. All the layers grown were obtained without an intentional doping, the concentration of residual impurities in the silicon being approximately 10^{16} cm^{-3}. The number of germanium monolayers (ML) N_{Ge} in the structures varied from 0 to 25. In the structures with $N_{Ge} \le 4$ ML, the two-dimensional growth of pseudomorphous germanium layers occurs, and in the structures with a large nominal thickness of germanium layer the strained QDs are formed at the wetting germanium layer and have a pyramidal shape. The further increase of N_{Ge} results in the change of the QD shape from the so-called "hut clusters" to "dome clusters" [1–7]. A typical QD height is about 3 nm, and the dimension of the base increases from ≈7 to 30 nm with an increase of N_{Ge} from 6 to 25 ML. Beginning with $N_{Ge} \approx 12$ ML, a relaxation of elastic strains occurs in the structures owing to the introduction of misfit dislocations in them, and at $N_{Ge} \ge 15$ ML, QDs begin to merge [5]. A small planar size of QD was ensured by growth at a low temperature, equal to T_g = 200–300°C. The concentration of QDs in the structures is independent of N_{Ge} and is approximately equal to $N_{QD} = 10^{11}$ cm^{-2}. The structures and methods of their formation are described in detail elsewhere [3, 6–8]. The nonrectifying contacts were formed by deposition of indium on the surface of a structure. The dependence of planar resistance of the structure on the intensity of the band-to-band optical excitation was measured in the constant-current mode at the temperature T = 4.2 K and had a symmetrical shape with respect to the polarity of the voltage applied. A steady-state band-to-band excitation of the structure was performed using a diode emitting light in the red region of the spectrum. The light-emitting diode (LED) was mounted in the immediate vicinity of a reasonably small sample, which ensured the uniform illumination of the sample surface area. The radiation intensity of the light-emitting diode

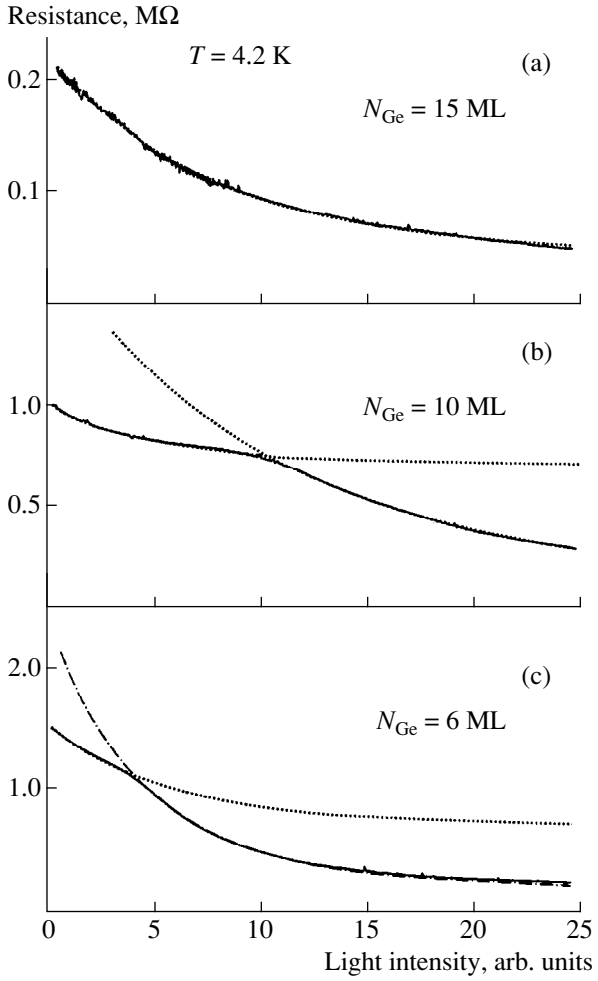

Fig. 1. Experimental dependences of the resistance of Si/Ge/Si-structures with the nominal thickness of germanium layers N_{Ge} = (a) 6, (b) 10, and (c) 15 ML on the band-to-band optical excitation intensity. T = 4.2 K. The current flowing through the structures is equal to (a) 8.7, (b) 5.0, (c) 3.6 Å. The dotted curves were obtained using formula (1) and the dashed curves were obtained using formula (2). Formulas are given in the text.

was governed by the current flowing through the LED and did not exceed 2 mW/cm^2.

EXPERIMENTAL RESULTS

The typical experimental dependences of the resistance (R) for three structures with N_{Ge} = 6, 10, and 15 ML on the excitation intensity (I) for a fixed magnitude of the current flowing through the structures are shown in Fig. 1. In the unstrained structures (N_{Ge} = 15 and 25 ML), the experimental curves are accurately described by the following dependence:

$$R = \Delta R_0 \exp(-I/I_0) + R_\infty. \quad (1)$$

Here, $\Delta R_0 = R_0 - R_\infty$, R_0 is the resistance of the structure in the dark, R_∞ is the resistance of the structure for a fairly high light intensity (R_∞ is independent of the light intensity); and I_0 is the illumination intensity at which ΔR_0 decreases by e times. The magnitude of ΔR_0 is about 80% of that of R_0. As the current through the structure increases, an increase in I_0 and in the relative fraction of R_∞ is observed as a rule.

In the strained structures (N_{Ge} = 6 and 8 ML), the curve $R(I)$ for low values of current through the structures is described by the exponential (1), and, as the current increases, the second portion appears, which also has an exponential shape

$$R = \Delta R_1 \exp[-(I/I_1)^{1/2}] + R_{1\infty}, \quad (2)$$

as can be seen from Fig. 1a for the structure with N_{Ge} = 6 ML. In the structure with N_{Ge} = 10 ML, both portions of the curve $R(I)$ (see Fig. 1b) are described by the same expression (1), but with different characteristic intensities (I_0 and I_0') and with different values of R_∞.

In the structures with $N_{Ge} \le 4$ ML, in which the self-organizing QDs have not yet been formed, the resistance is inversely proportional to the optical excitation intensity in a wide range of excitation intensities. Such a dependence testifies a band mechanism of conduction, when the concentration of nonequilibrium charge carriers is proportional to the excitation intensity.

The dependences of the I_0^* and I_1^* on the nominal thickness N_{Ge} of a germanium layer are shown in Fig. 2; this thickness governs the size of the germanium QDs. The values of I_0^* and I_1^* were obtained from the corresponding values of I_0 and I_1 by extrapolating to zero the magnitude of current flowing through the structures. Thus, the influence of the electric field on the nonequilibrium conduction of structures and the tunneling processes is eliminated; the latter are considered elsewhere. It can be seen from Fig. 2 that, for the strained structures with 10 ML, the magnitude of I_0^* is larger by about a factor of 4 than in the structures with 6 and 8 ML and the magnitude of I_1^* decreases almost by a factor of 3 as N_{Ge} increases from 6 to 8 ML. The value of $I_0'^*$ for the structure with N_{Ge} = 10 ML is also given in Fig. 2; this value by approximately an order of magnitude exceeds that of I_1^* for N_{Ge} = 8 ML. In the unstrained structures, as can be seen from Fig. 2, the magnitude of I_0^* insignificantly decreases with increasing N_{Ge}.

DISCUSSION OF RESULTS

A schematic fragment of a structure with QDs in the plane of their formation is shown in Fig. 3a together with the band diagrams for two cross sections of the structure, A and B (Figs. 3b, 3c). The band diagram of the structure across the cross section A, which does not intersect the QD, is shown in Fig. 3c. It can be seen from Fig. 3 that the wetting germanium layer is a quan-

tum well (QW) for holes and a barrier for electrons. Charge carriers generated by the illumination are separated in the space: the holes are localized in the germanium layer, and the electrons are localized near the barrier due to the Coulomb attraction. As a result, in the vicinity of the germanium layer, a quasi-two-dimensional (quasi-2D) layer of nonequilibrium electrons is produced. The energy diagram of the structure in the cross section *B* intersecting two neighboring QDs is shown in Fig. 3b. Due to the large sizes of QDs in comparison with the thickness of the wetting germanium layer, the ground energy level of holes in the QDs is deeper than the hole depth in a 2D germanium QW; therefore, the holes are captured at the QD level and are not involved in the band conduction. As a result of the Coulomb interaction of nonequilibrium electrons with the holes localized at QDs, the state of an electron bound by a QD is produced (localization of type I). Such a state can be considered as an exciton bound by a QD, or as an "artificial" donor. In addition, in the strained structures, electrons can localize in the regions between QDs (localization of type II) [16], where they are confined by the energy barriers. These barriers are formed due to the deformation of a silicon matrix, which contracts near a germanium QD. The magnitude of a silicon lattice strain along the structure plane decreases away from the QD as a result of an increase in the strained silicon volume. If this strain diminishes at a distance comparable with that between neighboring QDs, the edge of the conduction band of the silicon matrix undergoes a planar modulation with the minimums occurring between the QDs (see Fig. 3a). The potential barriers (between the neighboring QDs) induced by the strain probably have a saddle shape (see in Fig. 3b, the dotted curve). One should note that the deformation potential around a QD pushes the localized states of type I into a continuous spectrum. Similar localized states between the neighboring QDs can also be produced for holes. An exact calculation of the energy spectrum of Si/Ge/Si structures containing QDs with allowance made for elastic strain of the silicon matrix, as far as we know, has not yet been carried out. The calculations for GaAs/InAs/GaAs structures with InAs QDs carried out recently [18] show that a characteristic region of the elastic strain relaxation around the QD in these structures is comparable with QD sizes. Both types of localized states for nonequilibrium electrons in the plane of QD formation are schematically shown in Fig. 3a.

The relaxation of elastic strains occurs in the structures with $N_{Ge} > 12$ ML, and the localized states of type II disappear. Such states appear again for $N_{Ge} \geq 15$ ML as a result of electron-motion limitation in the conduction band of the silicon matrix close to Si/Ge heteroboundaries due to merging of QD bases [5]. In this case, no localized states of type I form owing to the disappearance of the closed electron orbit around a QD.

We believe that the observed exponential dependence of the resistance of structures with QDs on the band-to-band optical-excitation intensity may be explained within the framework of the model described above, i.e., the hopping conduction of nonequilibrium electrons over unordered localized states. The conduction along the type-I states is similar to the hopping conduction over the impurity states, and, in this case, we control the concentration of these states by the light intensity. The dependence of the resistivity of structures for the hopping mechanism of conduction on the concentration of the localized states has the following form for the 2D case [19]:

$$\rho = \rho_0 \exp\{\beta/[r(N)^{1/2}]\}. \quad (3)$$

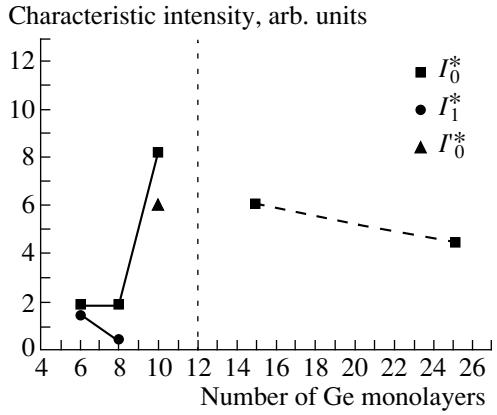

Fig. 2. Dependence of the characteristic optical excitation intensity on the number of germanium monolayers in Si/Ge/Si structures. The dashed line separates the regions of strained and unstrained structures.

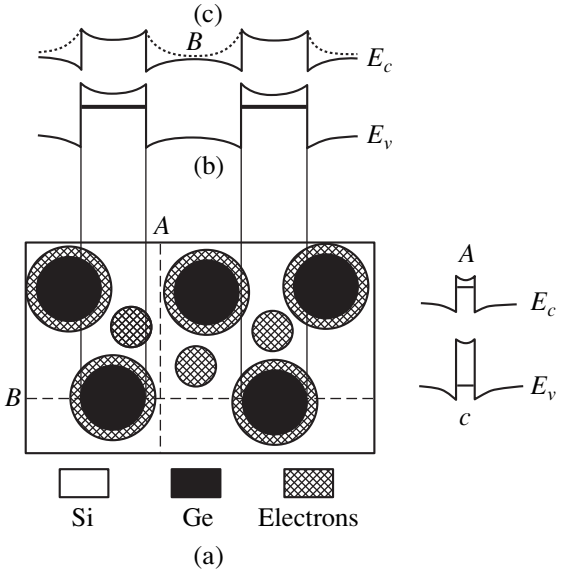

Fig. 3. (a) Schematic representation of the electron localized states for the strained Si/Ge/Si structure with germanium quantum dots; (b) the energy diagram of the structure across the cross section *B*, which intersects two neighboring germanium quantum dots; and (c) the band diagram of the structure across the cross section *A*, which does not intersect the quantum dots.

Here, N is the concentration of QDs, which is equal to $N = N_0 + \Delta N$, where N_0 is the concentration of QDs occupied by the equilibrium charge carriers; r is a radius of the localized state of electrons; and $\beta = 2.39$, according to the percolation theory for the 2D case. Concentration ΔN in the case of the linear recombination of nonequilibrium charge carriers is equal to $\Delta N = \tau I$, where τ is the lifetime of nonequilibrium charge carriers. For the low illumination intensities, when the condition $\Delta N \ll N_0$ is met, formula (3) transforms into a dependence of the form (1). As is known [20], the charge carrier recombination at the traps (the QDs serve as the traps in this case) is linear independent of the band-to-band excitation intensity. Consequently, the first portion of the curve $R(I)$ for the strained structures (Fig. 2), which is described by expression (1), is caused by the hopping conduction over the localized states of type I. We believe that the hole hopping conduction between QDs is insignificant compared to electron conduction, since the probability of a hop between neighboring QDs depends on the carrier localization radius and the localization region of the holes, which is defined by the QD size, and is smaller than the localization region size of electrons around a QD.

The conduction over the localized states of type II, similar to the continuum problem of the percolation theory [19], becomes possible if the nonequilibrium electron quasi-Fermi level μ_F reaches the percolation band level ε_3; the corresponding resistivity is given by

$$\rho = \rho_0 \exp\{(\varepsilon_3 - \mu_F)/kT\}, \qquad (4)$$

where kT is a thermal energy of electrons and $\mu_F = N/D$, with D standing for 2D density of II-type states. Hence, expression (1) follows in the case of a linear recombination of charge carriers and expression (2) for a quadratic-recombination, when $\Delta N = (I/\gamma)^{1/2}$; here, γ is a quadratic recombination coefficient [20]. Then, the second portion of the curve $R(I)$ for the strained structures with QDs of small dimensions (N_{Ge} = 6 and 8 ML) is described by expression (2) and is consistent with the conduction over the localized type-II states of nonequilibrium charge carriers, for which a quadratic recombination is characteristic. In this case, the band-to-band recombination of charge carriers occurs in the relatively large regions of the silicon matrix, which are confined by the saddle barriers of low height. The optical transitions are direct due to the carrier quasi-momentum scattering by QDs [16].

Thus, a complicated shape of experimental curve $R(I)$ for the strained structures is caused by the presence of two types of localized states, over which the hopping conduction of electrons takes place. The total resistance of these structures combines together from two parallel resistance nets, the resistances of which depend differently on the excitation intensity. In the unstrained structures, the dependence $R(I)$ involves a single region, which corresponds to the hopping conduction of electrons over the localized type-II states.

The meaning of the characteristic quantity I_0^* consists in the fact that this is the excitation intensity for which the neighboring localized states of type I in the strained structures are populated by electrons. The further increase in the excitation intensity does not affect the concentration of the occupied localized states, which cannot be larger than the concentration N_{Ge} but results in the formation of multiple-charged centers at QDs. Knowing the QD concentration, one can estimate the lifetime of nonequilibrium charge carriers localized in the type-I states from the expression $N_{QD} = \tau I_0^*$. The values of lifetime for such charge carriers in the structures with N_{Ge} equal to 6, 8, and 10 ML are 10^{-4}, 10^{-4}, and 3×10^{-5} s, respectively. The value of lifetime of the nonequilibrium charge carriers obtained for the structure with N_{Ge} = 6 ML is considerably larger than $\tau_1 = 3.9 \times 10^{-6}$ s s obtained in [16] from the measurements of the photoluminescence-decay kinetics for a structure with the same value of N_{Ge}, but synthesized at a higher growth temperature. This difference is caused by the fact that QDs in the structures we studied have considerably smaller planar sizes than the QDs in the structures studied in [16]. The decrease in the lifetime with increasing N_{Ge} up to 10 ML is likely to be connected with a sharp increase in the deformation potential around a QD, which is caused by the change of the QD shape from the hut- to dome-shape clusters [1, 7]. The latter process occurs in the structures studied by us with an increase in N_{Ge} from 8 to 10 ML.

The physical meaning of the characteristic optical excitation intensities I_1^* and $I_0'^*$ in the strained and I_0^* in the unstrained structures consists in the fact that, for this excitation intensity, the electron quasi-Fermi level reaches the percolation level. The evaluation of the percolation level from the experimental data is hampered owing to the uncertainty of parameters D, γ, and τ. The behavior of the characteristic values of the excitation intensity, which describe the localized type-II states (see Fig. 2), reflects a qualitative dependence of the percolation level magnitude on N_{Ge}. By changing N_{Ge} from 8 to 10 ML, as can be seen from Fig. 2, a significant increase in the characteristic excitation intensity is observed, as well as the change in the shape of dependence from (2) to (1); the latter describes the second region of $R(I)$. These features are connected, in our opinion, with the QD-shape change that results in a considerable increase in the amplitude of the saddle barrier, which separates the localized type-II states, i.e., in an increase in the percolation level. As a consequence, the appearance of the levels of quantum-confinement type-II states (zero-dimensional traps) takes place, which actually explains the change in the recombination type observed. The reason for the decrease in the value I_1^* with an increase in N_{Ge} from 6 to 8 ML is not yet clear.

A comparatively slight change in the value of I_0^* characteristic of dependence $R(I)$, which describes the conduction over the localized type-II states by transition from the strained structure with $N_{Ge} = 10$ ML to the unstrained structure with $N_{Ge} = 15$ ML (Fig. 2), is indicative of the proximity of the percolation level values, though the nature of the saddle barriers is different. With a further increase in N_{Ge} from 15 to 25 ML, a decrease in I_0^* is connected with the decrease in the sizes for localized type-II states, which results in an enhancement of the quantum-size energy for electrons and in a reduction in the number of levels below the percolation level; the number of such levels apparently tends to a constant value.

CONCLUSION

In this study, the influence of a steady-state band-to-band optical excitation on the planar resistance of Si/Ge/Si structures containing self-organizing germanium QDs was investigated. The exponential decrease in the structure resistance with the increase in the band-to-band optical excitation intensity was observed. In the elastically strained structures with small QDs, two different exponential portions of this dependence are observed, and, in the unstrained structures with large QDs, a single is observed region. The experimental results obtained are explained within the framework of the model of nonequilibrium-electron hopping conduction over the localized states of the two types. The states of type I are formed by filling the germanium QDs with nonequilibrium holes, and the states of type II are localized between the QDs. In the strained structures, the localization of the type-II charge carriers is caused by the deformation potential of the silicon matrix, and in the unstrained structures, by the heteroboundary Si/Ge barriers of the merging germanium islands. In the strained structures, the first portion of the structure-resistance dependence on the excitation intensity is connected with the change in the concentration of localized type-I states, and the second, with the occupation of the type-II states. As the nominal thickness of germanium layer in the strained structures increases, a sharp increase in the characteristic optical excitation intensities is observed as well as the change of dependence $R(I)$, which is caused by the change of the germanium island shape. In the unstrained structures, the localized type-I states disappear, and the dependence observed is caused by the occupation only of the localized type-II states by the nonequilibrium electrons.

ACKNOWLEDGMENTS

This study was supported by the Russian Foundation for Basic Research, project no. 97-02-18408.

REFERENCES

1. Y.-W. Mo, D. E. Savage, B. S. Swartzentruber, and M. G. Lagally, Phys. Rev. Lett. **65**, 1020 (1990).
2. R. Notzel, Semicond. Sci. Technol. **11**, 1365 (1996).
3. A. I. Yakimov, V. A. Markov, A. V. Dvurechenskii, and O. P. Pchelyakov, J. Phys.: Condens. Matter **6**, 2574 (1994).
4. G. Abstreiter, P. Schittenhelm, C. Engel, *et al.*, Semicond. Sci. Technol. **11**, 1521 (1996).
5. A. B. Talochkin, V. A. Markov, S. P. Suprun, and A. I. Nikiforov, Pis'ma Zh. Éksp. Teor. Fiz. **64**, 203 (1996) [JETP Lett. **64**, 219 (1996)].
6. V. A. Markov, A. I. Nikiforov, and O. P. Pchelyakov, J. Cryst. Growth **175/176**, 736 (1997).
7. O. P. Pchelyakov, V. A. Markov, A. I. Nikiforov, and L. V. Sokolov, Thin Solid Films **306**, 299 (1997).
8. A. I. Yakimov, V. A. Markov, A. V. Dvurechenskiĭ, and O. P. Pchelyakov, Pis'ma Zh. Éksp. Teor. Fiz. **63**, 423 (1996) [JETP Lett. **63**, 444 (1996)].
9. G. Capellini, L. Di Gaspare, F. Evangelisti, and E. Palange, Appl. Phys. Lett. **70**, 493 (1997).
10. Xun Wang, Zui-min Jiang, Hai-jun Zhu, *et al.*, Appl. Phys. Lett. **71**, 3543 (1997).
11. H. Sunamura, N. Usami, Y. Shiraki, and S. Fukatsu, Appl. Phys. Lett. **66**, 3024 (1995).
12. D. J. Eaglesham, F. C. Unterwald, and D. C. Jacobson, Phys. Rev. Lett. **70**, 966 (1993).
13. H. Chen, W. G. Cheng, X. G. Xie, *et al.*, Appl. Phys. Lett. **70**, 446 (1997).
14. V. Ya. Aleshkin, N. A. Bekin, N. G. Kalugin, *et al.*, Pis'ma Zh. Éksp. Teor. Fiz. **67**, 46 (1998) [JETP Lett. **67**, 48 (1998)].
15. R. Apetz, L. Vescan, A. Hartmann, *et al.*, Appl. Phys. Lett. **66**, 445 (1995).
16. S. Fukatsu, H. Sunamura, Y. Shiraki, and S. Komiyama, Appl. Phys. Lett. **71**, 258 (1997).
17. P. D. Persans, P. W. Deelman, K. L. Stokes, *et al.*, Appl. Phys. Lett. **70**, 472 (1997).
18. A. D. Andreev, J. R. Downes, D. A. Faux, and E. P. O'Reilly, J. Appl. Phys. **86**, 297 (1999).
19. B. I. Shklovskiĭ and A. L. Éfros, *Electronic Properties of Doped Semiconductors* (Nauka, Moscow, 1979; Springer-Verlag, New York, 1984).
20. S. M. Ryvkin, *Photoelectric Effects in Semiconductors* (Fizmatgiz, Leningrad, 1963; Consultants Bureau, New York, 1964).

Translated by T. Galkina

Semiconductors, Vol. 34, No. 11, 2000, pp. 1316–1320. Translated from Fizika i Tekhnika Poluprovodnikov, Vol. 34, No. 11, 2000, pp. 1368–1372.

LOW-DIMENSIONAL SYSTEMS

The Emission from the Structures with Arrays of Coupled Quantum Dots Grown by the Submonolayer Epitaxy in the Spectral Range of 1.3–1.4 μm

B. V. Volovik*, D. S. Sizov*, A. F. Tsatsul'nikov*, Yu. G. Musikhin*, N. N. Ledentsov*, V. M. Ustinov*, V. A. Egorov, V. N. Petrov**, N. K. Polyakov**, and G. É. Tsyrlin****

** Ioffe Physicotechnical Institute, Russian Academy of Sciences, Politekhnicheskaya ul. 26, St. Petersburg, 194021 Russia*

*** Institute of Analytical Instrument Making, Russian Academy of Sciences, Rizhskii pr. 26, St. Petersburg, 198103 Russia*

Submitted April 26, 2000; accepted for publishing April 28, 2000

Abstract—Optical properties of structures with vertically coupled quantum dots grown by the combined submonolayer molecular-beam epitaxy were investigated. It is shown that the formation of the laterally coupled conglomerates of quantum dots are possible in upper rows for certain parameters of growth, with the corresponding photoluminescence emission being in the wavelength range of 1.3–1.4 μm at room temperature. *© 2000 MAIK "Nauka/Interperiodica".*

INTRODUCTION

The attainment of emission in the wavelength range of 1.3–1.55 μm on the basis of heterostructures grown on GaAs substrates is a topical problem of modern microelectronics because the lasers of this range are the basic components of modern systems of fiber-optics communication. The heterostructures on InP substrates used now for the development of these layers have a number of grave disadvantages. For example, such devices are characterized by a strong temperature sensitivity [typical values of a characteristic temperature T_0 = (60–80) K] [1]. Furthermore, the development of surface-emitting lasers in this system is hampered by an insufficient difference in refractive indices for the layers constituting the Bragg distributed reflectors. At present, the greatest success in developing the lasers at 1.3 μm on the GaAs substrates is attained using the InGaAsN/GaAs heterostructures [2] and the InGaAs/GaAs structures with quantum dots (QDs) [3, 4]. The purpose of this study is to investigate the possibility of realizing the long-wave emission in the latter system.

The generation of long-wave emission in the InGaAs/GaAs system is hampered by a large mismatch between the lattice parameters. For example, the maximum wavelength of oscillation of an InGaAs/GaAs quantum-well laser amounts to 1.21 μm [5]; a further long-wavelength shift leads to a catastrophic degradation in the structure quality owing to the formation of misfit dislocations. The usage of the assembled QDs makes it possible to substantially extend the emission range [6]. The long-wavelength emission of the In(Ga)As/GaAs QDs can be realized using various methods: the deposition of QDs with ultra-low growth rates [7]; the usage of the alternating submonolayer deposition of In, Ga, and As [3]; and also the overgrowing of QDs with an InGaAs layer [4, 8]. The last two methods resulted in the development of QD lasers emitting at a wavelength of 1.3 μm. In this study, we used the possibility of attaining emission at the wavelengths of up to 1.39 μm at room temperature using the structures with coupled QDs grown by the combined submonolayer molecular-beam epitaxy including the deposition of InAs-submonolayer coatings and the alternating deposition of In and As atoms [9] (the so-called method of submonolayer migration-stimulated epitaxy [10]).

EXPERIMENT

The structures under investigation were grown by molecular-beam epitaxy (MBE) in the ÉP1203 setup on semi-insulating singular and vicinal (100)GaAs substrates. The QD formation was monitored using a reflection high-energy electron diffraction (RHEED) pattern by means of the system of detection and analysis of the RHEED patterns. Every layer of QDs with a total thickness of 2.5 monolayers (MLs) of InAs was grown by the following method: the first 0.5 ML of InAs was deposited without interruption and the next 2.0 MLs of InAs were deposited by the submonolayer migration-enhanced epitaxy (SMEE) for which the indium and arsenic fluxes were directed to the substrate surface sequentially. In the process of the SMEE, four cycles of deposition were performed in each case. One cycle of deposition of indium atoms corresponded to the deposition of 0.5 ML of InAs; after every In deposition cycle, the surface was exposed to the arsenic flux for 10 s. During the indium sputtering, the (4×1) surface reconstruction was observed. During the arsenic-flux exposure of the surface, the heterostructure changes, first, for (1×1). After the deposition of 2 MLs of InAs,

1063-7826/00/3411-1316$20.00 © 2000 MAIK "Nauka/Interperiodica"

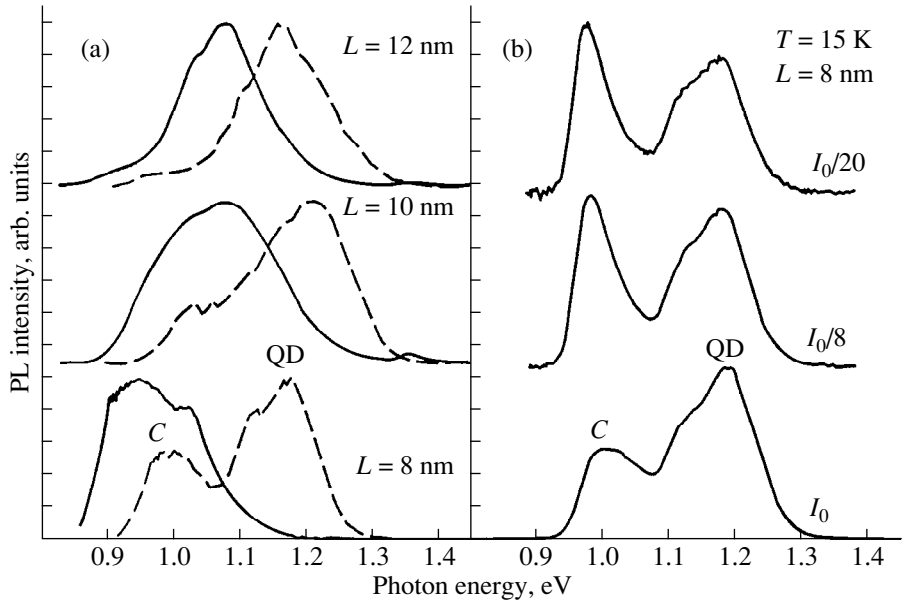

Fig. 1. Photoluminescence spectra for the samples with 10 rows of quantum dots: (a) separated by the GaAs barriers of various thickness L; solid and dashed lines refer to measurement temperatures T of 300 and 77 K, respectively; (b) for various excitation densities, T = 15 K, and L = 8 nm.

the bulk reflections indicating that three-dimensional islands are formed appear on strands. An active region located between the GaAs layers 6 nm thick on each side consists of 6–15 layers of InAs QDs separated by GaAs barriers 8–12 nm thick. For preventing the transfer of nonequilibrium charge carriers to the near-surface and substrate regions during the optical investigations, the active region was bounded on both sides by $Al_{0.25}Ga_{0.75}As$/GaAs short-period superlattices (five pairs, 25 Å/25 Å). The structure was covered by a GaAs layer 5 nm thick from the top. The growth temperature was 470–480°C for the active region [the moment of modification of the surface reconstruction from (2×4) to (4×4)] and 600°C for the remaining part of the structure [the moment of modification of the surface reconstruction from (2×4) to (3×1)]. The growth rates measured previously for the reference sample by means of the zero-reflection RHEED-intensity oscillation were 0.1, 0.3, and 0.77 ML/s for InAs, AlAs, and GaAs, respectively. A total pressure of arsenic vapors in the growth chamber measured by a PMM-46 gauge was constant in all the experiments and amounted to $(1.5–2.1) \times 10^{-6}$ Pa. The transmission-electron-microscopy (TEM) investigations were carried out using a Philips EM-420 electron microscope with an accelerating voltage of 100 keV. The photoluminescence was excited by the Ar^+ laser (a wavelength of 514.5 nm) and detected by a cooled Ge diode.

RESULTS AND DISCUSSION

In this study, we investigated the structures with several layers of QDs; each of which was formed as a result of deposition of 2.5 MLs of InAs. As was shown in our previous study [1], the multiplication of QDs obtained by depositing a large (3 MLs) quantity of InAs is possible only for a large thickness of the barrier, while a narrowing of the barrier leads to a reduction in the photoluminescence (PL) intensity owing to the formation of the misfit dislocations.

In Fig. 1, we show the PL spectra for the structures with several QD layers 2.5 ML thick separated by the GaAs barriers with a thickness from 8 to 12 nm. In the PL spectrum of each of the sample, there are two fundamental bands. The first band (the QD line) with a 1.16–1.18-eV peak at low temperature corresponds by its position to the emission from ordinary QDs formed by depositing 2.5 MLs of InAs. At the same time, the C band at longer wavelength is obviously of a different origin. This assumption is confirmed by the fact that, when the excitation density decreases at low temperature, relative intensities of the QD and C lines remain virtually unchanged (Fig. 1b). It may also be noted that the relative intensity of the C band increases with decreasing thickness of the GaAs barrier between the QD layers. Thus, it is possible to assume that this band corresponds to the emission from the coupled QDs formed during the multiplication of the QD layers with a small barrier thickness. At the same time, as the results of our previous investigations [12] show, a steady shift of the PL line towards the longer wavelengths with decreasing barrier thickness is observed in the case of the tunnel interaction between the electron states in the islands of adjoining layers. Since the degree of vertical correlation of the islands of adjoining rows is very high [13] for the barrier thicknesses of

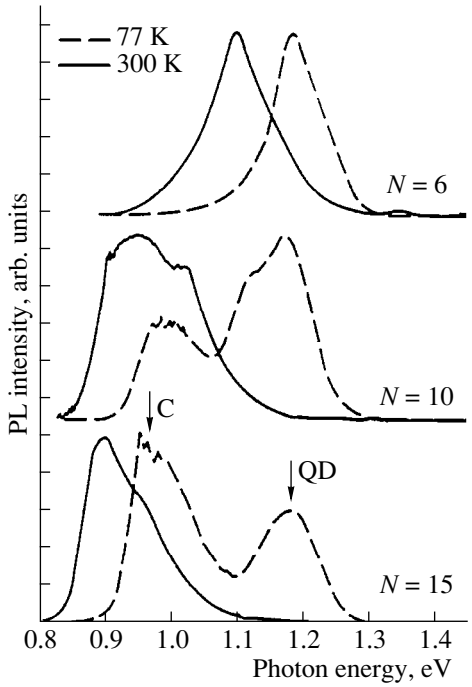

Fig. 2. Photoluminescence spectra for the samples with a various number of quantum-dot rows separated by the GaAs barriers (L = 8 nm); N is the number of quantum-dot rows; solid and dashed lines refer to measurement temperatures T of 300 and 77 K, respectively.

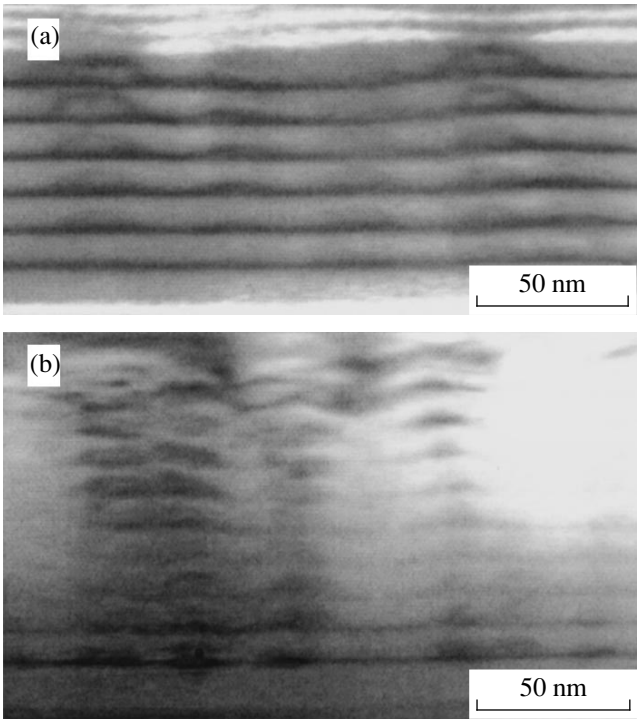

Fig. 3. Cross-sectional TEM images of the samples with the number of the quantum-dot rows N = (a) 6 and (b) 10. A GaAs-barrier width L = 8 nm.

8–12 nm used in these structures, the two PL lines cannot be related to the dots coupled and uncoupled in the vertical direction. Thus, we assume that the PL long-wavelength band is associated with the QD conglomerates formed in the upper rows for a reasonably small barrier thickness. As was shown previously [12, 14], in the case of depositing a reasonably large number of the QD planes, the lateral sizes of QDs in upper rows increase, whereas the density of the array is specified by the density of islands in the first row as a consequence of the vertical correlation. Thus, the overlapping of neighboring islands of upper rows is possible in the growth plane. A similar effect was previously described by us for the InGaAs QDs grown by the MBE without using the SMEE modes [14]. It should be noted that, for the QDs grown in the conventional MBE mode, the lateral-overlapping effect becomes important for substantially smaller GaAs barrier thicknesses. This is associated with the fact that the QDs grown in the SMEE mode are of a larger size than the QDs grown by the conventional MBE [10]. Consequently, in this case, an increase in the QD size in upper rows leads to lateral overlapping, even for larger barrier thicknesses.

We also investigated the structures in which the number of QD layers was varied for a constant thickness (8 nm) of the GaAs barrier. The PL spectra for such structures are shown in Fig. 2. It can be seen that, by increasing the number of rows, the long-wavelength region of the spectrum (the *C* band) becomes predominant, and its peak shifts to longer wavelengths of up to 1.39 μm for 15 QD layers. Thus, the PL data for these samples also confirm our assumption about the lateral overlapping of QDs of upper rows in the growth plane. In Fig. 3, we show the cross-sectional TEM images of the samples with 6 to 10 QD layers separated by the GaAs barriers 8 nm thick. In Fig. 3, the "columns" of dots can be seen, despite the fact that the degree of vertical correlation is very high. The lateral sizes of the islands of every next row exceed those of the dots of the previous row reaching ~30 nm for the upper QD row in the structure with 6 QD layers. For the sample with 10 QD layers, an increase in the lateral sizes of QDs in the upper layers leads to their lateral overlap, which can be seen in the TEM photograph. We assume that the *C* line in the PL spectrum is associated with such QD conglomerates. This line is in the wavelength range of 1.3–1.4 μm at room temperature. For the structure with 15 QD layers, the peak of the PL line is at the wavelength of 1.39 μm.

It may be noted that, at low temperatures, a relative intensity of the QD and *C* bands are comparable, whereas the *C* line becomes predominant in the spectrum at room temperature. This is associated with the fact that, with the increase in temperature, the thermal emission of carriers from islands is activated. In this case, the emission is more efficient for the QDs of smaller size having a lower localization energy (i.e., for those islands to which the QD line is related). Furthermore, at high temperatures, the probability of the trans-

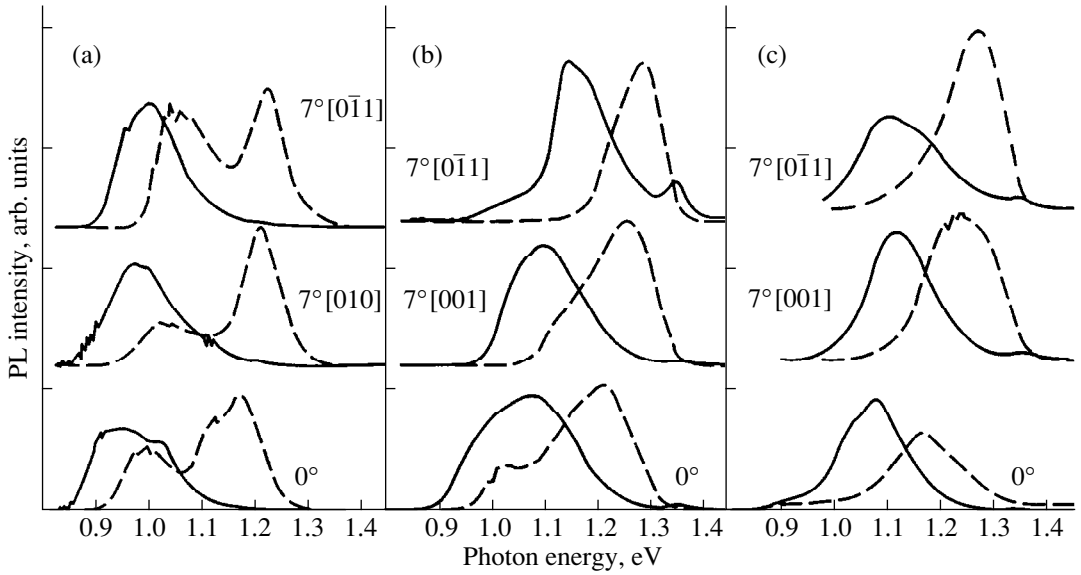

Fig. 4. Photoluminescence spectra for the samples with 10 quantum-dot rows separated by the GaAs barriers of various widths L grown on the singular and disoriented substrates; solid and dashed lines refer to measurement temperature T of 300 and 77 K, respectively; the barrier width L = (a) 8, (b) 10, and (c) 12 nm.

port of carriers between QDs increases both in the plane and in the growth direction. These factors lead to a decrease in the population of small QDs and, correspondingly, to a drop in the relative intensity of the QD line in the spectrum.

We also investigated the influence of substrate disorientation on the optical properties of the structures. In the same technological process, we grew the structures both on a singular (100) substrate and on the substrates disoriented by angles of 5°–7° (for various samples) along various crystallographic directions. In Fig. 4, we show the PL spectra for the samples with 10 QD layers and the barrier thickness of 8, 10, and 12 nm grown on the singular and disoriented substrates. The disorientation of a substrate by 7° leads to substantial modifications in the spectrum shape and in the positions of PL lines, the influence of the disorientation being different for the samples with different widths of the GaAs barrier between the QD rows. For the barrier width equal to 12 nm, the disorientation leads to the disappearance of the *C* line in the PL spectrum. For the sample with a barrier width of 10 nm, the disorientation along the [001] direction induces a decrease in the *C*-line intensity and its large shift towards shorter wavelengths, while the disorientation along the [0$\bar{1}$0] direction results in the disappearance of this line in the PL spectrum at a low temperature. At the same time, if the barrier width is decreased to 8 nm, the disorientation results in the shift towards shorter wavelengths both for the QD line and the *C* line by 40–60 meV with the relative intensity of the lines changing only slightly.

We relate this effect to the fact that, in the case of the substrate disorientation, the terraces are formed on the surface, which induces an increase in the density of the QD array and a decrease in their sizes [10, 11] for the QDs grown by the SMEE. We assume that, in this case, the stress fields caused by the QDs and inducing their vertical correlation are also changed, which leads to a drop in the lateral sizes of the QDs in upper rows. In this case, the probability of their lateral overlapping decreases and, correspondingly, the relative intensity of the *C* line in the spectrum drops as well. A decrease in the QD size is confirmed by the shift of the QD line to shorter wavelengths in the case of disorientation. For a large barrier width, the QD size in the upper rows is smaller, and the influence of the disorientation on the probability of the lateral overlapping is strong. The lateral overlapping remains significant at small barrier widths even for the growth on disoriented substrates. Thus, the disorientation of a substrate influences the formation of the QD conglomerates.

CONCLUSION

Thus, we investigated the optical properties of the structures obtained by multiplicating the QD layers grown by the submonolayer molecular-beam epitaxy. It was shown that, for a reasonably small GaAs-barrier width (less than 10 nm), an increase in the lateral sizes of the QDs in the upper rows leads to the overlap of the QDs in the growth plane, which is accompanied by the PL emission in the wavelength range of 1.3–1.4 μm at room temperature. It was shown that the disorientation of a substrate influences the formation of such conglomerates.

ACKNOWLEDGMENTS

This study was supported by the Ministry of the Science and Technologies of the Russian Federation under the program "Physics of Solid-State Nanostructures" (grant nos. 98-2029 and 99-2014), the Russian Foundation for Basic Research, the Volkswagen Foundation, and the INTAS (grant nos. 1999-0928 and 97-0751).

REFERENCES

1. A. F. Phillips, S. J. Sweeney, A. R. Adams, and P. J. A. Thijs, IEEE J. Sel. Top. Quantum Electron. **5**, 401 (1999) and references therein.
2. A. Yu. Egorov, D. Bernklau, D. Livshits, *et al.*, Electron. Lett. **35**, 318 (1999).
3. D. L. Huffaker, G. Park, Z. Zou, *et al.*, Appl. Phys. Lett. **73**, 2564 (1998).
4. A. E. Zhukov, A. R. Kovsh, V. M. Ustinov, *et al.*, IEEE Photonics Technol. Lett. **11**, 1345 (1999).
5. S. Sato and S. Satoh, Jpn. J. Appl. Phys. **38**, L990 (1999).
6. K. Mukai, N. Ohtsuka, M. Sugawara, and S. Yamazaki, Jpn. J. Appl. Phys. **33**, L1710 (1994).
7. R. Murray, D. Childs, S. Malik, *et al.*, Jpn. J. Appl. Phys. **38**, 528 (1999).
8. K. Nishi, H. Saito, and S. Sugou, Appl. Phys. Lett. **74**, 1111 (1999).
9. G. M. Guryanov, G. E. Cirlin, and V. N. Petrov, Surf. Sci. **352–354**, 651 (1996).
10. G. É. Tsyrlin, V. N. Petrov, V. G. Dubrovskiĭ, *et al.*, Fiz. Tekh. Poluprovodn. (St. Petersburg) **31**, 902 (1997) [Semiconductors **31**, 768 (1997)].
11. G. É. Tsyrlin, N. K. Polyakov, V. A. Egorov, *et al.*, Pis'ma Zh. Tekh. Fiz. **26** (9), 52 (2000) [Tech. Phys. Lett. **26**, 423 (2000)].
12. N. N. Ledentsov, V. A. Shchukin, M. Griundmann, *et al.*, Phys. Rev. B **54**, 8743 (1996).
13. Q. Xie, A. Madhukar, P. Chen, and N. P. Kobayashi, Phys. Rev. Lett. **75**, 2542 (1995).
14. A. F. Tsatsul'nikov, A. Yu. Egorov, A. E. Zhukov, *et al.*, Fiz. Tekh. Poluprovodn. (St. Petersburg) **31**, 851 (1997) [Semiconductors **31**, 722 (1997)].

Translated by V. Bukhanov

Semiconductors, Vol. 34, No. 11, 2000, pp. 1321–1326. Translated from Fizika i Tekhnika Poluprovodnikov, Vol. 34, No. 11, 2000, pp. 1373–1379.

LOW-DIMENSIONAL SYSTEMS

A Nonlinear Theory of Coherent Oscillations in a Resonance-Tunnel Diode in a Wide Frequency Range

V. F. Elesin, I. Yu. Kateev, and A. I. Podlivaev

Moscow State Institute of Engineering Physics (Technical University), Kashirskoe sh. 31, Moscow, 115409 Russia

Submitted February 25, 2000; accepted for publication May 17, 2000

Abstract—The Schrödinger equation with open boundary conditions was solved numerically; the solutions make it possible to describe the coherent oscillations in a resonance-tunnel diode in a wide range of frequencies and amplitudes of the fields. In an approximation linear in the field and in the adiabatic limit, the results of numerical and analytical calculations coincide with a high degree of accuracy. The dependences of the power of oscillations on the current and the parameters of the resonance-tunnel diode were derived. It is shown that, in the quantum-mechanical mode, oscillations with high power are possible at the frequencies that exceed the level width (i.e., in the terahertz range). © *2000 MAIK "Nauka/Interperiodica".*

1. INTRODUCTION

High-frequency oscillators based on resonance tunnel diodes (TDs) are regarded as promising. Oscillations with a frequency as high as 712 GHz have been reported [1]. However, wide use of oscillators based on resonance TDs is retarded by relatively low power levels and frequencies attained. The methods for increasing the power and frequency of oscillations remain unclear, which is related, in particular, to the difficulties with adequate theoretical description. In spite of the relatively large number of publications devoted to this problem, aspects of describing the dependences of the power of oscillations on frequency and resonance-TD parameters remain unclarified.

An exact expression for the dependence of the gain on frequency (albeit in the approximation linear in the field) was derived previously [2] in the context of a simple analytical model and the results reported in earlier publications were analyzed (see also review [3]).

The objective of this study was to describe the coherent oscillations in a resonance TD in a wide range of the frequencies and the field amplitudes by numerically solving the Schrödinger equation with the open boundary conditions.

2. FORMULATION OF THE PROBLEM. MAIN EQUATIONS. THE METHOD FOR NUMERICAL SOLUTION

The developed program makes it possible to basically consider a wide range of models of coherent oscillations in a resonance TD. In this paper, we elaborate on a simple model used previously [2]. This will allow us to test the program, compare the results of computations with exact analytical results [2, 4], and obtain new data that can be interpreted in the simplest way.

Thus, similarly to [2], we consider a one-dimensional quantum well (QW) with barriers in the form of a delta function at the points $x = 0$ and $x = a$ (see Fig. 1). From the left ($x = -\infty$), a steady-state electron flux proportional to q^2 is fed to the QW, with electrons having the energy ε that is approximately equal to the energy ε_R of the resonance level. In the region of QW, there is an alternating electric field $E(t)$ with the potential $v(x, t)$; i.e.,

$$v(x, t) = v(x)\cos\omega t, \tag{1}$$

$$v(x) = \begin{cases} eE_0 x\Theta(x), & x < a, \\ eE_0 a, & x > a. \end{cases} \tag{2}$$

The wave function $\Psi(x, t)$ satisfies the Schrödinger equation

$$i\hbar\frac{\partial\Psi}{\partial t} = -\frac{\hbar^2}{2m^*}\frac{\partial^2\Psi}{\partial x^2} + [\alpha\delta(x) + \alpha\delta(x-a)]\Psi(x, t) + v(x, t)\Psi(x, t). \tag{3}$$

The alternating field induces the polarization current

$$J_c(x, t) = -\frac{ie}{\hbar}\left\{\Psi^*(x, t)\frac{\partial\Psi(x, t)}{\partial x} - \Psi(x, t)\frac{\partial\Psi^*(x, t)}{\partial x}\right\} \equiv J_c(x)\cos\omega t + \sum_{k=2} J_k\cos k\omega t. \tag{4}$$

This current is calculated [5] as

$$J_c = \frac{1}{a}\int_0^a J_c(x)dx. \tag{5}$$

1063-7826/00/3411-1321$20.00

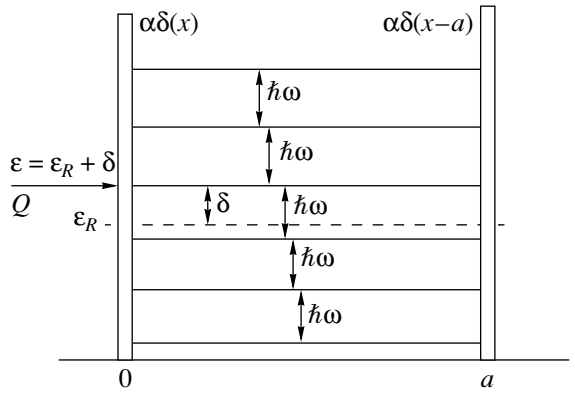

Fig. 1. A quantum-well structure with δ-function barriers at the points $x = 0$ and $x = a$.

We follow [2] to derive the boundary conditions to the above equation. Assuming that the frequency ω is low and the amplitude of the potential eEa is small compared to the electron energy ε_R, we obtain

$$\Psi(0,t)\left(1-\frac{\alpha}{ip}\right)+\frac{\Psi'(0,t)}{ip} = q\exp\left(-\frac{i\varepsilon t}{\hbar}\right),$$
$$\Psi(a,t)\left(1-\frac{\alpha}{ip}\right)-\frac{\Psi'(a,t)}{ip} = 0, \quad p^2 = \varepsilon. \tag{6}$$

Boundary condition (6) describes the electron flux that arrives from the left and is proportional to q^2, reflection of electrons, and their departure to the region $x > a$. It is noteworthy that the QW parameters are chosen in such a way that the half-width Γ of the resonance level is small compared to ε_R.

The main factor governing the accumulation of errors in numerical solution of problem (1) is the presence of two processes that occur with widely different characteristic times. These are the time of variation in the wave-function phase and the time of variation in the external potential. In the algorithm under consideration, the problem is normalized by replacing the sought-for wave function Ψ with the function φ as $\Psi(x, t) = \varphi(x, t)\exp(-i\varepsilon t/\hbar)$. A solution of the problem for φ is sought by the sweep method (the conventional method for solving the Schrödinger equation [6]) at a discrete mesh with a step in the coordinate of $dx = L/500$ and a step in time of $dt \approx 2\pi/200\omega$.

3. LINEAR THEORY OF COHERENT OSCILLATIONS

A solution to Eq. (3) with boundary conditions (6) was derived previously [2] in the linear approximation in the field; an expression for the current J_c [2] is given by

$$\bar{J}_c(\omega,\delta) = \frac{4J_c}{e^2EaQ}$$
$$= -\frac{\delta\Gamma^2}{[(\delta-\omega)^2+\Gamma^2][(\delta+\omega)^2+\Gamma^2]}, \tag{7}$$
$$\delta = \varepsilon-\varepsilon_R, \quad \Gamma = \frac{4p^3}{\alpha^2 a}, \quad Q = q^2p.$$

Here, Γ is the half-width of the resonance level and Q is the pump current of monoenergetic electrons. Using (7), the dependences of the amplification (absorption) coefficient $\tilde{J}_c$ on frequency and mismatch δ were analyzed [2]. It was shown [2] that two modes of oscillations are possible (classical and quantum-mechanical), depending on the ratio δ/Γ. For δ/Γ < 1 (the classical mode), $\tilde{J}_c$ has a maximum for ω = 0, with the highest gain being attained for $\delta = \Gamma/\sqrt{3}$ (see Fig. 2). In the quantum-mechanical mode (δ/Γ > 1), the gain is highest at the frequency (Fig. 2) of

$$\omega_m^2 = \delta^2-\Gamma^2. \tag{8}$$

The new maximum of $\tilde{J}_c$ corresponds to quasi-resonance transitions between the states ε_R and ε, because, for $\omega \gg \Gamma$, equality (8) yields the condition for a "quasi-resonance" as $\omega = \varepsilon - \varepsilon_R$. Consequently, if the mismatch is chosen as $\delta = \omega \gg \Gamma$ (i.e., outside the range of the largest negative differential conductance), oscillations are possible at a frequency that exceeds Γ. Figures 2 and 3 show the dependences $\tilde{J}_c(\omega/\Gamma)$ for $\delta = 4\Gamma$, $\delta = 0.9\Gamma$, and $\delta = (1/\sqrt{3})\Gamma$. The dependences were derived either analytically using (7) or numerically. It can be seen that analytical and numerical results coincide with a high degree of accuracy. Comparison was also performed for a number of other dependences, and excellent agreement between analytical and numerical results was obtained. Obviously, we may regard the coincidence of the results as a successful test of performance of the numerical program.

4. NONLINEAR THEORY OF OSCILLATIONS IN THE ADIABATIC LIMIT

A nonlinear theory of coherent oscillations in a resonance TD has been developed previously [4] in the adiabatic limit $\omega \ll \Gamma$. In this case, the gain $\tilde{J}_c$ is given by [4]

$$\tilde{J}_c = -\frac{\Gamma}{\sqrt{2}\tilde{E}^2}\frac{\sqrt{\sqrt{x^2+y^2}-x}}{\sqrt{x^2+y^2}}, \tag{9}$$

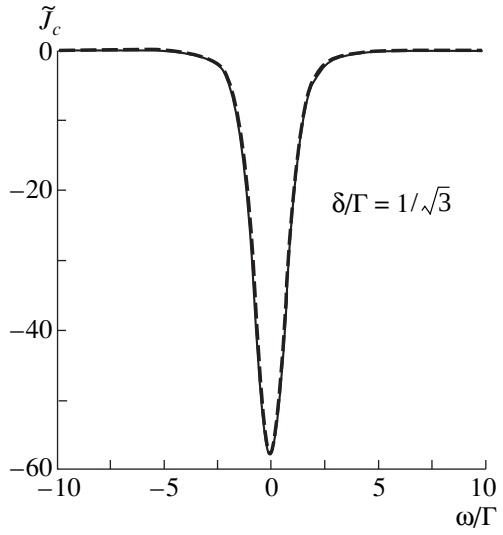

Fig. 2. The frequency dependence of dynamic conductance J_c/eEa for the optimal mode of oscillations. The solid line shows the results of numerical calculations, and the dashed line represents the analytical theory.

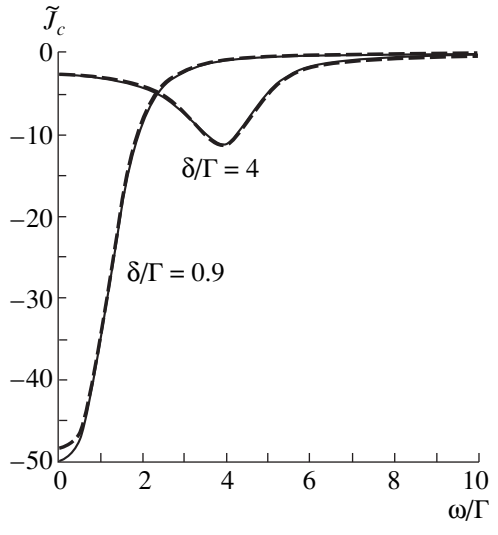

Fig. 3. The frequency dependences of dynamic conductance J_c/eEa for quantum-mechanical and classical modes of oscillations. The solid line corresponds to numerical calculation, and the dashed line corresponds to analytical theory.

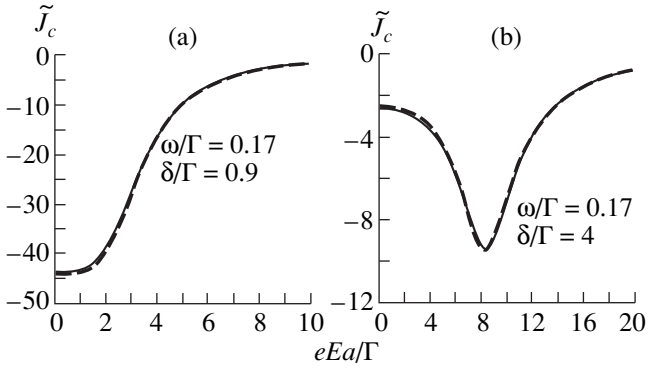

Fig. 4. Dependences of dynamic conductance J_c/eEa on the amplitude of alternating electric field for (a) classical and (b) quantum-mechanical modes of oscillations. Solid line corresponds to numerical solution, and the dashed line corresponds to analytical solution.

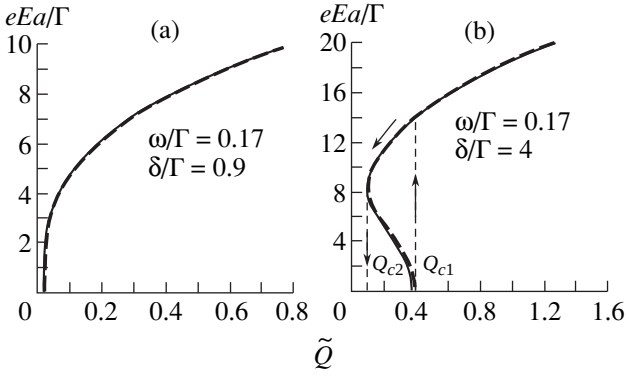

Fig. 5. Dependences of the generated field eEa/Γ on the dimensionless pump current $\tilde{Q}$ for (a) classical and (b) quantum-mechanical modes of oscillations. Q_{c1} and Q_{c2} are the currents corresponding to initiation and quenching of oscillations, respectively. The solid line corresponds to numerical solution, and the dashed line corresponds to analytical solution.

where

$$x = 1 + \frac{\tilde{E}^2(\Gamma^2 - \delta^2)}{(\Gamma^2 + \delta^2)^2},$$
$$y = \frac{2\delta\Gamma\tilde{E}^2}{(\Gamma^2 + \delta^2)^2}, \quad \tilde{E} = \frac{eEa}{2}. \tag{10}$$

The dependences of $\tilde{J}_c$ on the dimensionless field eEa/Γ are shown in Figs. 4a ($\delta = 0.9\Gamma$) and 4b ($\delta = 4\Gamma$). It can be seen that the shapes of the curves for $\tilde{J}_c$ differ radically in the classical ($\delta/\Gamma < 1$) and quantum-mechanical ($\delta/\Gamma > 1$) modes. In the first case, the gain decreases steadily with increasing field. In the quantum-mechanical mode, the gain $\tilde{J}_c$ first increases, attains a maximum, and then decreases. Such behavior gives rise to radical distinctions in the oscillations in a resonance TD for the quantum-mechanical mode (see below).

In order to determine the field for occurrence of oscillations in a resonance TD, we should substitute the

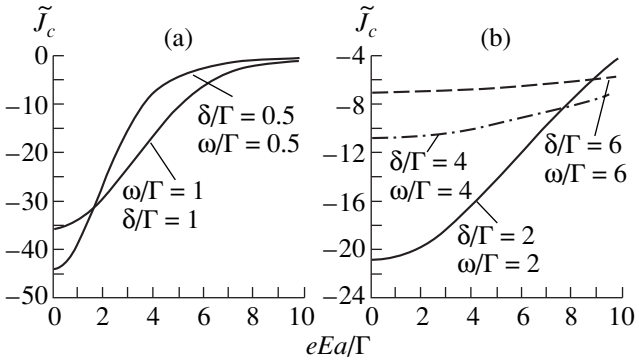

Fig. 6. Dependences of the dynamic conductance J_c/eEa on the amplitude of alternating electric field for (a) classical and (b) quantum-mechanical modes of oscillations.

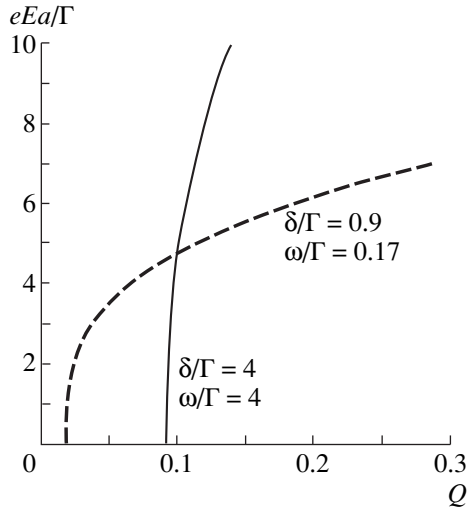

Fig. 7. The pump-current dependences of the field that sustains oscillations.

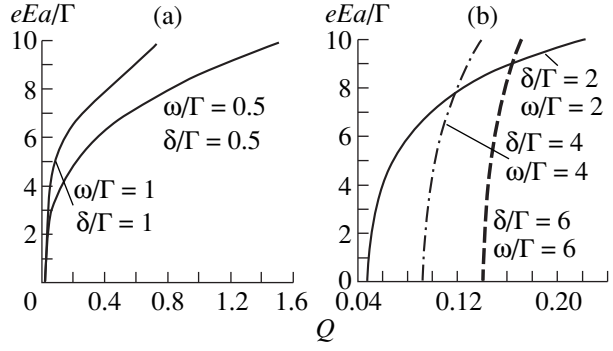

Fig. 8. The pump-current dependences of the field ensuring the oscillations for (a) small and (b) large values of frequency and the mismatch parameter.

expression for current (9) into the equation for the field (see [2, 4])

$$\frac{E_0}{\tau_0} = \frac{4\pi\tau}{\chi} J_c, \qquad (11)$$

where τ_0 is the time characterizing the losses in the cavity and χ is the permittivity.

Expression (11) makes it possible to determine the characteristic field (and power) of oscillations in relation to $\tilde{Q} = -1/\tilde{J}_c$, $\tilde{Q} = 4\pi\tau_0 eaQ/\chi$, and the parameters of a resonance TD. Figures 5a ($\delta = 0.9\Gamma$) and 5b ($\delta = 4\Gamma$) show eEa/Γ as a function of $\tilde{Q}$. It can be seen that, in the classical case, the soft mode of oscillation takes place in a resonance TD. If $\delta/\Gamma > 1$, the hard mode is observed, in which case oscillations set in abruptly for a certain critical value Q_{c1}. As $\tilde{Q}$ decreases, oscillations are quenched for $Q_{c2} < Q_{c1}$; i.e., a hysteresis occurs. Figures 4 and 5 also show the results of numerical calculations in the case of adiabatic limit for $\omega = 0.17\Gamma$. Good agreement between the analytically and numerically derived dependences is evident again, which demonstrates that the program performs adequately in the case of nonlinear theory as well.

5. NONLINEAR THEORY OF OSCILLATIONS IN A WIDE FREQUENCY RANGE

As far as we know, there are neither analytical nor numerical data on the dependence of the gain $\tilde{J}_c$ on the field amplitude in the most interesting frequency range of $\Gamma \le \omega \ll \varepsilon_R$. The program we developed makes it possible to obtain these data. Figures 6a and 6b show typical dependences of the gain $\tilde{J}_c$ on the field in the case of the additional condition for the quasi-resonance $\delta = \omega$. There are two special features of this set of the curves. Firstly, there is a steady decrease of $\tilde{J}_c$ with the field. Secondly, the rate of a decrease in the gain with the field decreases with increasing frequency. This fundamental result means that, in the quantum-mechanical mode, the fields attained when the condition for quasi-resonance is met are much higher than those attained in the classical mode. This is clearly evident from Fig. 7. In fact, it can be seen that, for $Q \ge 0.1$, the field in the quantum-mechanical mode ($\delta = \omega = 4\Gamma$) far exceeds the field in the classical mode ($\delta = 0.9\Gamma$ and $\omega = 0.17\Gamma$). Thus, the quantum-mechanical mode makes it possible to obtain higher power levels at high frequencies. The dependences of the field on Q for a wide range of parameters are shown in Figs. 8a and 8b. An analysis of these dependences makes it possible to optimize the conditions for oscillations by choosing the most suitable relations between the threshold, field, and frequency of oscillations.

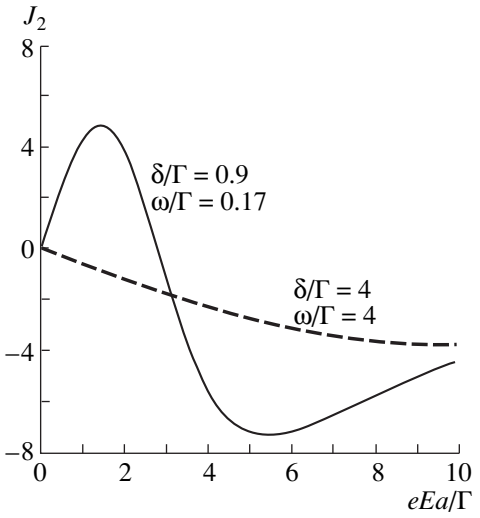

Fig. 9. The field-amplitude dependences of the second harmonic of current.

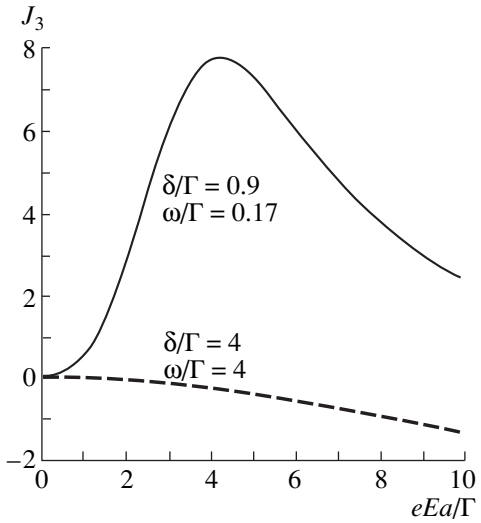

Fig. 10. The field-amplitude dependences of the third harmonic of current.

6. BEHAVIOR OF HIGHER HARMONICS

Generation of higher harmonics is possible owing to nonlinearity inherent in a resonance TD; i.e., the currents varying with frequencies that are multiples of $k\omega$ ($k = 2, 3, \ldots$) may appear. It is of interest to calculate the magnitude and sign of corresponding currents.

Figures 9 and 10 show the dependences of the second (J_2) and third (J_3) harmonics on the field for two different sets of parameters. It is worth noting that the current J_3 is always positive at low frequency, whereas J_2 changes sign with increasing field and becomes negative. Analytical results for adiabatic limit [4] are also shown. In the quantum-mechanical mode, J_2 and J_3 are negative but are small in absolute value.

7. CONCLUSION

Thus, the developed program for solving the Schrödinger equation supplemented with open boundary conditions made it possible to describe the coherent oscillations in a resonance TD within wide ranges of frequencies and field amplitudes. In the linear approximation and adiabatic limit, numerical results agree to a high accuracy with analytical results reported previously [2, 4]. In nonlinear approximation and for a wide range of frequencies, we obtained new results that allowed us to determine the dependence of the oscillation field on the current and the parameters of resonance TD. An important implication of these results is that, in the quantum-mechanical mode, high-power oscillations at frequencies exceeding the level width (i.e., in the terahertz range) are possible.

The program permits a generalization to more realistic models that, in particular, account for actual barriers, energy distribution of electrons, accumulation of charge, a constant external field, and so on.

APPENDIX

CALIBRATION USING A MODEL PROBLEM

The program was tested by comparing the numerical results with exact analytical solution to a model problem with a potential $v(x, t)$. Let us assume that the potential $v(x, t)$ has the form

$$v(x,t) = \begin{cases} \dfrac{U_1 + U_2}{U_3}, & x \in (0, L), \\ 0, & x \notin (0, L). \end{cases} \tag{A1}$$

Here,

$$U_1 = i\hbar\left\{\frac{dB}{dt}\cos^2\left(\frac{\pi x}{2L}\right)\exp(-ikx) + \frac{dC}{dt}\sin^2\left(\frac{\pi x}{2L}\right)\exp(ikx)\right\},$$

$$U_2 = \frac{\hbar^2}{2m^*}\frac{\pi}{L}\left\{\left(\frac{\partial\psi_2}{\partial t} - \frac{\partial\psi_1}{\partial t}\right)\sin\left(\frac{\pi x}{L}\right) + \frac{\pi}{2L}(\psi_2 - \psi_1)\cos\left(\frac{\pi x}{L}\right)\right\},$$

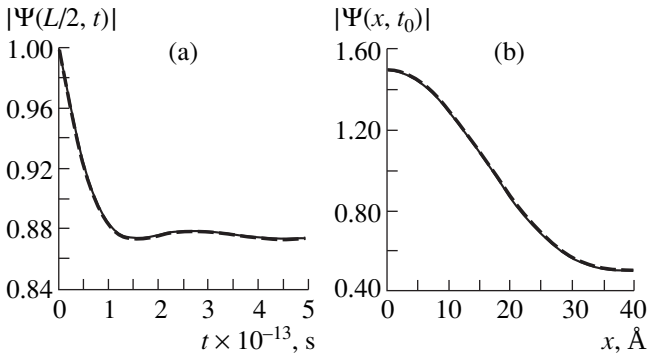

Fig. 11. Dependences of the wave-function magnitude $|\Psi|$ on (a) time t and (b) coordinate x ($t_0 = 5 \times 10^{-13}$ s corresponds to the time at which δ attains a maximum) for $\omega = 10^{13}$ Hz ($\delta_{max} = 3 \times 10^{-3}$). The dashed line represents the results of numerical calculation, and the solid line corresponds to analytical theory.

$$U_3 = \psi_1 \cos^2\left(\frac{\pi x}{2L}\right) + \psi_2 \sin^2\left(\frac{\pi x}{2L}\right),$$

$$C(t) = \frac{A}{2}[1 + \cos^2(\omega_0 t)\exp(-\omega_0 t)],$$

$$B(t) = A - C(t),$$

$$\psi_1 = A\exp(ikx) + B(t)\exp(-ikx),$$

$$\psi_2 = C(t)\exp(ikx), \quad \psi_0(x) = A\exp(ikx),$$

$$k = \sqrt{\frac{2m^*E}{\hbar^2}}, \quad A = 1,$$

$$E = 82 \text{ meV}, \quad L = 40 \text{ Å}, \quad m^* = 0.042m_e,$$

where m_e is the mass of free electron. For $\psi_0(x) = A\exp(ikx)$, a solution to Eq. (3) with potential (A1) is given by

$$\Psi_{teor}(x, t) = \begin{cases} \psi_1 \exp(-i\omega t), & x < 0, \\ [\psi_1 \cos^2(\pi x/2L) \\ + \psi_2 \sin^2(\pi x/2L)]\exp(-i\omega t), \\ 0 \le x \le L, \\ \psi_2 \exp(-i\omega t), & x > L, \end{cases}$$

$$\omega = \frac{E}{\hbar}.$$

The analytically and numerically determined dependences of the wave-function modulus $|\Psi|$ on the time t and coordinate x are shown in Fig. 11 for different values of ω_0. It can be seen that the degree of exactness of numerical solution to the problem is fairly high. The error in numerical solution is defined by the parameter

$$\delta = \frac{\int_0^L |\Psi_{teor} - \Psi_{numer}|\,dx}{\int_0^L |\Psi_{teor}|\,dx}$$

and does not exceed 3×10^{-3} for the calculation under consideration.

ACKNOWLEDGMENTS

We are grateful to Yu.V. Kopaev for his fruitful participation in discussions of the results. This study was performed under framework of the Special Federal Program "Integration" (project no. AO133) and was supported by the Ministry of Science of Russian Federation under the Program "Physics of Solid-State Nanostructures" (project no. 99-1140).

REFERENCES

1. E. R. Brown, T. C. L. G. Sollner, C. D. Parker, *et al.*, Appl. Phys. Lett. **55**, 1777 (1989); E. R. Brown, J. R. Södestrom, C. D. Parker, *et al.*, Appl. Phys. Lett. **58**, 2291 (1991).
2. V. F. Elesin, Zh. Éksp. Teor. Fiz. **116**, 704 (1999) [JETP **89**, 377 (1999)].
3. H. C. Liu and T. C. L. G. Sollner, Semicond. Semimet. **41**, 359 (1994).
4. V. F. Elesin, Phys. Low-Dimens. Structur. (1999) (in press).
5. V. I. Siforov, *Radio Receivers* (Nauka, Moscow, 1954).
6. A. A. Samarskiĭ and E. S. Nikolaev, in *Method for Solving the Difference Equations* (Nauka, Moscow, 1978), p. 83.

Translated by A. Spitsyn

Semiconductors, Vol. 34, No. 11, 2000, pp. 1327–1329. Translated from Fizika i Tekhnika Poluprovodnikov, Vol. 34, No. 11, 2000, pp. 1380–1382.

LOW-DIMENSIONAL SYSTEMS

Optical-Absorption Spectra of PbS/C-Based Fibonacci Superlattices with Phonon-Assisted Transitions

S. F. Musikhin*, O. V. Rabizo*, V. I. Il'in*, A. S. Fedorov*, and L. V. Sharonova**

** St. Petersburg State Technical University, Politekhnicheskaya ul. 29, St. Petersburg, 195251 Russia*

*** Ioffe Physicotechnical Institute, Russian Academy of Sciences, Politekhnicheskaya ul. 26, St. Petersburg, 194021 Russia*

Submitted May 23, 2000; accepted for publication May 24, 2000

Abstract—The method of laser-induced evaporation was used to form the Fibonacci superlattices in an *n*-PbS/C system (C stands for diamond-like carbon). The optical-absorption spectra in the range of 1.12–3.25 eV were compared with the electron energy spectrum calculated on the basis of the Kronig–Penney model. The electron-affinity energy in the diamond-like carbon was found to be 0.25 ± 0.05 eV. Fine structure in the absorption spectrum in the range of 1.7865–1.7914 eV is attributed to band-to-band transitions that involve phonons with energies of $(0.92–2.35) \times 10^{-3}$ eV. © *2000 MAIK "Nauka/Interperiodica".*

Nonperiodic Fibonacci superlattices (SLs) feature a specific energy spectrum that exhibits the manifestations of quasi-periodicity. Furthermore, this spectrum has a fractal structure if there is a large number of layers in an SL. The absence of strict periodicity in the energy spectrum gives rise to an irregular set of steps and plateaus in the absorption spectra. Such a feature of the spectrum allows one to determine the main parameters of the heterostructure (in particular, the energy-band offsets [1, 2]) by comparing the experimental and theoretical spectra.

In this paper, we report the results of studying the optical transmission spectra of SLs composed of the lead sulfide and diamond-like carbon layers and grown according to the rule of the Fibonacci sequence. The object of this investigation is SLs that contain two structural elements. Element *A* was composed of a 15-Å thick lead-sulfide layer and a 5-Å thick layer of diamond-like carbon; element *B* included a lead-sulfide layer 30 Å thick and a 5-Å thick layer of diamond-like carbon. The superlattice *S* = *ABAABABAABAABABAABABA* contained 21 pair of the layers grown by the method of the pulsed laser-assisted evaporation in vacuum [3]; the quartz substrates were used. The PbS films had the *n*-type conductivity with the electron concentration of 4×10^{17} cm^{-3}.

The transmission spectra were measured using an MDR-23 monochromator. In the range of photon energies of E = 1.12–3.25 eV, a high-power quartz incandescent lamp was used as the radiation source. In a narrow spectral range of E = 1.7865–1.7914 eV, the SL was irradiated with a helium–neon laser with the emission peaked at 1.78958 eV. The use of the laser made it possible to enhance the energy resolution in the spectrum to 8×10^{-6} eV and resolve the fine structure of the SL optical spectrum.

In optical spectra (see figure), the quantity $1 - T$, where T is the transmission coefficient of SL, is plotted on the vertical axis. This quantity is proportional to the absorption coefficient. In the case of irradiation with the light from an incandescent lamp, optical spectra of SL exhibit the features in the form of "steps" and absorption peaks that, as is known [1], are related to interband and intraband transition in the SL and also to optical ionization of quantum wells.

The energy spectrum of charge carriers in a Fibonacci SL was calculated using the Kronig–Penney model for interacting quantum wells separated by tunneling-transparent barriers. The potential-well depth for the conduction-band electrons is governed by the conduction-band offset $\Delta E_c = \chi_{PbS} - \chi_C$, where χ_{PbS} and χ_C are the electron affinities of lead sulfide and diamond-like carbon, respectively. The value of χ_{PbS} = 4.35 eV was determined in the studies of photoelectric properties of heterojunctions [4]. The data on the value of χ_C have a significant spread. Therefore, in order to determine the value of χ_C, we calculated the energy spectra of charge carriers in the SL for various values of ΔE_c. In the energy range of 3.50–4.35 eV, the calculation was performed with a step of 0.05 eV. The best fit of the results of calculations to experimental data was obtained for $\Delta E_c = (4.10 \pm 0.05)$ eV, which yielded $\chi_C = (0.25 \pm 0.05)$ eV.

The Fibonacci SL energy spectrum calculated for ΔE_c = 4.1 eV consists of six allowed minibands that are common for the entire SL in the conduction-band potential well and contain 53 electron levels E_K^N, where the superscript N denotes the number of a miniband and the subscript K stands for the level number in the miniband. The energy spectrum in the valence-band potential well consists of three minibands of allowed states

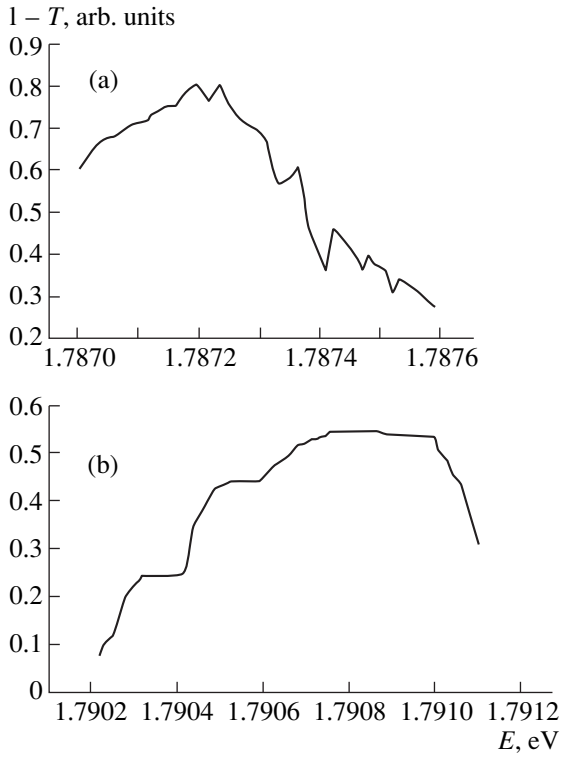

Absorption spectrum of PbS/C superlattice irradiated with a helium–neon laser. Panels (a) and (b) correspond to different spectral ranges.

with 18 allowed levels H_K^N. Since the lead-sulfide films had the *n*-type conductivity, the intraband transitions in the conduction-band potential well, interband transitions, and optical ionization of quantum wells are possible in the studied SLs.

The calculation was performed on the assumption that the first miniband in the conduction band $E_1^1 - E_8^1$ is occupied incompletely. The general shape of the SL absorption spectrum is consistent with the results of calculations.

The figure shows the spectra of optical absorption in the case when the SL was irradiated with a helium–neon laser. The spectral range of 1.7865–1.7914 eV overlaps in part with a "step" observed in studying the SL absorption spectra using an incandescent lamp. A characteristic feature of the spectra is their fine structure; i.e., there are six narrow absorption peaks located at energies lower than that corresponding to a maximum in the laser radiation (1.78958 eV) and three steps at the energies of 1.7903–1.7904, 1.7905–1.7906, and 1.7907–1.7910 eV that exceed the photon energy of the laser radiation. The first and third steps correspond to the energies of interband transitions $H_7^1 - E_1^2$ and $H_8^1 - E_1^2$ between the nearest allowed levels located in the first miniband of the valence-band potential well in PbS. Therefore, the emergence of the second step is not related to the band-to-band transitions because the latter would require a lower energy. Similarly, a series of six absorption peaks in the energy range of 1.78723–1.78756 eV is also unrelated to band-to-band transition in SL as the minimal difference in energy for two closest interband transitions exceeds severalfold the entire energy range where these absorption peaks are observed.

Parameters of the absorption peaks

Peak no.	Energy of the peak, eV (experiment)	Phonon energy, 10^{-3} eV
1	1.7823	2.35
2	1.78730	2.28
3	1.78735	2.23
4	1.78742	2.16
5	1.78750	2.08
6	1.78756	2.02
7	1.7905–1.7906	0.92–1.02

The obtained results can be explained if we assume that phonons are involved in the absorption processes the SL.

For the first six of the observed absorption peaks (see table), a photon with $E = 1.78958$ eV (a maximum of the laser radiation) is absorbed with accompanying emission of a phonon whose energy is no larger than 2.35×10^{-3} eV. A narrow "shelf" located in the energy range of 1.7905–1.7906 eV (higher than the energy of the maximum of the laser radiation) is related to absorption of a photon with an energy of $E = 1.78958$ eV and absorption of a phonon with an energy that is no higher than 1.02×10^{-3} eV.

The experimentally obtained values of phonon energies are several times lower than the energy of transverse optical phonon 8.2×10^{-3} eV for lead sulfide [5]. This distinction is explained by quantization of the phonon spectrum and a corresponding decrease in the range of variation in the wave vector of phonons in the Brillouin zone in the quantum-confinement structures [6].

Thus, the method of laser-assisted evaporation was used to deposit the *n*-PbS/C nonperiodic Fibonacci SLs onto the quartz substrates. We studied the SL transmission spectra in the energy ranges of 1.12–3.25 and 1.7865–1.7914 eV using an incandescent lamp and a helium–neon laser, respectively, as the radiation sources. We calculated the SL energy spectrum using the Kronig–Penney model for potential wells of various depths. On the basis of the obtained data, we found that the electron affinity of diamond-like carbon is equal to 0.25 ± 0.05 eV. Study of optical spectra excited by irradiation of SL with a helium–neon laser showed that the spectra has a fine structure. The spectral peaks related to absorption of photons in an SL accompanied by

emission or absorption of phonons with energies in the range of $(0.92–2.35) \times 10^{-3}$ eV were observed.

ACKNOWLEDGMENTS

This study was performed under the Program "Integration," project no. 75.

REFERENCES

1. A. Ya. Shik, *Two-Dimensional Electron Systems* (S-Peterburgs. Gos. Tekhn. Univ., St. Petersburg, 1993).
2. M. Qulichini, Rev. Mod. Phys. **69**, 277 (1997).
3. L. G. Bakueva, V. I. Il'in, S. F. Musikhin, and L. V. Sharonova, Fiz. Tekh. Poluprovodn. (St. Petersburg) **27**, 1868 (1993) [Semiconductors **27**, 1029 (1993)].
4. L. G. Bakueva, V. I. Il'in, and T. I. Zubkova, Fiz. Tekh. Poluprovodn. (Leningrad) **13**, 345 (1979) [Sov. Phys. Semicond. **13**, 199 (1979)].
5. Yu. I. Ravich, B. A. Efimova, and I. A. Smirnov, *Semiconducting Lead Chalcogenides* (Plenum, New York, 1970); *Methods for Studying the Semiconductors as Applied to Lead Chalcogenides PbTe, PbSe, and PbS* (Nauka, Moscow, 1968).
6. A. I. Kasiyan, *Kinetic Effects in Semiconductors of Various Dimensionalities* (Shtiintsa, Kishinev, 1989).

Translated by A. Spitsyn

Semiconductors, Vol. 34, No. 11, 2000, pp. 1330–1333. Translated from Fizika i Tekhnika Poluprovodnikov, Vol. 34, No. 11, 2000, pp. 1383–1385.

AMORPHOUS, VITREOUS, AND POROUS SEMICONDUCTORS

Electrical Properties of Hydrogenated Amorphous $Ge_{0.90}Si_{0.1}:H_x$ Films

B. A. Nadzhafov

Radiation Research Department, Azerbaijan Academy of Sciences, Baku, 370143 Azerbaijan

Submitted November 24, 1999; accepted for publication May 21, 2000

Abstract—Amorphous 1-μm thick films of the $Ge_{0.90}Si_{0.1}:H_x$ solid solution (x = 1.3, 5.1, 8.7, 14.2, and 23.7 at. %) were grown in a hydrogen atmosphere under various partial hydrogen pressures. The method of plasmachemical deposition with a rate of 0.3–0.5 Å/s was employed. Electrical conductivity of the films was measured within a temperature range of 100–420 K. The dark conductivity of the films was measured. The activation energy of hopping at T = 100 K, the hop range, the mobility of electrons at the levels ε_F and ε_C, and the activation energy of conductivity were calculated. © *2000 MAIK "Nauka/Interperiodica".*

The amorphous solid solutions of $Ge_{1-x}Si_x$ have attracted considerable interest in recent years as promising materials for applications in semiconductor electronics.

The hydrogenated amorphous solid solutions (a-$Ge_{1-x}Si_x$:H) possess an optimal band gap (1.1–1.85) eV for the conversion of solar energy to electricity, and the best optoelectronic properties in the long-wavelength range of the visible spectrum. They also are more thermodynamically stable and radiation-resistant compared to other amorphous materials. This makes it possible to use them as solar cells [1–3]. There are several publications devoted to the study of electrical properties of hydrogenated amorphous $Ge_{1-x}Si_x$:H films [4–6]. However, there is a lack of information about alloys with the low silicon content, though they are of a particular interest for optoelectronics in the near-IR and visible spectral regions. The objective of this study was to gain insight into the effect of hydrogen concentration on the electrical properties of the amorphous $Ge_{0.90}Si_{0.10}:H_x$ films (x is the amount of hydrogen in at. %). The nonhydrogenated amorphous $Ge_{1-x}Si_x$ films are known to possess a high density of states in the band gap. In order to reduce the number of these states the introduction of hydrogen is necessary. This can be achieved by growing the films in a hydrogen atmosphere.

The a-$Ge_{0.90}Si_{0.10}:H_x$ films were obtained by the plasmachemical deposition (at the Radiation Research Department of the Azerbaijan Academy of Sciences). The platelets of the crystalline $Ge_{0.90}Si_{0.10}$ alloy of 60–63 mm in diameter were used as targets. The material was deposited on a substrate under various hydrogen pressures. Based on these experiments, the optimal regime of deposition and hydrogenation of the material was determined. The temperature of the substrate (NaCl) was 420 K, the rate of the deposition of the material on the substrate was about 0.3–0.5 Å/s, and the distance between the target and the substrate was $l \approx 25$ cm. The growth of films lasted approximately one hour.

The electric field intensity during the measurements was no higher than 10^3 V/cm. An incandescent lamp with emissive power of about 90 mW/cm^2 was used as a light source. The absorption coefficient (β) within the range of photon energies utilized was as large as 10^4 cm^{-1} [4]. The quantity $\varepsilon_C - \varepsilon_V$ varied, depending on hydrogen content in the range of 0.83–1.17 eV because of the decrease in the density of the localized state in the mobility gap. The amorphism of the a-$Ge_{0.90}Si_{0.10}:H_x$ films was checked by electron diffraction. The thickness of the a-$Ge_{0.90}Si_{0.10}:H_x$ films, determined by the interference method [7], was 1.0 μm. The hydrogen content in the films was determined by the effusion method and from the absorption spectra [8, 9], and was in the range from 1.3 to 23.7 at. %.

The measurement of the electrical conductivity within the temperature range studied showed that two regions can be distinguished in $\sigma(T)$ dependence.

The high-temperature portion of $\sigma(T)$ is determined by the band conductivity (Fig. 1) and can be described by the well-known expression

$$\sigma_T = \sigma_0 \exp(-\Delta E/kT),$$
$$\sigma_0 = \text{const}\frac{e^2}{\hbar a}. \quad (1)$$

Assuming that const = 0.026 and a = 3 Å, we obtain $\sigma_0 = 200\ \Omega^{-1}\ \text{cm}^{-1}$ and greater at T = 300 K. The quan-

1063-7826/00/3411-1330$20.00

tity ΔE for electrons is given by $\Delta E = E_C - E_F$, where e is the elementary charge, $\hbar$ is Planck's constant, and a is the interatomic distance [10]. The low-temperature region is determined by the hopping conductivity over the localized states in the mobility gap as evidenced by a linear dependence of $\log\sigma$ on $T^{-1/4}$ (Fig. 2).

Within the temperature range studied, the electrical conductivity decreases with increasing hydrogen content in a film. Variation of electrical conductivity with the increase in hydrogen content in a high-temperature region occurs due to the increase in density of the states at the top of the valence band, whereas, in the low-temperature region, this can be a consequence of a decrease both in the mobility of charge carriers and in the density of states near the Fermi level (ε_F).

At comparatively low temperatures, a variable activation energy is observed, which can be interpreted as a fulfillment of Mott's law [10]:

$$\sigma = \sigma_1 \exp\left[-(T_0/T)^{\frac{1}{4}}\right], \qquad (2)$$

where

$$T_0 = 18\alpha^3/kN(\varepsilon_F). \qquad (3)$$

Here, σ_1 is the electrical conductivity of a film for $1/T \longrightarrow 0$ (for extrapolation, the experimental $\log\sigma$ vs. $T^{-1/4}$ dependences were used), k is the Boltzmann constant, $N(\varepsilon_F)$ is the density of states at the Fermi level (ε_F), and α is the wave-function damping parameter of electrons in the localized state and can be determined from the experimental data using equations (2) and (3). For x = 1.3–23.7 at. %, the reciprocal value of α is 7–9 Å. We note that the radius of wave functions for localized electrons in most amorphous materials is about 10 Å [11, 12], and the density of states is $N(\varepsilon_F) \approx 2 \times 10^{18}$–$2 \times 10^{19}$ cm^{-3} eV^{-1}. The analysis of the experimental field-effect data and the electron spin resonance (ESR) study [4, 13, 14] show that the density of states in the $Ge_{0.90}Si_{0.10}$:H_x films obtained by plasmachemical deposition is $N(\varepsilon_F) \approx 10^{19}$–$7 \times 10^{20}$ cm^{-3} eV^{-1}. This value is obtained from the intensity of the ESR absorption signal according to relation $N_s = \chi N(\varepsilon_F)kT$ (where the coefficient $\chi \approx 3$ [15]). The investigation shows that, in the amorphous $Ge_{0.90}Si_{0.10}$:H_x films (x = 1.3–23.7 at. %), a sufficiently intense ESR signal is observed, suggesting a high concentration of dangling bonds which stabilize unordered structures, with the density of paramagnetic centers decreasing from $N_s = 2 \times 10^{19}$ to 3×10^{17} cm^{-3} eV^{-1} with increasing hydrogen content from 1.3 to 23.7 at. % [4, 6]. This gives grounds to assume that the introduction of hydrogen causes the recovery of the dangling bonds and the reduction in the density of localized states in the band gap. Thus, the reduction of the electrical conductivity at low temperatures with increasing hydrogen content is mainly caused by the change in the density of states near the Fermi level. Based on the above parameters, it is concluded that the dark conductivity $\sigma_d(300)$ in the a-$Ge_{0.90}Si_{0.10}$ film decreases from 10^{-2} to 10^{-7} Ω^{-1} cm^{-1}. Using the data obtained in [10, 16] and other film parameters, we can estimate the activation energy, the

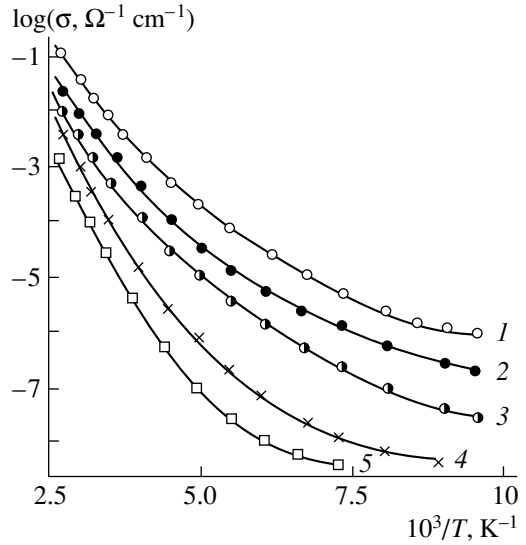

Fig. 1. The temperature dependences of dark electrical conductivity $\sigma(T)$ in $\log\sigma$ vs.$1/T$ coordinates for the amorphous a-$Ge_{0.90}Si_{0.10}$: H_x films; x = (*1*) 1.3, (*2*) 5.1, (*3*) 8.7, (*4*) 14.2, and (*5*) 23.7 at. %.

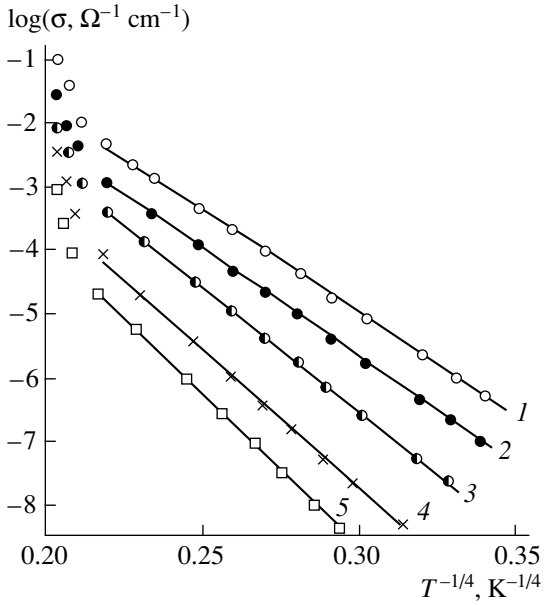

Fig. 2. The temperature dependences of dark electrical conductivity $\sigma(T)$ in $\log\sigma$ vs. $T^{-1/4}$ coordinates for the amorphous a-$Ge_{0.90}Si_{0.10}$:H_x films; x = (*1*) 1.3, (*2*) 5.1, (*3*) 8.7, (*4*) 14.2, and (*5*) 23.7 at. %.

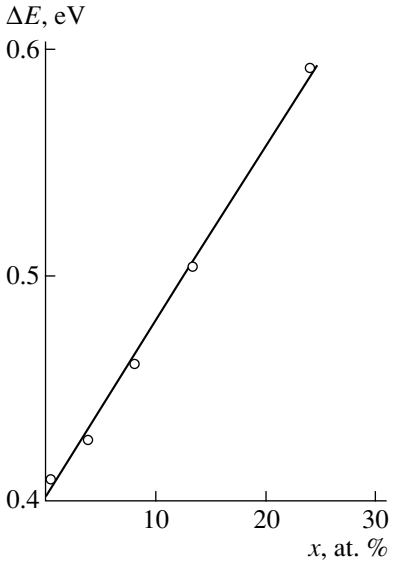

Fig. 3. Activation energy ΔE as a function of hydrogen concentration for the amorphous $Ge_{0.90}Si_{0.10}:H_x$ films.

hop range (E, R), and the mobility of electrons μ_F, μ_C at the ε_F and ε_C levels. The activation energy for hopping at 100 K can be calculated by the formula

$$E = \frac{2}{3}\alpha RkT = \left(T_0/3\pi^{\frac{1}{4}}\right)T^{\frac{3}{4}}, \quad (4)$$

where the hop range is given by

$$R = [9/8\pi\alpha N(\varepsilon_F)kT]^{\frac{1}{4}}. \quad (5)$$

It follows that at a temperature of 100 K, R = 110–150 Å, depending on hydrogen concentration. Then, the activation energy is found to be

$$E = (0.03\text{–}0.012)T^{\frac{3}{4}}\ \text{eV}.$$

As is known [9, 10],

$$\sigma = \mu_C N(\varepsilon_C)ekT\exp\left\{-\frac{\varepsilon_C - \varepsilon_F}{kT}\right\}. \quad (6)$$

The quantity σ was determined from the $\sigma(T)$ vs. $1/T$ dependence (Fig. 1). The density of states $N(\varepsilon_C)$ at the mobility edge in the range of kT under consideration is equal in our case to 10^{21} cm^{-3} eV^{-1} [10, 12]. Then, the mobility at the ε_C levels can be determined from expression (6) as

$$\mu_C = \frac{\sigma}{eN(\varepsilon_C)kT}\exp\left\{-\frac{\varepsilon_C - \varepsilon_F}{kT}\right\}. \quad (7)$$

Similarly, we can find the mobility at the Fermi levels, because, for $E_C = E_F$, $\sigma = \sigma_0$, and σ_0 is determined from formula (1). Thus, we obtain

$$\mu_F = \frac{\sigma_0}{eN(\varepsilon_F)kT}. \quad (8)$$

Depending on hydrogen concentration, the obtained parameters vary within the following ranges:

$$\mu_F = (10^{-2}\text{–}10^{-4})\ \text{cm}^2/(\text{V s}),$$

$$\mu_C = (3\text{–}9)\ \text{cm}^2/(\text{V s}).$$

Thus, we may conclude that the electrical and optical properties of the a-$Ge_{0.90}Si_{0.10}$ film can be controlled over a sufficiently wide range by varying the hydrogen concentration [4]. The variation of the activation energy of the conductivity with hydrogen above room temperature amounts to ΔE = (0.41–0.59) eV. In all the films studied, the dependence of ΔE on the band gap, measured optically, can be approximated by the formula $\Delta E = 0.5E_g^{\text{opt}}$, which is consistent with the same dependence known for a-Ge:Si:H. The calculated dependence of the activation energy on the concentration of hydrogen atoms inside the films is linear in the temperature range 300–420 K (Fig. 3).

It should be pointed out that the film parameters obtained by various methods can differ from one another, which is the case in our experiments [12, 17]. The results obtained are of interest for the fabrication of solar cells and IR photodetectors based on the a-Ge:Si:H films.

REFERENCES

1. G. Nakamura, K. Sato, Y. Yukimoto, *et al.*, Jpn. J. Appl. Phys. **20**, 291 (1981).
2. P. K. Banerjee, R. Dutta, and S. S. Mitra, J. Non-Cryst. Solids **50**, 11 (1983).
3. F. S. Nasredinov, A. A. Andreev, O. A. Golikova, *et al.*, Fiz. Tekh. Poluprovodn. (Leningrad) **17**, 1871 (1983) [Sov. Phys. Semicond. **17**, 1196 (1983)].
4. B. A. Najafov, M. Ya. Bakinov, and V. S. Mamedov, Phys. Status Solidi A **123**, 67 (1991).
5. A. F. Khokhlov, A. I. Mashin, A. V. Ershov, *et al.*, Fiz. Tekh. Poluprovodn. (Leningrad) **19**, 2204 (1985) [Sov. Phys. Semicond. **19**, 1360 (1985)].
6. B. A. Nadzhafov, M. Ya. Bakirov, and V. S. Mamedov, Dokl. Akad. Nauk Azerbaĭdzhana **2**, 30 (1989).
7. A. V. Rakov, in *Spectrophotometry of Thin Films* (Nauka, Moscow, 1975), p. 175.
8. H. Shank, L. Ley, M. Cardona, *et al.*, Phys. Status Solidi B **100**, 17 (1980).
9. Y. Catherine and G. Turban, Thin Solid Films **70**, 107 (1980).
10. N. F. Mott and E. A. Davis, in *Electronic Processes in Non-Crystalline Materials* (Clarendon Press, Oxford, 1979; Mir, Moscow, 1982), Vol. 2.

11. A. M. Szpilka and P. Viscer, Philos. Mag. B **45**, 485 (1982).

12. A. A. Andreev, O. A. Golikova, M. M. Kazanin, and M. M. Mezdrogina, Fiz. Tekh. Poluprovodn. (Leningrad) **14**, 1859 (1980) [Sov. Phys. Semicond. **14**, 1110 (1980)].

13. R. J. Loveland, W. E. Spear, and A. Al-Sharbaty, J. Non-Cryst. Solids **13**, 55 (1973).

14. *The Physics of Hydrogenated Amorphous Silicon*, II: *Electronic and Vibrational Properties*, Ed. by J. D. Joannopouls and G. Lucovsky (Springer-Verlag, New York, 1984; Mir, Moscow, 1988).

15. *Amorphous Semiconductors*, Ed. by M. H. Brodsky (Springer-Verlag, New York, 1979; Mir, Moscow, 1982).

16. S. K. Bahl and S. M. Bhagat, J. Non-Cryst. Solids **17**, 409 (1975).

17. M. Ya. Bakirov, B. A. Najafov, V. S. Mamedov, and R. S. Madatov, Phys. Status Solidi A **114**, 45 (1989).

Translated by A. Zalesskiĭ

Semiconductors, Vol. 34, No. 11, 2000, pp. 1334–1337. Translated from Fizika i Tekhnika Poluprovodnikov, Vol. 34, No. 11, 2000, pp. 1386–1390.

AMORPHOUS, VITREOUS, AND POROUS SEMICONDUCTORS

Photoresponse and Electroluminescence of Silicon–⟨Porous Silicon⟩–⟨Chemically Deposited Metal⟩ Structures

L. V. Belyakov, D. N. Goryachev, and O. M. Sreseli*

Ioffe Physicotechnical Institute, Russian Academy of Sciences, Politekhnicheskaya ul. 26, St. Petersburg, 194021 Russia

** e-mail: Olga.Sreseli@pop.ioffe.rssi.ru*

Submitted May 15, 2000; accepted for publication May 17, 2000

Abstract—Photoelectric and electroluminescent properties of silicon–⟨porous silicon⟩ structures with chemically deposited metal contacts were investigated. The large specific surface area of the contact and selective metal deposition only on the macrocrystalline elements of the structure provide better photoelectric performance of the photodiodes compared to the structures with evaporated contacts, especially in the short-wavelength spectral range. The obtained electroluminescence spectra are explained by metal–silicon barrier properties under forward bias and by double carrier injection into nanocrystallites under reverse bias. © *2000 MAIK "Nauka/Interperiodica".*

1. INTRODUCTION

Currently, much attention is being given to porous silicon (*por*-Si), a silicon modification based on nanocrystallites. Despite the great number of publications concerned with the optical properties of *por*-Si, its photoelectric properties have been studied to a much lesser extent. In particular, the possibility of using *por*-Si in photodetectors has been discussed [1–4]. A quantum efficiency of almost 100% has been obtained in the 700–900 nm spectral range for thin *por*-Si layers in Schottky structures on silicon without antireflection coating [1]; thicker *por*-Si layers in similar structures give photodetector spectral characteristics similar to those of *por*-Si–Si heterojunctions [2].

Solid-state structures based on *por*-Si are usually regarded as prospective light-emitting diodes (LEDs). However, the different electroluminescence spectra under forward and reverse bias [5], large spread in the values of the obtained quantum efficiencies [6, 7], and different ranges of applied voltages [8, 9] indicate that these systems have a structure much more complicated than that of a simple diode.

This study is concerned with photoelectric and electroluminescent properties of the Si–*por*-Si structures with a chemically deposited metal contact. The area of the metal–silicon contact was expected to be larger owing to metal ion penetration inside pores. For comparison, samples prepared in a similar way, but with a vacuum evaporated contact, were studied.

2. EXPERIMENTAL

The *por*-Si layers were prepared using *n*-Si with resistivity of 2–4 Ω cm. Si wafers were subjected to electrolysis of varied duration in an electrolyte containing 40% hydrofluoric acid, water, and ethanol (HF : H_2O : C_2H_5OH = 1 : 1 : 2). The current density was 10–20 mA/cm^2, and during electrolysis, the samples were illuminated with white light of 10^{-2} W/cm^2 intensity. After electrolysis, the metallization of the *por*-Si layer was performed.

Photoluminescence (PL), electroluminescence (EL) and photoresponse spectra were measured at room temperature using a computer-based setup composed of an MDR-2 or SPEX-22 monochromator and a selective lock-in amplifier.

The light of a gas-filled lamp (2600 K) was modulated at a frequency of 18 Hz, passed through a monochromator, and focused on the outer (metal side) surface of the sample to stimulate the photoresponse. The biased and unbiased photovoltage and photocurrent modes were used.

The PL was stimulated by 10-ns laser pulses with λ = 337 nm at a 100-Hz repetition rate, and the EL, by current pulses at a repetition rate of 330 Hz with off-duty factor equal to 2. A FEU-79 photomultiplier and cooled germanium detector (North Coast) served as photodetectors.

The obtained PL and EL spectra were normalized with regard to the sensitivity of the entire system (detector and monochromator), and the photoresponse spectra were normalized only on the basis of the black-

1063-7826/00/3411-1334$20.00

body curve with the temperature at 2600 K (the Planck curve). As a result, the specific features of the optical system were retained in the photoresponse spectra (see a standard photodiode spectrum in Fig. 1, curve *4*).

3. RESULTS AND DISCUSSION

3.1. Specific Features of Chemically Deposited Metal Contact

In this study, we used the chemical deposition of silver, based on the substitution of deposited metal atoms for surface silicon atoms. This is a typical example of corrosive Si dissolution under the action of an oxidizing agent whose role can be played, in particular, by solutions of copper, silver, and gold salts. Under these conditions, the reduction of these compounds, associated with the silicon dissolution, results in the deposition of the respective metals onto the silicon surface. This method of metal deposition differs from vacuum evaporation or from electrolytic deposition in that the metal atoms are deposited onto an open, oxide-free silicon surface. Moreover, in our opinion, this method exhibits one more feature—selective metal deposition. Special deposition regimes can be selected, with metal deposited only onto the bulk silicon surface (bottom of pores and silicon macrocrystallites surface), rather than onto the nanocrystallites.

This differentiation is associated with the increase in the band gap (E_g) of silicon nanocrystallites as their size decreases and with the dependence of the corrosion resistance of the semiconductor on the E_g value. It is known that for atomic lattices of the Si, Ge, etc. types (if only the nature of their interatomic bonds remains unchanged) a certain parallelism exists in the behavior of the interatomic bond strength and the corresponding band gap [10]. This is the case when size-related changes in the band gap of silicon nanocrystallites occur. The wider the E_g, the stronger the interatomic bonds in a silicon crystallite and the higher its chemical and, in particular, corrosive resistance. As a result, a situation arises when the smallest nanocrystallites cannot be involved in the substitution of metal atoms for those of silicon.

The metal ions penetrate inside the porous layer through coarse pores and are deposited on the silicon surface between nanocrystallites coated with a thin oxide layer. Structures with varied properties are formed, depending on the quantity of deposited metal. If the metal layer is very thick, the nanocrystallites may be totally short-circuited by metallic filaments and dendrites penetrating into the pores. At the same time, the optimal choice of the amount of deposited metal makes it possible to take advantage of a closer contact (without oxide interlayer) with a large area without losing the specific features caused by the nanocrystallites.

Vacuum evaporation of a semitransparent gold layer onto chemically deposited metal forms a fairly complex structure comprising parallel- and series-connected Schottky barriers: ⟨bulk Si⟩–⟨chemically deposited metal⟩ and ⟨outer *por*-Si surface⟩–⟨evaporated metal⟩, and also Si–*por*-Si heterojunctions.

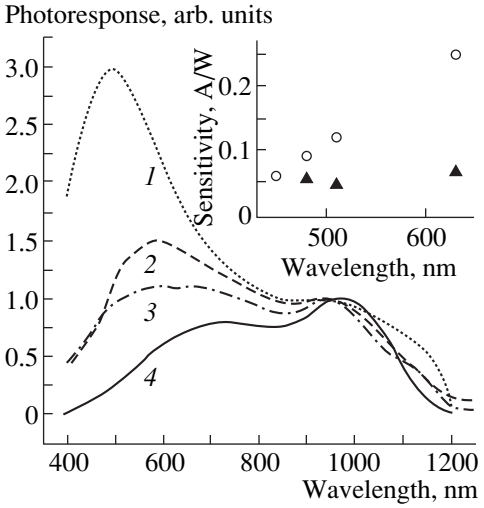

Fig. 1. The photoresponse spectra (open-circuit photovoltage) of various structures, calibrated to unity at 940 nm: (*1*) ⟨evaporated semitransparent Au layer⟩–⟨*por*-Si⟩–⟨Si substrate⟩; (*2*, *3*) structures with chemically deposited silver contact, differing in Ag deposition time; and (*4*) commercial silicon photodiode. Insert: spectral efficiencies of one of the structures studied (triangles) and a conventional Si photodiode (circles).

3.2. Photoelectric Properties

It was found experimentally that the structures studied (Si–⟨*por*-Si with chemically deposited contact⟩) have a substantially lower resistance R_0 (differential resistance at zero bias) and smaller reverse current than structures with only an evaporated contact. This anticipated result explains the significant increase in the metal contact area and substantial improvement of the Schottky barrier quality.

The open-circuit photoresponse spectra of the samples (Fig. 1) are characterized, in addition to the main peak in the IR range, by a short-wavelength peak that is much more pronounced than that in similar structures on *p*-type substrates [2]. This peak is higher for structures with evaporated Schottky contact, in comparison with those with chemically deposited Ag (cf. curve *1* with curves *2*, *3*, Fig. 1). With the time of chemical metal deposition increasing and/or the porous layer becoming thinner, the short-wavelength peak becomes lower (curves *2*, *3*) to the point of a nearly complete coincidence of the spectrum with that of a silicon photodiode (Fig. 1, curve *4*).

The short-wavelength PL peak is close in position to the PL band of porous silicon [2]. This peak is evidently associated with the absorption of light in this layer, whereas the absorption of light in bulk silicon is responsible for the long-wavelength portion of the spectrum.

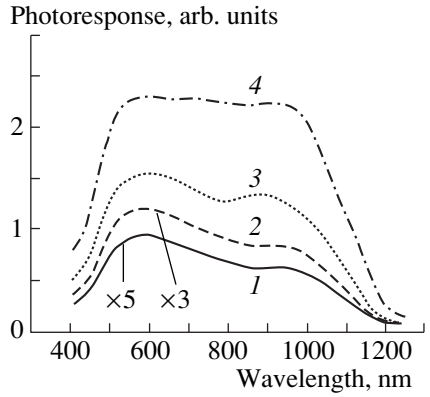

Fig. 2. Photoresponse (photocurrent) spectra of Au/Ag–*por*-Si–Si-substrate structure (for the photovoltage, see curve *2* in Fig.1) under the biases of (*1*) 0, (*2*) 0.4, (*3*) 1.5, and (*4*) 4.5 V.

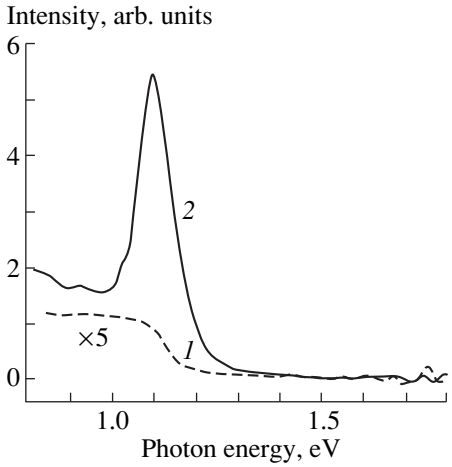

Fig. 3. EL of a ⟨chemically deposited metal⟩–*por*-Si–Si-substrate structure under forward bias. Current-pulse amplitude was (*1*) 0.2 and (*2*) 1 A.

In the open-circuit mode, the charge carriers photogenerated in the crystallites are separated at the metal–*por*-Si Schottky barrier with a tunneling-thin oxide: electrons drift in the substrate direction and holes are trapped at the oxide boundary. The electron–hole pairs generated in the substrate are separated in the space charge region of silicon, with holes accumulated at the Si–*por*-Si heterointerface. In the case of direct contact between the metal and the substrate, the separation of carriers absorbed in silicon may also occur at the metal–Si barrier.

The changes in the photoresponse spectra induced by the variations in the amount of deposited metal can be explained as follows: With an increase in the chemical deposition time, the nanocrystallites responsible for the short-wavelength portion of the spectrum are progressively embedded in the metal layer being deposited and are short-circuited by metallic filaments. For technological reasons, this overgrowth starts from the surface, where the majority of the small nanocrystallites are located. For metals with large thickness, and with deep and wide enough pores accessible to the electrolyte, the metal–silicon junction remains the only junction contributing to the photoresponse. Its spectrum approaches that of a conventional silicon photodiode.

When the external circuit includes a certain load and a bias is applied, the relative resistances of all the contact components are to be taken into account, namely, the metallic filaments, *por*-Si crystallites, and also nonlinear resistances of Schottky barrier and heterojunction, which depend on the sign and magnitude of the applied bias.

In the short-circuit mode, with the load connected, the relative magnitude of the short-wavelength peak decreases. A similar effect is observed when external reverse bias is applied to the structure (Fig. 2), with the total photocurrent increasing with bias. This behavior is explained by the strong nonlinearity of the *por*-Si–metal junction responsible for the short-wavelength portion of the spectrum. This junction is characterized by a smaller photocurrent [11], compared with the more ideal metal–Si junction and the *por*-Si–Si heterojunction.

It should be noted that, with the proper choice of the porous layer thickness and the amount of deposited metal, a photodiode structure can be obtained with a short-wavelength sensitivity higher than that of a common silicon photodiode. As an example, the insert in Fig. 1 shows the spectral efficiency of one of the structures studied and a conventional silicon photodiode. It may be noted that the structure is not optimized and has no antireflection coating. The high efficiency of the structure is primarily due to the highly developed contact surface, absorption of light in the porous silicon crystallites, and the well-known hydrogen passivation of the surface of porous silicon, diminishing the rate of surface carrier recombination practically to zero.

3.3. Electroluminescence

Structures with chemically deposited contacts demonstrate much more intense EL at smaller currents than structures with evaporated contact. The EL is observed both under forward (with the Si substrate negative) and under reverse biases, with markedly different EL spectra. Under forward bias (Fig. 3), the emission mainly occurs in the long-wavelength spectral range, while under reverse bias a broad spectrum is observed, with the peak corresponding to the PL of porous silicon (Fig. 4). The EL spectrum considerably varies in shape with increasing voltage under forward bias. A peak with a position closer to that of the peak observed for a Schottky structure formed on a smooth single-crystal silicon surface appears at high biases (Fig. 3, curve *2*).

Based on the model of the porous-layer structure and metal contact (chemically deposited or vacuum-

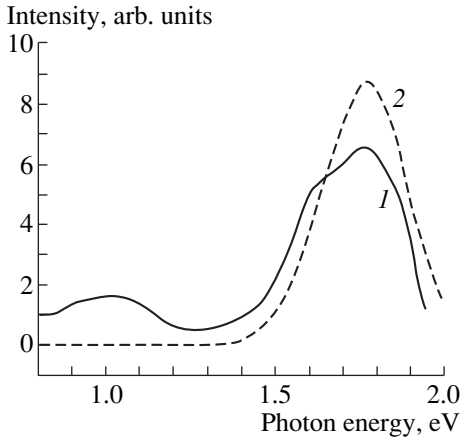

Fig. 4. Spectra of (*1*) EL under reverse bias at a current of 70 mA and (*2*) PL for one of the samples studied.

sputtered), we assume that, under forward bias, the current flows through the metal layer that short-circuits the microcrystallites, i.e., directly through the contact of the silicon substrate with the metal. During small biases, we observe a spectrum due to the injection of electrons into the metal (luminescence with energy lower than the Schottky barrier height). With an increase in the forward current, holes start to tunnel into silicon and undergo a band-to-band recombination there. The factor of hole injection from the metal is fairly high because of the contact inhomogeneity and the resulting high local current densities. Owing to the high resistance of nanocrystallites, only a small fraction of the total current flows through them, giving rise to a low-intensity short-wavelength spectral EL component decaying at about 2 eV.

Under reverse bias, a small leakage current flows through the Schottky barrier. An increase in the reverse bias leads to a double injection of carriers into the nanocrystallites through oxide barriers, similar to double injection into a luminophor crystal with two insulating barriers. The holes are injected from the semiconductor because of the band inversion at the heterojunction, and electrons are injected from the semitransparent metal contact. The thin oxide barriers form "wells" for electrons and holes, that are mainly responsible for the slow EL component. The luminescence spectrum is governed by the ensemble of isolated crystallites that are not coated with chemically deposited metal and coincides with the PL spectrum (Fig. 4, curves *1*, *2*).

4. CONCLUSION

(1) The results obtained demonstrate the complex nature of interaction and influence of three types of contacts (metal–*por*-Si, *por*-Si–Si, and metal–Si) on the photoresponse and EL.

(2) A metal contact that is well developed and penetrates inside the porous layer is of interest owing to its large area and selective metal deposition on the macrocrystalline elements of the layer. Moreover, the optimal ratio between the thicknesses of the porous layer and metal coating is very vital; this ratio governs the contributions of various types of contacts to structure parameters and the shape of their photoelectric characteristics.

(3) Structures with chemically deposited metal contacts show better photoelectric characteristics than those with vacuum-sputtered contacts. Combined with the presence of a heterojunction with a wide-gap window in the structure, this feature makes the structures studied promising as photodiodes for the short-wavelength (0.4–0.55 μm) spectral range.

(4) The EL from the structures may be of interest for further investigations of the current flow mechanisms in developing light-emitting devices based on porous silicon.

ACKNOWLEDGMENTS

This study was supported in part by the Program "Physics of Solid-State Nanostructures" of the Ministry of Science of the Russian Federation, project nos. 99-1107 and 97-1035.

REFERENCES

1. J. P. Zheng, K. L. Jiao, W. P. Shen, *et al.*, Appl. Phys. Lett. **61** (4), 459 (1992).
2. L. V. Belyakov, D. N. Goryachev, O. M. Sreseli, and I. D. Yaroshetskiĭ, Fiz. Tekh. Poluprovodn. (St. Petersburg) **27** (8), 1371 (1993) [Semiconductors **27**, 758 (1993)].
3. P. M. Fauchet, J. von Behren, K. D. Hirschman, *et al.*, Phys. Status Solidi A **165** (3), 3 (1998).
4. D. Dimova-Malinovska, J. Lumin. **80**, 207 (1999).
5. D. Dimova-Malinovska, M. Tzolov, N. Tzenov, and D. Nesheva, Thin Solid Films **297**, 285 (1997).
6. A. Loni, A. J. Simons, T. I. Cox, *et al.*, Electron. Lett. **31**, 1288 (1995).
7. A. J. Simons, T. I. Cox, A. Loni, *et al.*, in *Proceedings of International Symposiun on Advanced Luminescent Materials*, Ed. by D. J. Lockwood, P. M. Fauchet, N. Koshida and S. R. J. Brueck (Electrochemical Society, Pennington, 1996), PV 95–25, p. 73.
8. L. Tsybeskov, S. P. Duttagupta, K. D. Hirschman, and P. M. Fauchet, Appl. Phys. Lett. **68** (15), 2058 (1996).
9. T. Oguro, H. Koyama, T. Ozaki, and N. Koshida, J. Appl. Phys. **81** (3), 1407 (1997).
10. B. F. Ormont, *Introduction to Physical Chemistry and Crystal Chemistry of Semiconductors* (Vysshaya Shkola, Moscow, 1982).
11. A. M. Vasil'ev and A. P. Landsman, in *Semiconductor Converters* (Sov. Radio, Moscow, 1971), Chap. 4, p. 160.

Translated by D. Mashovets

Semiconductors, Vol. 34, No. 11, 2000, pp. 1338–1340. Translated from Fizika i Tekhnika Poluprovodnikov, Vol. 34, No. 11, 2000, pp. 1391–1393.

PHYSICS OF SEMICONDUCTOR DEVICES

Laser Waveguide with a Reverse Gradient of the Refractive Index

E. Yu. Kotel'nikov, I. V. Kudryashov, M. G. Rastegaeva, A. A. Katsnel'son, A. S. Shkol'nik, and V. P. Evtikhiev

Ioffe Physicotechnical Institute, Russian Academy of Sciences, Politekhnicheskaya ul. 26, St. Petersburg, 194021 Russia

Submitted April 11, 2000; accepted for publication April 13, 2000

Abstract—A nonconventional design of waveguide for a semiconductor injection laser is suggested; this design makes it possible to reduce the power density at the laser-diode mirror as a result of a more uniform distribution of the main-mode field. The second advantage of using this type of waveguide is the possibility of exerting a more pronounced suppression of lasing at high-order transverse modes. An additional advantage is that such a waveguide can accommodate several active regions separated by a large distance, so that the optical-confinement factor for them is nearly the same. The essence of the design consists in using a profile of the refractive index that decreases up to the middle of the waveguide. *© 2000 MAIK "Nauka/Interperiodica".*

Progress in obtaining a high-power emission from semiconductor injection lasers is associated [1] with the use of heterostructures that have a broadened waveguide (WG). This is due to the fact that the use of a broadened WG makes it possible to attain low internal losses and reduce the optical-power density at the laser-diode mirrors. However, a further increase in the WG width is hampered by the fact that the high-order even transverse modes become dominant in the far-field radiation zone of such a laser. In this paper, we suggest a new laser-WG design that makes it possible both to reduce the power density at the mirror and to further suppress lasing at the high-order modes. The basis of the proposed WG design consists in that the refractive index of the WG material is made larger at the WG periphery than in the middle.

Such a distribution of the refractive index is the opposite of that used conventionally in the so-called gradient-index (GRIN) WGs. As calculations show, the mode field fills the volume of the suggested reverse-gradient-index (RGRIN) WG more uniformly. The maximum power density at the mirror is reduced owing to a more uniform filling of the WG. Consequently, we may hope that a laser with the RGRIN WG will deliver a larger optical power restricted by the catastrophic degradation of the mirrors.

As an example, we calculated [2] the distributions of the mode fields for three different types of laser WGs. Figure 1 shows the mode distribution for a conventional constant-index WG, with the emitters being made of $Al_{0.6}Ga_{0.4}As$, and the WG of $Al_{0.3}Ga_{0.7}As$. For the sake of comparison, Fig. 2 shows the corresponding distribution for a "conventional" GRIN WG with a linear law of variation in the refractive index, and Fig. 3 shows the distribution for a RGRIN WG. In the latter case, the law of variation in the refractive index was also linear.

A comparison of Figs. 1–3 makes it possible to infer that a WG with a "conventional" gradient of the refractive index confines the main mode better; therefore, this WG allows one to obtain a larger optical-confinement factor Γ and, consequently, a lower threshold-current density. However, in a wide WG, the mode is confined by the WG itself rather than by the emitter boundaries, as is the case for the conventional constant-index WG. This effect becomes evident for a large WG thickness; it results in a larger width of the far-field zone than in the case of a constant-index WG.

A constant-index WG is intermediate in the factor Γ between the GRIN and RGRIN WGs; it confines a mode owing only to a difference in the refractive indices at the emitter boundaries; as a result, the mode field penetrates deeper into the emitters if such a WG is used.

As can be seen from Fig. 3, an RGRIN WG can feature the zero mode with a "flat" top. The optical-confinement factor Γ in such a WG is obviously smaller than those in the two previous WGs; this is related to the fact that the mode fills the WG bulk more uniformly, whereas the power density in the vicinity of the WG center, where the power density is highest, is lower in such a WG. According to our estimations, it is possible to reduce the maximum power density by a factor of 1.3, leaving the near-field pattern unchanged.

Here, we should mention a certain difficulty. It is observed that, in the most widely used III–V compounds, the band gap decreases with an increasing refractive index. Thus, in a laser with a large reverse gradient of the refractive index, a built-in pseudoelectric field appears and impedes the arrival of charge carriers to the active region. However, in the WGs, where

1063-7826/00/3411-1338$20.00

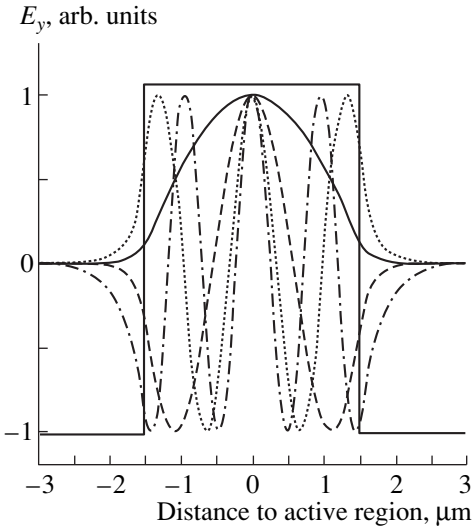

Fig. 1. The mode-field distribution in a laser with a constant-index waveguide. The emitters are made of $Al_{0.6}Ga_{0.4}As$, and the waveguide is made of $Al_{0.3}Ga_{0.7}As$. The wavelength of radiation is 0.98 μm.

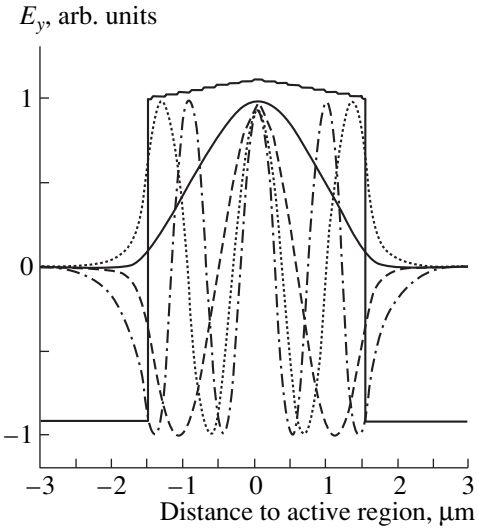

Fig. 2. Distribution of modes in a laser with a gradient-index waveguide. The composition of emitters is $Al_{0.6}Ga_{0.4}As$, the waveguide composition in the vicinity of the active region is $Al_{0.292}Ga_{0.708}As$, and the waveguide composition at the boundaries with emitters is $Al_{0.308}Ga_{0.692}As$. The emission wavelength is 0.98 μm.

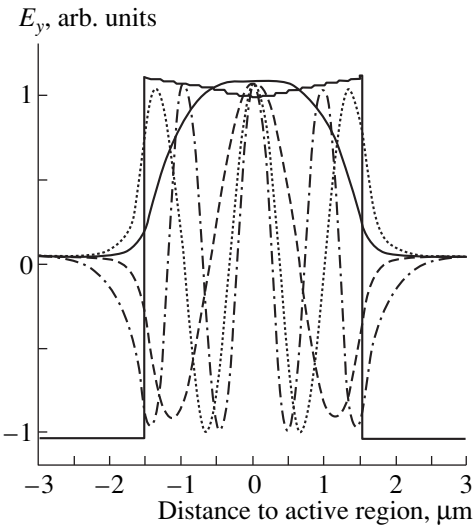

Fig. 3. Distribution of modes in a laser with a reverse-gradient-index waveguide. The material composition of emitters is $Al_{0.6}Ga_{0.4}As$, of the waveguide at its middle is $Al_{0.308}Ga_{0.692}As$, and of the waveguide at the boundary with emitters is $Al_{0.292}Ga_{0.708}As$. The emission wavelength is 0.98 μm.

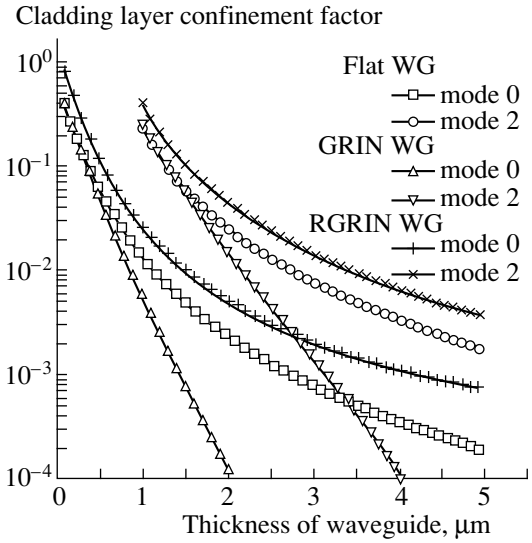

Fig. 4. The optical-confinement factor for emitters in waveguides of different designs. The emission wavelength is 0.98 μm. The waveguide designs correspond to those shown in Figs. 1–3. GRIN WG stands for a gradient-(refractive) index waveguide, and RGRIN WG stands for the reverse-index-gradient waveguide.

the diffusion length of electrons exceeds the WG thickness, details in the structure of the WG do not affect the charge-carrier collection. In wider WGs, a poorly pronounced reverse refractive-index gradient is sufficient for obtaining a flat-topped mode distribution. Thus, for example, in the WG 4 μm thick at a wavelength of 0.98 μm, it is sufficient to change the fraction of aluminum in an AlGaAs solid solution by merely 1.6%, which results in the WG nearly becoming a constant-index WG, because a change in the band gap in this case amounts to about 25 meV.

The second advantage of a WG with a reverse-gradient refractive index is that this WG provides the addi-

tional possibility of retaining the single-mode lasing in lasers with large WG thicknesses. As is known, we can eliminate all odd-order modes by locating the active region at the middle of a symmetric WG. It was noted previously [1] that, in order to suppress the high-order even modes, one can make use of the distinction between the field-distribution function for these modes and that for the main mode (the higher-order modes penetrate deeper into the emitter layers). This fact is used to introduce selective losses for these modes due to absorption in the emitter layers. Such losses give rise to free charge carriers and dopant atoms.

In order to assess the effectiveness of this method in various types of WGs, we calculated the factors of optical confinement for emitters (or, in other words, a fraction of the mode that propagates outside the WG over the emitter layers). Figure 4 shows the dependences of the above factors on the WG thickness for the main (zero) and second modes.

As would be expected, a classical gradient-index WG features the best ratio of optical-confinement factors for these two modes. In addition, this ratio increases with increasing WG width. However, very small values of this quantity, even for the second mode, make it difficult to attain the required discrimination of this mode in wide WGs. In a constant-index WG, the above ratio is smaller and remains virtually unchanged with increasing WG width. In the WGs with a reverse refractive-index gradient (RGRIN), the ratio of optical-confinement factors for emitters is slightly smaller and decreases with increasing WG width. However, this ratio remains equal to about 8–10 even in very wide WGs. This is quite sufficient for the suppression of the second and higher modes. Moreover, since the field of any mode decays exponentially in the emitter and the exponent in this exponential function increases with decreasing mode number, the use of the spacer layers may increase the optical-confinement factor for emitters when it is required. Such a situation provides reasons to believe that, in spite of the small ratio of the optical-confinement factors in the active region for the main and second modes, it is possible to attain the lasing at the main mode in such a WG.

It should be noted that it is also possible to increase the optical-confinement factor for emitters by using a weak optical confinement (i.e., a slight difference in the refractive indices between the WG and emitters). However, in this case, we would apparently have a slight confinement for nonequilibrium charge carriers, which would result in a decrease in the injection factor.

The third advantage of using a WG with a reverse-gradient of the refractive index is that, in the region of the highest field density, one can arrange several widely separated active regions so that the optical-confinement factors would be nearly the same for them. This fact ensures a wider choice in the design of lasers with several active regions. Such an arrangement of active regions is inherent, in particular, in the lasers based on quantum dots in which case the active-region material has the lattice constant differing from that of the substrate and the gain in a single active region is not sufficiently high.

CONCLUSION

The design of the semiconductor injection laser WG we suggest yields a more uniform distribution of the main-mode field over the cavity mirrors, which makes it possible to increase by a factor of about 1.3 the maximum power density restricted by the catastrophic degradation of the mirrors. In view of pronounced penetration of the higher-order modes into emitter regions of the laser, there arises an additional possibility of suppressing the lasing at these modes as a result of high optical losses in the doped regions. The mode-field distribution in the proposed WG makes it possible to arrange several active regions in such a way that the optical-confinement factors for these regions would be nearly the same.

ACKNOWLEDGMENTS

This study was supported by the Russian Foundation for Basic Research.

REFERENCES

1. A. Al-Muhanna, L. I. Mawst, D. Botez, *et al.*, Appl. Phys. Lett. **71**, 1142 (1997).
2. R. F. Kazarinov, O. V. Konstantinov, V. I. Perel', and A. L. Éfros, Fiz. Tverd. Tela (Leningrad) **7**, 1506 (1965) [Sov. Phys. Solid State **7**, 1210 (1965)].

Translated by A. Spitsyn

Semiconductors, Vol. 34, No. 11, 2000, pp. 1341–1342. Translated from Fizika i Tekhnika Poluprovodnikov, Vol. 34, No. 11, 2000, pp. 1394–1395.

PHYSICS OF SEMICONDUCTOR DEVICES

The Power Density Giving Rise to Optical Degradation of Mirrors in InGaAs/AlGaAs/GaAs-Based Laser Diodes

E. Yu. Kotel'nikov*, A. A. Katsnel'son*, I. V. Kudryashov*, M. G. Rastegaeva*, W. Richter, V. P. Evtikhiev*, I. S. Tarasov*, and Zh. I. Alferov***

** Ioffe Physicotechnical Institute, Russian Academy of Sciences, Politekhnicheskaya ul. 26, St. Petersburg, 194021 Russia*

*** Friederich-Schiller University, Jena, Germany*

Submitted April 11, 2000; accepted for publication April 13, 2000

Abstract—The InGaAs/AlGaAs/GaAs double laser heterostructures of separate confinement with a quantum well were formed by molecular-beam epitaxy. The study of characteristics of laser diodes with a wide contact (100 μm) showed that the power corresponding to the catastrophic degradation of mirrors may attain nearly the highest values ever achieved (20 MW/cm^2) that were previously obtained for laser diodes based on InGaAsP/GaAs heterostructures alone. © *2000 MAIK "Nauka/Interperiodica".*

In recent years, a number of publications have been concerned with attaining a high power of emission from laser diodes. The highest ever levels of optical power have been obtained by using a new design of laser diodes with a broadened waveguide and by employing the heterostructures based on solid solutions that do not contain aluminum. In many publications, it is reasoned that one of the main factors that limit the radiation power of semiconductor lasers is the catastrophic degradation of the mirrors. An increase in the waveguide width reduces the optical-power density at the laser mirror and, thus, should make it possible to attain a higher laser output power. It is reasoned [1] that the highest optical power is limited by the surface-recombination rate in the material of which the active region is made. Thus, the output power of a laser diode is found to be related to the type of the active-region material. At present, it is generally acceptable to separate the heterostructures into those containing aluminum and those that do not contain aluminum; it is believed that the use of the aluminum-containing compositions would not yield high levels of laser-radiation power. On the other hand, the technology for fabricating the lasers in an AlGaAs system is less expensive and is better developed.

The objective of this study was to estimate the limiting values of the optical-power density at the mirrors of aluminum-containing laser diodes. The InGaAs/AlGaAs/GaAs laser double heterostructures (DHs) featuring separate confinement and incorporating a quantum well (QW) were grown by molecular-beam epitaxy (MBE) on the precisely oriented n^+-GaAs(001) substrates; a TsNA-4 MBE system was used. A schematic energy-band diagram of a typical heterostructure is shown in Fig. 1. The structure includes $Al_{0.6}Ga_{0.4}As$ emitters 0.8 μm thick, with a 85-Å QW located within a waveguide 1 μm thick. The waveguide is made in the form of an AlAs/GaAs superlattice with a linearly varying band gap which corresponds to the variation in a band gap in an $Al_{0.43}Ga_{0.57}As$–$Al_{0.29}Ga_{0.71}As$ material [2]. This structure was used to fabricate the 100-μm stripe lasers. The reflection coefficient of the output mirror coated with SiO_2 was 25%, and the reflection coefficient of the other mirror was close to 100%. Figure 2 shows the voltage–current and the power–current characteristics of the lasers that had a cavity 2.85 mm in length and were subjected to continuous pumping; the measurements were performed at 285 K. The highest optical power was 6.3 W for the pump current of 7.75 A. Such a level of output power did not cause the laser charac-

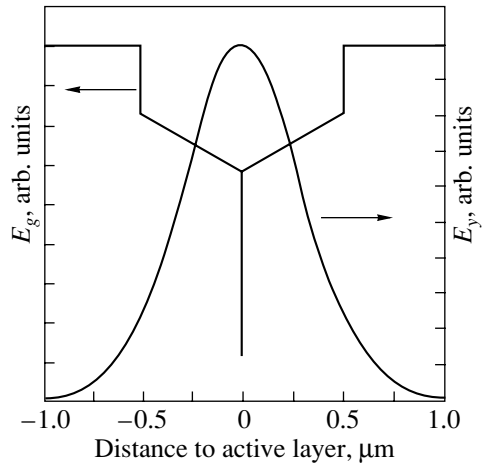

Fig. 1. The energy-band diagram of the laser heterostructure and the distribution of the main-mode field in the laser waveguide.

1063-7826/00/3411-1341$20.00 © 2000 MAIK "Nauka/Interperiodica"

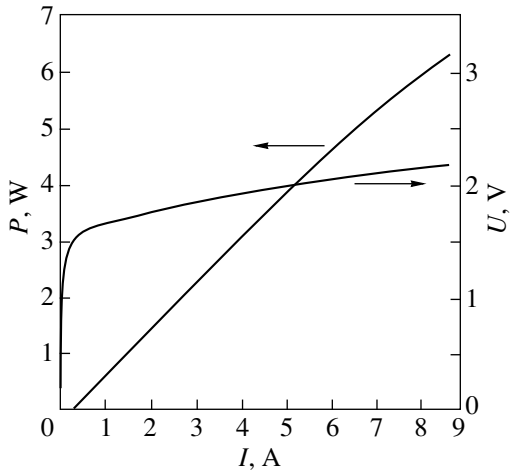

Fig. 2. The voltage–current and power-current characteristics of the laser under test.

teristics to degrade. In order to calculate the optical-power density, we used the formula

$$P_{\mathrm{COMD}} = P_{\max}/\left(\frac{d}{\Gamma}W\frac{1-R}{1+R}\right),$$

where $P_{\max}$ is the maximal optical power, W is the width of the emitting region, R is the reflection coefficient of the output mirror, d is the thickness of the active region, and Γ is the optical-confinement factor of the active region.

The calculated profile for the distribution of the electric-field strength of the laser emission is shown in Fig. 1. The ratio d/Γ was calculated to be 0.52. Under these conditions, the largest value of the optical-radiation power density is found to be close to 20 MW/cm^2. This value exceeds the best results obtained in the case of the continuous pumping of the separate-confinement DH QW lasers based on heterostructures that do not contain aluminum [3]. Almost the same value of the laser optical-power density (19 MW/cm^2) was reported previously [4]; unfortunately, the energy-band diagram of the structure of which the lasers were fabricated was not given. The result obtained by us provides reasons to hope that the InGaAs/AlGaAs/GaAs DH lasers with separate confinement and a QW could compete as the sources of high-power optical radiation with lasers that are more complex in fabrication and do not contain aluminum.

CONCLUSION

Studies of characteristics of InGaAs/AlGaAs/GaAs DH lasers with separate confinement and QWs showed that the maximal optical-power density at the mirrors of these lasers may attain the same record-breaking values as were obtained for the laser based on the structures that did not contain aluminum. Since the technology for the fabrication of the AlGaAs-based lasers is better developed and is less expensive, this inference has not only scientific but also practical importance.

ACKNOWLEDGMENTS

We are grateful to D.A. Livshits for his significant contribution to the fabrication of the lasers and measurements of the laser-diode characteristics.

This study was supported by the Russian Foundation for Basic Research.

REFERENCES

1. D. Botez, Appl. Phys. Lett. **74**, 3102 (1999).
2. V. P. Evtikhiev, E. Yu. Kotel'nikov, I. V. Kudryashov, *et al.*, Fiz. Tekh. Poluprovodn. (St. Petersburg) **33**, 634 (1999) [Semiconductors **33**, 590 (1999)].
3. A. Al-Muhanna, L. J. Mawst, D. Botez, *et al.*, Appl. Phys. Lett. **71**, 1142 (1997).
4. X. He, S. Srinivasan, S. Wilson, *et al.*, Electron. Lett. **34**, 2126 (1998).

Translated by A. Spitsyn

Semiconductors, Vol. 34, No. 11, 2000, pp. 1343–1350. Translated from Fizika i Tekhnika Poluprovodnikov, Vol. 34, No. 11, 2000, pp. 1396–1403.

PHYSICS OF SEMICONDUCTOR DEVICES

InAsSb/InAsSbP Double-Heterostructure Lasers Emitting at 3–4 μm: Part I

T. N. Danilova, A. N. Imenkov, V. V. Sherstnev, and Yu. P. Yakovlev*

Ioffe Physicotechnical Institute, Russian Academy of Sciences, Politekhnicheskaya ul. 26, St. Petersburg, 194021 Russia

** e-mail: yak@iropt1.ioffe.rssi.ru*

Abstract—Previous publications concerned with the development and investigation of InAsSb/InAsSbP double heterostructure lasers emitting at 3–4 μm fabricated by liquid phase epitaxy are reviewed. In pulsed mode, the maximum operating temperature of the lasers is 203 K, the characteristic temperature is 35 K, and differential quantum efficiency is 20 ± 5% at 77K. Mesa-stripe lasers with a 10- to 30-μm stripe width and a 200- to 500-μm cavity length can operate in CW mode up to 110 K. The total optical output power of more than 10 mW at λ = 3.6 μm is obtained at T= 82 K in CW mode. The output power per mode does not exceed 2 mW/facet. A single-mode lasing is achieved in the temperature range of 12–90 K. © *2000 MAIK "Nauka/Interperiodica".*

INTRODUCTION

The 3–4 μm spectral range attracts special attention owing to the fact that this range includes a much greater number of fundamental spectral absorption lines of numerous atmospheric and industrial gases than the near IR range, for which high-quality laser diodes are available. Furthermore, this spectral range includes no strong lines of water absorption, which is important for ranging. In this spectral range, fluoride glasses used in the new generation of fiber links exhibit low losses. Therefore, sources of the 3–4 μm radiation can find numerous technological and scientific applications in optical-communication links, lidars, high-sensitivity and high-speed gas analyzers for chemical analysis, medical diagnostics, environmental pollution monitoring, technological process control, and high-resolution molecular spectroscopy. In some cases, room-temperature sources of spontaneous emission in this spectral range are used. Nevertheless, a number of applications, such as high-resolution molecular spectroscopy, information transfer, coherent methods of signal processing, etc., require radiation sources with narrow, 1- to 10-MHz-wide, spectral lines (sometimes 10–100 MHz is sufficient). For lasers emitting in the vicinity of λ = 3 μm, this corresponds to 10^{-3}–10^{-2} Å. Semiconductor diode lasers are very promising in this spectral range, even though the lasers developed up to now need cooling in order to operate.

Previously, the possibility of developing lasers with λ = 3–4 μm has been investigated for IV–VI (lead salts), II–VI, and III–V narrow-gap semiconductor materials. Lasers that are based on lead salts and emit at ~4 μm can operate at temperatures of up to T = 282 K in pulsed mode [1] and 200 K in CW mode [2]. However, these lasers, like the II–VI-based lasers [3], also fail to produce a high output power, and the prospects for any progress are poor because of the low thermal conductivity of these semiconductors and the high sensitivity of such lasers to damage. III–V semiconductors have better metallurgical and thermal properties, and high quality substrates are available for them. For the spectral range in question, multicomponent III-V solid solutions based on InAs and GaSb are used, both ternary (InAsSb, InGaSb) and quaternary (GaInAsSb, InAsSbP, GaAlAsSb).

The fabrication of lasers emitting in the region of 3 μm was first reported in 1980 [4]. The p-$InAs_{0.82}P_{0.10}Sb_{0.08}$/$n$-$InAs_{0.94}P_{0.04}Sb_{0.02}$/$n$-$InAs_{0.82}P_{0.12}Sb_{0.06}$ double laser heterostructures were grown on (001) n-InAs substrates by liquid-phase epitaxy (LPE). The lasers had a threshold current density of j_{th} = 3 kA/cm^2 at 77 K, a characteristic temperature of T_0 = 23 K in the temperature range of 77–145 K, and a maximum operating temperature of T_{max} = 145 K. Laser structures were fabricated in stripe configuration, with a stripe width of 20 μm and a length of 350 μm. Their emission spectrum at a temperature of 77 K and a current of 0.6 A consists of a single (rather weak) spectral mode.

In the late 1980s, work on LPE-fabricated lasers emitting at λ = 3–4 μm was conducted at the Ioffe Physicotechnical Institute (St. Petersburg, Russia) [5–7], and at L'Université des Sciences et Techniques du Languedoc, (Montpellier, France) [8]. Laser structures with an active region comprising undoped n-InAs, n-InAsSb, n-InGaAs, and n-InGaAsSb layers were fabricated and studied [5–7]. Phosphorus-containing solid solutions $InAs_{1-x-y}Sb_xP_y$ ($0.05 \le x \le 0.06$ and $0.09 \le y \le 0.13$) were used as confining layers. The difference in refractive index between the confining and emitting layers was Δn = 0.02–0.05. The layers were isoperiodic with the substrate. The lattice mismatch amounted to $\Delta a/a \approx 0.05\%$ (a is the lattice parameter). Lasers fabricated by cleaving from four sides had dimensions of 200 × 300 μm^2. The CW mode of operation was

1063-7826/00/3411-1343$20.00

achieved at 77 K, with the threshold current density j_{th} = 240 A/cm^2 and wavelength $\lambda \approx 3.1$ μm. For other compositions of the active-region layers, a laser emission wavelength $\lambda \approx 3.5$ μm was achieved, with the threshold current density j_{th} = 117 A/cm^2 at 77 K.

Lasers that emitted at $\lambda \approx 3.2$ μm wavelength at 78 K and were fabricated by LPE on a (100) *n*-InAs substrate were reported in [8]. The lasers had an *n*-$InAs_{0.95}Sb_{0.05}$ active region and $InAs_{0.50}Sb_{0.19}P_{0.31}$ confining layers. The lattice mismatch between the epitaxial layers and the substrate was 3.5×10^{-3}, and the difference in refractive indices, Δn = 0.15–0.20. The laser was designed in the form of a Fabry–Perot cavity 100 μm wide and 300 μm long, with mirrors fabricated by cleavage. The threshold current density at 77 K j_{th} = 4.5 kA/cm^2, with characteristic and maximum working temperatures of T_0 = 30 K and T_{max} = 110 K in the pulsed mode of operation. The emission wavelength was 3.2 μm. The spectra were mainly multiple-mode, with some of the lasers having a practically single-mode spectrum.

Further goals in the development of lasers emitting in the 3–4 μm range were to achieve high emission power and to improve the emission spectrum, that is, to obtain a practically single-mode spectrum with the wavelength varying continuously with temperature or current, which is necessary for laser applications, in particular, in high-resolution spectroscopy.

In the 1990s, much progress was made in molecular-beam epitaxy (MBE) and metal–organic chemical vapor deposition (MOCVD). These methods made it possible to grow $In_xGa_{1-x}As_ySb_{1-y}$ and $InAs_{1-x-y}Sb_yP_x$ solid-solution layers in a wide composition range, while the LPE technique allows the growth of $In_xGa_{1-x}As_ySb_{1-y}$ solution only with compositions close to either GaSb ($0 < x < 0.29$) or InAs ($0.74 < x < 1$) [9]. The $InAs_{1-x-y}Sb_yP_x$ solid solution has been obtained by LPE only for compositions $0 < x < 0.35$ [10]. The existence of wide ranges of compositions that are beyond the reach of the LPE technique is due to limitations imposed by the immiscibility of solid solutions, namely, the existence of a spinodal decomposition range, and also to limitations imposed by the molecularity of the melt [9].

The LPE method gives no way of controlling the growth of very thin layers ~10 Å thick. Such layers can be grown by MBE and MOCVD, thus enabling the fabrication of quantum wells (QWs) in the active region. Usually, structures are grown with thick confining layers isoperiodic with the substrate and an active region based on strained QWs. In lasers with an active region consisting of multiple strained QWs, the temperature dependence of the threshold current is weaker, because the Auger recombination rate can be reduced by varying the valence-band profile in the strained QW. By varying the quantum well width, the laser emission wavelength can be changed to some extent. Nevertheless, operation at room temperature has not been achieved for 3–4 μm lasers. The best results were obtained for lasers with an $InAs_{0.935}Sb_{0.065}$ active region emitting at 3.2–3.55 μm. The lasers had a maximum operating temperature of 225 K in the pulsed mode of operation and 175 K in CW operation [11]. A somewhat higher maximum operating temperature has been obtained for lasers emitting in the 3 μm range: 255 K in the pulsed mode and 170 K in CW operation. The lasers were fabricated by MBE on the basis of a double heterostructure (DH) with a metastable solid solution layer in the active region [12]. Recently, the fabrication of a diode laser emitting at λ = 3.3 μm in the pulsed mode of operation at room temperature has been reported [13]. For this laser, the multiple-mode spectrum width at 300 K does not exceed 12 nm. The active region comprises 5 or 10 periods, composed of InAs/GaInSb/InAs/AlGaSb layers, having a *W*-like conduction band profile in each period. An extended cavity is created by surrounding the active region on the *n*- and *p*-sides with 0.6-μm-thick AlGaAsSb layers, followed by optical-confinement layers. Much success has been achieved with MBE-grown quantum cascade lasers; however, these lasers emit at longer wavelengths ($\lambda > 5$ μm).

The differential quantum efficiency of the quantum cascade lasers may substantially exceed unity. Quantum cascade lasers relying on intersubband transitions can operate at room temperature, and even at 320 K in pulsed mode [14, 15]. Quantum cascade lasers relying on optical transitions between the conduction and valence bands emit in the 3–4 μm region. A high output power is achieved (4 W per side), but the maximum operating temperature is only 210 K in pulsed mode. At 100 K, the external differential quantum efficiency is as high as 480%, and the emission wavelength is 3.8–3.9 μm [16]. A theoretical model has been developed for a quantum cascade laser relying on interband transitions, emitting at 3.15 μm and operating at room temperature [17].

However, mention should be made of the fact that the MBE and MOCVD techniques are relatively complex and expensive, and, therefore, LPE remains attractive for the manufacture of optoelectronic devices.

In this paper, we review our publications concerned with the development and investigation of LPE-grown lasers based on DHs and emitting in the 3–4 μm range. Two goals were set: first, to produce lasers with high limiting operating temperatures, and, second, to develop lasers with spectral characteristics that would allow their use in high-resolution spectroscopy. The review can be divided into two parts, corresponding to these two tasks.

1. FABRICATION TECHNIQUES

Laser structures were produced by LPE on (100) InAs substrates. All the laser layers were grown isope-

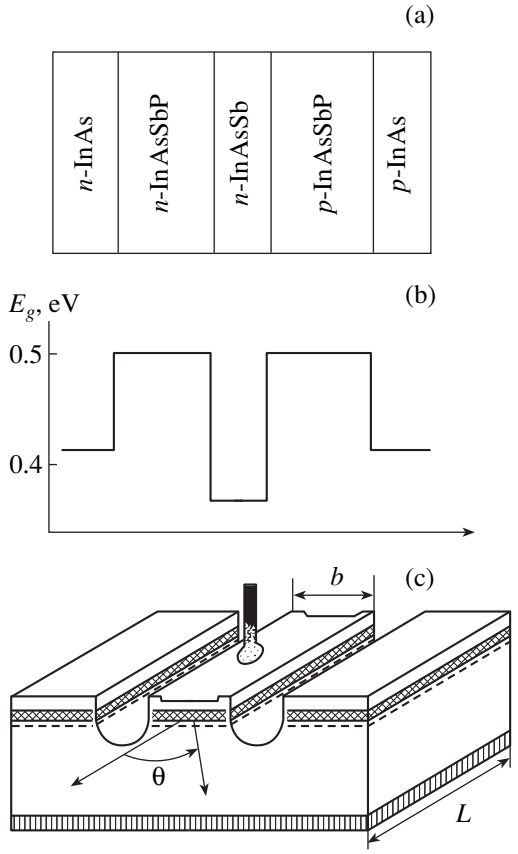

Fig. 1. Structure of a three-layered DH diode laser: (a) Layer arrangement, (b) layer-by-layer profile of the band gap, and (c) schematic of a mesa-stripe laser.

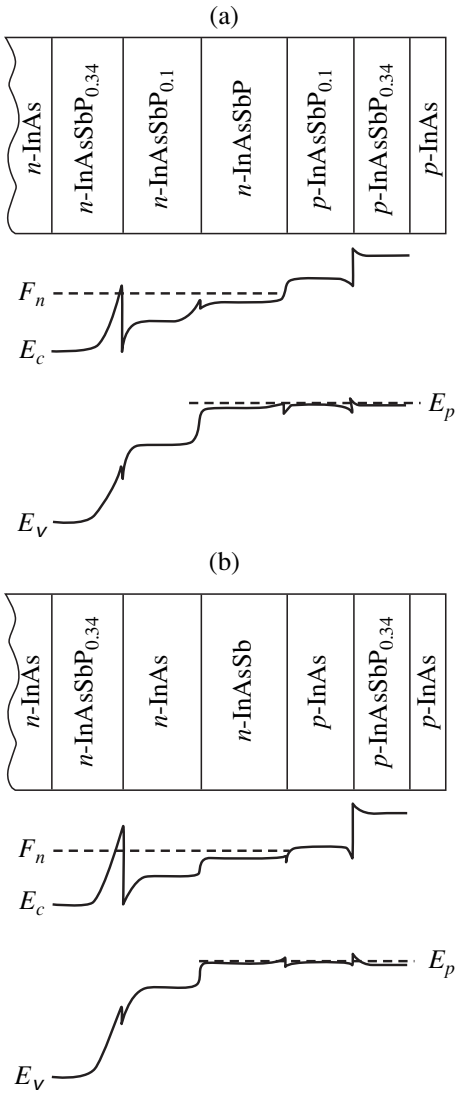

Fig. 2. Layer arrangement for five-layered separate confinement DH lasers and band diagrams under operating conditions for lasers with type-I (a) and type-II heterojunctions (b).

riodic with the substrate and with lattice mismatch $\Delta a/a = 1 \times 10^{-4}$–$6 \times 10^{-3}$. The lasers were three-layered DHs *p*-InAsSbP/*n*-InAsSb/*n*-InAsSbP (Fig. 1) and five-layered, with separate electron and optical confinement (SC) DHs of two types: *p*-$InAsSbP_{0.34}$/*p*-$InAsSbP_{0.1}$/*n*-InAsSb/*n*-$InAsSbP_{0.1}$/*n*-$InAsSbP_{0.34}$ (Fig. 2a) and *p*-$InAsSbP_{0.34}$/*p*-InAs/*n*-InAsSb/*n*-InAs/*n*-$InAsSbP_{0.34}$ (Fig. 2b). Three-layered DHs had a type-I heterointerface. Five-layered SC DHs had a type-I heterointerface with an active region for the $InAsSbP_{0.1}$ electron confinement layer, and a type-II heterointerface for an InAs electron confinement layer. The active narrow-gap region was not doped intentionally, and it had *n*-type conduction with an electron concentration of $\sim 10^{16}$ cm^{-3}. The band gap E_g in the active region varied within 0.31–0.41 eV. It is extremely difficult to grow wide-gap optical confinement layers based on quaternary InAsSbP solutions by LPE. We considered the conditions for LPE growth of the InAsSbP solid solution in terms of the model of liquid and solid phases [18]. It was found that the intersection point of the curves outlining the regions of spinodal-decomposition and molecularity limitations corresponds to the theoretical limiting phosphorus content ($x \approx 0.40$) in the quaternary solid solution. The epitaxial temperature of ~820 K corresponds to this point. We obtained an $InAsSbP_x$ solid solution on an InAs substrate with the maximum phosphorus content $x = 0.35$ at an epitaxy temperature of ~570°C [19]. Confining layers with a phosphorus content of $x = 0.25$–0.35 were used, with their composition corresponding to $E_g = 0.55$–0.6 eV at 77 K. Wide-gap *p*-layers were commonly doped with Zn, and in some cases with Mn, and had a free hole concentration of $(2–5) \times 10^{18}$ cm^{-3}. Wide-gap *n*-InAsSbP layers were doped with Sn and had a free electron concentration of $\sim 10^{18}$ cm^{-3}. The thickness of these layers was 2–3 μm. The calculated difference between the refractive indices of the optically active and optical-confinement regions $\Delta n = 0.02$–0.09.

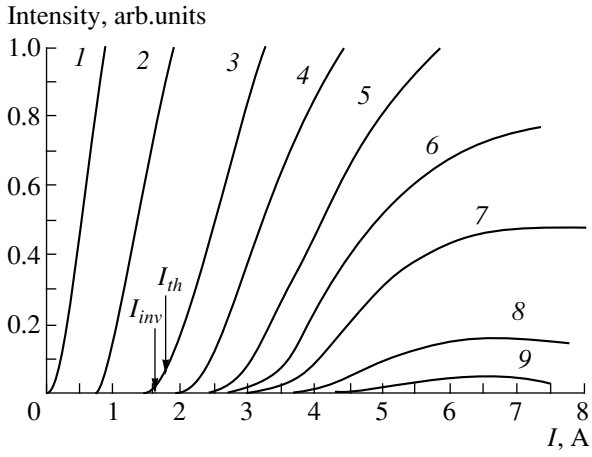

Fig. 3. Emission intensity vs. laser current for InAsSb/InAsSbP DH laser (V1126-80) at temperatures T = (*1*) 83, (*2*) 140, (*3*) 153, (*4*) 162, (*5*) 167.5, (*6*) 170, (*7*) 173, (*8*) 177, and (*9*) 180 K.

Mesa-stripe lasers were formed on the obtained structures using chemical etching and photolithography. An etchant, $HCl/CrO_3/HF/H_2O$, was proposed, ensuring isotropic etching [20]. The stripe width (b) was 10–60 μm. Fabry–Perot laser cavities of length L = 50–2000 μm were produced by cleavage.

The lasers were studied in the pulsed mode of operation, in the quasi-CW mode with meandrous current pulses characterized by an off-duty factor of 2, and under CW conditions.

2. MAXIMUM OPERATING TEMPERATURE OF THE LASERS

The maximum operating temperature (T_{max}) depends mainly on the temperature dependences of the threshold current (I_{th}) and the differential quantum efficiency (η_d). These characteristics were determined from the dependences of the emission intensity on current I [21] (Fig. 3). Figure 3 shows experimental data for an InAsSb/InAsSbP DH laser (V1126-80) with a stripe width of b = 45 μm and a cavity length of L = 300 μm. For this laser, the maximum operating temperature, determined by the occurrence of lasing, T_{max} = 170 K, with the limiting current I_{th}^{lim} = 4.3 A. The population inversion was observed up to 180 K. At 80–150 K, the characteristic temperature was T_0 = 25 K, and the ratio between the lasing threshold current and the inversion current was $I_{th}/I_{inv} \approx 1.07$. With the temperature raised further, I_{th} grows faster than I_{inv}.

Taking into account that the I_{th} increases with temperature mainly owing to an increase in the Auger recombination rate, different for laser diodes with type-I and type-II heterointerfaces, we compared SC DH lasers [22] having a type-I or type-II heterojunction at the boundary between the active and the electron-confinement regions (Fig. 2). The lasers had identical active regions of $InAs_{0.95}Sb_{0.05}$ with $E_g \approx 0.376$ eV, which corresponds to $\lambda \approx 3.3$ μm, and the same optical confinement layers of $InAs_{0.5}Sb_{0.16}P_{0.34}$ with $E_g \approx 0.593$ eV. The electron confinement layers were composed of InAs ($E_g \approx 0.413$ eV), forming a type-II heterojunction at the active region boundary, with valence band $\Delta E_v \approx 0.052$ eV and conduction band $\Delta E_c \approx 0.015$ eV offsets, the ratio between these being $\Delta E_v/\Delta E_c \approx 3.4$. This ratio is the most favorable for suppressing the Auger recombination in type-II heterojunctions, in accordance with the theory [23]. The electron confinement layers in the laser structure with a type-I heterointerface had the composition $InAs_{0.85}Sb_{0.05}P_{0.1}$, with $E_g \approx 0.464$ eV and band offsets at the active region boundary, $\Delta E_v \approx 0.039$ eV and $\Delta E_c \approx 0.025$ eV. The aforementioned band gaps and band offsets were calculated for T = 77 K.

Figure 4 shows temperature dependences of the threshold current density (j_{th}) for lasers with type-I and type-II heterojunctions (curve *1* and *2*, respectively). The measurements were taken in the pulsed mode, with a pulse width of 100 ns and a repetition rate of 10^5 Hz. As can be seen, the laser with a type-II heterojunction (V1133-3N1) has a higher characteristic temperature $T_0 \approx 35$ K and higher maximum temperature $T_{max} \approx 203$ K, compared to the laser with the type-I heterojunction (S286), having $T_0 \approx 22$ K and $T_{max} \approx 145$ K. It should be noted that, at T = 77 K, the j_{th} for the type-I heterojunction laser was smaller (j_{th} = 800 A/cm^2) than that for the type-II heterojunction laser (j_{th} = 1000 A/cm^2). To analyze the temperature behavior of j_{th}, we present in Fig. 4 the temperature dependences of j_{th}, calculated for the prevalent bulk recombination with consideration either of the radiative recombination exclusively (curve *3*) or of the Auger recombination exclusively (CHCC and CHHS transitions) (curve *4*), and the overall dependence (curve *5*). The calculations were performed in terms of the theory described in [24]. In this study, we deal with thick (~2 μm) lasers with an InGaAsSb active region (E_g = 0.62 eV) and GaAlAsSb optical confinement layers. The theoretical temperature dependence of j_{th} coincided with the experimental curve (see [24]).

When the radiative recombination is dominant in the bulk, the threshold current density j_{th} for our lasers must increase with temperature as $j_{th} \propto T^{3/2}$ (Fig. 4, curve *3*). If the Auger recombination via CHCC and CHHS transitions is dominant, $j_{th} \propto T^7$, (Fig. 4, curve *4*). The calculated rates of the radiative and nonradiative recombination are equal at about 170 K. The temperature dependences of the total current densities (Fig. 4, curve *5*) are expressed as $j_{th} \propto T^{2.5}$ at 77–90 K and $j_{th} \propto T^7$ at 180–200 K.

The threshold current density in the lasers studied is nearly an order of magnitude higher than the value calculated for T = 77–90 K, but it increases with temperature with the same slope in the coordinates of Fig. 4. The small slope indicates that the radiative recombination is dominant, but the fact that the experimental values of j_{th} are higher than those calculated for the bulk recombination shows that the radiative recombination occurs at the interface. This recombination is stronger in lasers with a type-II heterointerface than in those with a type-I heterointerface. At 180–200 K, the Auger recombination at the interface is presumably suppressed in lasers with a type-II heterointerface [23], since the experimental current density is close to the calculated value. The Auger recombination is presumably important in lasers with the type-I heterointerface: over the entire temperature range, the experimental current density exceeds by nearly an order of magnitude the value calculated with account of the Auger recombination in the bulk.

The substantial role of the interfacial recombination in our lasers is confirmed by a study of the laser emission polarization. Lasers with type-I or -II heterointerfaces demonstrated predominantly TM polarization, with the electric field vector **E** of the light wave perpendicular to the *p*–*n* junction plane. As shown in [25], the predominantly TM polarization corresponds to optical transitions without momentum conservation under the conditions of the interconversion of light and heavy holes in reflection from the heterointerface. The degree of polarization σ is determined by the well-known relation

$$\sigma = (P_{TM} - P_{TE})(P_{TM} + P_{TE}), \qquad (1)$$

where P_{TM} and P_{TE} are the emission intensities for TM- and TE-polarized light, respectively. The maximum value of σ for the lasers studied was 80% for the structures with type-II heterojunction, and 73% for those with type-I heterojunction at a current $I = 1.5I_{th}$ [22]. The value of σ and its variation with current are independent of the active-region width [25]. The DH lasers also demonstrated mainly TM-polarization of ~89%; for lasers with a Mn-doped emitter, the value of σ was 96% [25].

It should be noted that, for all of the lasers studied, coherent emission appears at the peak of the spontaneous emission band, with deviations to higher or lower energies of no more than ~1 meV [25]. The threshold current depends on the active region thickness only slightly.

The fact that the threshold current and the degree of polarization are independent of the active-region thickness and the absence of the long-wavelength shift of the coherent emission with respect to the spontaneous emission indicate that the main contribution to the emission intensity comes from narrow regions near the heterointerface. The thickness of these regions is on the order of the thermal de Broglie wavelength of carriers,

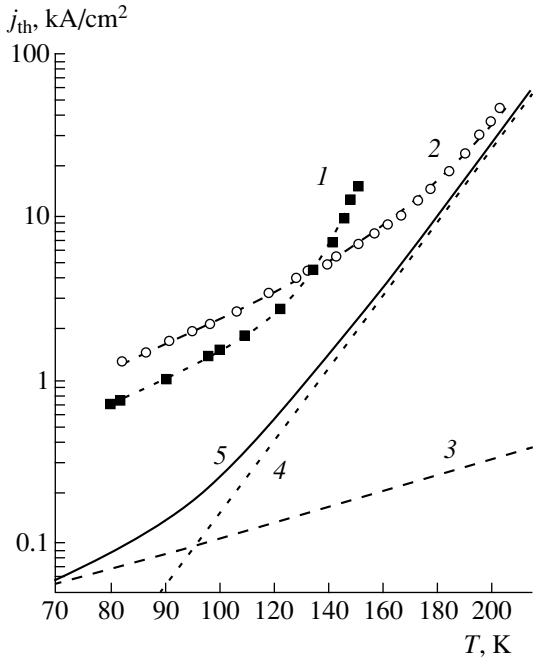

Fig. 4. Temperature dependences of the threshold current: experimental for (*1*) lasers with type-I (S286) and (*2*) type-II heterojunctions (V1133-3 N1); theoretical for dominant (*3*) bulk radiative recombination, (*4*) Auger recombination via CHCC- and CHHS-transitions, and (*5*) overall theoretical dependence.

$\lambda_T \approx h/(2m_c kT)^{1/2} \approx 0.02$ μm, where m_c is the electron effective mass. The thickness λ_T is much less than the DH active-region thickness (~1 μm).

The laser threshold current depends on the cavity length L [26] and stripe width b [21]. At T = 77 K, the $I_{th}(L)$ dependence has a minimum at $L \approx 300$ μm (Fig. 5). For $L < 200$ μm, I_{th} increases sharply with decreasing L, and, for $L = 50$ μm, no lasing was observed. The sharp increase in I_{th} with decreasing L for $L \le 150$ μm can be explained by the gain limitation at the heterointerface. For $L > 350$ μm, I_{th} increases gradually with L, because of the increasing intraband losses. The temperature dependences of I_{th} for lasers with varied cavity length L show that the temperature at which the $I_{th}(T)$ slope starts to grow lowers with decreasing in L. This is a consequence of the increasing internal losses, uncompensated even by the maximum gain.

We have studied the I_{th} dependence on the stripe width [21]. For comparison, Fig. 6 shows the temperature dependences of I_{th}, taken in pulsed mode of operation for two lasers with the stripe widths of 15 and 55 μm ($L \approx 300$ μm), fabricated from the same wafer (V-1133). As can be seen, the laser with a wider stripe (curve *1*) has T_{max} = 203 K and T_0 = 35 K. The threshold current at maximum operating temperature is I_{th} = 7.5 A, which corresponds to the current density j_{th} = 45 kA/cm^2. The laser with a narrower stripe (curve *2*) has T_{max} = 170 K, T_0 = 23 K, I_{th} = 3 A, and j_{th} =

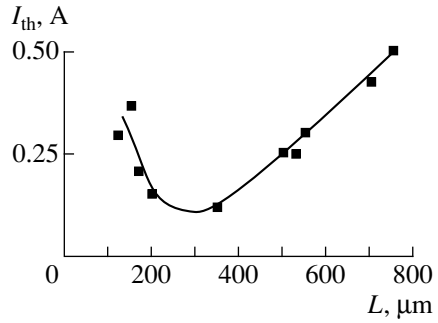

Fig. 5. Threshold current I_{th} vs. the cavity length L at T = 77 K.

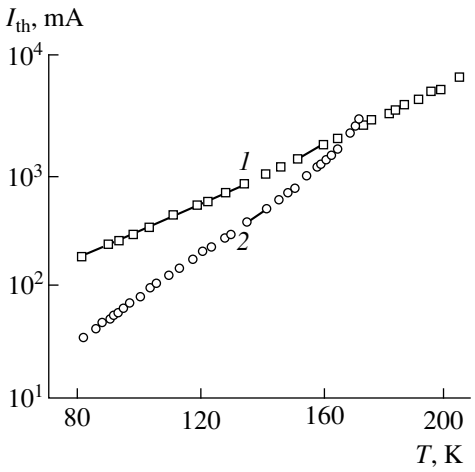

Fig. 6. Temperature dependence of the lasing threshold current for SC DH lasers with type-II heterojunction (V1133) and stripe widths b = (*1*) 55 (T_0 = 35 K) and (*2*) 15 μm (T_0 = 23 K).

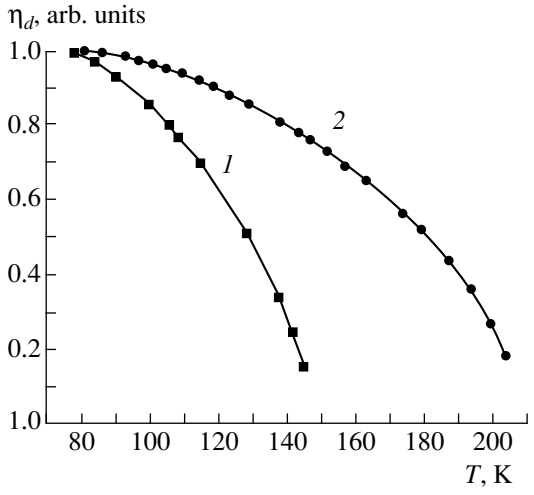

Fig. 7. Temperature dependences of the differential quantum efficiency for lasers with (*1*) type-I (S286) and (*2*) type-II (V1133) heterojunctions.

67 kA/cm^2. These data show that the lasers with wider stripes are preferable as regards the temperature dependences of the threshold current and the threshold current density. Probably, narrow-stripe lasers have additional losses compared with the wide-stripe devices. These losses may be associated with leakage currents due to surface recombination: it affects the narrow-stripe lasers more strongly, because in this case it constitutes a larger part of the total current. The surface recombination on the lateral face of the stripe in layers of InAs-based solid solutions is due to the formation of an *n*-type inversion layer on the *p*-layer surface.

Now we discuss the temperature dependence of the differential quantum efficiency of the lasers under consideration. Figure 7 shows $\eta_d(T)$ dependences for lasers with type-I (curve *1*) and type-II heterojunctions (curve *2*) for the same lasers as those used in I_{th} comparison [22]. The differential quantum efficiency decreases steeply with increasing temperature, this behavior being more pronounced for lasers with the type-I heterojunction. Since the differential quantum efficiency is mainly determined by free-carrier absorption, its decrease with increasing temperature means that the free-carrier losses grow at higher temperatures, and this effect is more pronounced in lasers with type-I heterojunction. As mentioned above, the active and the optical-confinement regions are the same in the lasers compared, and, therefore, higher absorption losses in lasers with a type-I heterointerface occur either in the electron confinement layers or at their heteroboundaries. The curve describing the decrease of the differential quantum efficiency with increasing temperature has no inflections. At 77 K, η_d is 20 ± 5%. Mesa-stripe lasers with a 10–30 μm stripe width can operate in the CW mode up to 110 K. The total output power of the CW lasers exceeds 10 mW at 82 K and λ = 3.6 μm; the optical power per mode is limited to 2 mW per surface [27]. The rise in the emission losses with increasing current beyond the inversion threshold may exceed the gain increase, so that lasing becomes impossible at this temperature.

We estimated the maximum operating temperature for our lasers in terms of a simplified model with an energy-independent carrier density. There is much evidence that this model is realized in some of the lasers studied [25], in which self-coordinated QWs appear at the interfaces between the active region and the confining layers.

The maximum contribution to the gain comes from allowed states at the QW bottom. In this case, the gain g_0 is given by

$$g_0 \approx g_m \frac{e^{F/kT} - 1}{e^{F/kT} + 1 + e^{F_i/kT}}, \qquad (2)$$

where g_m is the maximum possible gain for $F \longrightarrow \infty$ (F is the excess of the external potential over that necessary to create population inversion), and F_i is the

position of the quasi-Fermi level in the allowed band of carriers with smaller mass (electrons) at the inversion threshold.

Lasing sets in at $F = F_g$ for which $g_0\Gamma = \alpha_\Sigma$, where Γ is the coefficient of laser emission coupling with the amplifying media, and α_Σ is the total loss. At low temperatures, when radiative recombination prevails, F_g can be conveniently determined from the ratio between the experimentally determined inversion current I_{inv} and the lasing current I_{th}. Calculations show that

$$\frac{F_g}{F_i} \approx \frac{I_{th}}{I_{inv}} - 1. \quad (3)$$

The maximum gain g_m is given by

$$g_m F \approx \alpha_\Sigma \frac{e^{F_i/kT} + 1}{(F_{i/kT})[I_{th}/I_{inv} - 1]}. \quad (4)$$

Using our experimental data [$I_{th}/I_{inv} = 1.07$, $\alpha_\Sigma = \alpha_L = (1/L)\ln(1/R) \approx 40$ cm^{-1}, (α_L is the output loss), $L = 0.03$ cm, $R = 0.3$ is the mirror reflectance, and $F_i = 2kT$], we obtain $g_m\Gamma = 250$ cm^{-1}.

With increasing temperature, the importance of free-carrier absorption becomes more pronounced. It is assumed that the transitions from heavy hole to light hole make the major contribution to emission absorption. These losses (α_p) can be expressed by

$$\alpha_p = \alpha_0 \exp\left\{-\left(\frac{m_l}{m_h}h\nu + F_p\right)/kT\right\} \times \exp\{F/(kT + F_i)\}, \quad (5)$$

where α_0 is a coefficient; m_l and m_h are the light- and heavy-hole effective masses, respectively; F_p is the depth of the hole levels in the QW; and $h\nu$ is the photon energy. The total radiation losses are given by

$$\alpha_\Sigma = \alpha_p + \alpha_L + \alpha_d, \quad (6)$$

where α_d represents the scattering losses.

With increasing F, the ratio $g_0\Gamma/\alpha_\Sigma$ (4) first increases, passes through a maximum at $\alpha_\Sigma \approx 0.7g_m\Gamma$, and then decreases. The temperature at which α_Σ reaches the value $0.7g_m\Gamma$ is the exact maximum lasing temperature (T_{max}). At this temperature, $F = F_i + kT$. The expression for T_{max} has the form

$$kT_{max} \approx \left(\frac{m_l}{m_h}h\nu + F_p\right)\Big/\left(1 + \frac{\alpha_L + \alpha_d}{0.7g_m\Gamma} + \ln\frac{\alpha_0}{0.7g_m\Gamma}\right). \quad (7)$$

Using $m_l/m_h \approx 0.1$, $h\nu = 0.36$ eV, $F_p = 0.003$ eV, $g_m\Gamma = 250$ cm^{-1}, $\alpha_L + \alpha_d \approx 40$ cm^{-1}, and $\alpha_0 = 700$ cm^{-1}, we obtain $T_{max} = 173$ K. This value corresponds to the average of the experimental values for the lasers studied.

The maximum lasing temperature can be increased by diminishing α_0, α_L, and α_d and raising Γ. For example, α_L can be minimized by depositing a reflective coating onto cavity mirrors, and Γ can be increased by increasing the phosphorus content in the confining layers or by fabricating several QWs. T_{max} can be raised to 190 K only by minimizing α_L, and, if, in addition, $g_m\Gamma$ is doubled, $T_{max} = 265$ K can be obtained.

The best maximum lasing temperature achieved for the lasers produced by LPE and studied here is $T_{max} = 203$ K. This value was obtained for structures with separate optical and electron confinement, with a type-II heterojunction between the active region and the electron confinement layer. The stripe width in these lasers was 55 μm, and the cavity length, 300 μm. No reflective coatings were deposited onto the cavity mirrors.

ACKNOWLEDGMENTS

This study was supported in part by the European Office of Aerospace Research and Development (US) under contract no. F61775-99-WE016 and the Russian Foundation for Basic Research, project nos. 99-02-18109 and 00-02-17047.

REFERENCES

1. Z. Shi, M. Tacke, A. Lambrecht, and H. Böttner, Appl. Phys. Lett. **66**, 2537 (1995).
2. Z. Feit, D. Kostyk, R. J. Woods, and P. Mak, Appl. Phys. Lett. **58**, 343 (1991).
3. J. M. Arias, M. Zandian, R. Zucca, and J. Singh, Semicond. Sci. Technol. **8**, S255 (1993).
4. Kobayashi and Y. Horikoshi, Jpn. J. Appl. Phys. **19**, L641 (1980).
5. M. Sh. Aĭdaraliev, N. V. Zotova, S. A. Karandashev, *et al.*, Pis'ma Zh. Tekh. Fiz. **13** (9), 563 (1987) [Sov. Tech. Phys. Lett. **13**, 232 (1987)].
6. M. Sh. Aĭdaraliev, N. V. Zotova, S. A. Karandashev, *et al.*, Pis'ma Zh. Tekh. Fiz. **14** (17), 1617 (1988) [Sov. Tech. Phys. Lett. **14**, 704 (1988)].
7. M. Sh. Aĭdaraliev, N. V. Zotova, S. A. Karandashev, *et al.*, Pis'ma Zh. Tekh. Fiz. **15** (15), 49 (1989) [Sov. Tech. Phys. Lett. **15**, 600 (1989)].
8. H. Mani, A. Joullie, G. Boissier, *et al.*, Electron. Lett. **24**, 1542 (1988).
9. A. N. Baranov, A. A. Guseĭnov, A. M. Litvak, *et al.*, Pis'ma Zh. Tekh. Fiz. **16** (5), 33 (1990) [Sov. Tech. Phys. Lett. **16**, 177 (1990)].
10. T. N. Danilova, O. G. Ershov, A. N. Imenkov, *et al.*, Pis'ma Zh. Tekh. Fiz. **20** (4), 87 (1994) [Tech. Phys. Lett. **20**, 172 (1994)].
11. N. K. Choi, G. W. Turner, N. J. Manfra, and M. K. Connors, Appl. Phys. Lett. **68**, 2936 (1996).
12. N. K. Choi, S. J. Eglash, and G. W. Turner, Appl. Phys. Lett. **64**, 2474 (1994).
13. H. Lee, I. J. Olafsen, R. J. Menna, *et al.*, Electron. Lett. **35**, 1743 (1999).
14. J. Faist, F. Capasso, C. Sirtori, *et al.*, Electron. Lett. **32**, 560 (1996).

15. C. Gmachl, F. Capasso, J. Faist, *et al.*, Appl. Phys. Lett. **72**, 1430 (1998).
16. J. L. Bradshaw, R. Q. Yang, J. D. Bruno, *et al.*, Appl. Phys. Lett. **75**, 2362 (1999).
17. I. Vurgaftman, J. R. Meyer, and L. R. Ram-Mohan, IEEE Photonics Technol. Lett. **9**, 170 (1997).
18. A. N. Baranov, B. E. Dzhurtanov, A. M. Litvak, *et al.*, Zh. Neorg. Khim. **35**, 3008 (1990).
19. T. N. Danilova, O. G. Ershov, A. N. Imenkov, *et al.*, Pis'ma Zh. Tekh. Fiz. **20** (4), 87 (1994) [Tech. Phys. Lett. **20**, 172 (1994)].
20. E. A. Grebenshchikova, A. M. Litvak, V. V. Sherstnev, and Yu. P. Yakovlev, Pis'ma Zh. Tekh. Fiz. **24** (15), 27 (1998) [Tech. Phys. Lett. **24**, 593 (1998)].
21. T. N. Danilova, O. G. Ershov, A. N. Imenkov, *et al.*, Fiz. Tekh. Poluprovodn. (St. Petersburg) **30**, 1265 (1996) [Semiconductors **30**, 667 (1996)].
22. T. N. Danilova, A. P. Danilova, O. G. Ershov, *et al.*, Fiz. Tekh. Poluprovodn. (St. Petersburg) **31**, 976 (1997) [Semiconductors **31**, 831 (1997)].
23. G. G. Zegrya and A. D. Andreev, Zh. Éksp. Teor. Fiz. **109**, 615 (1996) [JETP **82**, 328 (1996)].
24. A. A. Andaspaeva, A. N. Baranov, B. A. Gel'mont, *et al.*, Fiz. Tekh. Poluprovodn. (Leningrad) **25**, 394 (1991) [Sov. Phys. Semicond. **25**, 240 (1991)].
25. T. N. Danilova, O. G. Ershov, G. G. Zegrya, *et al.*, Fiz. Tekh. Poluprovodn. (St. Petersburg) **29**, 1604 (1995) [Semiconductors **29**, 834 (1995)].
26. A. N. Baranov, T. N. Danilova, O. G. Ershov, *et al.*, Pis'ma Zh. Tekh. Fiz. **18** (22), 6 (1992) [Sov. Tech. Phys. Lett. **18**, 725 (1992)].
27. A. Popov, V. Sherstnev, Yu. Yakovlev, *et al.*, Appl. Phys. Lett. **68**, 2790 (1996).

Translated by D. Mashovets

Semiconductors, Vol. 34, No. 11, 2000, pp. 1351–1354. Translated from Fizika i Tekhnika Poluprovodnikov, Vol. 34, No. 11, 2000, pp. 1404–1407.

PHYSICS OF SEMICONDUCTOR DEVICES

A Coherent Laser Based on a Two-Well Structure

V. F. Elesin and A. V. Tsukanov

Moscow State Institute of Engineering Physics, Kashirskoe sh. 31, Moscow, 115409 Russia

Submitted March 6, 2000; accepted for publication May 17, 2000

Abstract—The theory of steady-state single-mode oscillations in a coherent cascade laser that incorporates two quantum wells is developed. The power and frequency of oscillations are determined in relation to the coherent-pump current and the structure parameters. It is shown that the conditions for self-tuning also exist in a two-well structure, which ensures an efficient lasing and a linear increase in power with increasing pump current.

1. After almost 20 years elapsed since the original suggestion by Kazarinov and Suris [1], a new type of semiconductor laser (a cascade laser) was developed by Capasso and his coworkers [2]. The laser was operated by diagonal transitions between the levels in the neighboring wells. A model with vertical transitions in a single well was considered in the publications [3, 4] devoted to the cascade-laser theory. It was found that a laser operating by vertical transitions has certain advantages (see also [5]). However, in a quantum well (QW), there may exist lasing that is basically different from the lasing in a cascade laser. Such a coherent laser was suggested previously [6]. A theory of coherent oscillations in a single QW (quantum dot) was developed previously [6]. In particular, the power and the electromagnetic-field frequency in relation to the coherent-pump current and the system parameters were determined. A simple model allowing for analytical solution in a wide range of fields was considered [6]. The processes of oscillations in an asymmetric two-well structure were studied [7] in the context of the above model. Coherent oscillations have certain specific features: there is no need for population inversion, the self-tuning conditions ensure high efficiency, and so on. The question arises whether effective coherent oscillations are possible with self-tuning for two and more wells. The aim of this study was to develop a coherent-oscillation theory for two wells.

2. In order to determine the main pattern, we study the following model of a cascade laser. Figure 1 shows a one-dimensional structure formed by three delta-function barriers at the points $x = 0$, $x = a$, and $x = 2a$. It is assumed that two levels exist in each of the wells. The potential profile of this structure has the shape of a step, and the step height is chosen in such a way that the lower level in the first well coincides with the upper level in the second well. The energies of these levels differ by the value of the corresponding electromagnetic-field frequency ω. A steady flux of electrons with the density proportional to q^2 and the energy approximately equal to the energy E_1 of the upper level in the first well is incident on the system from the left. The electromagnetic field, which may be regarded as classical to a good accuracy, is emitted in the transition of electrons from the upper to lower levels in each of the wells; i.e.,

$$E_x(z, t) = E(t)\sin kz\cos(\omega t + \varphi(t)). \qquad (1)$$

The field is polarized perpendicularly to the well plane (i.e., along the x-axis), whereas the wave vector lies in this plane (i.e., it is directed along the z-axis).

Under the conditions of a single-mode steady-state lasing, equations for the field E are written as

$$\left.\begin{aligned} \frac{E}{2\tau_0} &= -\frac{2\pi}{\kappa}J_c(k), \\ (\omega - \Omega)E &= -\frac{2\pi}{\kappa}J_s(k), \\ J_{c,s}(k) &= \int_0^a dx\exp(ikx)J_{c,s}(x), \end{aligned}\right\} \qquad (2)$$

where $J_{c,s}(k)$ are the Fourier components of the polarization currents that either coincide in phase (c) with the field or are shifted in phase by $\pi/2$(s) and describe the interlevel transitions, τ_0 is the photon lifetime in the cavity, Ω is the natural frequency of the cavity, and κ is the permittivity.

The polarization currents are expressed in terms of the system's wave function $\Psi(x, t)$ that satisfies the equation

$$\frac{i2m^*}{\hbar}\frac{\partial\Psi}{\partial t} = -\frac{\partial^2\Psi}{\partial x^2} + U(x)\Psi + V(x, t)\Psi, \qquad (3)$$

where m^* is the effective electron mass,

$$U(x) = \alpha[\delta(x) + \gamma\delta(x - a) + \beta\delta(x - 2a)]$$
$$+ \tilde{\omega}[1 - \Theta(x - a)]$$

1063-7826/00/3411-1351$20.00

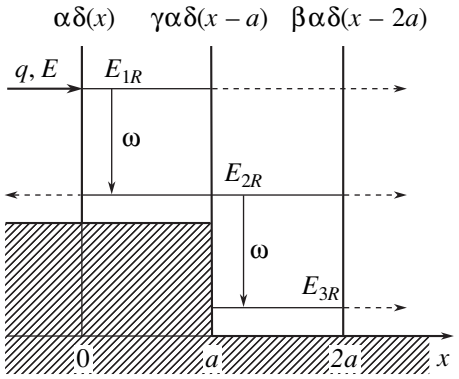

Fig. 1. Schematic representation of the process of lasing in a symmetric two-well structure formed by three delta-function barriers and steplike potential profile. The electron flux with the density proportional to q^2 and the energy approximately equal to the energy of the pump level E_1 is incident on the structure from the left. The electrons first execute a radiative transition to the level $E_2^{+(-)}$, then tunnel to the second well and execute a transition to the level E_3, and finally leave the structure.

is the potential energy of the barriers (γ and β are the relative barrier strengths), and

$$V\Psi = V(\exp(i\omega t) - \exp(-i\omega t))\frac{\partial\Psi}{\partial x}, \quad V = -\frac{eE}{\hbar\omega}$$

accounts for the interaction with the electromagnetic field (henceforth, $h = c = 1$).

We derive a time-independent solution to Eq. (3) by restricting ourselves to the contribution of resonance to the interaction of electrons with electromagnetic field; thus, we have

$$\Psi(x,t) = \begin{cases} [q\exp(ipx) + D_0\exp(-ipx)] \\ \times\exp(-iEt) + D_{-1} \\ \times\exp(-i(E-\omega)t - ip_-x), \quad x < 0, \\ \Psi_0(x)\exp(-iEt) + \Psi_{-1}(x) \\ \times\exp(-i(E-\omega)t), \quad 0 < x < a, \\ \tilde{\Psi}_0(x)\exp(-i(E-\omega)t) \\ + \tilde{\Psi}_{-1}(x)\exp(-i(E-2\omega)t), \quad a < x < 2a, \\ C_0\exp(-i(E-\omega)t + ip(x-2a)) \\ + C_{-1}\exp(-(E-2\omega)t + ip_-(x-2a)), \\ x > 2a. \end{cases} \tag{4}$$

Here,

$$p = \begin{cases} \sqrt{E-\tilde{\omega}}, & k = 1, \\ \sqrt{E-\omega}, & k = 2, \end{cases}$$

$$p_- = \begin{cases} \sqrt{E-(\tilde{\omega}+\omega)}, & k = 1, \\ \sqrt{E-2\omega}, & k = 2 \end{cases}$$

are the momenta of electron at the upper and lower levels in each of the wells (k is the well number). We take into account that the step height is equal to $\tilde{\omega}$ and the energy parameter E is measured from $U = 0$.

The functions Ψ_0, Ψ_{-1}, $\tilde{\Psi}_0$, and $\tilde{\Psi}_1$ satisfy the system of equations

$$\left.\begin{aligned} \Psi_0'' + p^2\Psi_0 &= -V\Psi_{-1}' \\ \Psi_{-1}'' + p_{-1}^2\Psi_{-1} &= V\Psi' \end{aligned}\right\}. \tag{5}$$

We use (4) to represent the expressions for the currents $J_c(x)$ and $J_s(x)$ in terms of wave functions in the wells as

$$\begin{aligned} J_c(x) &= -\frac{ie}{2m^*}[\Psi_0^*\Psi_{-1}' + \Psi_{-1}^*\Psi_0' - \text{c.c.}], \\ J_s(x) &= \frac{e}{2m^*}[\Psi_{-1}^*\Psi_0' - \Psi_0^*\Psi_{-1}' + \text{c.c.}]. \end{aligned} \tag{6}$$

A solution to system (5) may be sought in the form

$$\begin{aligned} \Psi_n(x) &= A_n\exp\delta x, \\ \tilde{\Psi}_n(x) &= \tilde{A}_n\exp\delta(x-a), \end{aligned} \tag{7}$$

where $n = 0$ or -1.

Wave function coefficients are determined from the boundary conditions that are obtained from the requirement that the functions are continuous and from the conditions imposed on the corresponding derivatives (see [6]). Introducing the obtained wave functions into the expressions for currents and performing certain calculations, we obtain the equations for the field and frequency of oscillations as

$$\begin{aligned} 1 &= \frac{\tilde{Q}\Gamma_1}{|\tilde{\Delta}(\lambda)|^2}\left\{(\delta E_3^2 + \Gamma_3^2)(\delta E_2^+\Gamma_2^- + \delta E_2^-\Gamma_2^+)\right. \\ &\left.\times\frac{\gamma\alpha^2 a}{2p^3} + \left(\sin pa + \frac{p}{\alpha}\frac{\gamma+\beta}{\gamma\beta}\right) + \frac{\lambda^2\Gamma_3}{4}\right\}, \\ \omega - \Omega &= \frac{\tilde{Q}\Gamma_1}{2\tau_0|\tilde{\Delta}(\lambda)|^2}\left\{(\delta E_3^2 + \Gamma_3^2)\delta E_2^+\delta E_2^-\right. \\ &\left.\times\frac{\gamma\alpha^2 a}{2p^3}\left(\sin pa + \frac{p}{\alpha}\frac{\gamma+\beta}{\gamma\beta}\right) + \frac{\lambda^2\delta E_3}{4}\right\}, \end{aligned} \tag{8}$$

where

$$\delta E_1 = E - E_1, \quad \delta E_2^{\pm} = E - \omega - E_2^{\pm},$$

$$\delta E_3 = E - 2\omega - E_3;$$

$$\tilde{\Delta}(\lambda) = (\delta E_1 + i\Gamma_1)(\delta E_2^+ + i\Gamma_2^+)(\delta E_2^- + i\Gamma_2^-)$$

$$\times(\delta E_3 + i\Gamma_3)\frac{\alpha a}{2p^2} - \lambda^2\Big[(\delta E_3 + i\Gamma_3)\frac{\gamma\alpha}{p} \qquad (9)$$

$$\times\left(\sin pa + \frac{p\gamma + \beta}{\alpha}\frac{}{\gamma\beta}\right) + \frac{p_-\gamma\alpha}{p^2}$$

$$\times(\delta E_1 + i\Gamma_1)\left(\frac{p_-}{\alpha}\frac{1+\gamma}{\gamma} - \sin p_- a\right)\Big],$$

$$p_- = \sqrt{E - (\tilde{\omega} + \omega)}, \quad p = \sqrt{E - \omega},$$

and the reduced pump current is given by

$$\tilde{Q} = \frac{4\pi\tau_0\eta}{\kappa}Q,$$

$$Q = \frac{q^2 p}{m^*}, \quad \eta = \frac{(16epp_-)^2}{\omega^3 a^3}. \qquad (10)$$

The level corresponding to the energy E_2 is split; the quantities referred to the upper and lower split off levels are denoted by the "+" and "–" superscripts, respectively.

The reduced lasing power is given by $\lambda^2 = \dfrac{16pp_-\tilde{V}^2}{a^2}$ and satisfies the condition $\tilde{V}^2 = \dfrac{2p_-^2V^2}{\omega^2} \ll 1$. The widths of electronic levels are defined as

$$\Gamma_1 = \frac{2p^3}{\alpha^2 a}, \quad \Gamma_2^\pm = 0.5\Gamma_1\{k_0^3 + \beta^{-2} \pm (k_0^3 - \beta^{-2})$$

$$\times(1 + [\gamma\beta^{-1} + 1 - k_0^2(1+\gamma)]^{-1})^{-0.5}\},$$

$$\Gamma_3 = \Gamma_1 k_0^3\beta^{-2}, \quad k_0 = p_-/p.$$

3. We now assume that the electrons arriving at the upper level in the first well have an energy that is approximately equal to E_1. Coherent oscillations in each of the wells under the conditions of resonance tunneling of electrons occur if the frequency of electromagnetic field applied to the structure is equal to the rate of transitions between the operating levels $\omega = \omega_{12} = \omega_{23}$. This can be attained by properly choosing the parameter $\tilde{\omega}$. The above condition implies that the inequality $\left|\frac{1}{\beta} - 1\right| > \frac{4}{3}\frac{1}{\gamma}$ holds. In the case where $\beta < 1$, the lasing occurs by the upper split off level E_2^+; in the case of $\beta > 1$, the lower level is involved. We use

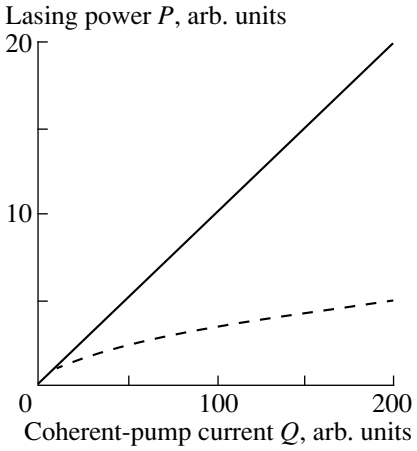

Fig. 2. Dependences of the lasing power (per unit length) $P = \lambda^2$ on the pump current Q for a single-well structure in the cases where there is no self-tuning ($\xi = 0$, the dashed line) and there is self-tuning ($\xi \neq 0$, the solid line).

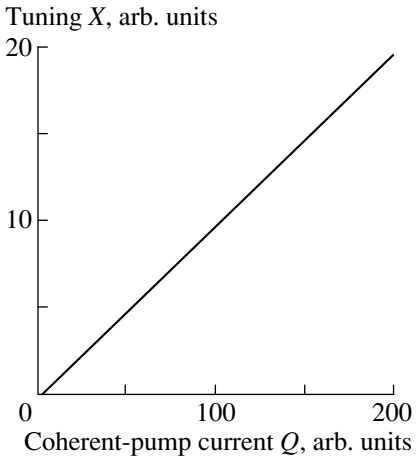

Fig. 3. The self-tuning $X = \xi^2$ as a function of the pump current Q for a two-well structure.

Eqs. (8) to derive the following expression for the threshold current ($\lambda^2 = 0$):

$$\tilde{Q}_{\text{th}} = \frac{4\tilde{\Gamma}_2^\pm}{1 \pm \sqrt{1 - k^{-1}}} \qquad (11)$$

(for details, see [8]). In this case, the pump-current dependence of the lasing power $P = \lambda^2$ is nonlinear and tends towards leveling off.

Basically another scheme of lasing takes place if the energy of incident electrons differs from the resonance energy by a certain quantity ξ. In the case of lasing in a one-dimensional structure [6], such conditions bring about a multifold increase in the radiation power

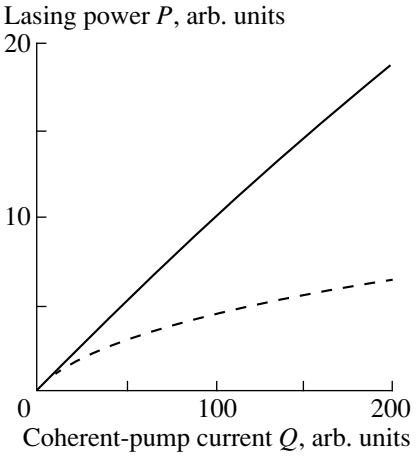

Fig. 4. Dependence of the lasing power (per unit length) $P = \lambda^2$ on the pump current Q for a two-well structure in the absence of self-tuning ($\xi = 0$, the dashed line) and in the presence of self-tuning ($\xi \neq 0$, solid line).

(Fig. 2). Equation (8) for the power may be now rewritten as

$$1 = \frac{0.125\tilde{Q}}{\left|\tilde{\Delta}^{\pm}(\tilde{\lambda})\right|^2}\{2\tilde{\Gamma}_2^{\pm}(\tilde{\xi}^2 + \tilde{\Gamma}_3^2) \times (1 \pm \sqrt{1-k^{-1}} + \tilde{\lambda}^2 k^{-1}\tilde{\Gamma}^3)\},$$
$$\tilde{\Delta}^{\pm}(\tilde{\lambda}) = (\tilde{\xi} + i)(\tilde{\xi} + i\tilde{\Gamma}_2^{\pm})(\tilde{\xi} + i\tilde{\Gamma}_3) - \tilde{\lambda}^2 \times \left[\tilde{\xi} + i\frac{\tilde{\Gamma}_3 + 1}{2} + i\frac{\tilde{\Gamma}_3 - 1}{2}\sqrt{1-k^{-1}}\right], \quad (12)$$

where $k = \left(1 - \frac{p_-^2}{p^2}\right)^2 (\gamma/\beta - \gamma)^2$ (all the quantities are expressed in the units of Γ_1). Calculations show that, if the dependence of the tuning ξ^2 on the pump current Q is chosen properly (see Fig. 3), the dependence $\lambda^2(Q)$ becomes linear and significantly excels the corresponding dependence for $\xi = 0$. Figure 4 shows the plots for a structure with $\tilde{\Gamma}_2^+ = 0.5$ and $\tilde{\Gamma}_3 = 5$. It is expedient to choose a broadening of the second level that is smaller than the broadening of the first level (the pump level) because this ensures a decrease in the threshold current and reduces the outflow of electrons to the region $x < 0$. Conversely, the broadening of the third level should be chosen larger than that of the first level because this is conducive to tunneling of electrons to the second well and to the region $x > 2a$ after completion of radiative transition to the third level.

We now compare the lasing conditions for the single- and two-well structures. As can be seen from Figs. 2 and 4, the pump-current dependences of the power (per unit length) for these structures are nearly the same. This makes it possible to conclude that, in a two-well structure, the lasing power is twofold larger than in a single-well structure; i.e., two wells operate coherently. Thus, the coherent mode with tuning is possible for two quantum wells as well.

ACKNOWLEDGMENTS

This study was performed within the framework of the "Physics of Solid-State Nanostructures" Program of the Ministry of Science and Technology of the Russian Federation (project no. 99-1140) and the Federal Special Program "Integration" (project no. A0133).

REFERENCES

1. R. Kazarinov and R. Suris, Fiz. Tekh. Poluprovodn. (Leningrad) **6**, 120 (1972) [Sov. Phys. Semicond. **6**, 96 (1972)].
2. J. Faist, F. Capasso, and D. L. Sivco, Science **264**, 553 (1994).
3. V. F. Elesin and Yu. V. Kopaev, Solid State Commun. **96**, 987 (1995).
4. V. F. Elesin and Yu. V. Kopaev, Zh. Éksp. Teor. Fiz. **108**, 2186 (1995) [JETP **81**, 1192 (1995)].
5. J. Faist, F. Capasso, and C. Sirtori, Appl. Phys. Lett. **66**, 538 (1995).
6. V. F. Elesin, Zh. Éksp. Teor. Fiz. **112**, 483 (1997) [JETP **85**, 264 (1997)].
7. V. F. Elesin, V. V. Kapaev, Yu. V. Kopaev, and A. V. Tsukanov, Pis'ma Zh. Éksp. Teor. Fiz. **66**, 709 (1997) [JETP Lett. **66**, 742 (1997)].
8. V. F. Elesin and A. V. Tsukanov, Preprint No. 004-99, MIFI (Moscow Institute of Engineering Physics, Moscow, 1999).

Translated by A. Spitsyn